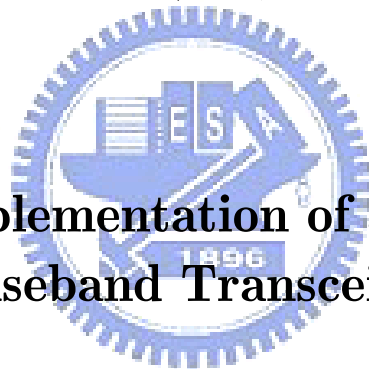


國立交通大學

資訊科學與工程研究所
博士論文

多重輸入輸出正交分頻多工基頻收發機
之設計與實現



Design and Implementation of a MIMO-OFDM
Baseband Transceiver

研究生：孫明福

指導教授：許騰尹

中華民國九十八年六月



多重輸入輸出正交分頻多工基頻收發機
之設計與實現

Design and Implementation of a MIMO-OFDM
Baseband Transceiver

研究生：孫明福

Student: Ming-Fu Sun

指導教授：許騰尹 博士

Advisor: Dr. Terng-Yin Hsu



A Dissertation

Submitted to Department of Computer Science

College of Computer Science

National Chiao Tung University

in Partial Fulfillment of the Requirements

for the Degree of Doctor of Philosophy

in

Computer Science

June 2009

Hsinchu, Taiwan, Republic of China

中華民國九十八年六月



多重輸入輸出正交分頻多工基頻收發機 之設計與實現

孫明福

國立交通大學資訊科學與工程研究所

指導教授：許騰尹教授

摘要

本研究探討了 4×4 多重輸入輸出正交分頻多工無線通訊系統與進階的接收技術，其中包含了抗 I/Q 不平衡效應的自動頻率調整器、訓練序列輔助的 I/Q 不平衡效應偵測、適應性通道偵測、以及數位波束成型。

為了偵測在 I/Q 不平衡效應干擾下的載波頻率偏移量，發展了一個基於虛擬載波頻率偏移技巧的載波頻率偏移偵測演算法。此演算法透過注入虛擬的載波頻率於三個連續的訓練序列來改善載波頻率偏移偵測的精準度。從模擬的結果中，演算法的偵測錯誤量大約是 0.3 ppm，並且低於傳統載波頻率偏移偵測演算法。透過 0.13- μm CMOS 製程，此演算法實現在一個測試晶片上。此測試晶片的面積為 $3.3 \times 0.4 \text{ mm}^2$ ，耗電量為 10 mW。

在直接降頻的架構下，必須同時考慮頻率相關 I/Q 不平衡與載波頻率偏移效應。本文提出一個利用訓練序列來偵測載波頻率偏移干擾下的 I/Q 不平衡效應。在載波頻率偏移干擾下的頻率相關 I/Q 不平衡效應可透過資料子載波與干擾子載波之間的關係偵測出來。模擬與實驗平台的結果顯示提出的方法可以有效改善系統效能。此外本文所提出的方法也相容於目前的無線區網標準。

最近對於移動下的無線通訊需求有增加的趨勢。為了達到高效能的接收機，就需要具備快速的通道追蹤能力。越快取得精確的通道狀態資訊並達到成功的傳輸是非常重要的。針對 4×4 多重輸入輸出正交分頻多工無線通訊系統，我們發展一個在時變通道下的適應性頻域通道偵測器。此適應性頻域通道偵測器利用每四組符號來確保通道偵測的精準度。為了降低硬體複雜度，利用了 Alamouti 矩陣的特性來設計有效率的 VLSI 架構。

最後透過0.13- μm CMOS製程，此適應性頻域通道偵測器的面積為 $3 \times 3.1 \text{ mm}^2$ ，另外 4×4 多重輸入輸出正交分頻多工無線通訊系統晶片在1.2V電壓下耗電量為62.8 mW。

此外，本研究也探討了數位波束成型在多重輸入輸出正交分頻多工通訊系統上的應用。數位波束成型是一種方向性濾波的技术，能有效的消除不必要的干擾，並正確的接收訊號。因此，數位波束成型技術可用來增加系統的容量與傳輸距離。

本研究探討收發機設計與元件實作。此外也建構了一個基於軟體定義的收發機平台來提供快速的原型機驗證。透過整體的效能指標評估，可在實作權衡上有效取得平衡。



Design and Implementation of a MIMO-OFDM Baseband Transceiver

by

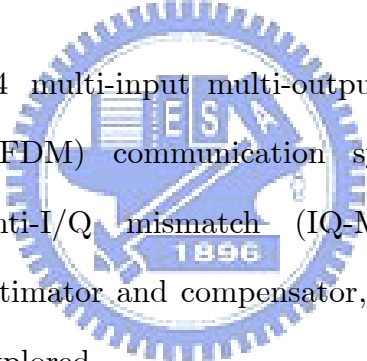
Ming-Fu Sun

Department of Computer Science

National Chiao Tung University

Advisor: Terng-Yin Hsu

Abstract



In this study, a 4×4 multi-input multi-output (MIMO) orthogonal-frequency division multiplexing (OFDM) communication system and advanced receiving techniques, including anti-I/Q mismatch (IQ-M) auto frequency controller, preamble-assisted IQ-M estimator and compensator, adaptive channel estimator, and digital beamforming are explored.

In order to estimate the carrier frequency offset (CFO) value under the conditions of IQ-M for direct-conversion structures, a pseudo-CFO (P-CFO) algorithm is developed. The proposed P-CFO algorithm rotates three training symbols by adding extra frequency offset into the received sequence to improve CFO estimation. Simulation results indicate that the estimation error of the proposed method is about 0.3 ppm, which is lower than those of two-repeat preamble-based methods. The proposed scheme is implemented as part of an OFDM wireless receiver fabricated in a 0.13- μm CMOS process with $3.3 \times 0.4 \text{ mm}^2$ core area and 10 mW power consumption.

In direct-conversion receivers, the impact of frequency-dependent IQ-M with CFO

must be considered. A preamble-assisted estimation is developed to circumvent the frequency-dependent IQ-M with CFO. The frequency-dependent IQ-M with CFO can be estimated by taking advantage of the relationship between desired sub-carriers and image sub-carriers. Both simulation and experiment results indicate that the proposed method can meet system requirements by preventing frequency-dependent IQ-M from significantly degrading the performance. Moreover, the proposed scheme is compatible with current wireless local area network standards.

Recently, the request for wireless communication under mobile conditions is increased. The ability of fast channel tracking is therefore needed to achieve high performance receivers. For successful transmissions, obtaining accurate channel state information as soon as possible is extremely important. An adaptive frequency-domain channel estimator (FD-CE) for equalization of 4×4 MIMO-OFDM system in time-varying frequency-selective fading is developed. The proposed adaptive FD-CE ensures the channel estimation accuracy in each set of four MIMO-OFDM symbols. To decrease complexity, the rich feature of Alamouti-like matrix is exploited to derive an efficient VLSI solution. Finally, this adaptive FD-CE using an in-house $0.13\text{-}\mu\text{m}$ CMOS library occupies an area of $3 \times 3.1 \text{ mm}^2$, and the 4×4 MIMO-OFDM modem consumes about 62.8 mW at 1.2V supply voltage.

In addition, digital beamforming for MIMO-OFDM communications is also studied. Digital beamforming is a method of spatial filtering, which can eliminate unwanted interferences and receive desired signal accurately. Consequently, digital beamforming can be used to increase system capacity and transmission range.

In this study, the transceiver design and circuit implementation are presented. A software-defined radio is also constructed for rapid verification and fast prototyping. Based on the overall system performance index, the implementation trade-offs can be balanced.

Acknowledgments

This dissertation describes the research work I performed in the Integration System and Intellectual Property (ISIP) Laboratory during my graduate studies at National Chiao Tung University. This work would not be possible without the support of many people. I would like to express my most sincere gratitude to all those who have made this possible.

First of all, I would like to thank Prof. Terng-Yin Hsu for the advice, guidance, and funding he has provided me with. I feel honored by being able to work with him. I would like to thank the committee members for their contribution for reviewing the manuscript and providing me with valuable feedback.

I would like to warmly thank many of present and former ISIP members: You-Hsien Lin, Wei-Chi Lai, Ta-Yang Juan, Shih-Lin Lo, Frank Hsiao, Jin-Hwa Guo, Chueh-An Tsai, Ming-Yeh Wu, Ming-Feng Shen, Li-Sheng Lu, Jyun-Rong Li, Hsin-Nan Chen, Kan-Si Lin, I-Yin Liu, Chuen-Tai Wang, Cheng-Yuan Lee, Yen-Her Chen, Shao-Hung Lu, and Chang-Ying Chuang, whose contributions were instrumental in the development of ideas. I also want to thank Min-Zheng Shieh, Ja-Hsing Kao, and Chon-Jei Lee for their friendship.

In addition, I gratefully acknowledge the constructive comments provided by Dr. Chien-Ching Lin and the wisdom of life experience shared by Prof. Terng-Ren Hsu.

Most of all, I am indebted to my family for their unconditional love and support they provide me with. It means a lot to me.

Ming-Fu Sun

Hsinchu, Taiwan



Table of Contents

List of Tables	xi
List of Figures	xii
List of Acronyms	xvi
Chapter 1 Introduction	1
1.1 Motivation.....	1
1.2 Dissertation Overview.....	4
Chapter 2 Overview of MIMO-OFDM Systems	7
2.1 MIMO Wireless Communications.....	7
2.1.1 Antenna Configurations.....	7
2.1.2 Capacity Results.....	9
2.1.3 Space-Time Processing.....	11
2.1.4 MIMO-OFDM Systems.....	15
2.2 Non-Ideal Front-End Effects.....	16
2.2.1 Effects of Carrier Frequency Offset.....	17
2.2.2 Effects of I/Q Mismatch.....	23
2.2.3 Effects of Non-linearity.....	27
2.2.4 DC Offset.....	29
2.2.5 Quantization Noise and Clipping.....	30
2.3 Wireless Channel Models.....	32
2.3.1 AWGN.....	32
2.3.2 Multipath.....	34
2.3.3 MIMO Channel: TGn Channel Model.....	36
2.4 Summary.....	37

Chapter 3 Anti-I/Q Mismatch Auto Frequency Controller	39
3.1 System Model.....	42
3.2 Estimation for Carrier Frequency Offset.....	44
3.2.1 Conventional Algorithm.....	44
3.2.2 The Proposed Pseudo CFO Algorithm.....	48
3.3 Simulation and Performance.....	53
3.4 Implementation Hints.....	60
3.4.1 Design Methodology.....	60
3.4.2 Architecture of P-CFO Algorithm.....	61
3.4.3 Verification Platform.....	64
3.5 Summary.....	67
Chapter 4 Preamble-Assisted Estimation for I/Q Mismatch	69
4.1 System Model.....	71
4.2 Constant IQ-M Estimation.....	74
4.2.1 Constant IQ-M Estimation without CFO.....	74
4.2.2 Constant IQ-M Estimation with CFO.....	79
4.3 Frequency-Dependent IQ-M Estimation.....	87
4.3.1 The Proposed Method.....	87
4.3.2 Simulation and Experiment Results.....	91
4.4 Transmitter IQ-M Estimation.....	97
4.4.1 Problem Statement.....	97
4.4.2 The Proposed Method.....	99
4.5 Summary.....	104
Chapter 5 Adaptive Channel Estimation	105
5.1 System Description and Problem Statement.....	108
5.1.1 Modem Specification.....	108
5.1.2 Problem Statement.....	109
5.2 STBC Decoder and Equalization.....	110
5.3 The Proposed Method.....	112
5.3.1 Adaptive Frequency-Domain Channel Estimator.....	112
5.3.2 Discussion.....	118
5.4 Performance Evolution.....	122
5.5 Architecture and Implementation.....	123

5.5.1	Proposed Architecture.....	123
5.5.2	Implementation Results.....	130
5.6	Summary.....	133
Chapter 6	Digital Beamforming	135
6.1	The Basics of Digital Beamforming.....	136
6.2	Angle-of-Arrival Estimation.....	140
6.2.1	Capon AOA Estimate.....	142
6.2.2	MUSIC AOA Estimate.....	145
6.3	Array Factor Calculation.....	147
6.4	Digital Beamforming in MIMO Transmission.....	154
6.5	Summary.....	157
Chapter 7	Conclusion	159
7.1	Summary.....	159
7.2	Future Work.....	161
References		165
Appendix A	Derivation of (2.15)	175
Appendix B	Derivation of (3.13)	179
Appendix C	Derivation of (4.12)	181
Appendix D	Supplementary of OFDM-Based System Specification	183
D.1	SISO-OFDM Systems.....	183
D.1.1	Air Interface.....	183
D.1.2	Major Parameters.....	184
D.1.3	Frame Structure.....	186
D.2	MIMO-OFDM Systems.....	188
D.2.1	Air Interface.....	188
D.2.2	Major Parameters.....	189
D.2.3	Frame Structure.....	192
Appendix E	Some Circuit Implementation Issues	194
E.1	Complex Multiplier.....	194
E.2	Fast Fourier Transform.....	195
E.3	Numerically Controlled Oscillator.....	197
Appendix F	Fourier Transforms and Operations	199

About the Author

200

Publication Lists

201



List of Tables

TABLE 2-1	AM-AM and AM-PM Models.....	28
TABLE 3-1	Simulation Parameters.....	55
TABLE 3-2	Required SNR.....	60
TABLE 3-3	Complex Multiplier.....	62
TABLE 3-4	The Complexity (Gate Count) of P-CFO.....	62
TABLE 3-5	Chip Summary.....	63
TABLE 4-1	Experiment Parameters.....	93
TABLE 5-1	Operation of the Adaptive FD-CE.....	117
TABLE 5-2	Experimental Parameters.....	132
TABLE 5-3	Synthesized Results (Gate Count).....	132
TABLE 5-4	Chip Summary of The 4×4 MIMO-OFDM Modem.....	132
TABLE 6-1	Weight Vectors for the Two-Element Array.....	152
TABLE 6-2	Weight Vectors for the Four-Element Array.....	152
TABLE D-1	Modulation Parameters.....	185
TABLE D-2	Timing Related Parameters.....	186
TABLE D-3	Modulation Parameters.....	191
TABLE D-4	Timing Related Parameters.....	192
TABLE F-1	Fourier Transforms.....	199
TABLE F-2	Fourier Operations.....	199

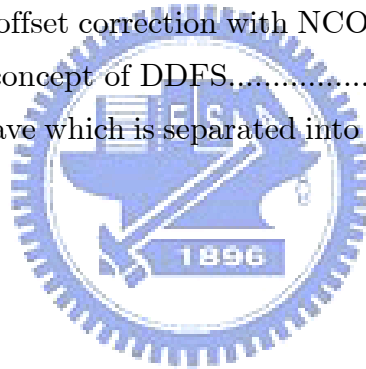
List of Figures

Figure 1-1	Data rate versus mobility of wireless communication standards.....	2
Figure 2-1	Different antenna configurations.....	8
Figure 2-2	Block diagram of the MIMO system.....	10
Figure 2-3	Block diagram of the 2×2 MIMO system with Alamouti's scheme.....	12
Figure 2-4	Space-time block code in the MIMO-OFDM system.....	13
Figure 2-5	Block diagram of the 4×4 MIMO-OFDM system.....	16
Figure 2-6	Direct-conversion receiver.....	17
Figure 2-7	(a) I/Q demodulation. (b) Signal spectrum.....	18
Figure 2-8	The behavior of the CFO in the spectrum domain.....	19
Figure 2-9	The received sub-carriers in the presence of CFO.....	21
Figure 2-10	QPSK constellation in the case of the AWGN channel. (a) CFO: 0 ppm. (b) CFO: 5 ppm.....	22
Figure 2-11	Direct-conversion receiver with I/Q mismatch.....	23
Figure 2-12	16-QAM constellation. (a) Without I/Q mismatch. (b) Gain error: 1dB, Phase error: 10 degree.....	25
Figure 2-13	Image suppression as a function of the I/Q mismatch.....	26
Figure 2-14	Power transfer function.....	27
Figure 2-15	AM-AM and AM-PM function model.....	28
Figure 2-16	The effect of AM-AM on a 64-QAM constellation.....	29
Figure 2-17	Effects of quantization noise and clipping.....	31
Figure 2-18	(a) Gaussian distribution. (b) Rayleigh distribution.....	33
Figure 2-19	Multiple paths.....	34
Figure 2-20	Power delay profile.....	35
Figure 3-1	OFDM receiver with IQ-M and CFO.....	42

Figure 3-2	The preamble structure of the IEEE 802.11a/g.....	45
Figure 3-3	(a) Complex plane for the terms in (3.9). (b) CFO estimation by two-repeat preamble-based method under 19 dB SNR.....	47
Figure 3-4	Inverse cosine function.....	51
Figure 3-5	The flowchart of the proposed P-CFO algorithm.....	53
Figure 3-6	Frequency offset estimation.....	55
Figure 3-7	CFO estimation by the two-repeat preamble-based method.....	56
Figure 3-8	CFO estimation by the proposed P-CFO algorithm.....	56
Figure 3-9	PDF of 50 ppm CFO: (a) P-CFO algorithm. (b) Two-repeat preamble-based method.....	58
Figure 3-10	Mean square error (MSE) of frequency estimation vs. SNR under different I/Q imbalance conditions with 50 ppm CFO.....	59
Figure 3-11	Average of the estimation error.....	59
Figure 3-12	Hardware architecture of the P-CFO algorithm.....	63
Figure 3-13	Chip micrograph.....	64
Figure 3-14	The photo of platform.....	65
Figure 3-15	Estimated CFO of measurement vs. simulation.....	65
Figure 3-16	Measurements of QPSK constellation: (a) P-CFO method. (b) Two-repeat preamble-based method.....	66
Figure 4-1	Direct-conversion receiver with I/Q mismatch and CFO.....	72
Figure 4-2	Received signal with I/Q mismatch: (a) Amplitude. (b) Angle.....	73
Figure 4-3	The estimated channel frequency response.....	76
Figure 4-4	Data flow of the constant IQ-M estimation and compensation.....	79
Figure 4-5	(a) The block diagram for the IQ-M estimation. (b) The compensation blocks for IQ-M and CFO.....	86
Figure 4-6	Mutual interference due to I/Q mismatch.....	88
Figure 4-7	The proposed frequency-dependent IQ-M estimation architecture.....	90
Figure 4-8	BER performance of 16-QAM and 64-QAM modulation.....	92
Figure 4-9	PER performance of 16-QAM and 64-QAM modulation.....	93
Figure 4-10	Experiment setup for verification.....	94
Figure 4-11	Measurement of constellation diagram: (a) Before compensation. (b) After compensation.....	96
Figure 4-12	Channel frequency response.....	97
Figure 4-13	An OFDM system with transceiver IQ-M and CFO.....	98

Figure 4-14	Block diagram representation of the proposed method. (a) Transmitter part with pre-compensation scheme. (b) Receiver part with joint compensation scheme.....	104
Figure 5-1	Block diagram of the 4×4 STBC MIMO-OFDM modem.....	109
Figure 5-2	Space-time block code in the 4×4 MIMO-OFDM system.....	111
Figure 5-3	Sub-carrier frequency allocation.....	113
Figure 5-4	Block diagram of the adaptive frequency-domain equalizer.....	114
Figure 5-5	Relationship between decided symbol and decoded symbol.....	116
Figure 5-6	(a) The block diagram of the $2 \times N$ MIMO system. (b) The block diagram of the $3 \times N$ MIMO system with STBC matrix C_3	119
Figure 5-7	BER and PER performance.....	123
Figure 5-8	Architecture of the adaptive FD-CE.....	124
Figure 5-9	Flowchart of matrix inverse computation.....	125
Figure 5-10	Architecture of MI. The bit width includes real and image parts. (a) Matrix multiplier for $\mathbf{H}_{21,k} \mathbf{H}_{11,k}^{-1}$ and $\mathbf{H}_{21,k} \mathbf{H}_{11,k}^{-1} \mathbf{H}_{12,k}$. (b) Matrix multiplier for $\mathbf{D}_k^{-1} \mathbf{H}_{21,k} \mathbf{H}_{11,k}^{-1}$	127
Figure 5-11	Architecture of matrix inverter (Alamouti matrix).....	128
Figure 5-12	Architecture of MM. The bit width includes real and image parts.....	129
Figure 5-13	Software-defined radio platform.....	131
Figure 5-14	Chip microphotograph of the 4×4 MIMO-OFDM modem.....	133
Figure 6-1	A generic digital beamforming system.....	136
Figure 6-2	Two-element array for interference suppression.....	137
Figure 6-3	(a) Array factor for a non-weighted two-element array. (b) Array factor for a weighted two-element array.....	139
Figure 6-4	M -element array with arriving signals.....	140
Figure 6-5	M -element array with two arriving signals.....	143
Figure 6-6	Capon pseudospectrum.....	144
Figure 6-7	MUSIC pseudospectrum.....	147
Figure 6-8	Five-element antenna array.....	148
Figure 6-9	(a) Array factor for $\theta_D = 0^\circ$. (b) Array factor for $\theta_D = 30^\circ$	151
Figure 6-10	Corresponding array factors. (a) Weight vector = $[+1 +1]$. (b) Weight vector = $[+1 -1]$	152
Figure 6-11	Corresponding array factors. (a) Weight vector = $[+1 +1 +1 +1]$. (b) Weight vector = $[+1 -1 +1 -1]$. (c) Weight vector =	

	$[+1 -j -1 +j]$. (d) Weight vector = $[+1 +j -1 -j]$	153
Figure 6-12	2×2 MIMO WLAN system.....	154
Figure 6-13	Channel with angle-time pattern.....	155
Figure 6-14	Space-time beamforming architecture.....	156
Figure D-1	Transmitter block diagram for IEEE 802.11g (ERP-OFDM only)....	183
Figure D-2	PSDU frame format.....	187
Figure D-3	OFDM training structure.....	187
Figure D-4	Transmitter block diagram for MIMO-OFDM systems.....	189
Figure D-5	(a) The block diagram of the SISO system. (b) The block diagram of the MIMO system with Alamouti scheme.....	191
Figure D-6	PSDU frame format.....	193
Figure E-1	The radix-2 single-path delay feedback architecture.....	195
Figure E-2	Radix-2 SDF butterfly unit.....	196
Figure E-3	The processing for IFFT operations.....	196
Figure E-4	Frequency offset correction with NCO.....	197
Figure E-5	The basic concept of DDS.....	198
Figure E-6	The sine wave which is separated into four regions.....	198



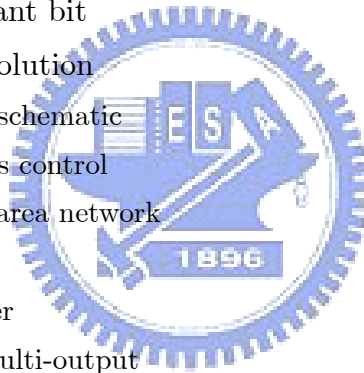
List of Acronyms

The following acronyms are used through this text.

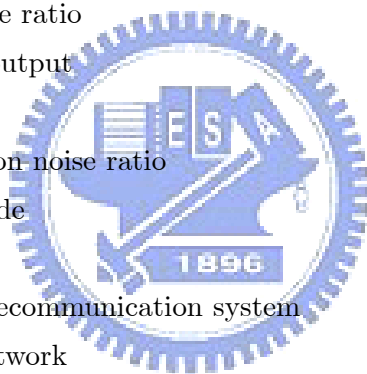
3G	third-generation
3GPP	3 rd Generation Partnership Project
ADC	analog-to-digital converter
AFC	auto frequency controller
AOA	angle-of-arrival
AOD	angle-of-departure
API	application programming interface
APR	auto place and routing
AS	angular spread
ASIC	application-specific integrated circuit
AWGN	additive white Gaussian noise
BER	bit error rate
BPSK	binary phase shift keying
CFO	carrier frequency offset
CFR	channel frequency response
CMOS	complimentary metal-oxide-semiconductor
CORDIC	coordinate rotation digital computer
CP	cyclic prefix
CRLB	Cramér-Rao lower bound
CSI	channel state information
DA	data-aided
DAB	digital audio broadcasting
DAC	digital-to-analog converter
DC	direct current
DOA	direction of arrival
DRC	design rule checking
DVB-T	digital video broadcasting terrestrial TV



EVM	error vector magnitude
FD-CE	frequency-domain channel estimator
FEC	forward error correction
FFT	fast Fourier transform
FPGA	field programmable gate array
GI	guard interval
GIB	guard interval based
HDL	hardware-description language
ICI	inter-carrier interference
IFFT	inverse fast Fourier transform
I/Q	in phase/quadrature phase
IQ-M	I/Q mismatch
IRR	image rejection ratio
LO	local oscillator
LPF	low-pass filter
LSB	least significant bit
LTE	long term evolution
LVS	layout versus schematic
MAC	medium access control
MAN	metropolitan area network
MG	mirror gain
MI	matrix inverter
MIMO	multi-input multi-output
MISO	multiple-input single-output
ML	maximum likelihood
MM	matrix multiplier
MMSE	minimum mean square error
MSE	mean square error
MUSIC	multiple signal classification
NCO	numerically controlled oscillator
NDA	non-data-aided
NLS	nonlinear least squares
OFDM	orthogonal frequency-division multiplexing
OFDMA	orthogonal frequency-division multiple access
P-CFO	pseudo carrier frequency offset
PDA	personal digital assistant
PDF	probability density function
PDP	power delay profile



PER	packet error rate
PHY	physical layer
PLCP	physical layer convergence procedure
PPDU	PLCP protocol data unit
PSDU	physical layer service data unit
QAM	quadrature amplitude modulation
QPSK	quadrature phase shift keying
R2SDF	radix-2 single-path delay feedback
RF	radio frequency
RMS	root mean square
RX	receiver
SC-FDMA	single carrier-frequency division multiple access
SDM	spatial-division multiplexing
SG	signal gain
SIMO	single-input multiple-output
SIR	signal-to-interference ratio
SISO	single-input single-output
SNR	signal-to-noise ratio
SQNR	signal-to-quantization noise ratio
STBC	space-time block code
TX	transmitter
UMTS	universal mobile telecommunication system
VANET	vehicular ad hoc network
VHT	very high throughput
VLSI	very-large-scale integration
WLAN	wireless local area network
ZF	zero-forcing



Chapter 1

Introduction

1.1 Motivation



In recent years, there is an increasing application for higher spectrum efficient, higher data rate, better quality of service, and higher system capacity. The data rate and mobility of some wireless communication standards are shown in Figure 1-1. There is a trend that multi-input multi-output (MIMO) transmission has emerged as a potential technology in the future standards. Specifically, MIMO techniques have been integrated into third-generation (3G) cellular systems [1], wireless local area networks (IEEE 802.11n) [2], and broadband wireless access networks (IEEE 802.16e) also known as WiMAX [3]. MIMO communication systems are defined by considering that multiple antennas are used at the transmit part as well as at the receive part. By using the spatial and polarization properties of the multipath channels, MIMO communication systems offer new dimensions that can be used to enhance the quality of communication.

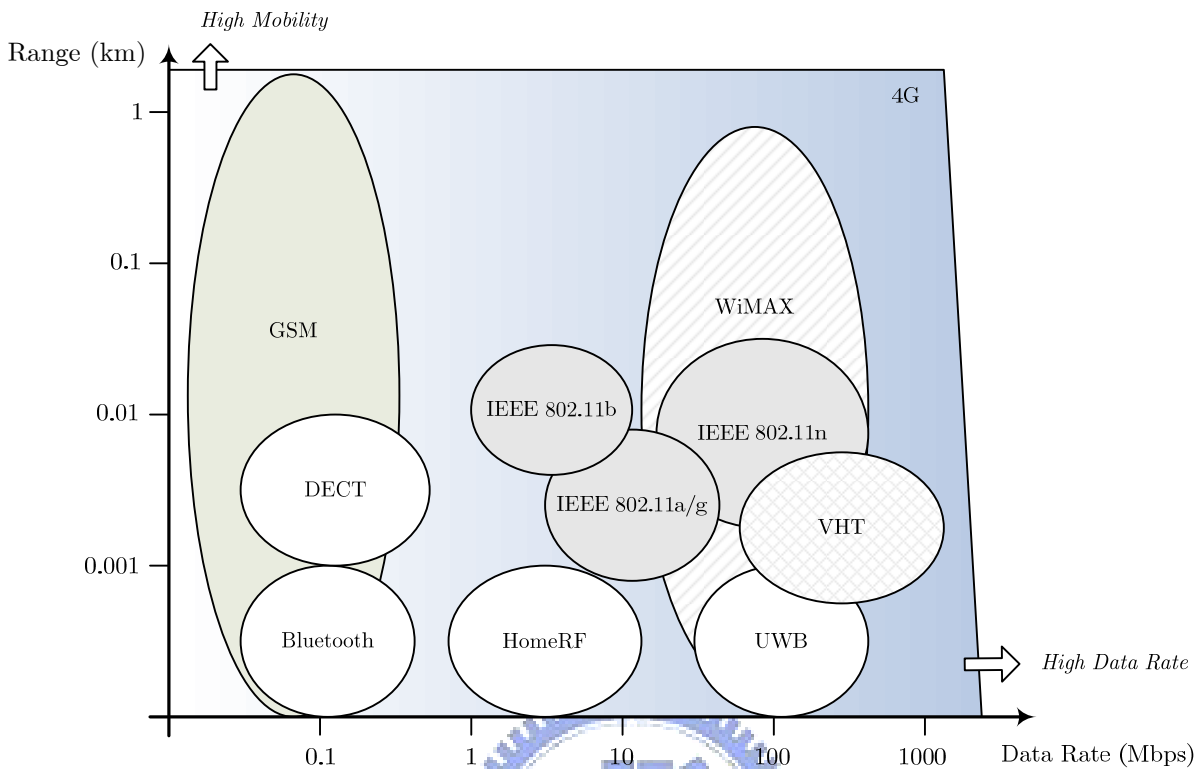


Figure 1-1. Data rate versus mobility of wireless communication standards.

Due to the use of antenna arrays, spatial diversity can be obtained. The concept of spatial diversity is that the signal-to-noise ratio is significantly improved by combining the signal transmitted from different antennas. In order to approach the capacity of MIMO channels, the space-time processing is employed. Space-time processing is a tool for improving the overall economy and efficiency of a MIMO communication system. Space-time processing can improve the signal-to-interference ratio through co-channel interference cancellation, mitigate fading through receive diversity, offer higher signal-to-noise ratio through array gain, and reduce inter-symbol interference through spatial equalization.

In addition, orthogonal-frequency division multiplexing (OFDM) is a popular technique which operates with specific orthogonality constraints between sub-carriers. Because of these constraints, OFDM modulation is a spectrally efficient signaling

method for communication over frequency-selective fading channels. OFDM modulation has been utilized by many standards, including IEEE 802.11a/g/n-based WLAN systems [2], [4], [5], digital audio broadcasting (DAB) [6], and digital video broadcasting terrestrial TV (DVB-T) [7]. Therefore, MIMO-OFDM arrangements have been suggested for frequency-selective fading channels, where space-time coding or space-frequency coding is used across the different antennas in conjunction with OFDM [8].

In this study, a 4×4 MIMO-OFDM communication system and advanced receiving techniques are explored. The transceiver design and implementation are also presented. In order to realize the 4×4 MIMO-OFDM communication system, some impairments are taken into account. For instance, synchronization tasks, such as timing synchronization and frequency synchronization, are essential in the practical implementation. Other impairments which can degrade the system performance are channel effects and non-ideal front-ends. To support reliable reception of the transmitted data, robust algorithms must be developed.

A software-defined radio is also constructed for rapid verification and fast prototyping. This experimental platform comprises of MATLAB model, field programmable gate array (FPGA) board, and radio frequency (RF) front-end. The proposed design is directly mapped onto the FPGA chips with on-board 14-bit digital-to-analog converters (DACs) to transform the digital data into analog signals. The signals are then transmitted by RF front-ends. After down-converting RF signals to baseband at receiver part, the analog signals are fed into 14-bit analog-to-digital converters (ADCs).

Another important issue is the implementation cost. In order to achieve low hardware cost and low power consumption, low complexity algorithms and efficient very-large-scale integration (VLSI) architectures are preferable. For instance, the

proposed algorithms are evaluated using additional factors, such as numerical precision, relative VLSI architecture, and memory requirements. Based on the overall system performance index, the implementation trade-offs can be balanced.

1.2 Dissertation Overview

The system considerations and channel models are introduced in Chapter 2. A brief introduction of the MIMO-OFDM system is given. The fundamental understanding of MIMO technology and space-time processing is presented. In addition, the impact of impairments on the system performance is also discussed. In order to maintain the system performance, some essential algorithms are developed.

In Chapter 3, an anti-I/Q mismatch (IQ-M) auto frequency controller (AFC) is developed. Frequency synchronization is a critical problem for the MIMO-OFDM system. Various frequency offset estimation algorithms have been developed in the open literature. However, it is shown that some methods are not suitable for current wireless systems since the packet format is not compatible with current standards. The proposed carrier frequency offset (CFO) estimation method, based on pseudo CFO (P-CFO) technology, can estimate the CFO value under the conditions of IQ-M. Additionally, the proposed P-CFO algorithm is also compatible with the conventional method.

In Chapter 4, preamble-assisted estimation methods are developed to circumvent the effect of IQ-M. Because IQ-M can degrade the accuracy of CFO estimation and introduce image interference, the compensation for IQ-M is necessary. Many IQ-M estimation methods are published in the open literature. However, most methods focus on the constant IQ-M only. Because of the impairment in the analog components, the low-pass filters of I and Q channels are not identical, resulting in frequency-dependent

IQ-M. The proposed methods can estimate not only constant IQ-M but also frequency-dependent IQ-M.

In Chapter 5, an adaptive channel estimator in STBC MIMO-OFDM modems is developed. In order to realize the gains obtained from MIMO channels, obtaining accurate channel state information in time-varying environments is extremely important. In order to reduce the hardware cost, the proposed adaptive channel estimator utilizes the property of the Alamouti-like matrix to decrease the cost of complex operators.

In Chapter 6, digital beamforming for wireless communications is presented. In order to improve the signal quality, digital beamforming is performed digitally to form the desired output.

Finally, Chapter 7 describes the conclusions of this work and indicates some promising directions for future research.





Chapter 2

Overview of MIMO-OFDM Systems

This chapter serves as a brief introduction to multi-input multi-output (MIMO) orthogonal frequency-division multiplexing (OFDM) wireless communication systems. The impact of non-ideal front-ends on system performance is also discussed.



2.1 MIMO Wireless Communications

2.1.1 Antenna Configurations

Figure 2-1 shows different antenna configurations. Single-input single-output (SISO) which uses one transmit antenna and one receive antenna is the well-known configuration, single-input multiple-output (SIMO) uses one transmit antenna and multiple receive antennas, multiple-input single-output (MISO) has multiple transmit antennas and a single receive antenna, and, finally, MIMO has multiple transmit

antennas and multiple receive antennas.

With MIMO, the system can effectively provide the array gain [9]-[12]. Array gain is the average increase in the signal-to-noise ratio (SNR) at the receiver that arises from the coherent combining effect of multiple antennas at the receiver, transmitter or both. If the channel is known to the multiple antenna transmitter, the transmitter can weight the transmission with weights, depending on the channel state information, so that there is coherent combining at the single antenna receiver. The array gain in this case is called transmitter array gain. For the SIMO system with perfect knowledge of the channel at the receiver part, the receiver can suitably weight the incoming signals so that the signals are coherently added up at the output. This case is called receiver array gain. In order to achieve the array gain, multiple antenna systems require perfect channel knowledge at the transmitter, receiver or both.

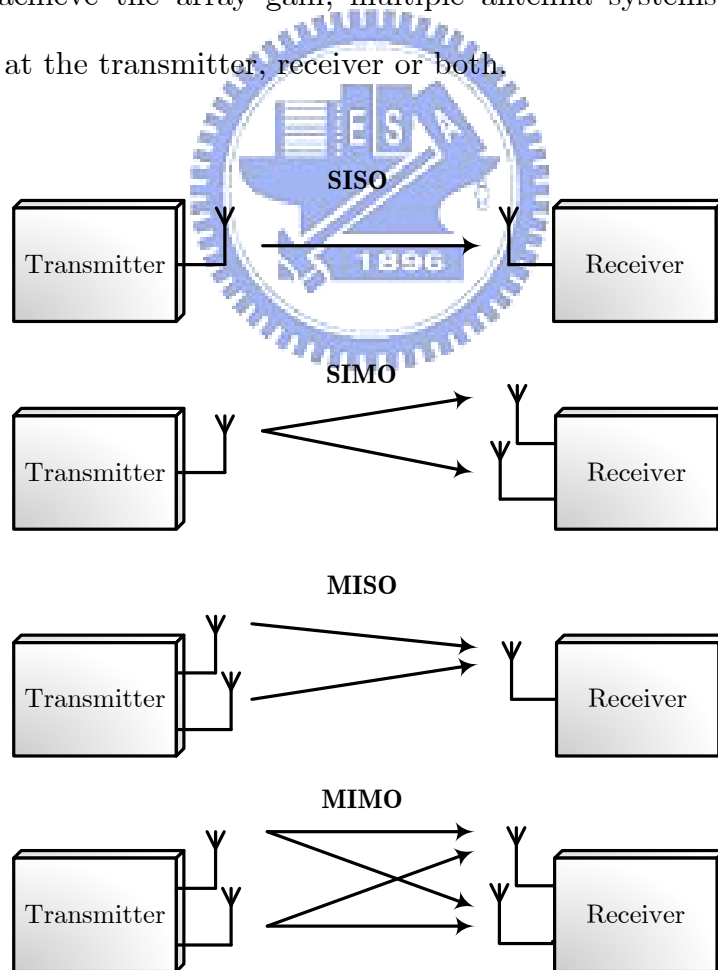


Figure 2-1. Different antenna configurations.

2.1.2 Capacity Results

Based on Shannon's theorem, capacity is a measure of the maximum transmission rate for reliable communication on a given channel. Firstly, let us consider the SISO system on the additive white Gaussian noise (AWGN) channel. The capacity of the channel is expressed as

$$C = \log_2(1 + P) \quad (\text{bits/s/Hz}) \quad (2.1)$$

where P is the average signal-to-noise ratio (SNR) at the receiver. The capacity, as defined in (2.1), is also known as the spectral efficiency. If the transmission rate is less than C bits/s/Hz, then an appropriate coding scheme exists that could lead to reliable and error-free communication. On the contrary, if the transmission rate is more than C bits/s/Hz, then the received signal, regardless of the employed coding scheme, will involve bit errors. MIMO communication technology has received significant attention due to the rapid development of high-speed wireless communication systems employing multiple transmit and receive antennas. Theoretical results show that MIMO systems can offer significant capacity gain over traditional SISO channels. This increase in capacity is enabled by the fact that in rich scattering environments, the signals from each transmitter appear highly uncorrelated at each of the receive antennas, i.e., the signals corresponding to each of the individual transmit antennas have attained different spatial signatures. The receiver exploits these differences in spatial signatures to separate these signals.

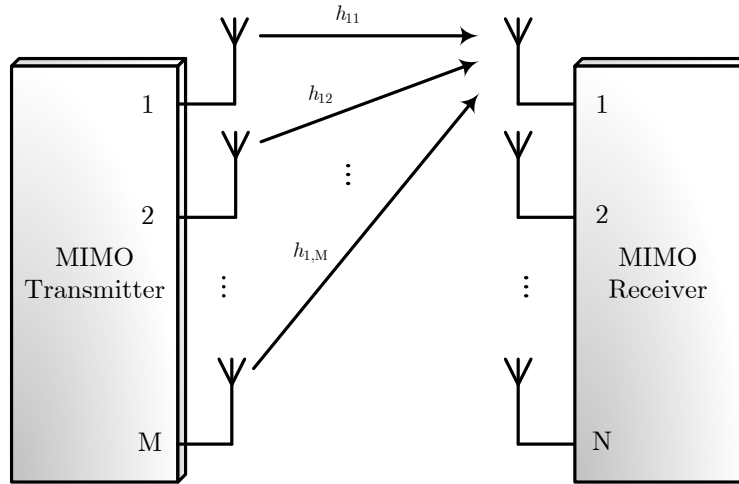


Figure 2-2. Block diagram of the MIMO system.

Figure 2-2 shows the block diagram of the MIMO system with M transmit antennas and N receive antennas. The input-output relationship of this system is expressed as

$$\mathbf{Y} = \mathbf{H}\mathbf{X} + \mathbf{W} \quad (2.2)$$

where $\mathbf{X} = [x_1 \ x_2 \ \dots \ x_M]^T$ is the transmitted data vector, $\mathbf{Y} = [y_1 \ y_2 \ \dots \ y_N]^T$ is the received data vector, and $\mathbf{W} = [w_1 \ w_2 \ \dots \ w_N]^T$ is the noise vector. \mathbf{H} denotes the $N \times M$ channel matrix which is defined by

$$\mathbf{H} = \begin{bmatrix} h_{11} & h_{12} & \cdots & h_{1,M} \\ h_{21} & h_{22} & \cdots & h_{2,M} \\ \vdots & \vdots & \ddots & \vdots \\ h_{N,1} & h_{N,2} & \cdots & h_{N,M} \end{bmatrix} \quad (2.3)$$

where h_{ij} is the complex gain from the j th transmit antenna to the i th receiver antenna.

If the channel matrix is known at the receiver, the capacity equation of the MIMO

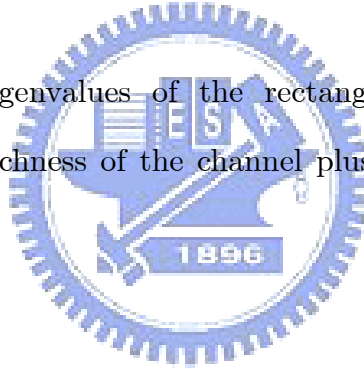
channel is given by [13]

$$C = \log_2 \left(\det \left(\mathbf{I} + \frac{P}{M} \mathbf{H}\mathbf{H}^H \right) \right) \quad (\text{bits/s/Hz}) \quad (2.4)$$

where \mathbf{I} denotes the identity matrix, the superscript H indicates the conjugate transpose, and P is the per-receive antenna SNR. In order to gain insight on the capacity, (2.4) can be expressed as [13]

$$C = \sum_{i=1}^{\min\{N,M\}} \log_2 \left(1 + \frac{P}{M} \lambda_i \right) \quad (\text{bits/s/Hz}) \quad (2.5)$$

where λ_i denotes the eigenvalues of the rectangular $\mathbf{H}\mathbf{H}^H$ matrix. Mainly, the capacity is equal to the richness of the channel plus a term depending on the power level.



2.1.3 Space-Time Processing

In order to improve the reliability for MIMO communication, space-time coding techniques are developed. A pioneering work in the area of space-time coding for MIMO channels has been carried out by Tarokh *et al.* in [14]-[15]. However, the coding scheme in [14]-[15] requires high decoding complexity. Afterward, Alamouti developed the most famous space-time block coding (STBC) scheme for two transmit and multiple receive antennas [16]. The complexity of the maximum likelihood decoder for Alamouti's code is very low. Figure 2-3 shows the block diagram of the 2×2 MIMO system with Alamouti's code. The encoding rule of Alamouti's scheme is

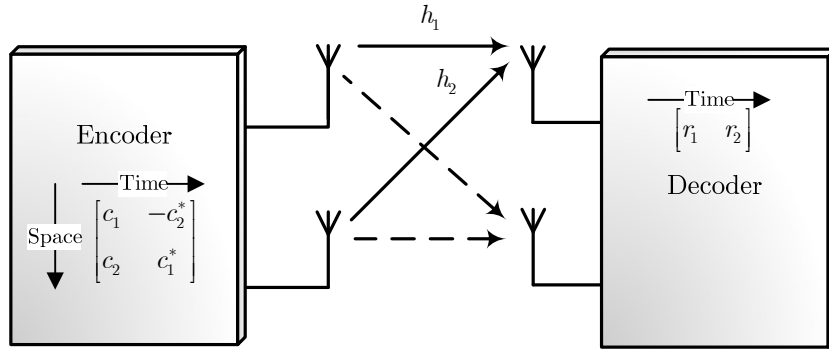


Figure 2-3. Block diagram of the 2×2 MIMO system with Alamouti's scheme.

$$\begin{bmatrix} c_1 & c_2 \end{bmatrix} \rightarrow \begin{bmatrix} c_1 & -c_2^* \\ c_2 & c_1^* \end{bmatrix} \quad (2.6)$$

where c_i , $i = 1, 2$ terms represent the transmitted complex symbols. In the first time slot, antenna one transmits c_1 and antenna two transmits c_2 . In the next time slot, antenna one transmits $-c_2^*$ and antenna two transmits c_1^* . The columns of the matrix represent time slots and the rows denote transmit antennas. Since two time slots are required to transmit two symbols, the code rate for Alamouti's scheme is equal to one. Assuming that the channel coefficients are constant in both consecutive symbol periods, the symbols received by antenna one over two consecutive time slots are given by

$$\begin{bmatrix} r_1 \\ r_2^* \end{bmatrix} = \begin{bmatrix} h_1 & h_2 \\ h_2^* & -h_1^* \end{bmatrix} \begin{bmatrix} x_1 \\ x_2 \end{bmatrix} + \begin{bmatrix} w_1 \\ w_2^* \end{bmatrix} \quad (2.7)$$

Assuming that the receiver has knowledge of the channel coefficients, the decision statistics are given by

$$\begin{bmatrix} \hat{x}_1 \\ \hat{x}_2 \end{bmatrix} = \left(|h_1|^2 + |h_2|^2 \right)^{-1} \begin{bmatrix} h_1 & h_2 \\ h_2^* & -h_1^* \end{bmatrix}^{-1} \begin{bmatrix} r_1 \\ r_2^* \end{bmatrix} \quad (2.8)$$

Adding all the decision statistics from all N receive antennas, the estimated symbols will be a scale version. In order to estimate the symbols, we can scale the decision statistics. This result presented above can be directly extended to other STBC codes.

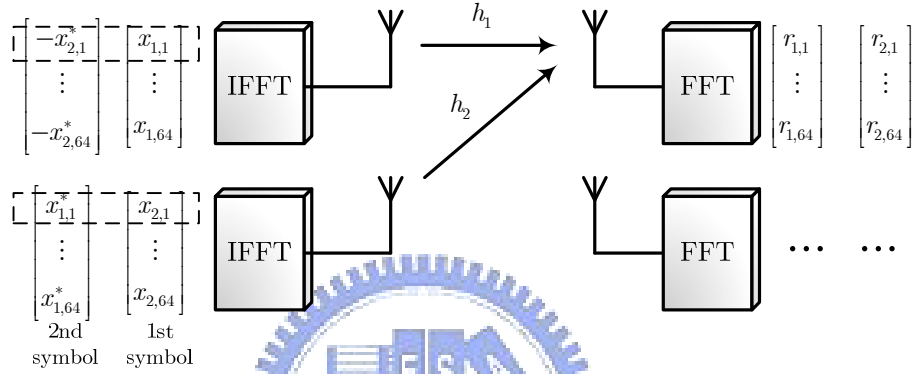


Figure 2-4. Space-time block code in the MIMO-OFDM system.

Figure 2-4 shows the STBC scheme applied to a MIMO-OFDM system. In MIMO-OFDM systems, STBC is used independently to each sub-carrier [17]. For the convenience of explanation, two transmit antennas and one receive antenna are considered. Let $r_{i,k}$ denote the k th received sub-carrier at the i th symbol duration. The received data over two consecutive symbol periods at receiver one are expressed as

$$\begin{aligned} r_{1,k} &= h_{1,k}x_{1,k} + h_{2,k}x_{2,k} + w_{1,k} \\ r_{2,k} &= -h_{1,k}x_{2,k}^* + h_{2,k}x_{1,k}^* + w_{2,k} \end{aligned} \quad (2.9)$$

where $h_{i,k}$ is the channel frequency response for the k th sub-carrier from the i th transmit antenna to the receiver and $w_{i,k}$ is the noise term. The received data are then rewritten in matrix form as

$$\begin{aligned} \begin{bmatrix} r_{1,k} \\ r_{2,k}^* \end{bmatrix} &= \begin{bmatrix} h_{1,k} & h_{2,k} \\ h_{2,k}^* & -h_{1,k}^* \end{bmatrix} \begin{bmatrix} x_{1,k} \\ x_{2,k} \end{bmatrix} + \begin{bmatrix} w_{1,k} \\ w_{2,k}^* \end{bmatrix} \\ \Rightarrow \mathbf{R}_k &= \mathbf{H}_k \mathbf{X}_k + \mathbf{W}_k \end{aligned} \quad (2.10)$$

where \mathbf{R}_k , \mathbf{X}_k , and \mathbf{W}_k are 2×1 vectors and \mathbf{H}_k is a 2×2 matrix. The received symbols can be decoded by the STBC decoder with the estimated channel state information (CSI). The data are then equalized by the following equation.

$$\hat{\mathbf{X}}_k = \mathbf{H}_k^{-1} \mathbf{R}_k \quad (2.11)$$

In contrast with STBC scheme, spatial-division multiplexing (SDM) technique is used to achieve higher throughput [18]. With SDM, multiple transmit antennas transmit independent data streams, which can be individually recovered in the receiver. An applicable method is required to separate each transmitted stream from other transmitted streams (interference cancellation). Many approaches, such as zero-forcing (ZF), minimum mean square error (MMSE), and maximum likelihood (ML) detectors, are known for the detection of SDM signals. However, the computation complexity of performing a full search for ML detection is too high to be suitable for practical applications. In order to reduce the complexity, various MIMO detection methods, such as sphere decoding technique [19] or K-best algorithm [20], have been proposed. Different detection methods have different criteria, and therefore it is preferred to adopt a reduced-complexity data detection scheme for MIMO systems.

2.1.4 MIMO-OFDM Systems

OFDM has been shown to be an effective technique to combat multipath fading in wireless channels [21]-[23]. It has been used in various wireless communication systems such as wireless local area network (WLAN) and wireless metropolitan area network (WMAN). OFDM is a multi-carrier technique that operates with specific orthogonality constraints between the sub-carrier. OFDM is attractive since it admits relatively easy solutions to some difficult challenges that are encountered when using single-carrier modulation schemes on wireless channels. Due to the demand for high speed wireless applications and limited radio frequency (RF) signal bandwidth, OFDM is being considered in the standard that considers MIMO systems, where multiple antennas are used for the purpose of spatial multiplexing or to provide increased spatial diversity.

Figure 2-5 displays the block diagram of the 4×4 MIMO-OFDM system. In the MIMO-OFDM system, the incoming bit stream is first encoded by the one-dimensional encoder (FEC encoder), and then the encoded bits are mapped onto three dimensions (time, frequency, and space) by the space-time coding. The receiver uses the preambles to complete the synchronization, and transforms the signal from time to frequency domain. Spatial streams are then demodulated to bit-level streams, which are de-interleaved and merged into a data stream. Finally, the data stream is decoded by the forward error correction decoder.

Although OFDM is robust against the multi-path propagation, it is very sensitive to the non-ideal front-end effects that destroy the orthogonality between sub-carriers. For example, OFDM is vulnerable to non-linearity, timing offset and frequency offset [21]. Hence, MIMO-OFDM systems also inherit these disadvantages of the OFDM modulation. In the following section, the non-ideal front-end effects will be discussed.

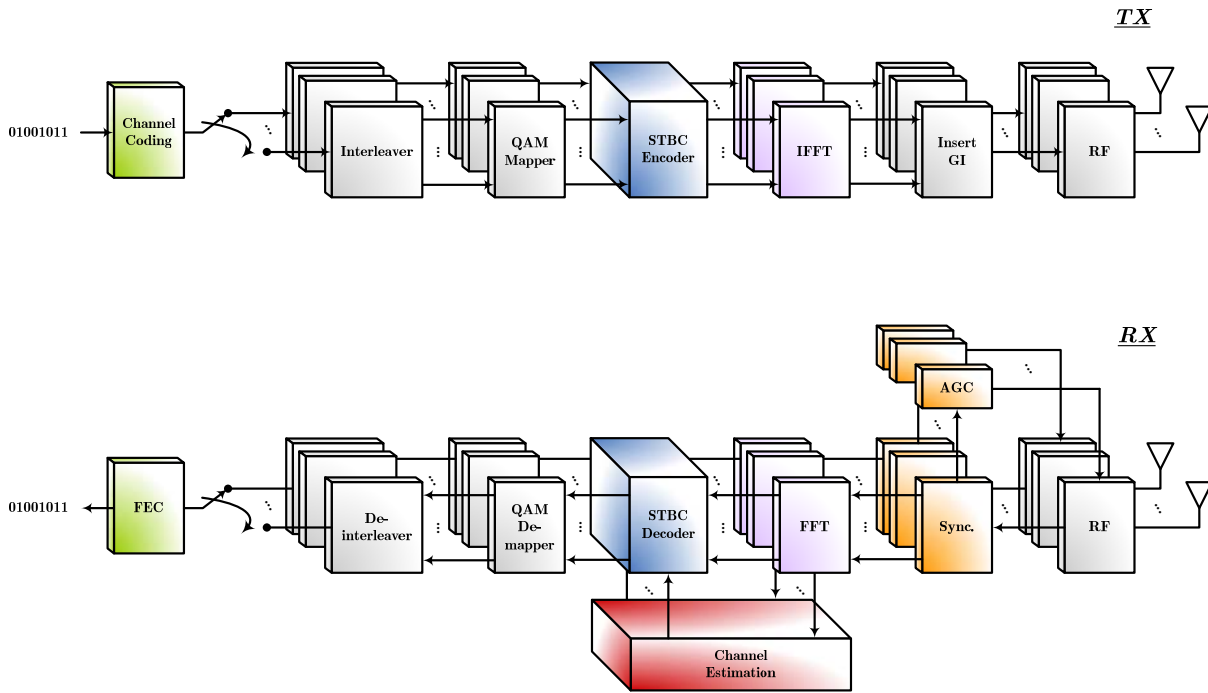


Figure 2-5. Block diagram of the 4×4 MIMO-OFDM system.

2.2 Non-Ideal Front-End Effects



The receiver architecture adopted in this work is based on the direct-conversion architecture. A block diagram of the direct-conversion receiver is shown in Figure 2-6. The direct-conversion receiver converts the carrier of the desired channel to the zero frequency immediately in the first mixers [24]-[26]. Hence, the direct-conversion is often called also as a zero-intermediate frequency (IF) receiver. Since the direct-conversion receiver has no IF, the evident benefit of this architecture is low hardware cost. However, the direct-conversion receivers are sensitive to several non-ideal effects caused in the front-end. These non-idealities will be covered in the following subsections.

In this work, the MIMO-OFDM system shares the local oscillator (LO) and the sampling clock. In this way, the synchronization error is common to all receive branches, resulting in a simplified implementation.

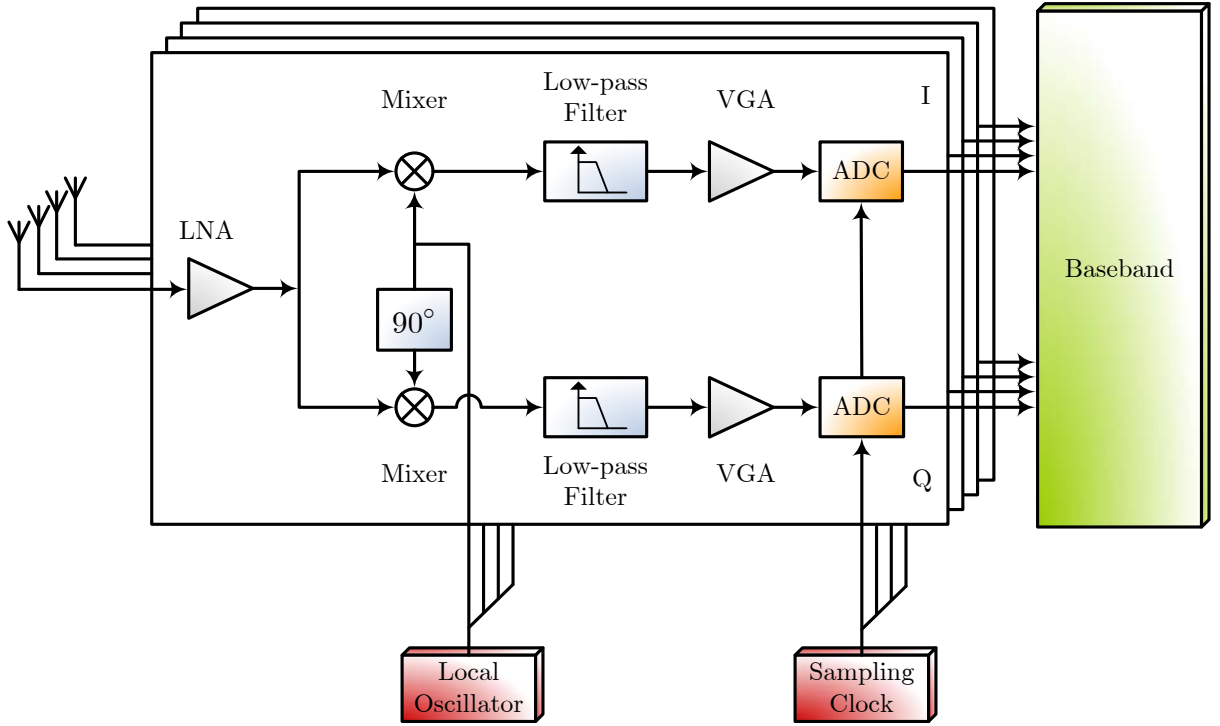


Figure 2-6. Direct-conversion receiver.

2.2.1 Effects of Carrier Frequency Offset

Basically, the band-pass signal $y_{RF}(t)$ at carrier frequency f_c can be expressed as

$$\begin{aligned}
 y_{RF}(t) &= \text{Re} \{ r(t) e^{2\pi f_c t} \} \\
 &= \text{Re} \{ r(t) \} \cos(2\pi f_c t) - \text{Im} \{ r(t) \} \sin(2\pi f_c t) \\
 &= \frac{1}{2} \left[r(t) e^{2\pi f_c t} + r^*(t) e^{-2\pi f_c t} \right]
 \end{aligned} \tag{2.12}$$

where $r(t)$ is the complex baseband signal and the initial phase of the carrier is neglected. $\text{Re}\{r(t)\}$ and $\text{Im}\{r(t)\}$ denote the in-phase component and the quadrature component of $r(t)$, respectively. Based on the direct-conversion receiver, the down-converted signal is expressed as

$$\begin{aligned}
 y_{RF}(t) \cdot 2e^{-2\pi f_c t} &= [r(t)e^{2\pi f_c t} + r^*(t)e^{-2\pi f_c t}]e^{-2\pi f_c t} \\
 &= r(t) + r^*(t)e^{-2\pi(2f_c)t}
 \end{aligned}
 \tag{2.13}$$

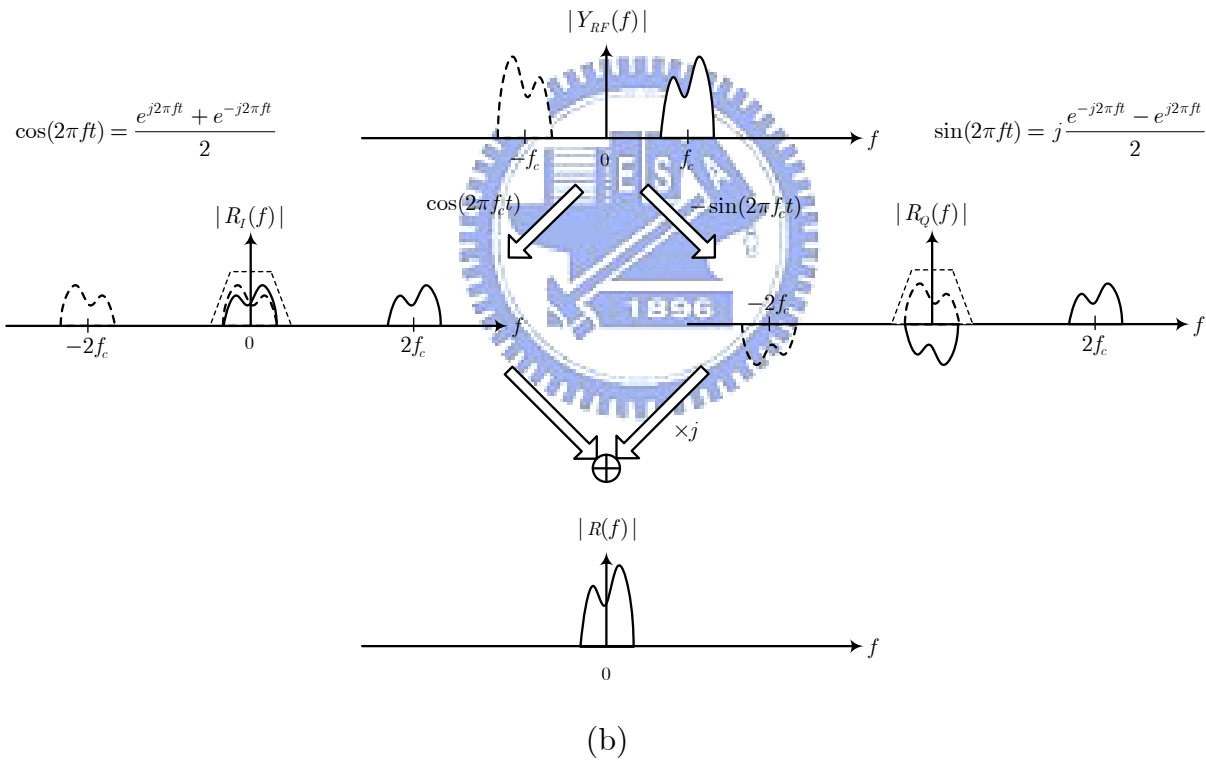
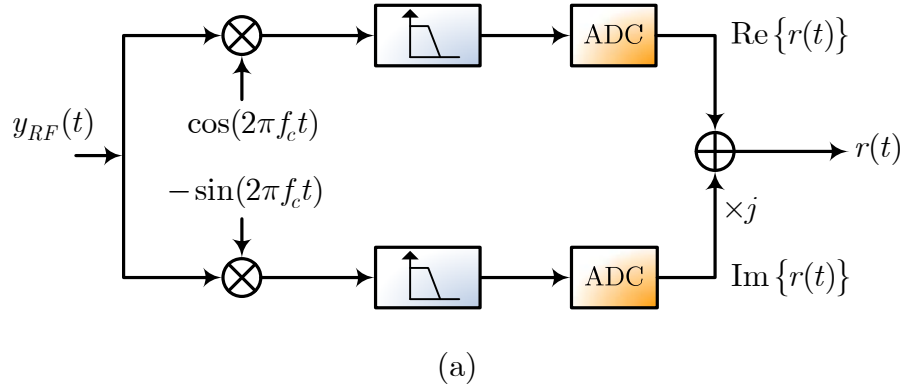


Figure 2-7. (a) I/Q demodulation. (b) Signal spectrum.

After passing through the low-pass filters (LPFs), the complex baseband signal $r(t)$ is regenerated. The process (I/Q demodulation) in the spectrum domain is shown in Figure 2-7.

In practice, OFDM is sensitive to carrier frequency offset (CFO) due to the mismatch of LOs between the transmitter and the receiver. The presence of CFO introduces inter-carrier interference (ICI), which can degrade the system performance significantly. When the system suffers from CFO Δf , the received signal after baseband processing is given by [27]

$$\begin{aligned}
 y(t) &= r(t)e^{j2\pi\Delta ft} + w(t) \\
 &= \cos(2\pi\Delta ft) \operatorname{Re}\{r(t)\} - \sin(2\pi\Delta ft) \operatorname{Im}\{r(t)\} \\
 &\quad + j\{\sin(2\pi\Delta ft) \operatorname{Re}\{r(t)\} + \cos(2\pi\Delta ft) \operatorname{Im}\{r(t)\}\} \\
 &\quad + w(t)
 \end{aligned} \tag{2.14}$$

where $w(t)$ denotes the representations of the additive white Gaussian noise (AWGN). From (2.14), the CFO effect results in phase shift in the time domain. The behavior of CFO in the spectrum domain is shown in Figure 2-8. It is clear that the spectrum is shifted with a frequency Δf . After digitizing the signal and passing through the FFT block, the frequency domain data is given by (see Appendix A for details) [28]

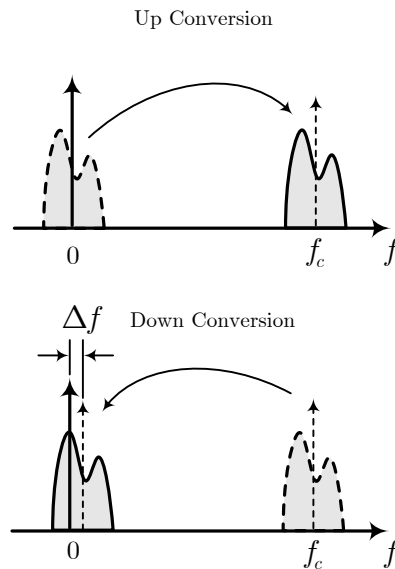


Figure 2-8. The behavior of the CFO in the spectrum domain.

$$\begin{aligned}
Y_k &= \text{FFT}_N \{y(n)\} \\
&= X_k H_k \left\{ \frac{(\sin \pi \varepsilon)}{N (\sin \pi \varepsilon / N)} \right\} e^{j\pi \varepsilon (N-1) / N} \\
&\quad + \sum_{k=-K, l \neq k}^K X_l H_l \left\{ \frac{(\sin \pi \varepsilon)}{N (\sin \pi (l-k + \varepsilon) / N)} \right\} e^{j\pi \varepsilon (N-1) / N} e^{-j\pi (l-k) / N} + W_k
\end{aligned} \tag{2.15}$$

where the subscript N denotes the FFT size. X_k and H_k denote the data carrier and channel frequency response, respectively. The frequency offset Δf is normalized to sub-channel bandwidth, and the relative frequency offset is shown as ε . In (2.15), the first term of the right hand side is the decayed original signal transmitted in the k th sub-carrier, and the second term denotes the inter-carrier interference (ICI) from others. All sub-carriers in an OFDM symbol are orthogonal if they all have a different integer number of cycles within the FFT interval. If there is CFO, the number of cycles in the FFT interval will not be an integer. When the LOs between the transmitter and the receiver are not aligned, CFO occurs and the frequency spectrum is not sampled at the optimum peaks of the sinc functions. The property is shown in Figure 2-9. In Figure 2-9, the received data on each sub-carrier is not the original transmitted data when there is CFO. The effect of frequency offset on a QPSK constellation is depicted in Figure 2-10. With 5 ppm CFO value, the constellation points have rotated over the decision boundaries after 10 OFDM symbols. Since the phase rotation is increasing with time, it has to be compensated even for a small CFO.

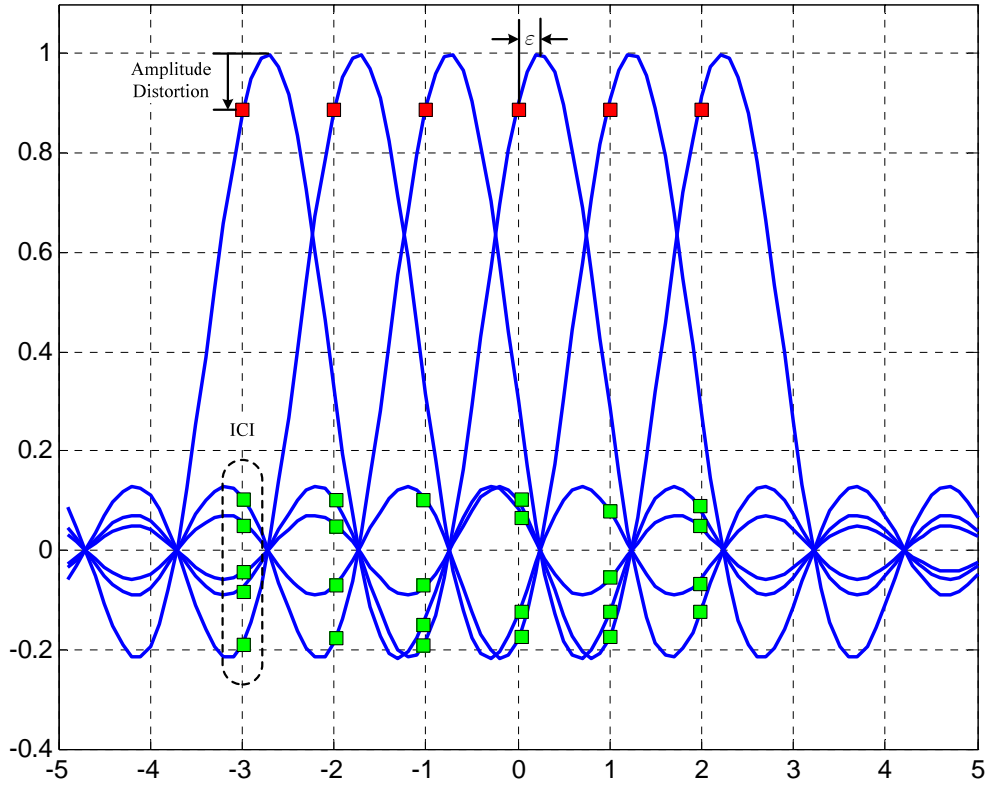


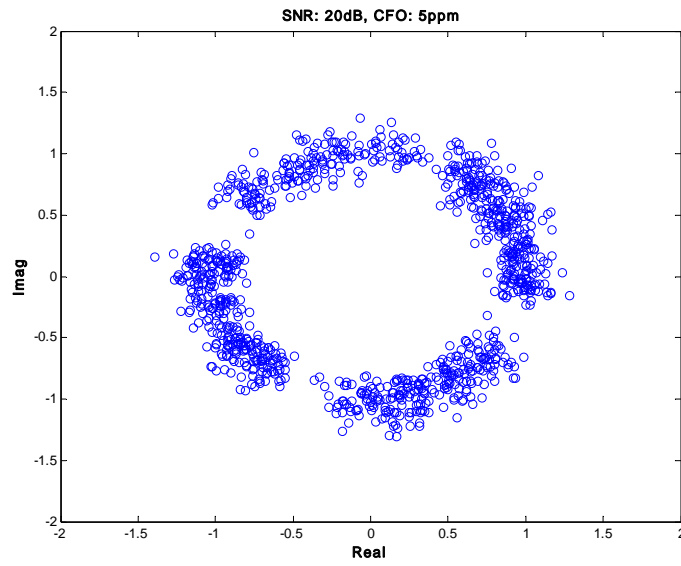
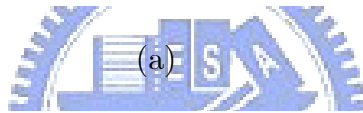
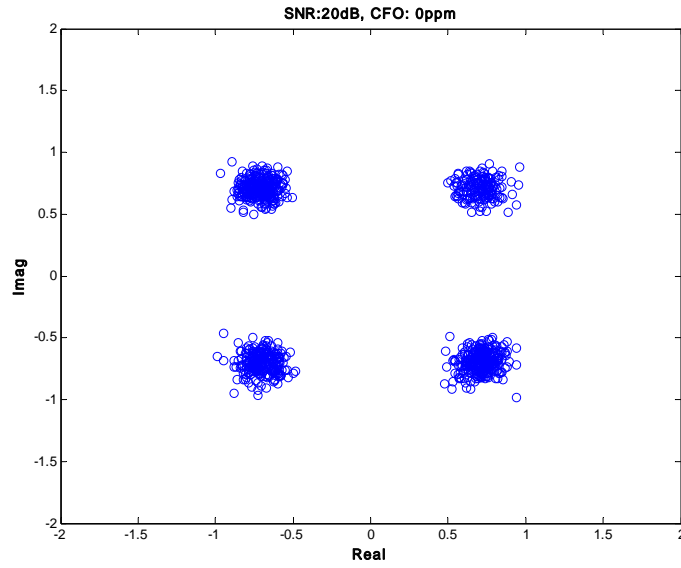
Figure 2-9. The received sub-carriers in the presence of CFO.

Another reason causing CFO is the Doppler shift of the RF carrier. As the result of the relative motion between the transmitter and the receiver, each multipath wave is subject to a frequency shift. The frequency shift of the received signal caused by the relative motion is called the Doppler shift, which is proportional to the speed of the mobile unit. When a signal with carrier frequency f_c is transmitted and the received signal comes at an incident angle θ with respect to the direction of the vehicle motion, the Doppler shift f_D of the received signal is given by [29]

$$f_D = \frac{v}{c} \cos(\theta) \quad (2.16)$$

where v and c denote the vehicle speed and the speed of light, respectively. In

practical conditions, the Doppler effect adds some hundreds of Hz in frequency spreading.



(b)

Figure 2-10. QPSK constellation in the case of the AWGN channel. (a) CFO: 0 ppm. (b) CFO: 5 ppm.

2.2.2 Effects of I/Q Mismatch

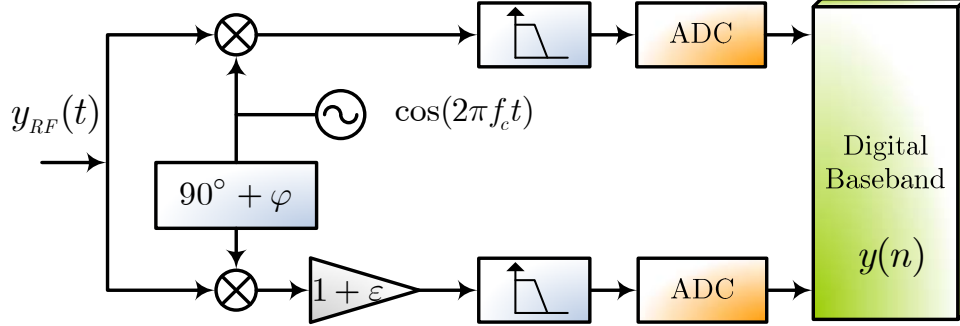


Figure 2-11. Direct-conversion receiver with I/Q mismatch.

Figure 2-11 depicts the block diagram of a direct-conversion architecture. I/Q mismatch (IQ-M) arises when the phase and gain differences between I and Q branches are not exactly 90 degree and 0 dB, respectively [26]. The mismatched LO output signals are modeled as

$$\begin{aligned} I &: \cos(2\pi f_c t) \\ Q &: -(1 + \varepsilon) \sin(2\pi f_c t + \varphi) \end{aligned} \quad (2.17)$$

where ε and φ denote the constant amplitude and phase mismatch, respectively. Multiplying the band-pass signal by the mismatched LO signals and passing through the LPFs, the baseband signal is expressed as [30]-[31]

$$\begin{aligned} y(n) &= \text{Re}\{r(n)\} + j(1 + \varepsilon)[\text{Im}\{r(n)\} \cos \varphi - \text{Re}\{r(n)\} \sin \varphi] + w(n) \\ &= 0.5(1 + (1 + \varepsilon)e^{-j\varphi})r(n) + 0.5(1 - (1 + \varepsilon)e^{j\varphi})r^*(n) + w(n) \\ &= \alpha r(n) + \beta r^*(n) + w(n) \end{aligned} \quad (2.18)$$

If neither gain nor phase error exists, α remains at unity, and β decreases to zero. In

the OFDM system, the received signal is further passed through the FFT block. After the FFT operation, the frequency-domain data can be expressed as

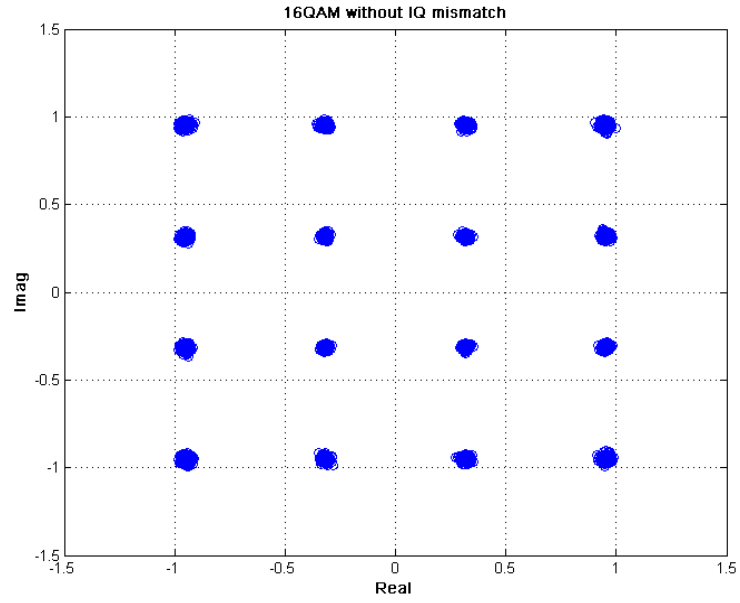
$$\begin{aligned}
 Y_k &= \text{FFT}_N \{y(n)\} \\
 &= \alpha R_k + \beta R_{-k}^* + W_k \\
 &= \alpha H_k X_k + \beta H_{-k}^* X_{-k}^* + W_k
 \end{aligned} \tag{2.19}$$

Equation (2.19) shows that IQ-M can cause the symbol at the sub-carrier k to be scaled by the complex factor α . Moreover, the complex conjugate of the symbol at sub-carrier $-k$ multiplied by another complex factor β will be present. The desired sub-carrier k will include the unwanted interference related to the sub-carrier $-k$, implying that IQ-M can distort the accuracy of received signal. The effect of IQ-M on the 16-QAM constellation is depicted in Figure 2-12. As a result of the IQ-M, the constellation is distorted severely. It implies that IQ-M can limit the ability of the receiver to achieve better performance especially for high constellation size, e.g., 64-QAM constellation.

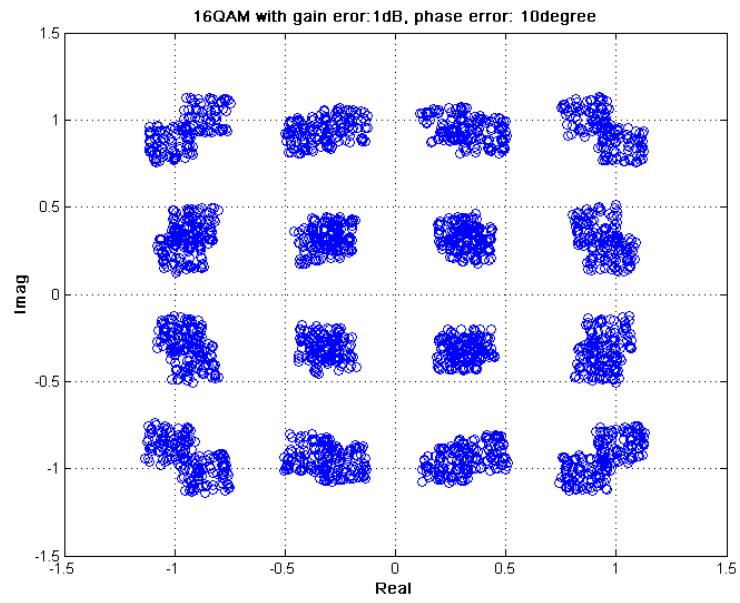
The image reject ratio (IRR) as a function of the mismatch is given by [32]

$$\text{IRR} = 10 \cdot \log \left[\frac{1 + (1 + \varepsilon)^2 + 2(1 + \varepsilon) \cos(\varphi)}{1 + (1 + \varepsilon)^2 - 2(1 + \varepsilon) \cos(\varphi)} \right] \quad (\text{dB}) \tag{2.20}$$

A plot of (2.20) is shown in Figure 2-13. In order to achieve an IRR of at least of 55 dB, the gain error must be smaller than 0.3% and the phase error must be smaller than 0.1 degree. Another design choice is that the gain error must be smaller than 0.1% and the phase error must be smaller than 0.2 degree.



(a)



(b)

Figure 2-12. 16-QAM constellation. (a) Without I/Q mismatch. (b) Gain error: 1dB, Phase error: 10 degree.

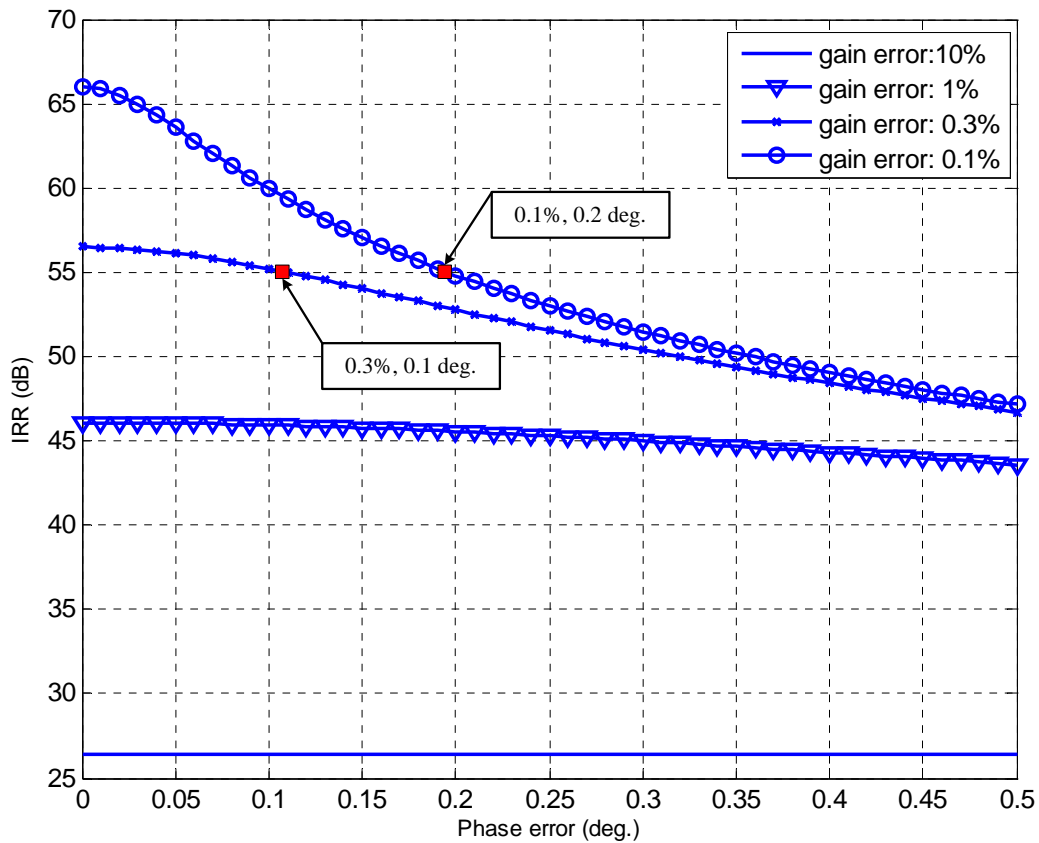


Figure 2-13. Image suppression as a function of the I/Q mismatch.



This mismatch can occur at the transmitter, receiver or both. Moreover, due to the impairment in the analog components, the low-pass filters (LPFs) of I and Q channels are not identical. The mismatched LPFs result in frequency-dependent IQ-M. Frequency-dependent IQ-M means that the imbalances can vary with frequency. This will be further discussed in Chapter 4.

2.2.3 Effects of Non-linearity

The power transfer function of a power amplifier is shown in Figure 2-14. In Figure 2-14, the 1 dB compression point is labeled as P_{1dB} and is defined as the point at which a 1 dB increase in input power results in 1 dB decrease in the linear gain of the amplifier [26]. For low values of the input power, the output power grows approximately linear. For intermediate values, the output power falls below that linear growth and it runs into a saturation as the input power grows higher. The dynamic range of amplifier, which also corresponds to the linear region of operation for an amplifier, is defined between the noise-limited region and the saturation region. In order to recognize the signal, saturation should be avoided as much as possible.

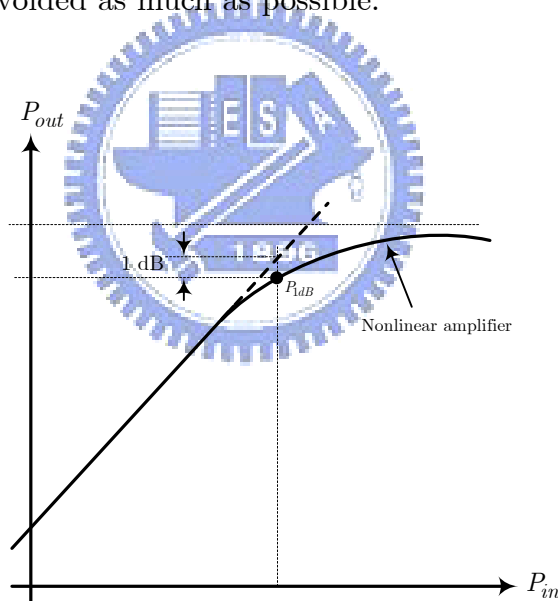


Figure 2-14. Power transfer function.

The actual saturation behavior is difficult to model. Common AM-AM (amplitude modulation/amplitude modulation) and AM-PM (amplitude modulation/phase modulation) models are the third-order model and the Saleh model [33]. These mathematical models are listed in TABLE 2-1. In TABLE 2-1, coefficients a_i , α_i and β_i are used to model the non-linear effects. Figure 2-15 shows the non-linear model [27].

Considering an OFDM complex baseband signal $x(t) = a(t)e^{j\phi(t)}$ with amplitude $a(t)$ and phase $\phi(t)$ that passes a non-linear amplifier, the output is expressed as

$$y(t) = f(a(t))e^{j(g(a(t))+\phi(t))} \quad (2.21)$$

where $f(a(t))$ and $g(a(t))$ describe the AM-AM and AM-PM characteristics, respectively. An example of distortion on a 64-QAM constellation due to AM-AM is displayed in Figure 2-16. In addition, non-linearity can cause spectral widening of the transmit signal resulting in unwanted out-of-band noise. At the transmitter part, the transmitted signal itself is degraded by nonlinearities, resulting in increased bit error rates in the receiver.

TABLE 2-1. AM-AM and AM-PM Models.

	$f(a(t))$	$g(a(t))$
Third-Order	$a(t) \left(a_1 + \frac{3a_3}{4} a(t) \right)$	1
Saleh	$\frac{\alpha_1 a(t) }{1 + \beta_1 a(t) ^2}$	$\frac{\alpha_2 a(t) ^2}{1 + \beta_2 a(t) ^2}$

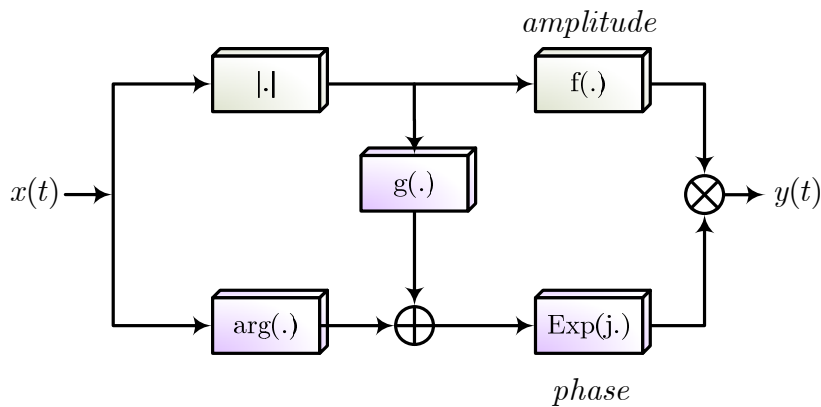


Figure 2-15. AM-AM and AM-PM functional model.

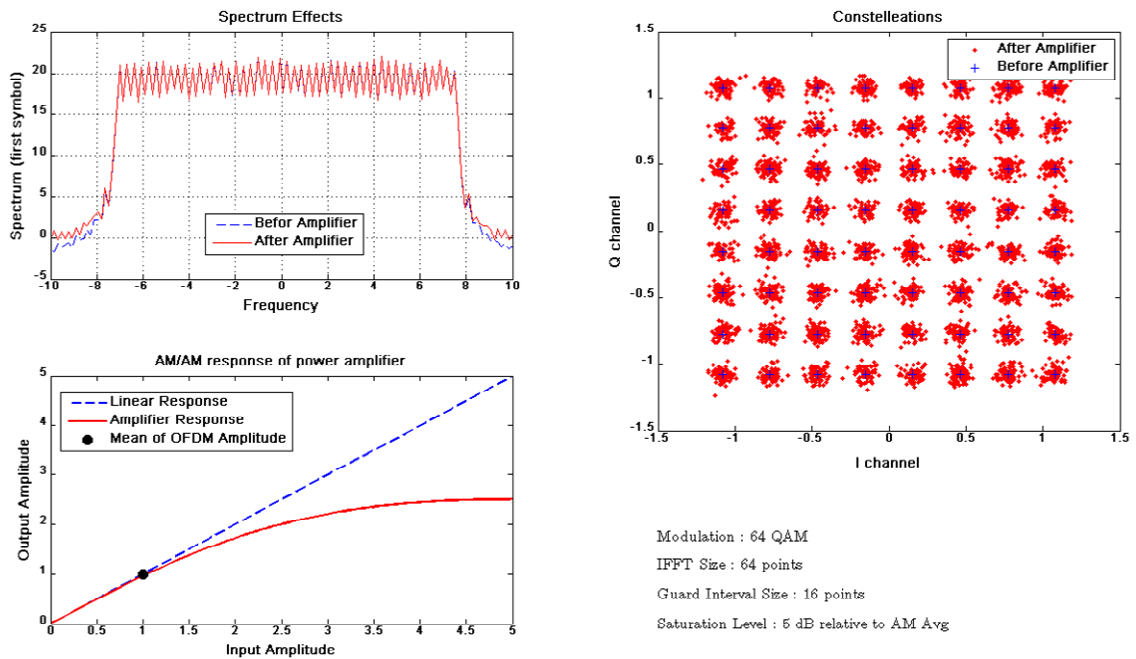


Figure 2-16. The effect of AM-AM on a 64-QAM constellation.



2.2.4 DC Offset

Another important source for reduction of the dynamic range in the analog part is direct current (DC) offset. Static DC offset may be generated by bias mismatch in the baseband chain, but also generated from self-mixing of the RF signal with the LO due to imperfect LO–RF isolation on the same substrate [24]–[26]. In addition, dynamic DC offset can be introduced by mixing of close-in interference with the LO signal. In general, the OFDM system uses null DC. The reason is that the DC offset can be removed by applying a DC blocking filter since there is no information around DC.

2.2.5 Quantization Noise and Clipping

In order to reduce the cost and power consumption, the number of bits of the analog-to-digital converter (ADC) and digital-to-analog converter (DAC) must be kept as low as possible [27], [34]. On the other hand, it is desirable to have a large number of bits to reduce the quantization noise. Assuming the input analog voltage range is from $-V_p$ to $+V_p$ volt and the ADC has N bit output words, the least significant bit (LSB) value is

$$A_{LSB} = \frac{2V_p}{2^N} = \frac{V_p}{2^{N-1}} \quad (2.22)$$

Assuming a linear conversion slope, the amplitude error is comprised between $-A_{LSB}/2$ and $+A_{LSB}/2$. If the quantization error v is uniform over $[-A_{LSB}/2, +A_{LSB}/2]$, the variance of the quantization error is

$$\sigma^2 = \int_{-A_{LSB}/2}^{+A_{LSB}/2} v^2 dv = \frac{A_{LSB}^2}{12} \quad (2.23)$$

Replacing A_{LSB} in (2.23) with $A_{LSB} = 2V_p/2^N$, (2.23) can be written as

$$\sigma^2 = \frac{(2V_p)^2}{12 \cdot (2^N)^2} = \frac{V_p^2}{3 \cdot 2^{2N}} \quad (2.24)$$

If the signal input is a full-scale sinusoidal signal, the signal-to-quantization noise ratio (SQNR) is

$$\begin{aligned}
\text{SQNR}_{\text{ADC}} &= 10 \log_{10} \left(\frac{\text{input signal}}{\text{quantization noise}} \right) \\
&= 10 \log_{10} \left(\frac{A_p^2/2}{A_{\text{LSB}}^2/12} \right) \\
&= 10 \log_{10} \left(\frac{2^{2N-2} A_{\text{LSB}}^2/2}{A_{\text{LSB}}^2/12} \right) \\
&= 10 [\log_{10}(6) + (2N - 2) \cdot \log_{10}(2)] \\
&= 6.02N + 1.76 \quad (\text{dB})
\end{aligned} \tag{2.25}$$

From (2.25), it is clear that quantization in the ADC sampling process introduces noise. In the receiver chain, the received signal is adjusted to make the signal fit in the ADC dynamic range. If the signal is strongly amplified, the signal peaks can be clipped, resulting in severe distortion. Figure 2-17 shows the effects of quantization noise and clipping. During implementation, there is a trade-off between quantization noise and clipping.

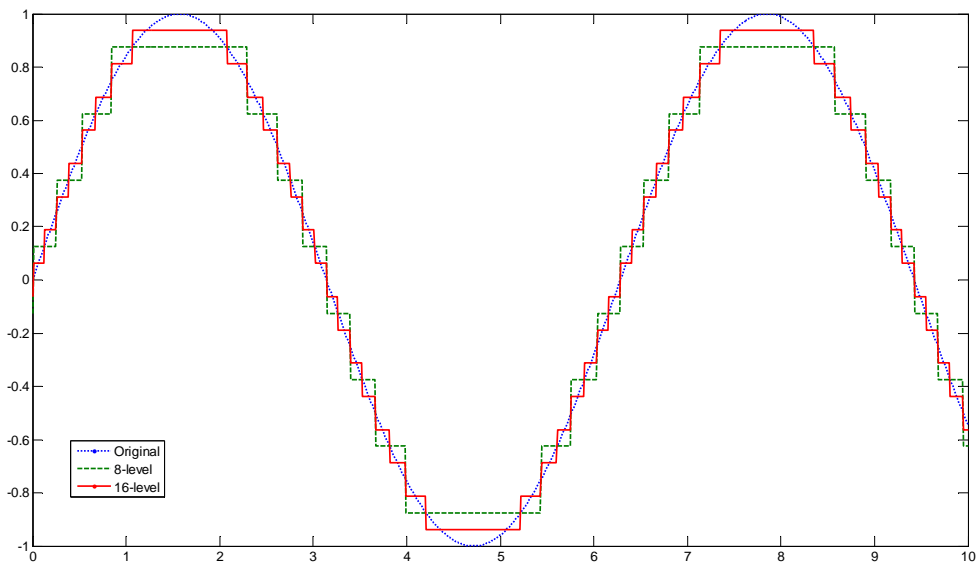
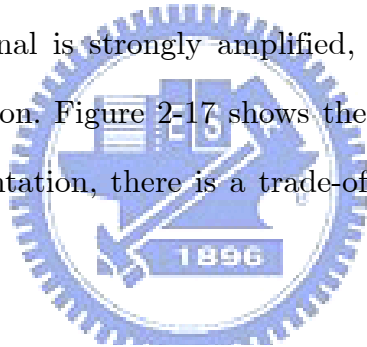
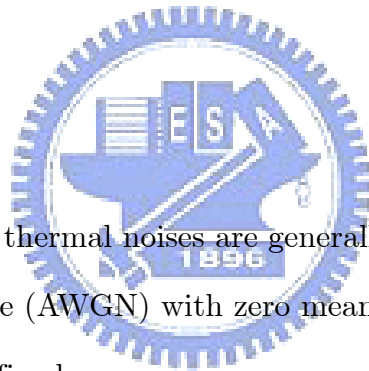


Figure 2-17. Effects of quantization noise and clipping.

2.3 Wireless Channel Models

In communication system design, communication channel plays an important role since the transmitter and receiver designs have to be optimized with respect to the target channel. Without loss of generality, we discuss the channel characterization based on the SISO system. Some frequently used statistical models are reviewed in the following subsections.

2.3.1 AWGN



In the baseband, electronic and thermal noises are generally combined and modeled as an additive white Gaussian noise (AWGN) with zero mean and standard deviation σ . The Gaussian distribution is defined as

$$p(x) = \frac{1}{\sigma\sqrt{2\pi}} e^{-\frac{(x-\mu)^2}{2\sigma^2}} \quad (2.26)$$

where μ is the mean and σ^2 denotes the variance. When modeling AWGN in the phasor domain, the amplitudes of the real and imaginary parts are independent variables which follow the Gaussian distribution model. When combined, the resultant phasor's magnitude is a Rayleigh distribution while the phase is uniformly distributed from 0 to 2π . The Rayleigh distribution is defined as

$$p(r) = \frac{r}{\sigma^2} e^{\frac{-r^2}{2\sigma^2}}, \quad r = \sqrt{x^2 + y^2} \text{ where } x \sim N(0, \sigma^2), \quad y \sim N(0, \sigma^2) \quad (2.27)$$

A plot of the Gaussian distribution and Rayleigh distribution is shown in Figure 2-18.

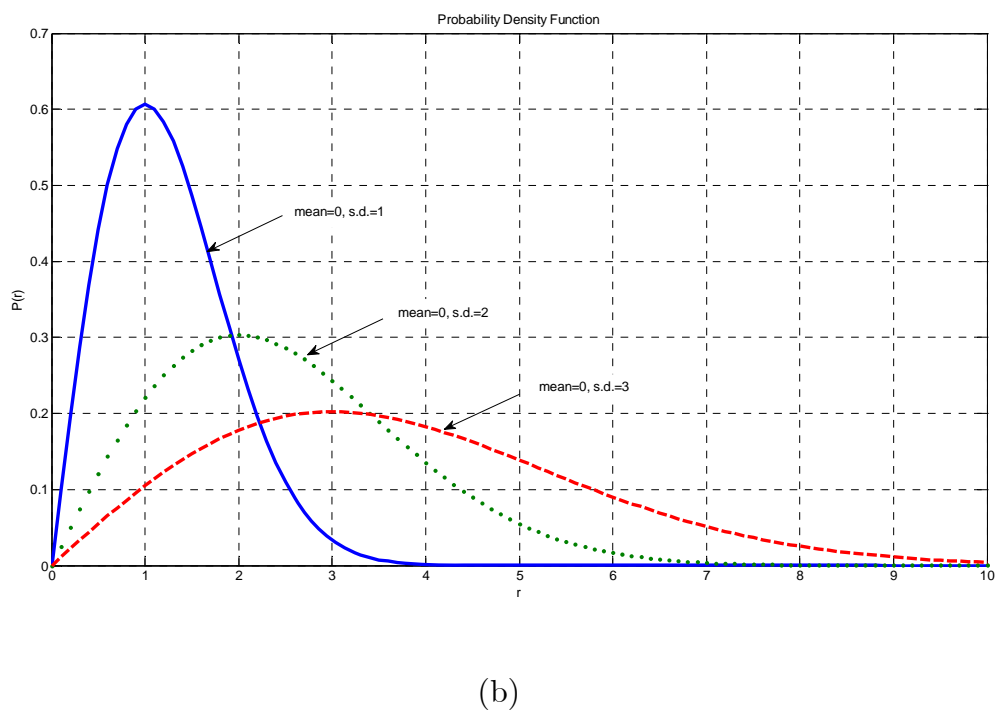
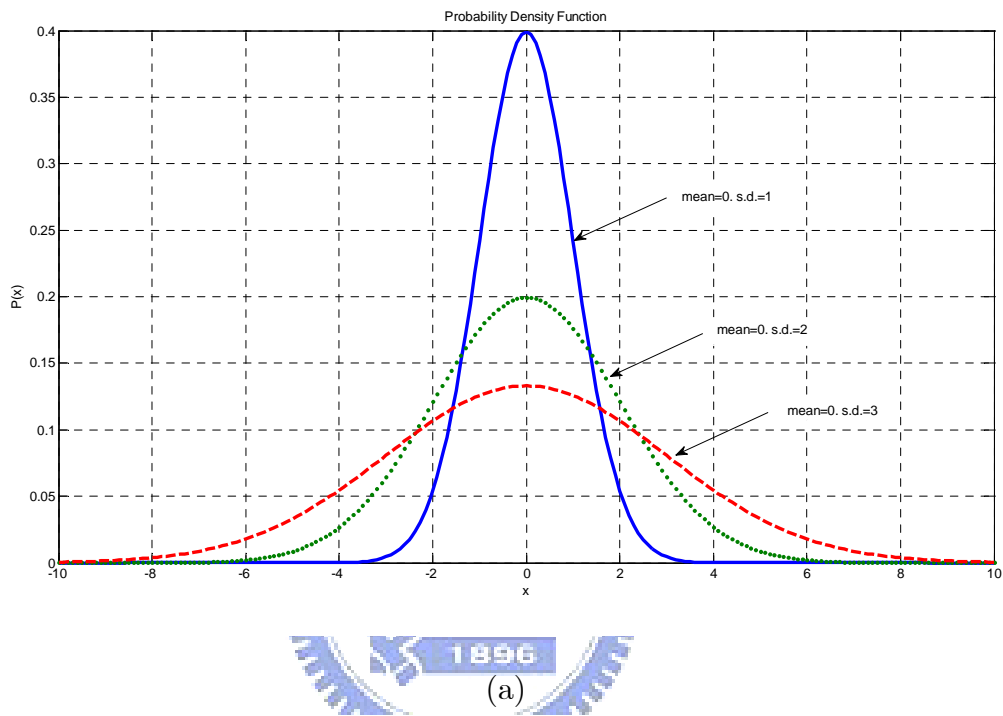


Figure 2-18. (a) Gaussian distribution. (b) Rayleigh distribution.

2.3.2 Multipath

In terrestrial wireless communications, signals travel to the receiver via multiple paths, and this creates additional distortion to the transmitted signals. Figure 2.19 shows a propagation channel with several mechanisms for creating multiple paths. These candidate mechanisms include scattering, reflection, refraction and diffraction [29].

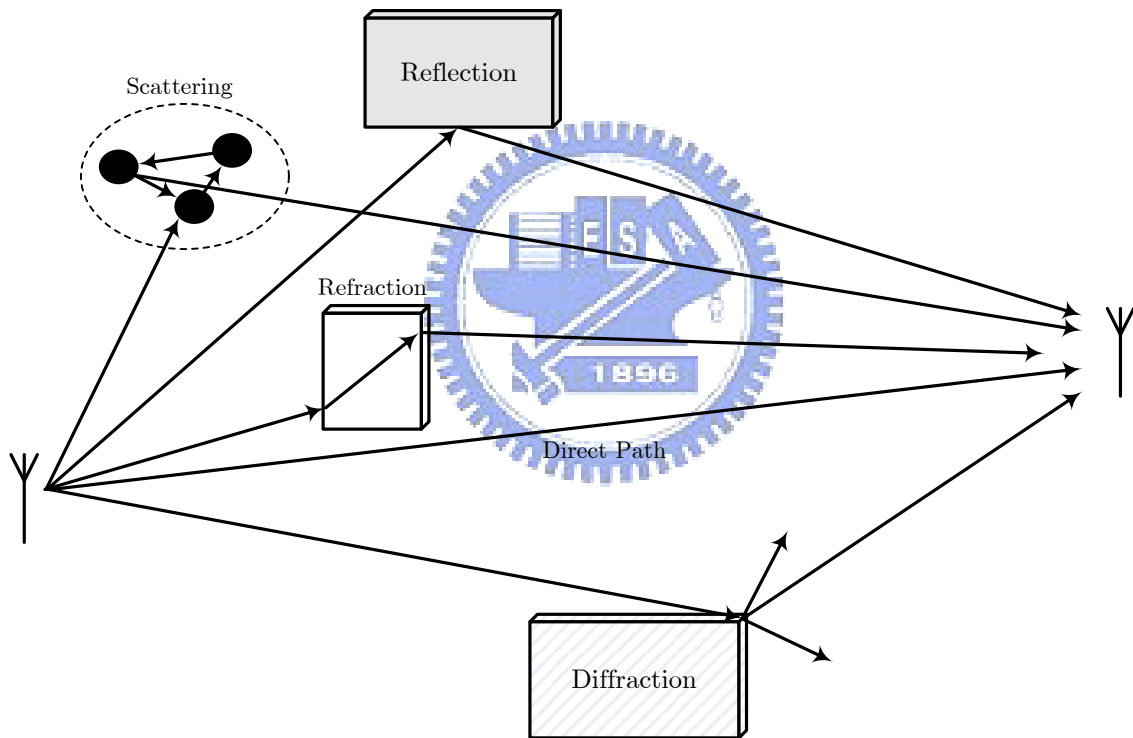


Figure 2-19. Multiple paths.

From Figure 2-19, a transmitted signal is delayed in the channel and the arrival times of different paths are spread in time. This phenomenon is called delay spread. The received signal $y(t)$ at time t can be found from the transmitted signal $x(t)$ by convolving the $x(t)$ and the channel impulse response $h(t, \tau)$ as it appears at time t , so

$$\begin{aligned}
 y(t) &= x(t) \otimes h(t, \tau) \\
 &= \int_{-\infty}^{\infty} h(t, \tau)x(t - \tau)d\tau
 \end{aligned}
 \tag{2.28}$$

where \otimes denote the convolution operator and τ is the delay variable. Moreover, the mean relative power of the taps are specified by the power delay profile (PDP) for the channel [29], thus

$$P(\tau) = \frac{E[|h(t, \tau)|^2]}{2}
 \tag{2.29}$$

Figure 2-20 shows the PDP of a typical multipath channel.

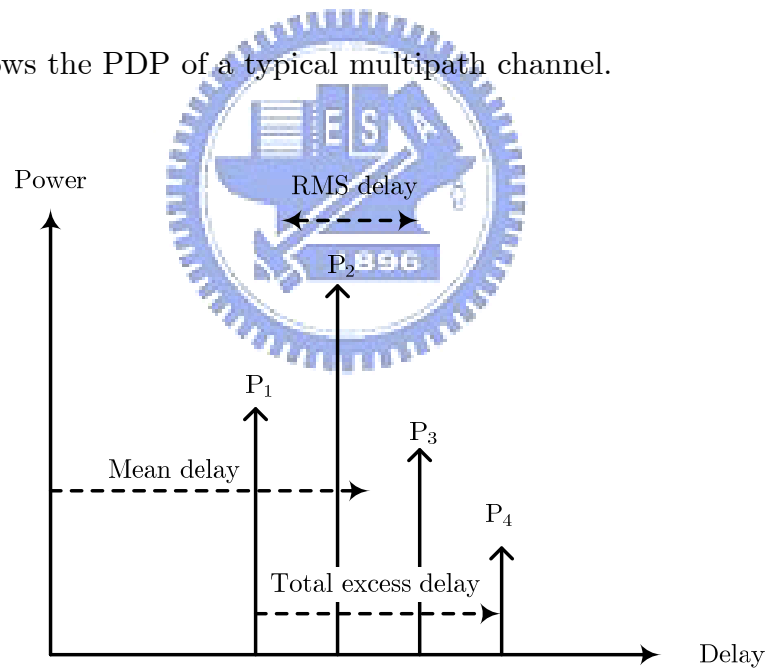


Figure 2-20. Power delay profile.

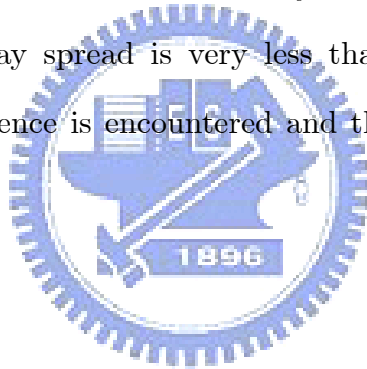
From Figure 2-20, an important parameter in the PDP is the root mean square (RMS) delay spread. The RMS delay spread is defined as [29]

$$\tau_{\text{RMS}} = \sqrt{\frac{1}{P_T} \sum_{i=1}^n P_i \tau_i^2 - \tau_0^2} \quad (2.30)$$

where P_i denotes the power of individual tap. τ_0 and P_T denote the mean delay and the total channel power, respectively.

$$\begin{aligned} \tau_0 &= \frac{1}{P_T} \sum_{i=1}^n P_i \tau_i \\ P_T &= \sum_{i=1}^n P_i \end{aligned} \quad (2.31)$$

The RMS delay spread is a good indicator of the system performance for moderate delay spreads. If the RMS delay spread is very less than the symbol duration, no significant inter-symbol interference is encountered and the channel may be assumed narrowband.



2.3.3 MIMO Channel: TGn Channel Model

In this work, we adopt the TGn model as reference model [35]. In TGn channel model specification, there are six models, which represent a variety of indoor environments, ranging from small environments, such as residential homes, with RMS delay spreads from 0 to 30 ns, up to larger areas, such as open spaces and office environments, with RMS delay spreads from 50 to 150 ns. The modeling process includes treating reflection paths as clusters of rays. Each cluster has a PDP, which is used in finding MIMO channel tap coefficients. This approach is known as cluster modeling [36]-[37]. The parameters are the angle-of-departure (AOD) from the transmitter, the angle-of-arrival

(AOA) at the receiver, and the angular spread (AS) at both sides. For detailed description, please refer to the references [35]-[38].

2.4 Summary

In this chapter, system considerations are addressed. MIMO-OFDM systems play an important role in numerous wireless standards, such as IEEE 802.11n and IEEE 802.16e. Firstly, understanding the impact of MIMO on system performance is key to assessing this technology. MIMO technology and space-time coding affect all aspects of transceiver design. The combination of MIMO transmission, OFDM technology, and space-time processing comprises a promising solution for next-generation wireless communications. In the practical transmission, channel effects can destroy the system performance. Therefore, acquiring accurate channel state information and providing essential compensation are very important. In addition, the proposed algorithms must also be computationally efficient to reduce the hardware cost. In order to achieve high performance and low power consumption, low complexity algorithms and efficient VLSI architectures are preferable.



Chapter 3

Anti-I/Q Mismatch Auto Frequency Controller



This chapter presents a novel carrier frequency offset (CFO) estimation algorithm, based on pseudo CFO (P-CFO), to estimate the CFO value under the conditions of I/Q mismatch for direct-conversion structures with 2 dB gain error and 20° phase error in frequency-selective fading channels. In order to circumvent CFO with I/Q mismatch, the proposed P-CFO algorithm rotates three training symbols by adding extra frequency offset into the received sequence to improve the CFO estimation. Simulation results indicate that the estimation error of the proposed method is about 0.3 ppm (0.002 subcarrier spacing), which is lower than those of two-repeat preamble-based methods. Additionally, the proposed P-CFO algorithm is compatible with the conventional method, and is appropriate for SoC implementation. The proposed scheme is implemented as part of an OFDM wireless receiver fabricated in a 0.13- μm CMOS process with $3.3 \times 0.4 \text{ mm}^2$ core area and 10 mW power consumption at 54 Mbits/s data rate.

OFDM is a spectrally efficient signaling method for communication over frequency-selective fading channels [21], [39]. OFDM has been utilized by many transmission systems, such as IEEE 802.11a/g/n-based WLAN systems [2], [4], [5], digital audio broadcasting (DAB) [6] and digital video broadcasting terrestrial TV (DVB-T) [7]. Unfortunately, OFDM systems are sensitive to imperfect synchronization and non-ideal front-end effects, leading to severe system performance degradation. Typically, OFDM is highly sensitive to carrier frequency offset (CFO), due to the Doppler shift of the radio frequency (RF) carrier, the phase noise of an oscillator, or the mismatch of local oscillators (LOs) between the transmitter and the receiver. Frequency offset can introduce inter-carrier interference (ICI) in an OFDM receiver because of the loss of orthogonality between sub-carriers, severely degrading the overall system performance without suitable correction. To avert performance degradation, OFDM systems have strict front-end specifications and expensive front-end implementations.

Recent investigations have concentrated on developing monolithic receiver architectures, particularly for low-cost technology [24]-[26]. Direct-conversion architecture is one potential candidate for simple integration among various receiver architectures. However, direct-conversion receivers also suffer from various impairments, including I/Q mismatch (IQ-M) of non-ideal RF circuits, due to the gain and phase mismatch between in-phase (I) and quadrature-phase (Q). Specifically, IQ-M arises when the phase and gain differences between I and Q are not exactly 90° and 0° , respectively. IQ-M not only introduces unwanted image interference into the desired signal, but also restricts the accuracy of CFO estimation.

In practice, the simultaneous occurrence of CFO and IQ-M significantly degrades the system performance. Several schemes for OFDM systems have been proposed to handle the frequency synchronization [28], [40]-[46]. These schemes can be categorized as follows: a) data-aided (DA) methods, in which special training symbols are inserted

into the transmitted data [28], [40]. b) non-data-aided (NDA) methods, in which the transmitted data are used without any other additional information [41]-[42] and c) guard-interval-based (GIB) methods, in which the received data before the FFT and the inserted guard interval in the OFDM signal frame are used to handle synchronization [43]-[44].

Some blind frequency estimators that rely on signal statistics have also been adopted to achieve frequency synchronization [45]-[46]. Although these methods can work well under frequency offset, they do not consider the IQ-M. Therefore, introducing the IQ-M phenomenon into the system increases the estimation error. Tubbax *et al.* [30] have presented an algorithm that addresses both CFO and IQ-M. Their method can compensate for the mismatch with a gain error of up to 0.414 dB (10% gain error) and phase error of 10° . Fouladifard and Shafiee [31] proposed an iteration algorithm, which, however, does not guarantee the convergence condition of the estimation when considering the packet-based WLAN standards. The performance of their algorithm is verified in the range of -47 kHz to $+47$ kHz (± 0.15 subcarrier spacing), which is smaller than the standard requirement of -125 kHz to $+125$ kHz (± 0.4 subcarrier spacing). Gil *et al.* [47] developed a joint estimation of CFO, channel and IQ-M based on maximum likelihood (ML) criterion. Their proposed method has an accuracy that almost reaches the Cramér-Rao lower bound (CRLB), but is computationally too expensive to be appropriate for hardware implementation. Xing *et al.* [48] proposed a nonlinear least squares (NLS) frequency estimator under IQ-M which has a high computational complexity for NLS matrix operations. Additionally, the synchronization format (training symbols) of the proposed NLS scheme differs from the state of the art in WLAN standards such as IEEE 802.11a/g. Therefore, NLS is incompatible with current standards.

To maintain and realize systems with imperfect RF distortions, this work focuses

on improving the frequency offset estimation accuracy under the conditions of the joint impairments in both CFO and IQ-M. The proposed synchronization algorithm must also be suitable for application-specific integrated circuit (ASIC) implementation. This work develops a novel frequency offset estimation algorithm based on pseudo-CFO (P-CFO) to circumvent the large CFO estimation error generated by IQ-M. P-CFO applies only three training symbols, which are deliberately rotated by an additional frequency offset, to carry out frequency offset estimation even if IQ-M causes interference. Simulation results indicate that the average estimation error of the proposed scheme is approximately 0.3 ppm (0.002 subcarrier spacing), making a high performance receiver possible.

The rest of this chapter is organized as follows. Section 3.1 describes the OFDM system model in the presence of CFO and IQ-M. Section 3.2 then introduces a novel algorithm for CFO estimation with IQ-M. Next, the simulation results and ASIC implementation are presented in Sections 3.3 and 3.4, respectively. Conclusions are finally drawn in Section 3.5.

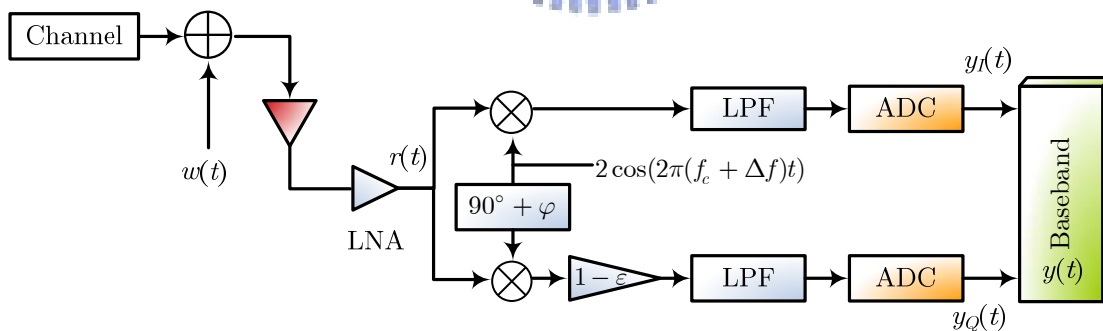


Figure 3-1. OFDM receiver with IQ-M and CFO.

3.1 System Model

Figure 3-1 schematically depicts a block diagram of a typical OFDM receiver in the presence of CFO and IQ-M. Based on the direct-conversion architecture in [25], [31] and [49], the received signal after baseband processing with CFO Δf and IQ-M is given by

$$\begin{aligned}
 y(t) = & \cos(2\pi\Delta ft) \operatorname{Re}\{r(t)\} - \sin(2\pi\Delta ft) \operatorname{Im}\{r(t)\} \\
 & + j(1 - \varepsilon) \{\sin(2\pi\Delta ft - \varphi) \operatorname{Re}\{r(t)\} + \cos(2\pi\Delta ft - \varphi) \operatorname{Im}\{r(t)\}\} \\
 & + w(t)
 \end{aligned} \tag{3.1}$$

where $r(t)$ and $w(t)$ denote the representations of the received signal in the receiver, and additive white Gaussian noise (AWGN), respectively and ε and φ represent the gain error and phase error introduced from the front-end, respectively. The discrete-time representation of (3.1) after the received signal is digitized can be expressed as

$$\begin{aligned}
 y(n) = & \cos(2\pi\Delta fnT_s) \operatorname{Re}\{r(n)\} - \sin(2\pi\Delta fnT_s) \operatorname{Im}\{r(n)\} \\
 & + j(1 - \varepsilon) \cdot \{\sin(2\pi\Delta fnT_s - \varphi) \operatorname{Re}\{r(n)\} + \cos(2\pi\Delta fnT_s - \varphi) \operatorname{Im}\{r(n)\}\} \\
 & + w(n)
 \end{aligned} \tag{3.2}$$

where T_s denotes the sampling period. Furthermore, (3.2) can be summarized as

$$y(n) = \xi \cdot r(n) \cdot e^{j(2\pi\Delta fnT_s)} + \sigma \cdot (r(n) \cdot e^{j(2\pi\Delta fnT_s)})^* + w(n) \tag{3.3}$$

where $(\cdot)^*$ denotes the complex conjugate operation. The received signal can thus be regarded as a gain, denoted by the signal gain (SG) ξ , from the original signal added to the conjugate multiplied by a delta value, called the mirror gain (MG) σ . The signal and mirror gains are represented as follows.

$$\begin{aligned}
SG : \xi &= 0.5(1 + (1 - \varepsilon)e^{-j\varphi}) \\
MG : \sigma &= 0.5(1 - (1 - \varepsilon)e^{j\varphi})
\end{aligned}
\tag{3.4}$$

If neither gain nor phase error exist, then SG remains at unity, and MG decreases to zero. Significantly, the phase rotation is inversed in the direction between the original signals and its conjugate if the CFO is present. Hence, the conventional compensation algorithm, which simply multiplies the data by an exponential term, must be modified in accordance with the gain and phase errors. This work mainly focuses on extracting the CFO value with the IQ-M error.

3.2 Estimation for Carrier Frequency Offset

3.2.1 Conventional Algorithm

Many OFDM WLAN standards include two preambles for synchronization, namely short and long training symbols. Figure 3-2 illustrates the preamble structure specified by the IEEE 802.11a/g [4], [5]. The OFDM packet preamble consists of 10 identical short training symbols t_i , $i = 1, 2, \dots, 10$, each containing 16 samples, and two identical long training symbols T_j , $j = 1, 2$, each containing 64 samples. The packet also contains a guard interval (GI) with 32 samples. GI is the cyclic prefix for the long training symbol T_1/T_2 , i.e., it is the extra replica of the last 32 samples of T_1/T_2 . Short training symbols are typically applied for coarse estimation, while long training symbols are utilized for fine estimation.

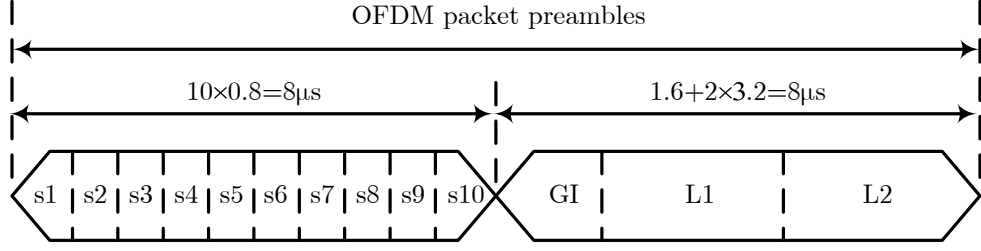


Figure 3-2. The preamble structure of the IEEE 802.11a/g.

All sub-carriers in the first symbol of a system with CFO are rotated by the same angle to the same sub-carriers in the second symbol. A basic strategy for computing the frequency offset is to employ two repeated training symbols. The following equation concerning DA methods shows the CFO estimation by two consecutive short training symbols in the time domain,

$$\Delta f = \frac{1}{2\pi N_s T_s} \tan^{-1} \left\{ \frac{\text{Im} \{y(n + N_s)y(n)^*\}}{\text{Re} \{y(n + N_s)y(n)^*\}} \right\} \quad (3.5)$$

where N_s denotes the data samples of a short training symbol [21]. However, the estimation error increases when the gain or phase error at the receiver is not zero. To illustrate this effect, let $y(n)_{iq}$ and $y(n + N_s)_{iq}$ represent two consecutive short preambles distorted by CFO and IQ-M, as shown below:

$$y(n)_{iq} = \xi r(n)e^{j(2\pi\Delta f n T_s)} + \sigma \left(r(n)e^{j(2\pi\Delta f n T_s)} \right)^* + w(n) \quad (3.6)$$

$$\begin{aligned} y(n + N_s)_{iq} \\ = \xi r(n + N_s)e^{j(2\pi\Delta f (n+N_s) T_s)} + \sigma \left(r(n + N_s)e^{j(2\pi\Delta f (n+N_s) T_s)} \right)^* + w(n + N_s) \end{aligned} \quad (3.7)$$

To simplify the derivation, the noise distribution is ignored for the analysis. Because the short training symbols are periodic, $r(n + mN_s)$, $m = 0, 1, \dots, 9$, can be replaced by

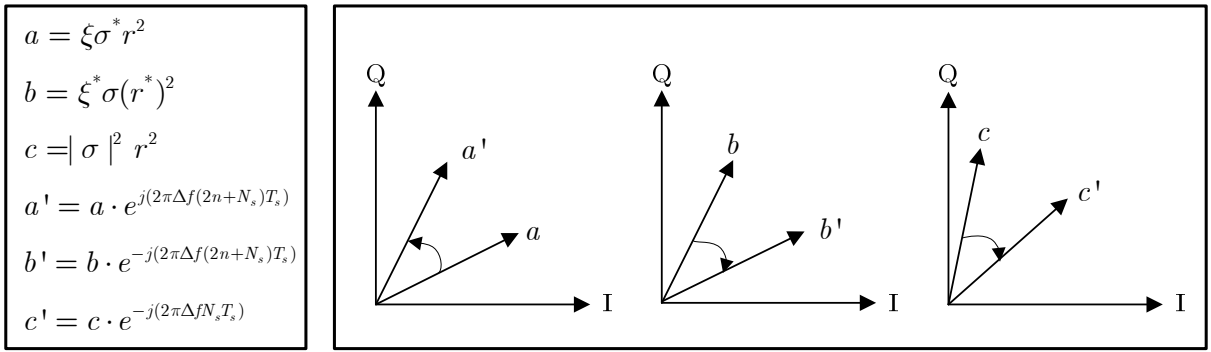
r . The phase difference between two consecutive symbols can then be expressed as

$$\arg\{y(n + N_s)_{iq}y(n)_{iq}^*\} = \arg\{|\xi|^2|r|^2 e^{j(2\pi\Delta f N_s T_s)} + \psi\} \quad (3.8)$$

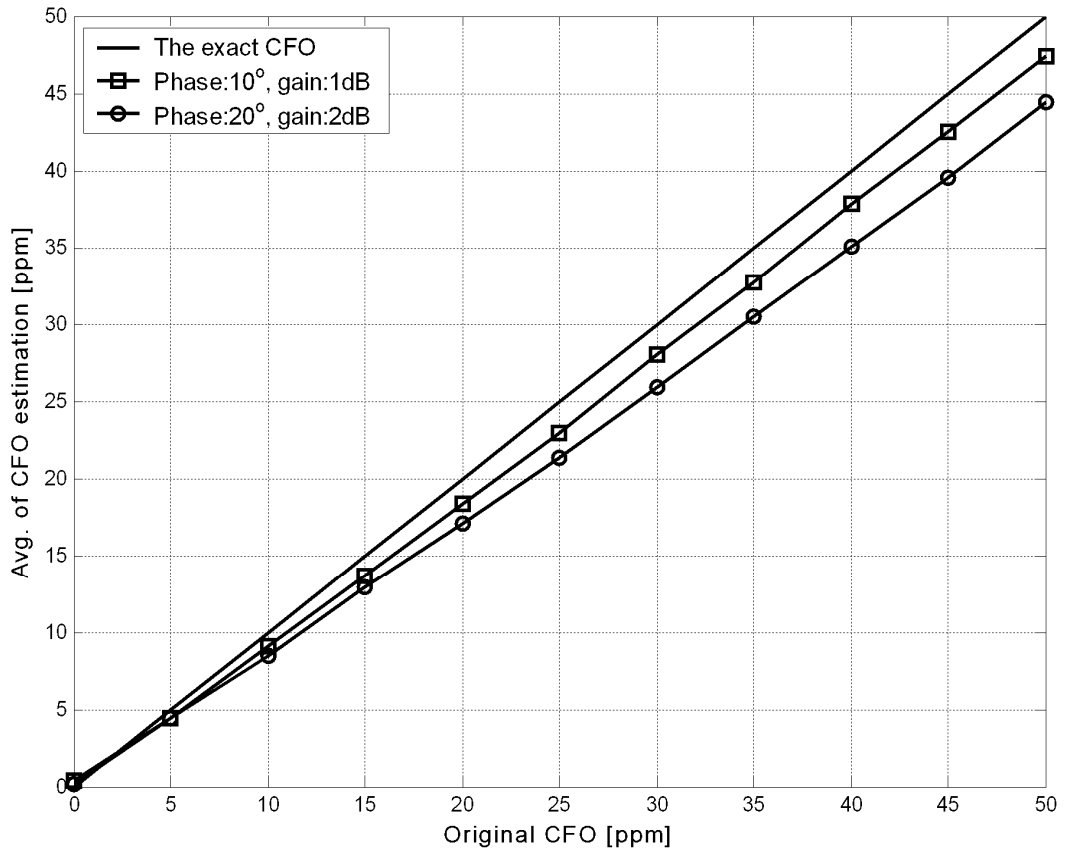
where $\arg\{\cdot\}$ denotes the phase of its argument. The term ψ represents the interference caused by CFO and IQ-M, given by

$$\begin{aligned} \psi = & \xi\sigma^*r^2e^{j(2\pi\Delta f(2n+N_s)T_s)} + \xi^*\sigma(r^*)^2e^{-j(2\pi\Delta f(2n+N_s)T_s)} \\ & + |\sigma|^2|r|^2 e^{-j(2\pi\Delta f N_s T_s)} \end{aligned} \quad (3.9)$$

Equation (3.9) indicates that a larger original CFO produces a larger estimation error. This effect always occurs if the scheme based on two identical symbols is applied. The terms in (3.9) can be interpreted geometrically as the vectors in the complex plane. Figure 3-3(a) shows how the terms in (3.9) change in the complex plane. As CFO is larger, the phase rotation increases, which results in significant degradation in the two-repeat preamble-based estimator. The effect is evident in Figure 3-3(b), which illustrates the estimation of frequency offset vs. the exact CFO value when the transmitting signal is distorted by noise, IQ-M and CFO. A modified method is developed in next subsection to improve the estimation accuracy.



(a)



(b)

Figure 3-3. (a) Complex plane for the terms in (3.9). (b) CFO estimation by two-repeat preamble-based method under 19 dB SNR.

3.2.2 The Proposed Pseudo CFO Algorithm

The proposed algorithm adopts three identical training symbols for frequency offset estimation. First, $y(n)_{iq}$, $y(n + N_s)_{iq}$, and $y(n + 2N_s)_{iq}$ are defined as three consecutive short preambles, which are distorted by CFO and IQ-M. The original frequency offset and the pseudo-frequency offset are assumed to be positive in the following mathematical derivations. The three preambles are then rotated by the pseudo-frequency offset. Therefore, the following equations hold:

$$\begin{aligned} y_1 &= y(n)_{iq} e^{j(2\pi\Delta\theta n T_s)} \\ &= \left[\xi r e^{j(2\pi\Delta f n T_s)} + \sigma r^* e^{-j(2\pi\Delta f n T_s)} \right] e^{j(2\pi\Delta\theta n T_s)} \end{aligned} \quad (3.10)$$

$$\begin{aligned} y_2 &= y(n + N_s)_{iq} e^{j(2\pi\Delta\theta(n+N_s) T_s)} \\ &= \left[\xi r e^{j(2\pi\Delta f(n+N_s) T_s)} + \sigma r^* e^{-j(2\pi\Delta f(n+N_s) T_s)} \right] e^{j(2\pi\Delta\theta(n+N_s) T_s)} \end{aligned} \quad (3.11)$$

$$\begin{aligned} y_3 &= y(n + 2N_s)_{iq} e^{j(2\pi\Delta\theta(n+2N_s) T_s)} \\ &= \left[\xi r e^{j(2\pi\Delta f(n+2N_s) T_s)} + \sigma r^* e^{-j(2\pi\Delta f(n+2N_s) T_s)} \right] e^{j(2\pi\Delta\theta(n+2N_s) T_s)} \end{aligned} \quad (3.12)$$

where $\Delta\theta$ denotes the pseudo-frequency offset. The extra P-CFO is used to resolve the transformation error resulting from noise disturbances, which is discussed later. The mathematical derivation indicates the following (see Appendix B for details)

$$\begin{aligned} &\text{Im}\{y_2\} \text{Re}\{y_1\} - \text{Im}\{y_1\} \text{Re}\{y_2\} \\ &\cong (1 - \varepsilon) \left(\text{Re}\{r\}^2 + \text{Im}\{r\}^2 \right) \sin(2\pi\Delta f N_s T_s) \cos(2\pi\Delta\theta N_s T_s) \cos(\varphi) \end{aligned} \quad (3.13)$$

$$\begin{aligned} &\text{Im}\{y_3\} \text{Re}\{y_1\} - \text{Im}\{y_1\} \text{Re}\{y_3\} \\ &\cong (1 - \varepsilon) \left(\text{Re}\{r\}^2 + \text{Im}\{r\}^2 \right) \sin(4\pi\Delta f N_s T_s) \cos(4\pi\Delta\theta N_s T_s) \cos(\varphi) \end{aligned} \quad (3.14)$$

Equations (3.13) and (3.14) demonstrate that

$$\begin{aligned}
\frac{(14)}{2(13)} &= \frac{\sin(4\pi\Delta f N_s T_s) \cos(4\pi\Delta\theta N_s T_s)}{2 \sin(2\pi\Delta f N_s T_s) \cos(2\pi\Delta\theta N_s T_s)} \\
&= \cos(2\pi\Delta f N_s T_s) \cos(2\pi\Delta\theta N_s T_s) \\
&\quad - \cos(2\pi\Delta f N_s T_s) \sin(2\pi\Delta\theta N_s T_s) \tan(2\pi\Delta\theta N_s T_s) \\
&= z_1
\end{aligned} \tag{3.15}$$

Since the sample time (T_s) is 50 ns and the P-CFO ($\Delta\theta$) is set to 30 ppm (± 0.23 subcarrier spacing), $2\pi\Delta\theta N_s T_s$ is small and approximated as $\tan(2\pi\Delta\theta N_s T_s)$ ($2\pi\Delta\theta N_s T_s = 2\pi \cdot 30 \cdot 10^{-6} \cdot 16 \cdot 50 \cdot 10^{-9}$). Accordingly, the following equation holds.

$$\tan(2\pi\Delta\theta N_s T_s) \cong \sin(2\pi\Delta\theta N_s T_s) \cong 0 \tag{3.16}$$

From (3.16), (3.15) can be approximated as

$$z_1 \cong \cos(2\pi(\Delta f + \Delta\theta) N_s T_s) \tag{3.17}$$

Consequently, the frequency offset can be computed from (3.17). The estimated frequency offset is given by

$$\Delta\hat{f} = \frac{\cos^{-1}(z_1)}{2\pi N_s T_s} - \Delta\theta \tag{3.18}$$

The same method also indicates that

$$\begin{aligned}
& \frac{\text{Im}\{y_3\} \text{Re}\{y_1\} - \text{Im}\{y_1\} \text{Re}\{y_3\}}{2(\text{Im}\{y_3\} \text{Re}\{y_2\} - \text{Im}\{y_2\} \text{Re}\{y_3\})} \\
&= \cos(2\pi\Delta f N_s T_s) \cos(2\pi\Delta\theta N_s T_s) \\
&\quad - \cos(2\pi\Delta f N_s T_s) \sin(2\pi\Delta\theta N_s T_s) \tan(2\pi\Delta\theta N_s T_s) \\
&= z_2 \\
&\cong \cos(2\pi(\Delta f + \Delta\theta) N_s T_s)
\end{aligned} \tag{3.19}$$

From (3.19), the estimated frequency offset can be expressed as

$$\Delta \hat{f} = \frac{\cos^{-1}(z_2)}{2\pi N_s T_s} - \Delta\theta \tag{3.20}$$

Therefore, the estimated of frequency offset can be averaged according to (3.18) and (3.20).

Figure 3-4 shows the inverse cosine (arccosine) function for real element of z in the domain $[-1, 1]$. This figure indicates that the arccosine value should be zero if the original CFO value is 0 ppm. However, there is a disadvantage of the cosine estimator ($\cos^{-1}(z)$). It is sensitive to even a small amount of noise disturbance when z is relatively small. Therefore, the noise disturbance will have great effect on the CFO estimation and lead to transformation errors. The proposed method to solve this problem is to multiply the training sequence by an extra exponential term and get a larger CFO value. A larger CFO value prevents inverse cosine from being affected by noise disturbance and reduces the possibility of transformation errors accordingly.

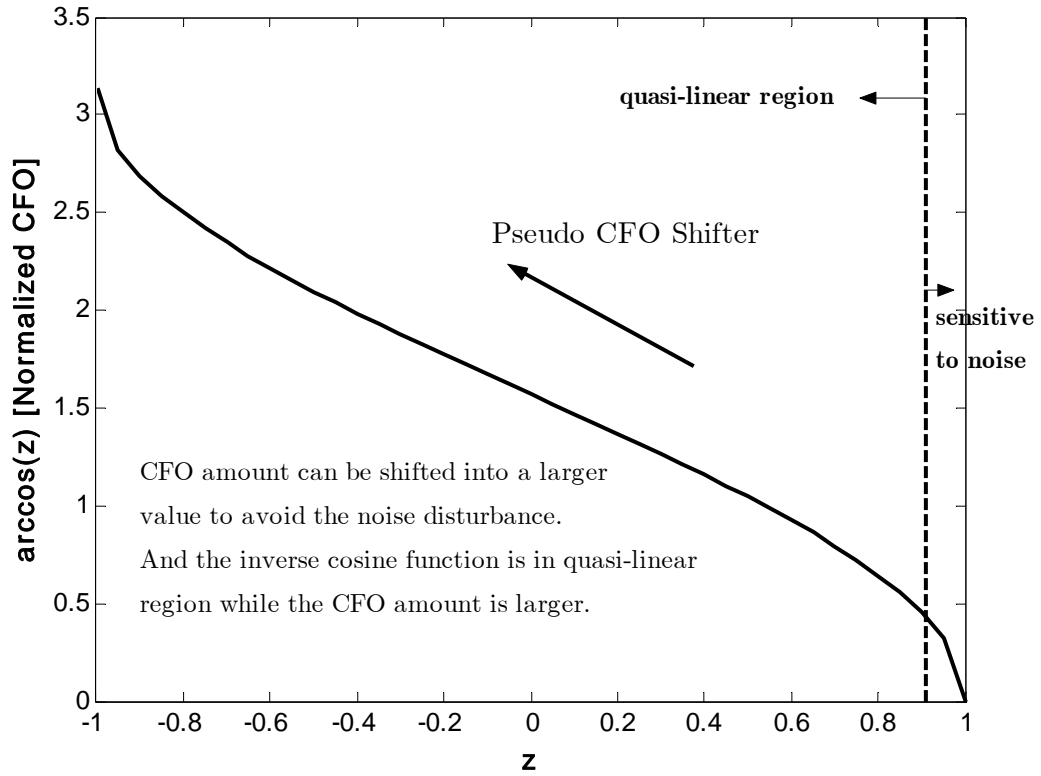


Figure 3-4. Inverse cosine function.



The maximum frequency error that can be estimated from a short training sequence is about 625 kHz, since the sample time is 50 ns, and the delay length is 16 [4]. The IEEE 802.11a standard specifies a maximum oscillator error of 20 ppm and a carrier frequency of approximately 5 GHz. Hence, the frequency difference between the transmitter and the receiver is ± 40 ppm, giving a maximum frequency offset of ± 200 kHz [4]. If the P-CFO is set to 50 ppm in the proposed algorithm, then the maximum frequency error is ± 450 kHz. Hence, the maximum possible frequency error is well within the above range. For the IEEE 802.11g system, the carrier frequency may be approximately 2.4 GHz, with 25 ppm (maximum) oscillator error. Therefore, the maximum frequency offset is about ± 120 kHz [5]. If the P-CFO is also set to 50 ppm, then the maximum frequency offset is ± 240 kHz. Although the proposed scheme uses an additional frequency offset to extract the frequency offset, it can meet the standard

specification.

The frequency offset can be estimated similarly if the original CFO is negative. The sign of the CFO can be determined using the following equation:

$$\begin{cases} \text{positive, } \text{Im}\{y(n + N_s)y(n)^*\} \geq 0 \\ \text{negative, } \text{Im}\{y(n + N_s)y(n)^*\} < 0 \end{cases} \quad (3.21)$$

Figure 3-5 shows the flowchart of the proposed P-CFO algorithm. The P-CFO estimator begins to compute the frequency offset with IQ-M after the frame detector detects a short training sequence. The sign of the original CFO is first determined according to (3.21), so that the P-CFO shifter module can begin to work at the sign signal. The CFO calculation module then employs the data from the P-CFO shifter module to compute the frequency offset. Since the arccosine value is positive, the estimated CFO from the CFO calculation module is multiplied by -1 if the original CFO is negative. Finally, the P-CFO is subtracted or added from the estimated frequency offset in order to obtain the CFO. The proposed P-CFO algorithm can be summarized as follows:

- 1) If $\text{CFO} \geq 0$, then rotate the received training symbols by an additional frequency offset based on (3.10) ~ (3.12); otherwise, rotate the symbols in the adverse direction.
- 2) Estimate the pseudo frequency offset according to the proposed scheme based on (3.13) ~ (3.17) and (3.19).
- 3) If $\text{CFO} \geq 0$, then subtract P-CFO from the estimated CFO as in (3.18) and (3.20); otherwise, multiply the estimated CFO by -1 and add P-CFO.
- 4) Compensate for the frequency offset obtained in Step 3.

After the long training symbols are successfully corrected for the effect of the

frequency offset, the effect of IQ-M can be corrected by the available techniques [50].

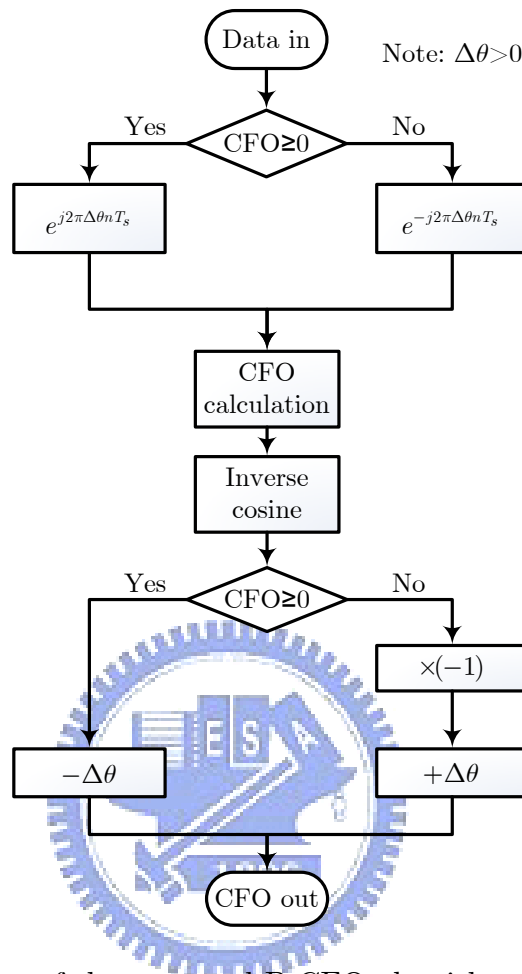


Figure 3-5. The flowchart of the proposed P-CFO algorithm.

3.3 Simulation and Performance

A typical OFDM system based on IEEE 802.11g for WLAN was adopted as a reference-design platform to evaluate the performance of the proposed algorithm. The parameters employed in the simulation platform were *OFDM symbol length 64 and cyclic prefix 16*. IEEE 802.11g includes ten short training symbols for coarse estimation, and two long preambles for fine estimation. A satisfactory accuracy can usually be reached if sufficient data samples are applied to compute the estimate from the short

training symbols. Consequently, the proposed method only uses short training symbols to measure the frequency offset under IQ-M conditions. In this experiment, the gain and phase errors were set to 2 dB and 20° , respectively. The CFO amount was simulated with values in the range of +50 ppm to -50 ppm at a carrier frequency of 2.4 GHz, and the additional P-CFO was set to 30 ppm. TABLE 3-1 lists the simulation parameters for frequency-selective fading channels. For a fair comparison, the two-repeat preamble-based scheme also used three training symbols to estimate the CFO value. Figure 3-6 shows the estimation of frequency offset vs. the exact CFO value, based on the simulation parameters in TABLE 3-1. Simulation results indicate that the proposed algorithm can estimate the frequency offset more accurately than the two-repeat preamble-based scheme.

Figures 3-7 and 3-8 illustrate the estimation errors of the frequency offset estimation under different IQ-M values, where the frequency offset is 50 ppm. These figures clearly demonstrate that the estimation error of the conventional (two-repeat preamble-based) method increases as IQ-M increases. The conventional method is thus insufficiently robust under different IQ-M conditions. Figure 3-8 clearly shows that the estimation error of the proposed method is independent of IQ-M, and provides smaller errors than the two-repeat preamble-based approaches. Pollet *et al.* [51] found that setting the maximum tolerable frequency offset to 1% of the sub-carrier spacing keeps the degradation as low as about 0.1 dB. For instance, the oscillator accuracy must be about 3 kHz or 1.25 ppm for an OFDM system at a carrier frequency of 2.4 GHz and a sub-carrier spacing of 312.5 kHz. Consequently, the proposed algorithm is accurate in estimating the frequency offset with IQ-M, preventing significant performance loss.

TABLE 3-1. Simulation Parameters.

<i>Parameter</i>	<i>Value</i>
Channel	RMS: 100 ns, Tap: 6
Packet Number	1,000
Data Rate	54 Mbits/s
Gain Error	1 dB, 2 dB
Phase Error	10°, 20°

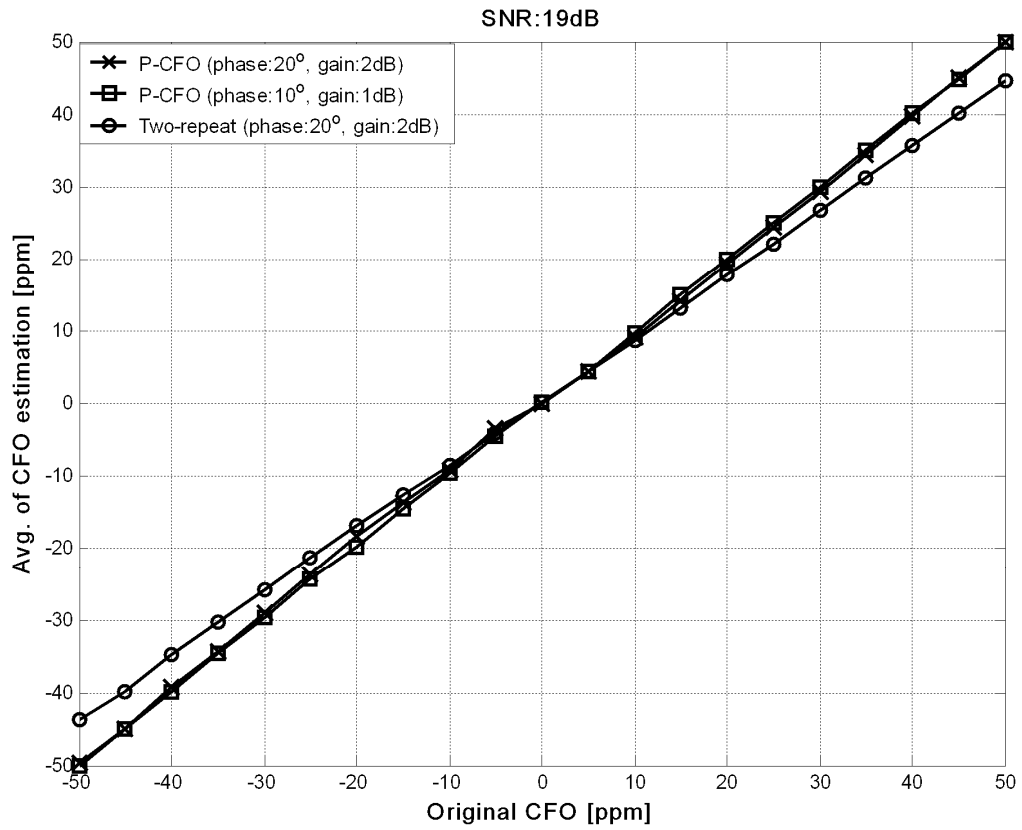


Figure 3-6. Frequency offset estimation.

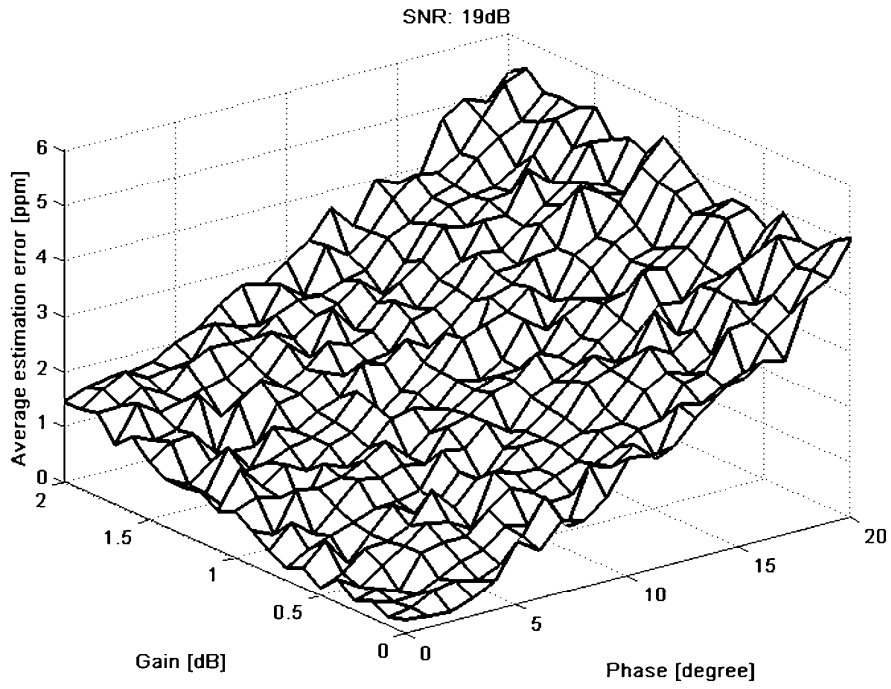


Figure 3-7. CFO estimation by the two-repeat preamble-based method.

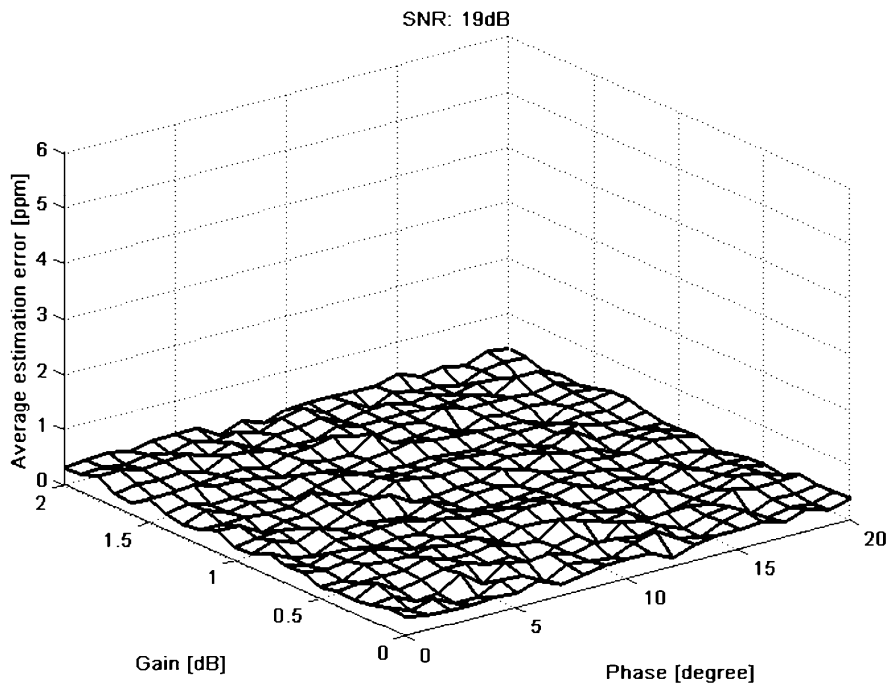
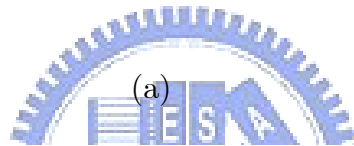
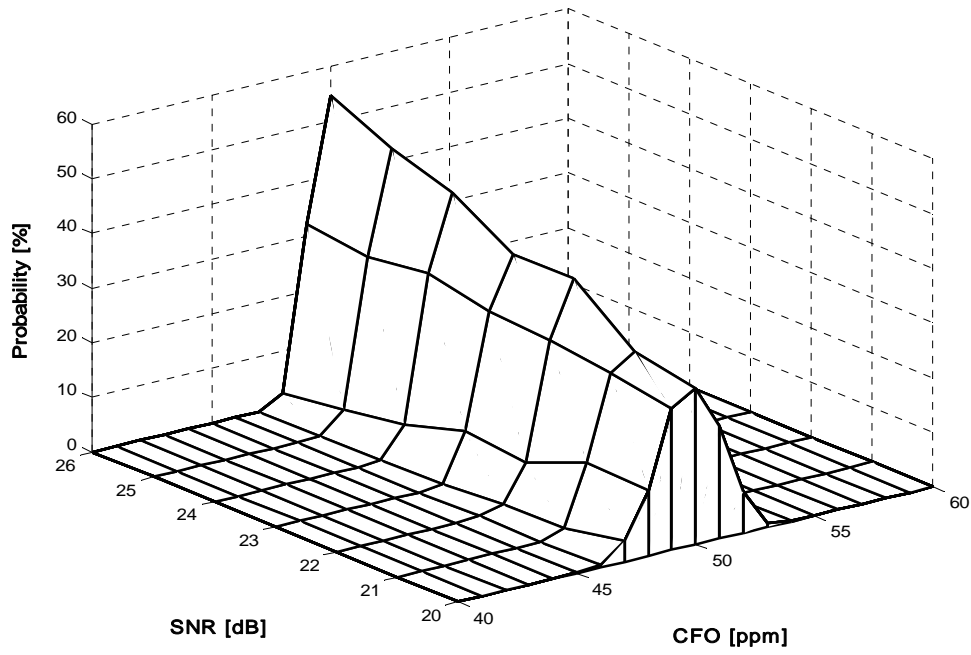


Figure 3-8. CFO estimation by the proposed P-CFO algorithm.

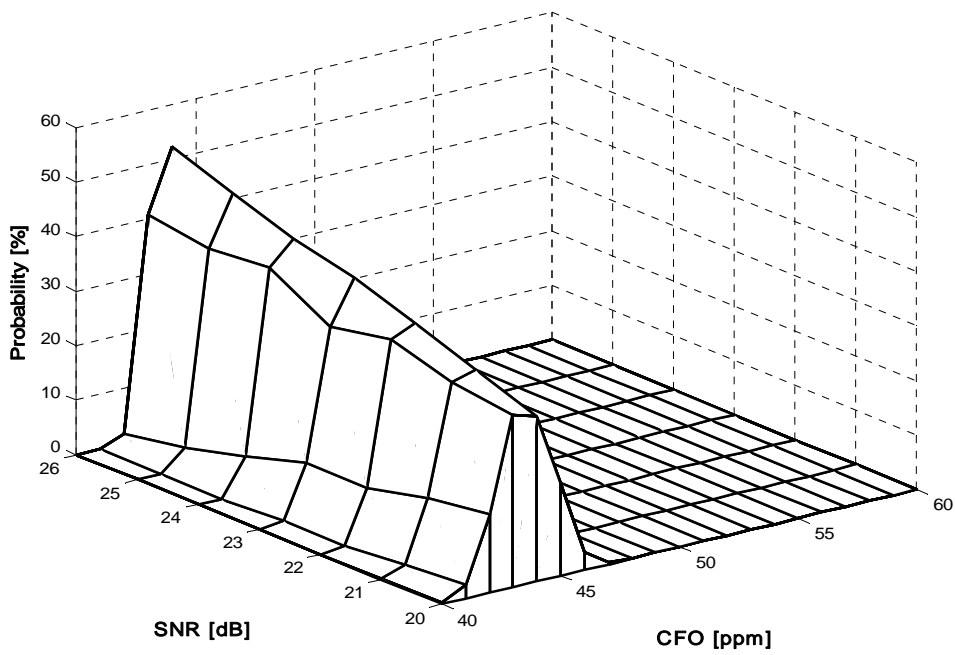
The estimated frequency offset under IQ-M can be characterized by a Gaussian probability density function (PDF), as shown in Figure 3-9. Figure 3-9(a) clearly shows that the mean of the proposed P-CFO algorithm was close that of the original CFO. However, the two-repeat preamble based method, as shown in Figure 3-9(b), always had bias. These figures indicate that the proposed P-CFO algorithm allows the correct CFO to be extracted under IQ-M conditions.

Figure 3-10 shows the mean square error (MSE) of frequency estimation vs. SNR under different IQ-M conditions. Figure 3-10 indicates that for almost the entire SNR range, the P-CFO algorithm under the condition of 2 dB gain error and 20° phase error performed better than conventional methods under the same condition or moderate IQ-M scenario, i.e., 1 dB gain error and 10° phase error. The P-CFO algorithm thus has better estimation accuracy under IQ-M than conventional methods. Since there are some approximations in the derivation, the MSE of the P-CFO algorithm is slightly weaker than the two-repeat preamble-based method under ideal I/Q. TABLE 3-2 summarizes the required SNR under 10^{-6} MSE.

Figure 3-11 indicates that the proposed method has a smaller estimation error than the two-repeat preamble-based method in the range -50 ppm to $+50$ ppm. In floating-point simulations, the proposed algorithm with a deterministic CFO has the same performance as that with a randomly generated CFO. However, fixed-point simulations have some performance degradation, which is still lower than that of the two-repeat preamble-based scheme. Since the proposed scheme significantly reduces the impact of CFO, it can utilize IQ-M compensation more easily than conventional methods [50].



(a)



(b)

Figure 3-9. PDF of 50 ppm CFO: (a) P-CFO algorithm. (b) Two-repeat preamble-based method.

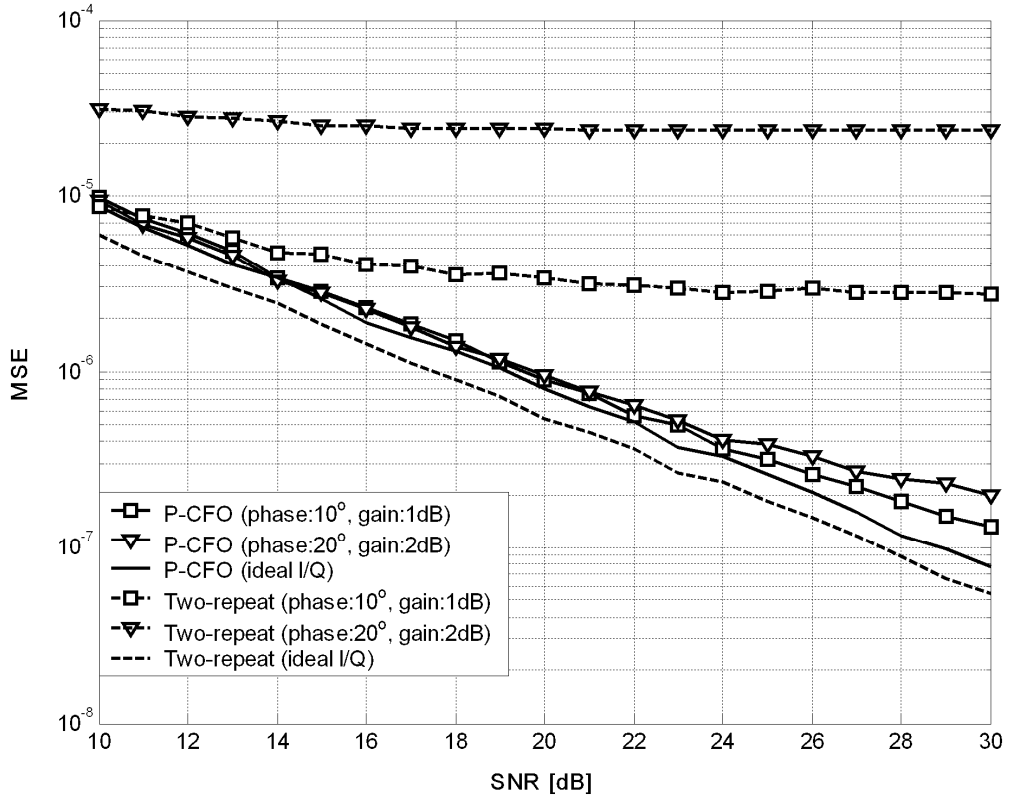


Figure 3-10. Mean square error (MSE) of frequency estimation vs. SNR under different I/Q imbalance conditions with 50 ppm CFO.

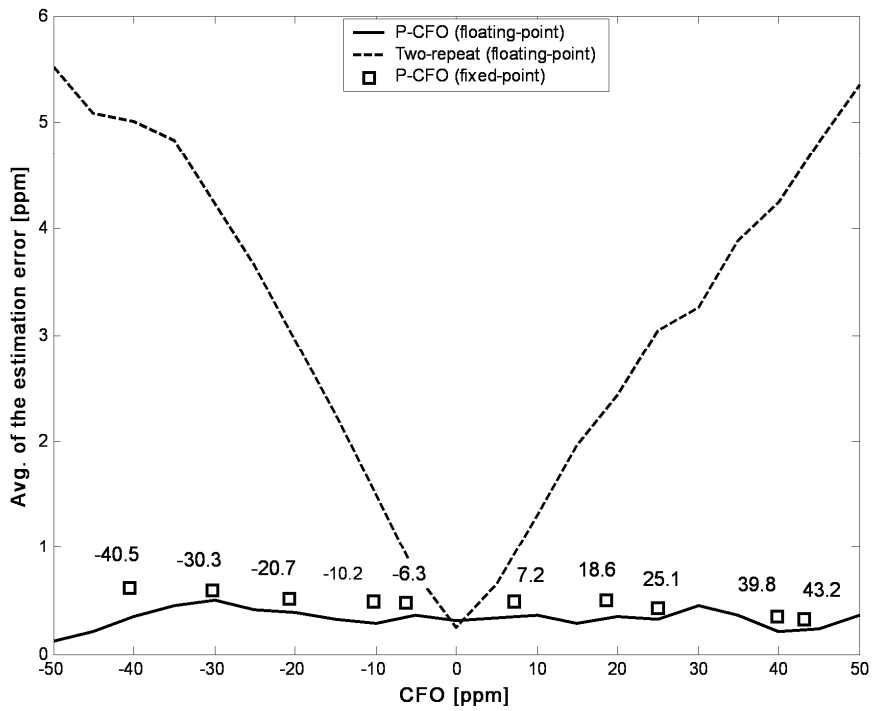


Figure 3-11. Average of the estimation error.

TABLE 3-2. Required SNR.

	<i>P-CFO</i>	<i>Two-repeat</i>
Gain: 2 dB, Phase: 20°	20	N/A
Gain: 1 dB, Phase: 10°	20	N/A
Gain: 0 dB, Phase: 0°	19	17.5

3.4 Implementation Hints

3.4.1 Design Methodology

The frequency estimator was implemented as a bit-and-cycle-true MATLAB model, where performance simulations and algorithmic exploration were performed. In the hardware design flows, the fixed-point function blocks replace the floating function blocks in the MATLAB model to specify a suitable signal wordlength. The Verilog source code was generated from the fixed-point MATLAB model after determining the architecture with fixed-point simulations. Additionally, a simulation environment was created to verify the frequency estimator by performing an automatic comparison check on the internal signals and on the output signals between the gate-level netlists and the fixed-point MATLAB model. Layout versus schematic (LVS) and design rule checking (DRC) were performed to verify the layout following its creation by the auto place and routing (APR) tools. Finally, post-layout simulations were also executed to verify the proposed design.

3.4.2 Architecture of P-CFO Algorithm

Figure 3-12 illustrates the architecture of the P-CFO algorithm. The P-CFO scheme contains three main parts, P-CFO shifter, CFO calculation and inverse cosine. The P-CFO shifter module begins to work when the training symbols arrive. The P-CFO shifter module rotates the received training symbols by the pseudo-frequency offset. As shown in Figure 3-12, the rotation is achieved by a look-up table and a complex multiplier. The direct implementation of the complex multiplier was modified to lower its complexity and hardware cost. TABLE 3-3 clearly indicates that the direct implementation employs four multipliers and two adders. However, the modified implementation only requires three multipliers and five adders to lower the hardware cost (if the wordlength is sufficiently long). The CFO calculation module starts to perform CFO estimation based on the proposed algorithm when the P-CFO shifter module finishes the rotation. Figure 3-12 shows that the estimation is realized by 6 multipliers (4 for multiplication and 2 for division) and 4 adders. The output of CFO calculation module is transmitted to the inverse cosine module after the CFO is calculated. The inverse cosine module determines the angle of the correlation calculated from the CFO calculation module, and then adds or subtracts the pseudo-frequency offset to extract the final CFO.

TABLE 3-4 lists the synthesis results of the proposed P-CFO algorithm. Based on the proposed architecture, a test chip compliant to OFDM receiver was implemented in a standard 0.13 μm CMOS technology with 10mW power consumption, and housed in a 144-pin CQFP package. P-CFO part occupies approximately 34K gates, which are roughly equal to 0.23 mm^2 in 0.13- μm CMOS technology. The chip micrograph is shown in Figure 3-13, and its parameters are listed in TABLE 3-5.

TABLE 3-3. Complex Multiplier.

	$(a + jb)(c - jd)$	<i>Gate Counts</i>
Modified	Real = $(ac + bd)$ Imag = $(a + b)(c - d) - ac + bd$	2,650
Direct Implementation	Real = $(ac + bd)$ Imag = $(bc - ad)$	2,954

TABLE 3-4. The Complexity (Gate Count) of P-CFO.

	<i>Blocks</i>	<i>Gate Counts</i>
P-CFO Shifter Module	P-CFO shifter (LUT)	333 (1%)
	Complex multiplier	2,650 (8%)
	Combinational	7,498 (22%)
	Non-combinational	6,190 (18.5%)
	Module 1	13,688 (40.5%)
CFO Calculation Module	Combinational	7,980 (23%)
	Non-combinational	6,826 (20%)
	Module 2	14,806 (43%)
Inverse Cosine Module	Inverse cosine (LUT)	339 (1%)
	Combinational	5,406 (16%)
	Non-combinational	162 (0.5%)
	Module 3	5,568 (16.5)
Total		34,062 (100%)

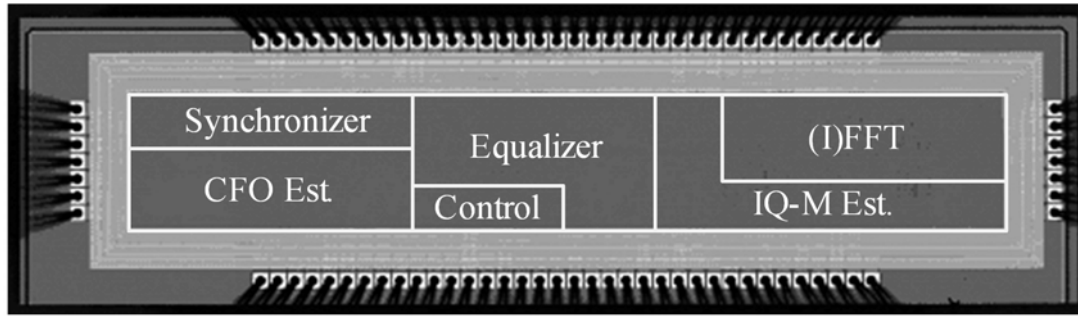


Figure 3-13. Chip micrograph.

3.4.3 Verification Platform

A verification platform was constructed to measure the performance of both the proposed method and the conventional method (two-repeat preamble-based method), as shown in Figure 3-14. The design was directly mapped onto the FPGA chips (Xilinx XtremeDSP, Virtex-II) with on-board 14-bit digital to analog converters (DACs) to transform the digital data into analog signals. Then the signals were transmitted by in-house RF front end. After down-converting RF signals to baseband at RX part, the analog signals are fed to 14-bit analog to digital converters (ADCs). The received data from ADCs was processed to calculate the CFO value using both the proposed method and the conventional method. In the meantime, the received data from ADCs was also applied to the chip testing, which was performed to verify the full functionality of the chip using Agilent 93000 SOC Test System. After the CFO estimation and chip testing processes, the results were collected to evaluate the performance of both the proposed method and the conventional method.



Figure 3-14. The photo of platform.

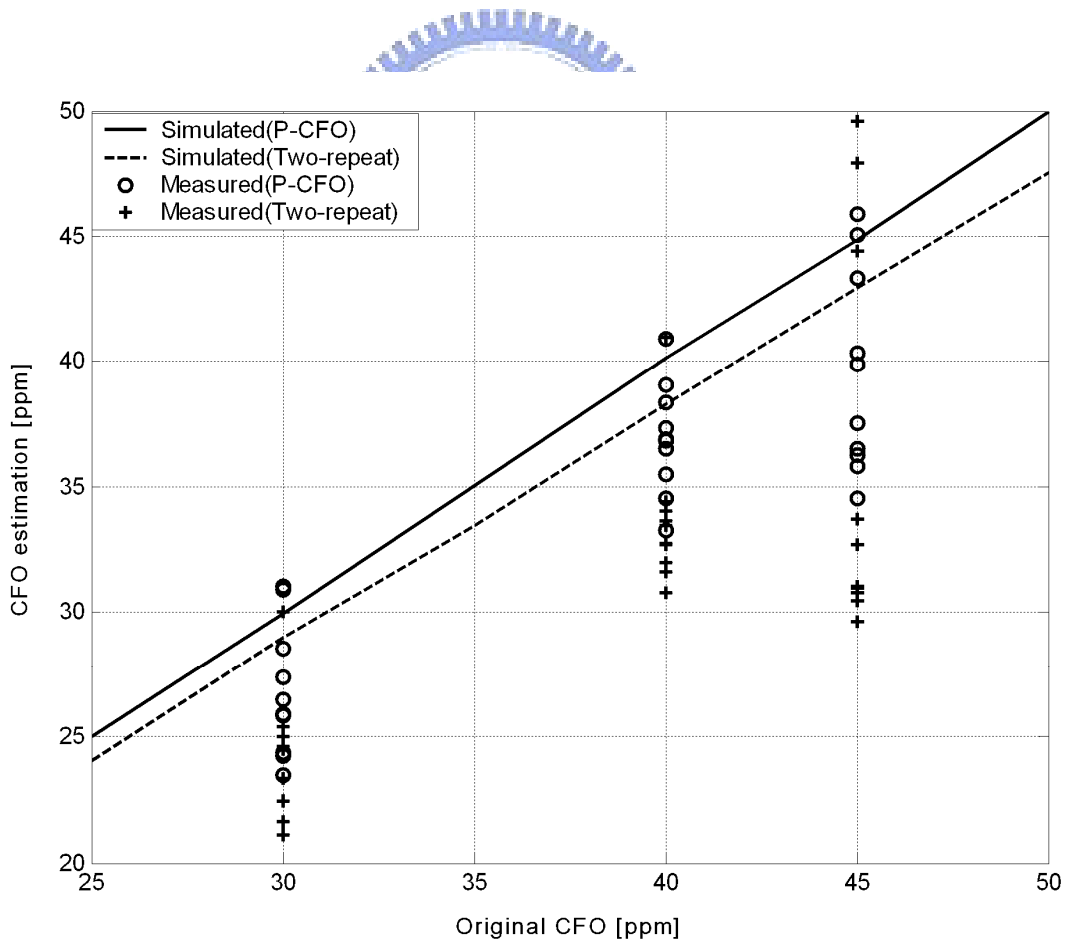
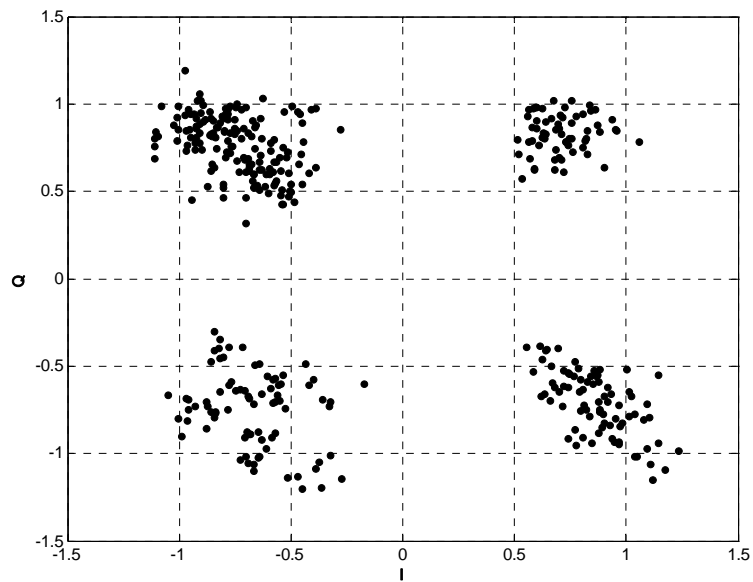
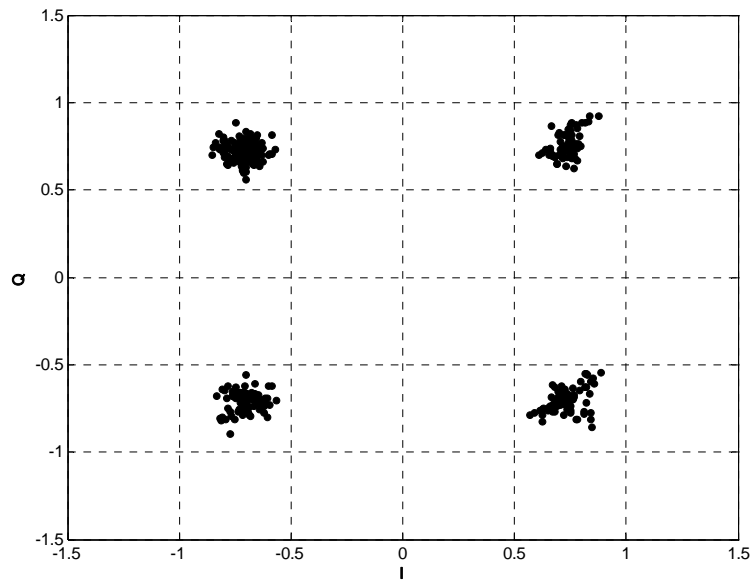


Figure 3-15. Estimated CFO of measurement vs. simulation.



(b)

Figure 3-16. Measurements of QPSK constellation: (a) P-CFO method. (b) Two-repeat preamble-based method.

The observed gain error and phase error are ~ 0.9 dB and $\sim 10^\circ$, respectively. Figure 3-15 shows both the measured and simulated CFO value. It indicates that the measured performance is a little worse than simulations since there are other spurious effects, noise, and nonlinearities in the front end. Although there is degradation in measured performance, the proposed method is still more accuracy. Figure 3-16 shows the baseband constellation for the QPSK modulation scheme. The error vector magnitude (EVM) for the proposed method is 7.4% (Figure 3-16(a)), while the EVM for the two-repeat preamble-based is 24.4% (Figure 3-16(b)). So the proposed solution is more robust than the conventional method under IQ-M conditions.

3.5 Summary

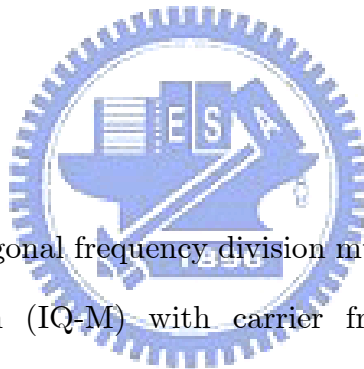


In this chapter, a novel algorithm is proposed to estimate the carrier frequency offset under the conditions of IQ-M in direct-conversion OFDM receivers. The proposed algorithm can adopt three training symbols to estimate the frequency offset from -50 ppm to $+50$ ppm under a 2.4 GHz carrier frequency with 2 dB gain error and 20 degree phase error in multipath environments. Simulation results indicate that the average estimation error of the proposed P-CFO algorithm can fulfill many system requirements, preventing obvious performance loss under different IQ-M conditions. The proposed design is implemented in an ASIC with 3.3×0.4 mm² core area and 10 mW power dissipation at 54 Mbits/s data rate. Hence, the proposed algorithm can enhance the performance of wireless OFDM systems, enabling small low-cost systems to be achieved.



Chapter 4

Preamble-Assisted Estimation for I/Q Mismatch



In direct-conversion orthogonal frequency division multiplexing (OFDM) receivers, the impact of I/Q mismatch (IQ-M) with carrier frequency offset (CFO) must be considered. A preamble-assisted estimation is developed to circumvent IQ-M with CFO. Both simulation and experiment results show that the proposed method could provide good estimation efficiency and enhance the system performance. Moreover, the proposed scheme is compatible with current wireless local area network (WLAN) standards.

OFDM is a spectrally efficient technique for high-speed wireless communications. OFDM systems are, however, susceptible to imperfect synchronization and non-ideal front-end effects, which cause serious performance degradation. Generally, OFDM systems are highly sensitive to CFO, which is the frequency mismatch of local oscillators between the transmitter and the receiver. CFO introduces inter-carrier interference in OFDM systems due to the loss of orthogonality between sub-carriers.

Recent research has also focused on developing monolithic OFDM receivers, particularly for low-cost technology. Direct-conversion architecture is one potential candidate for simple integration among different architectures. However, direct-conversion receivers suffer from mismatch between the I and Q channels, such as IQ-M of non-ideal radio frequency (RF) circuits [24], [25], [52]. Specifically, IQ-M arises when the phase and gain differences between I and Q branches are not exactly 90 degrees and 0 dB, respectively. IQ-M introduces the image interference into the desired signal and then degrades the system performance.

Due to the impairment in the analog components, the low-pass filters (LPFs) of I and Q channels are not identical. The mismatched LPFs result in frequency-dependent IQ-M. Frequency-dependent IQ-M means that the imbalances can vary with frequency. In an OFDM system with frequency-dependent IQ-M, the IQ-M parameters for every sub-carrier are different. Several schemes have been proposed to estimate constant IQ-M [63]-[66]. Although these methods can work well under constant IQ-M, they do not consider non-ideal LPFs and CFO phenomenon. Therefore, these methods are not robust to frequency-dependent IQ-M and CFO. Estimation for frequency-dependent IQ-M has also been studied in the open literature [48], [57]-[60], [62]. The effect and analysis of frequency-dependent IQ-M are given in [57]-[58]. Xing *et al.* [48] presented a method for frequency-dependent IQ-M. An optimal training sequence for frequency-dependent IQ-M has been proposed in [59]. However, these two methods have specific packet formats, making them incompatible with current WLAN standards, such as IEEE 802.11a/g [4]-[5]. Cetin *et al.* proposed an adaptive self-calibrating image rejection receiver [60]. This method needs a long converged time. Therefore it is not suitable for packet-based WLAN systems because the packet length is always limited.

In practice, frequency-dependent IQ-M and CFO arise simultaneously. However, only some references consider the frequency-dependent IQ-M with CFO. This study

mainly concentrates on the estimation of frequency-dependent IQ-M with CFO. To maintain and realize systems with imperfect front-end modules, a preamble-assisted estimation scheme is developed. Simulation results show that the performance loss is in the range of 1.6 to 1.8 dB at 10^{-4} bit error rate. Experiment results demonstrate that the proposed method could overcome joint impairments of frequency-dependent IQ-M and CFO, enabling a high performance receiver.

The remainder of the this chapter is organized as follows. Section 4.1 introduces the system model. Section 4.2 develops the constant IQ-M estimation. Section 4.3 then presents the frequency-dependent IQ-M estimation. Section 4.4 discusses the transmitter IQ-M. Conclusions are finally drawn in Section 4.5.

4.1 System Model

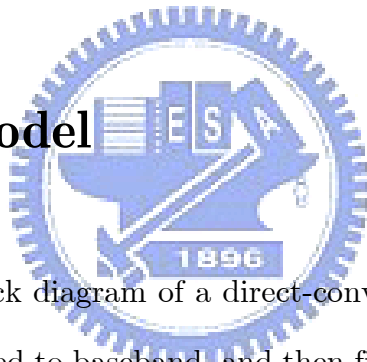


Figure 4-1 depicts the block diagram of a direct-conversion architecture. The received RF signal is down-converted to baseband, and then filtered out by the LPFs. Let $r(n)$ and $w(n)$ be the received signal and additive white Gaussian noise (AWGN), respectively. The baseband signal¹ with CFO Δf and IQ-M is given by [48], [57]

$$\begin{aligned}
 y(n) = & ((\alpha\psi(n) + \beta^*\xi(n)) \otimes r(n))e^{j2\pi\cdot\Delta f\cdot nT_s} \\
 & + ((\beta\psi(n) + \alpha^*\xi(n)) \otimes r^*(n))e^{-j2\pi\cdot\Delta f\cdot nT_s} \\
 & + w(n)
 \end{aligned} \tag{4.1}$$

where α and β denote the constant IQ-M parameters, and $\psi(n)$ and $\xi(n)$

¹ Equation (4.1) is based on discrete-time representation. Continuous time representation of (4.1) is expressed as

$$y(t) = ((\alpha\psi(t) + \beta^*\xi(t)) \otimes r(t))\exp(j2\pi \cdot \Delta f \cdot t) + ((\beta\psi(t) + \alpha^*\xi(t)) \otimes r^*(t))\exp(-j2\pi \cdot \Delta f \cdot t) + w(t).$$

represent the frequency-dependent IQ-M parameters. Note that the phase rotation is inverted in the direction between original signal and the conjugate signal if the CFO is present. The signal $r(n)$ can be further expressed as $r(n) = h(n) \otimes x(n)$, where $x(n)$ and $h(n)$ are the transmitted signal and channel impulse response, respectively. The symbol “ \otimes ” represents the convolution operator. From (4.1), the received signal can be regarded as the original signal added to the conjugate signal. The constant IQ-M parameters are expressed as [54]-[56]

$$\begin{aligned}\alpha &= 0.5(1 + (1 + \varepsilon)e^{-j\varphi}) \\ \beta &= 0.5(1 - (1 + \varepsilon)e^{j\varphi})\end{aligned}\tag{4.2}$$

where ε and φ denote the constant amplitude and phase mismatch, respectively. If neither gain nor phase error exists, α remains at unity, and β decreases to zero.

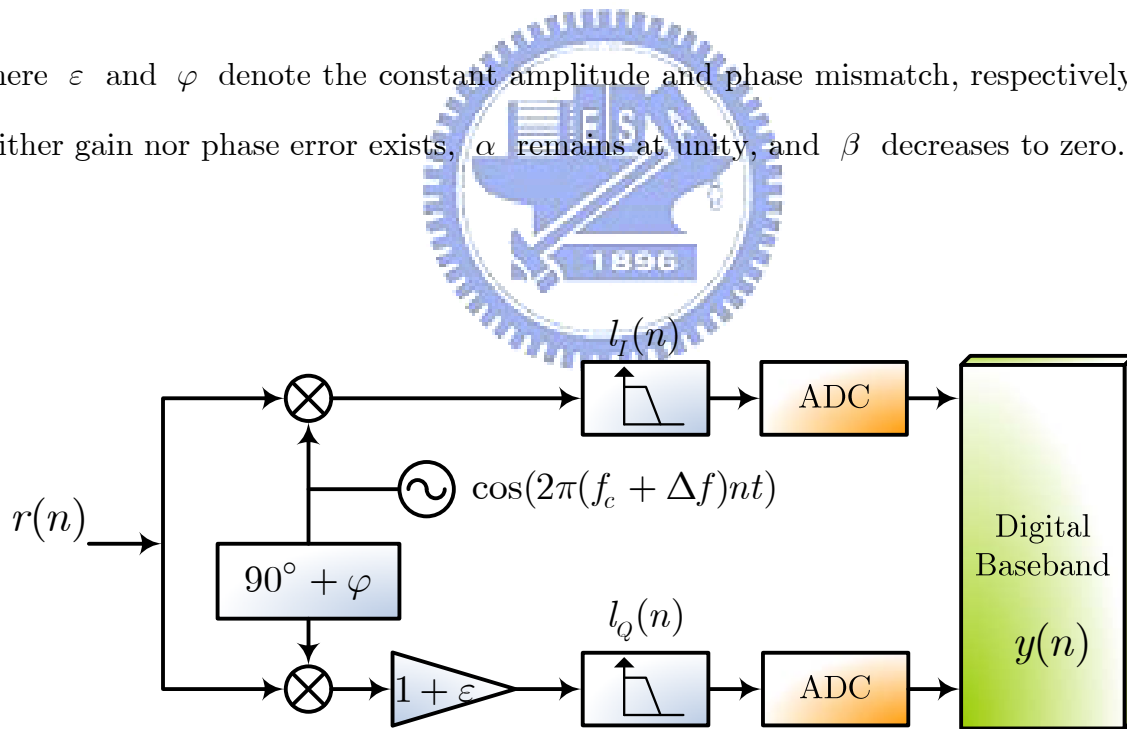
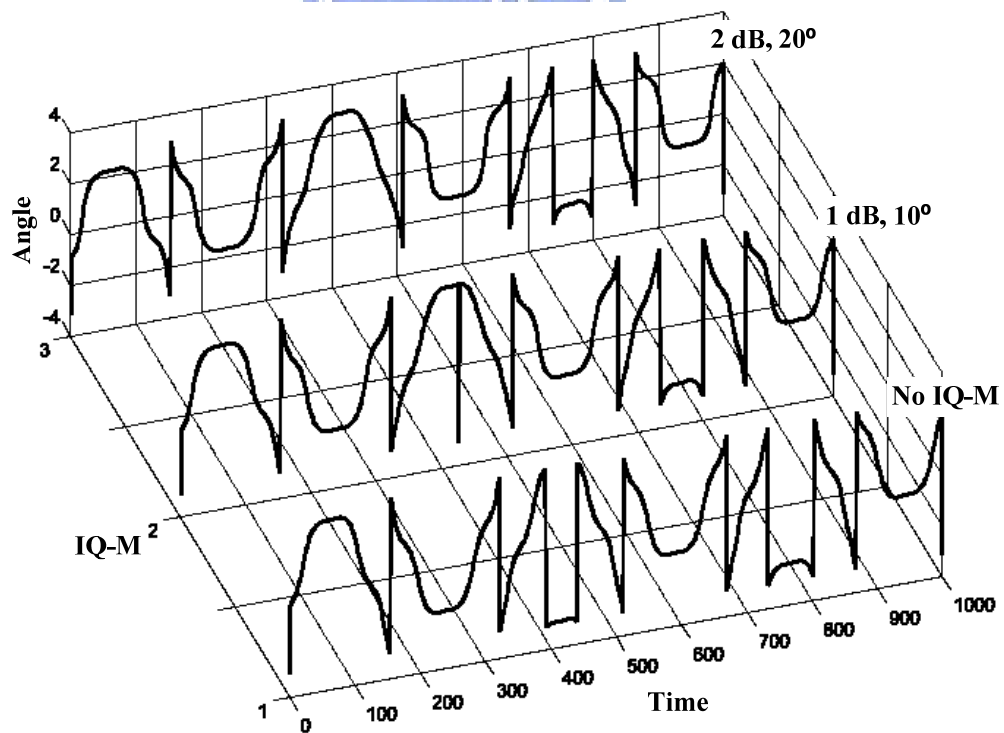
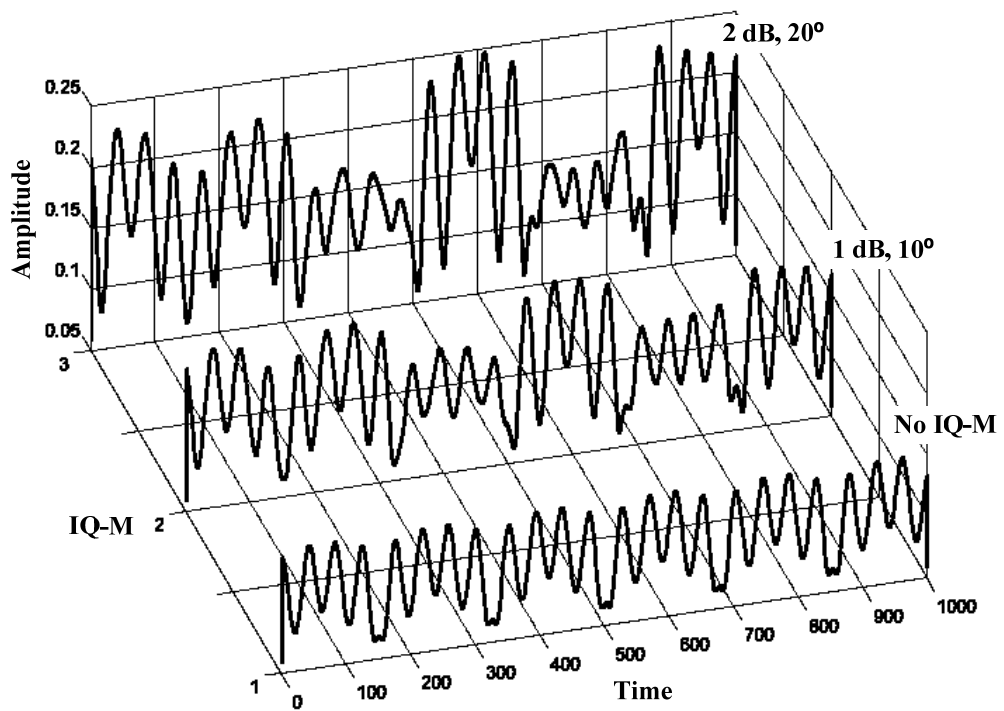


Figure 4-1. Direct-conversion receiver with I/Q mismatch and CFO.



(b)

Figure 4-2. Received signal with I/Q mismatch: (a) Amplitude. (b) Angle.

Moreover, the average filter response and response mismatch are defined as [48], [57]

$$\begin{aligned}\psi(n) &= 0.5(l_I(n) + l_Q(n)) \\ \xi(n) &= 0.5(l_I(n) - l_Q(n))\end{aligned}\tag{4.3}$$

where $l_I(n)$ and $l_Q(n)$ denote the LPFs of I and Q channels. If the LPFs of I and Q channels are identical, the response mismatch can be ignored. In Figure 4-2, it is clear that the signal with IQ-M has amplitude variations and phase jumps compared with the case without IQ-M. This effect causes the demodulation error and further degrades the system performance.



4.2 Constant IQ-M Estimation

4.2.1 Constant IQ-M Estimation without CFO

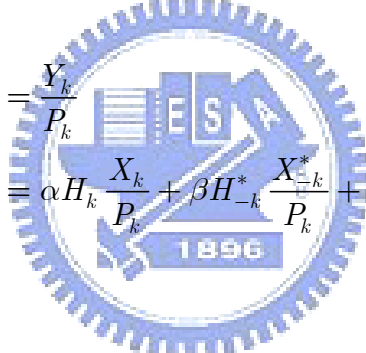
Here we analysis the effect of constant IQ-M in OFDM systems and propose a scheme to estimate IQ-M. If there is no CFO, (4.1) can be simplified to

$$y(n) = \alpha r(n) + \beta r^*(n) + w(n)\tag{4.4}$$

After the fast Fourier transform (FFT), the frequency-domain data can be expressed as

$$\begin{aligned}
Y_k &= \text{FFT}_N \{y(n)\} \\
&= \alpha R_k + \beta R_{-k}^* + W_k \\
&= \alpha H_k X_k + \beta H_{-k}^* X_{-k}^* + W_k
\end{aligned} \tag{4.5}$$

where the subscript N denotes the FFT size. Equation (4.5) shows that IQ-M can cause the symbol at the sub-carrier k to be scaled by the complex factor α . Moreover, the complex conjugate of the symbol at sub-carrier $-k$ multiplied by another complex factor β will be present. The desired sub-carrier k will include the unwanted interference related to the sub-carrier $-k$, implying that IQ-M can distort the accuracy of received signal. For instance, the channel estimation can be inaccuracy due to the interference caused by IQ-M. The effect of IQ-M on channel estimation can then be expressed as

$$\begin{aligned}
\hat{H}_k &= \frac{Y_k}{P_k} \\
&= \alpha H_k \frac{X_k}{P_k} + \beta H_{-k}^* \frac{X_{-k}^*}{P_k} + \frac{W_k}{P_k}
\end{aligned} \tag{4.6}$$


where P_k denotes the preamble pattern². In order to simplify the notation, the noise term is ignored in the following derivation. If X_k is the training symbol, (4.6) is rewritten as

$$\tilde{H}_k = \alpha H_k + \beta H_{-k}^* \frac{P_{-k}^*}{P_k} \tag{4.7}$$

From (4.7), it is obvious that IQ-M has large impact on the channel frequency response (CFR). If the influenced CFR is used to equalize the received data, the system

² The preamble pattern adopted in this study is shown as follows

$$\begin{aligned}
P_{-26 \sim -1, 1 \sim 26} &= \{1 \ 1 \ -1 \ -1 \ 1 \ 1 \ -1 \ 1 \ -1 \ 1 \ 1 \ 1 \ 1 \ 1 \ 1 \ -1 \ -1 \ 1 \ 1 \ -1 \ 1 \ -1 \ 1 \ 1 \ 1 \ 1, \\
&\quad 1 \ -1 \ -1 \ 1 \ 1 \ -1 \ 1 \ -1 \ 1 \ -1 \ -1 \ -1 \ -1 \ -1 \ 1 \ 1 \ -1 \ -1 \ 1 \ -1 \ 1 \ 1 \ 1 \ 1 \ 1\}
\end{aligned}$$

performance could be terrible especially for high order QAM constellation, e.g., 64-QAM. Thus, the challenge is to estimate precision IQ-M parameters and CFR at the same time.

The IQ-M is estimated by taking advantage of the relationship between desired sub-carriers and image sub-carriers. Figure 4-3 shows the estimated CFR. Note that only sub-carriers 26 to 1 and -1 to -26 of FFT output are shown in Figure 4-3. From Figure 4-3, there is a distinct difference between sub-carriers \tilde{H}_{25} and \tilde{H}_{24} . The difference between sub-carriers \tilde{H}_{24} and \tilde{H}_{25} can be expressed as

$$\tilde{H}_{24} - \tilde{H}_{25} = \alpha \cdot (H_{24} - H_{25}) + \beta \cdot \left(H_{-24}^* \frac{P_{-24}^*}{P_{24}} - H_{-25}^* \frac{P_{-25}^*}{P_{25}} \right) \quad (4.8)$$

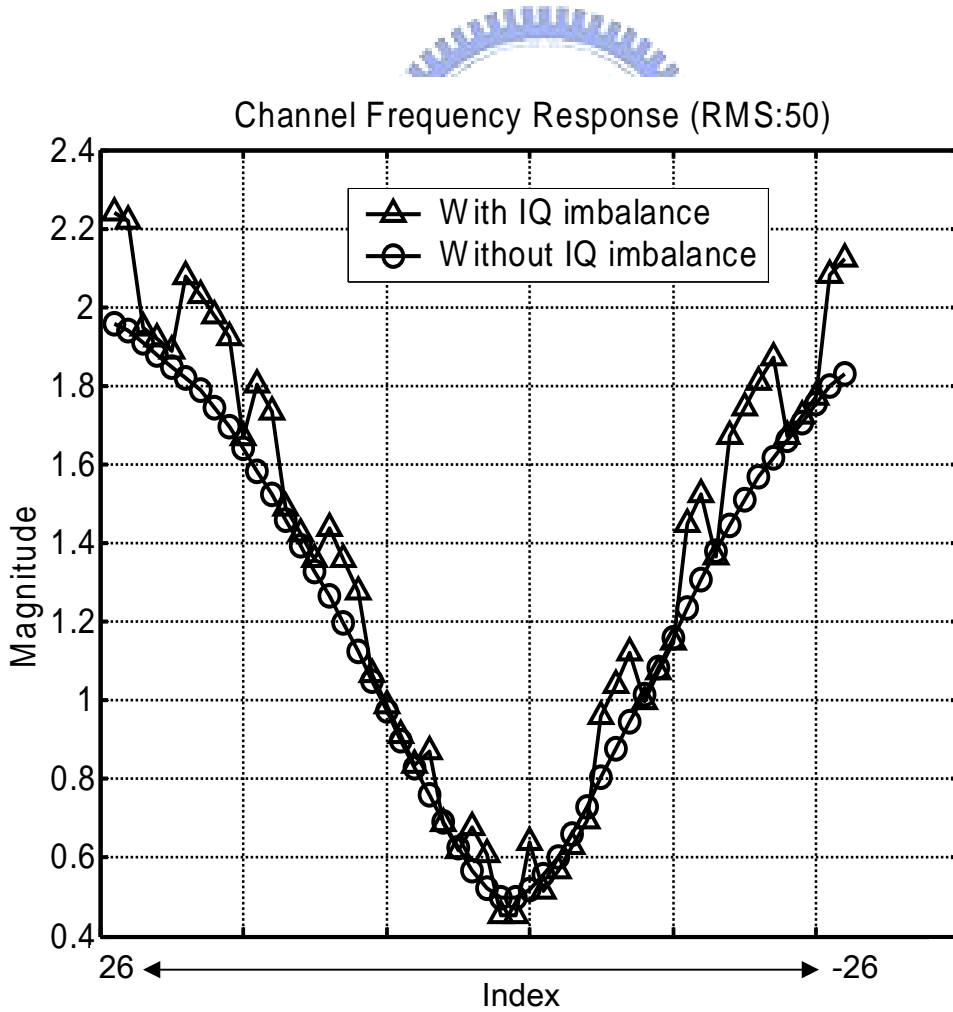


Figure 4-3. The estimated channel frequency response.

Because the coherency bandwidth of the channel is much larger than the inter-carrier spacing (channel bandwidth is 20 MHz, and the bandwidth of the inter-carrier spacing is 312.5 kHz), the variation of two consecutive channel carriers can be assumed to be small. It implies that $H_{24} \approx H_{25}$. Because $P_{-25}^*/P_{25} = -P_{-24}^*/P_{24} = 1$, $\alpha \approx 1$ and $\beta \approx 0$ (under slight IQ-M conditions), $\tilde{H}_{-24}^* + \tilde{H}_{-25}^*$ can be expressed as

$$\begin{aligned}
& \tilde{H}_{-24}^* + \tilde{H}_{-25}^* \\
&= \alpha^* \cdot (H_{-24}^* + H_{-25}^*) + \beta^* \cdot \left(\frac{P_{24}}{P_{-24}^*} H_{24} + \frac{P_{25}}{P_{-25}^*} H_{25} \right) \\
&= \alpha^* \cdot (H_{-24}^* + H_{-25}^*) + \beta^* \cdot (H_{25} - H_{24}) \\
&\approx H_{-24}^* + H_{-25}^*
\end{aligned} \tag{4.9}$$

Using the approximation in (4.9) leads to

$$\tilde{H}_{24} - \tilde{H}_{25} = -\beta (\tilde{H}_{-24}^* + \tilde{H}_{-25}^*) \tag{4.10}$$

The result for IQ-M parameters is

$$\begin{aligned}
\beta &= -(\tilde{H}_{24} - \tilde{H}_{25}) / (\tilde{H}_{-24}^* + \tilde{H}_{-25}^*) \\
\alpha &= 1 - \beta^*
\end{aligned} \tag{4.11}$$

After calculating IQ-M parameters and the CFR from the 1st long training symbol, we can use the information from the 2nd long training symbol to update IQ-M parameters. The final IQ-M parameters are expressed as (see Appendix C for details)

$$\beta = \left(\tilde{H}_{2,24} - \frac{\tilde{H}_{1,24}}{\tilde{H}_{1,25}} \tilde{H}_{2,25} \right) \left/ \left(\frac{P_{-24}^*}{P_{24}} \cdot H_{2,-24}^* - \frac{\tilde{H}_{1,24}}{\tilde{H}_{1,25}} \cdot \frac{P_{-25}^*}{P_{25}} \cdot H_{2,-25}^* \right) \right. \quad (4.12)$$

$$\alpha = 1 - \beta^*$$

where $\tilde{H}_{1,k}$ and $\tilde{H}_{2,k}$ denote CFR calculated from the 1st long training symbol and the 2nd long training symbol, respectively. Equation (4.12) shows that IQ-M parameters depend on not only the current CFR but also the previous one. From Figure 4-3, there are 20 transitions in the long preamble if the IQ-M exists. The proposed method can get 20 estimates and then average them to get accuracy value.

The proposed method can estimate exact IQ-M parameters and CFR at the same time. Since IQ-M parameters are static over many symbols, the influenced signal can be corrected by the IQ-M compensation. In this method, the IQ-M is estimated in the frequency domain, but the compensation scheme is applied in the time domain. It means the influenced signal can be compensated in the time domain, i.e. before the FFT operation. Naturally, time-domain compensation is inherently better than frequency-domain compensation because time-domain compensation can avoid some decision errors, which are inevitable in the decision directed approach. With the mathematical derivation, the received data can be corrected by

$$y(n) = \frac{\alpha_{final}^* \cdot r(n) - \beta_{final} \cdot r^*(n)}{|\alpha_{final}|^2 - |\beta_{final}|^2} \quad (4.13)$$

The data flow of the proposed method is depicted in Figure 4-4.

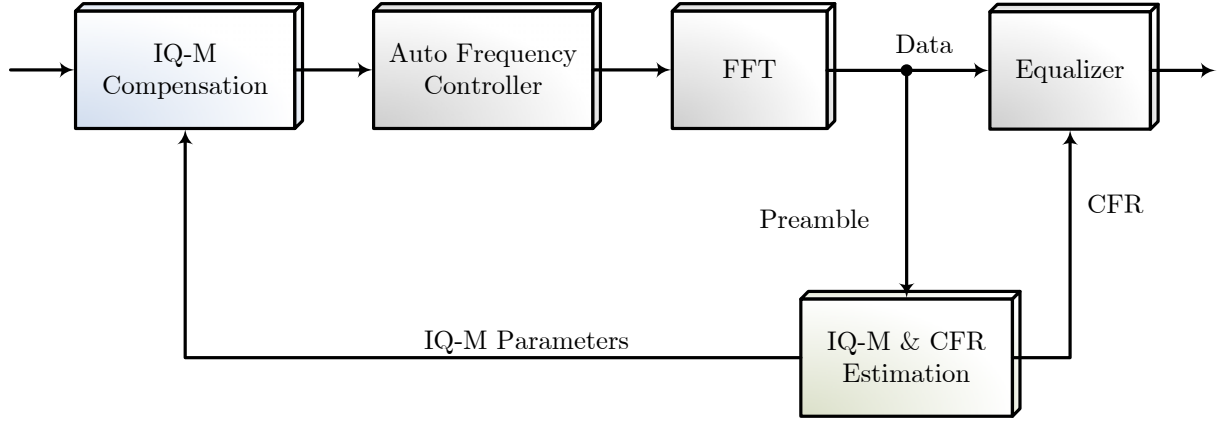


Figure 4-4. Data flow of the constant IQ-M estimation and compensation.

4.2.2 Constant IQ-M Estimation with CFO

In this section, an IQ-M estimation with CFO is developed. Some WLAN standards have specified training symbols for channel parameter estimation [4]-[5]. The CFR can thus be estimated by training symbols. However, the CFR estimation could be inaccurate if IQ-M is involved. Equation (4.5) shows that the desired sub-carrier is distorted by the image part under IQ-M conditions. In addition, if there is CFO and constant IQ-M, (4.1) can be simplified to

$$y(n) = \alpha r(n)e^{j2\pi\Delta f n T_s} + \beta (r(n)e^{j2\pi\Delta f n T_s})^* + w(n) \quad (4.14)$$

After the FFT operation, the frequency-domain data is expressed as

$$\begin{aligned} Y_k &= \text{FFT}_N \{y(n)\} \\ &= \alpha (R_k D_k + ICI_k) + \beta (R_{-k}^* D_{-k} + ICI_{-k}) + W_k \end{aligned} \quad (4.15)$$

The variables D_k , D_{-k} , ICI_k and ICI_{-k} are defined as (see Appendix A for details)

$$\begin{aligned}
D_k &= \left\{ \frac{(\sin \pi \varepsilon)}{N (\sin \pi \varepsilon / N)} \right\} e^{j\pi \varepsilon (N-1) / N} \\
D_{-k} &= \left\{ \frac{(\sin \pi \varepsilon)}{N (\sin \pi \varepsilon / N)} \right\} e^{j\pi (-\varepsilon) (N-1) / N} \\
ICI_k &= \sum_{k=-K, l \neq k}^K X_l H_l \left\{ \frac{(\sin \pi \varepsilon)}{N (\sin \pi (l-k+\varepsilon) / N)} \right\} e^{j\pi \varepsilon (N-1) / N} e^{-j\pi (l-k) / N} \\
ICI_{-k} &= \sum_{k=-K, l \neq -k}^K X_l^* H_l^* \left\{ \frac{-(\sin \pi \varepsilon)}{N (\sin \pi (l-k-\varepsilon) / N)} \right\} e^{j\pi (-\varepsilon) (N-1) / N} e^{-j\pi (l-k) / N}
\end{aligned} \tag{4.16}$$

where ε is the normalized frequency offset. From (4.16), D_k is the complex conjugate of D_{-k} . The estimated CFR is thus given by

$$\begin{aligned}
\tilde{H}_k &= \frac{Y_k}{P_k} \\
&= \alpha (H_k D_k) + \beta \left(H_{-k}^* \frac{P_{-k}^*}{P_k} D_k^* \right) + \left(\alpha \frac{ICI_k}{P_k} + \beta \frac{ICI_{-k}}{P_k} \right) + W_k'
\end{aligned} \tag{4.17}$$

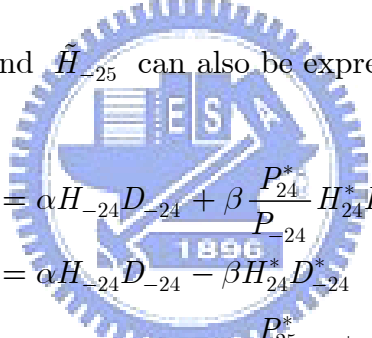
where $P_k \in \{-1, +1\}$ denotes the preamble pattern. If $P_k \neq P_{-k}$, it results in a obvious transition on the CFR. IQ-M parameters can then be estimated by taking advantage of this property illustrated in Figure 4-3. As can be seen from Figure 4-3, there are several sharp transitions, and we take the average of IQ-M parameters, which are estimated from these transitions. In order to simplify the notation, the noise term and ICI are ignored in the following derivation. To explain the proposed method, two sub-carriers, \tilde{H}_{24} and \tilde{H}_{25} , are utilize to complete the mathematical derivation. Thus, the following equation holds

$$\begin{aligned}
\tilde{H}_{24} &= \alpha H_{24} D_{24} + \beta \frac{P_{24}^*}{P_{24}} H_{-24}^* D_{24}^* \\
&= \alpha H_{24} D_{24} - \beta H_{-24}^* D_{24}^* \\
\tilde{H}_{25} &= \alpha H_{25} D_{25} + \beta \frac{P_{25}^*}{P_{25}} H_{-25}^* D_{25}^* \\
&= \alpha H_{25} D_{25} + \beta H_{-25}^* D_{25}^*
\end{aligned} \tag{4.18}$$

Subtracting \tilde{H}_{24} from \tilde{H}_{25} , the following equation holds

$$\begin{aligned}
\beta &= \frac{\tilde{H}_{25} - \tilde{H}_{24} - \alpha(H_{25}D_{25} - H_{24}D_{24})}{(H_{-25}D_{25} + H_{-24}D_{24})^*} \\
\alpha &= 1 - \beta^*
\end{aligned} \tag{4.19}$$

By the same way, \tilde{H}_{-24} and \tilde{H}_{-25} can also be expressed as



$$\begin{aligned}
\tilde{H}_{-24} &= \alpha H_{-24} D_{-24} + \beta \frac{P_{24}^*}{P_{-24}} H_{24}^* D_{-24}^* \\
&= \alpha H_{-24} D_{-24} - \beta H_{24}^* D_{-24}^* \\
\tilde{H}_{-25} &= \alpha H_{-25} D_{-25} + \beta \frac{P_{25}^*}{P_{-25}} H_{25}^* D_{-25}^* \\
&= \alpha H_{-25} D_{-25} + \beta H_{25}^* D_{-25}^*
\end{aligned} \tag{4.20}$$

From (4.20), $H_{-24}D_{24}$ and $H_{-25}D_{25}$ can be obtained by

$$\begin{aligned}
H_{-24}D_{24} &= \frac{\tilde{H}_{-24}D_{24}D_{-24}^{-1} + \beta H_{24}^* D_{-24}^* D_{24} D_{-24}^{-1}}{\alpha} \\
H_{-25}D_{25} &= \frac{\tilde{H}_{-25}D_{25}D_{-25}^{-1} - \beta H_{25}^* D_{-25}^* D_{25} D_{-25}^{-1}}{\alpha}
\end{aligned} \tag{4.21}$$

Substituting equation (4.21) into equation (4.19) leads into

$$\beta = \frac{\alpha^* (\tilde{H}_{25} - \tilde{H}_{24}) - |\alpha|^2 (H_{25} D_{25} - H_{24} D_{24})}{\left[(\tilde{H}_{-24} D_{24} D_{-24}^{-1} + \tilde{H}_{-25} D_{25} D_{-25}^{-1}) + \beta (H_{24}^* D_{-24}^* D_{24} D_{-24}^{-1} - H_{25}^* D_{-25}^* D_{25} D_{-25}^{-1}) \right]^*} \quad (4.22)$$

Before solving the equation for IQ-M parameters, the estimated CFO value based on P-CFO scheme is used to multiply the received signal with an inverse direction, i.e., CFO compensation. The compensated signal is written as

$$y(n)e^{-j2\pi\Delta f n T_s} = \alpha r(n) + \beta (r(n)e^{j4\pi\Delta f n T_s})^* + w(n) \quad (4.23)$$

After the FFT operation, the frequency-domain data is expressed as

$$\text{FFT}_N \left\{ y(n)e^{-j2\pi\Delta f n T_s} \right\} = \alpha R_k + \beta (R_{-k}^* D'_{-k} + ICI'_{-k}) \quad (4.24)$$

where D'_{-k} and ICI'_{-k} are defined as

$$D'_{-k} = \left\{ \frac{(\sin \pi \cdot 2\varepsilon)}{N (\sin \pi \cdot 2\varepsilon / N)} \right\} e^{j\pi(-2\varepsilon)(N-1)/N}$$

$$ICI'_{-k} = \sum_{k=-K, l \neq -k}^K X_l^* H_l^* \left\{ \frac{-(\sin \pi \cdot 2\varepsilon)}{N (\sin \pi (l - k - 2\varepsilon) / N)} \right\} e^{j\pi(-2\varepsilon)(N-1)/N} e^{-j\pi(l-k)/N} \quad (4.25)$$

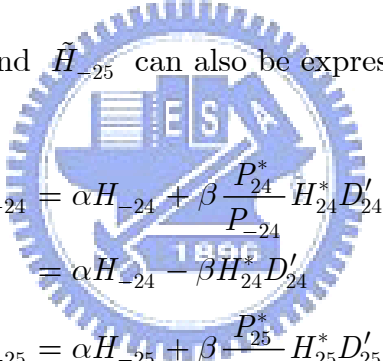
By the same technique described above, the following equation holds

$$\begin{aligned}
\tilde{H}_{24} &= \alpha H_{24} + \beta \frac{P_{-24}^*}{P_{24}} H_{-24}^* D'_{-24} \\
&= \alpha H_{24} - \beta H_{-24}^* D'_{-24} \\
\tilde{H}_{25} &= \alpha H_{25} + \beta \frac{P_{-25}^*}{P_{25}} H_{-25}^* D'_{-25} \\
&= \alpha H_{25} + \beta H_{-25}^* D'_{-25}
\end{aligned} \tag{4.26}$$

The IQ-M parameters are thus given by

$$\begin{aligned}
\beta &= \frac{\tilde{H}_{25} - \tilde{H}_{24} - \alpha(H_{25} - H_{24})}{H_{-25}^* D'_{-25} + H_{-24}^* D'_{-24}} \\
\alpha &= 1 - \beta^*
\end{aligned} \tag{4.27}$$

By the same way, \tilde{H}_{-24} and \tilde{H}_{-25} can also be expressed as



$$\begin{aligned}
\tilde{H}_{-24} &= \alpha H_{-24} + \beta \frac{P_{24}^*}{P_{-24}} H_{24}^* D'_{24} \\
&= \alpha H_{-24} - \beta H_{24}^* D'_{24} \\
\tilde{H}_{-25} &= \alpha H_{-25} + \beta \frac{P_{25}^*}{P_{-25}} H_{25}^* D'_{25} \\
&= \alpha H_{-25} + \beta H_{25}^* D'_{25}
\end{aligned} \tag{4.28}$$

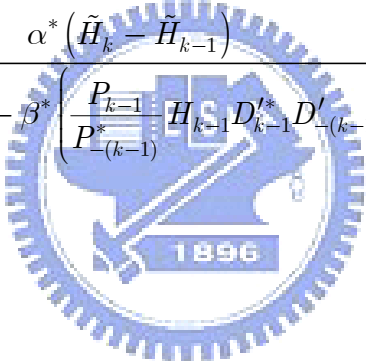
From (4.28), $H_{-24}^* D'_{-24}$ and $H_{-25}^* D'_{-25}$ can be obtained by

$$\begin{aligned}
H_{-24}^* D'_{-24} &= \frac{1}{\alpha^*} \left(\tilde{H}_{-24} D'_{-24} - \beta^* \frac{P_{24}}{P_{-24}^*} H_{24} D_{24}^* D'_{-24} \right) \\
H_{-25}^* D'_{-25} &= \frac{1}{\alpha^*} \left(\tilde{H}_{-25} D'_{-25} - \beta^* \frac{P_{25}}{P_{-25}^*} H_{25} D_{25}^* D'_{-25} \right)
\end{aligned} \tag{4.29}$$

Substituting equation (4.29) into equation (4.27) leads into

$$\begin{aligned}
\beta &= \frac{\alpha^* (\tilde{H}_{25} - \tilde{H}_{24}) - |\alpha|^2 (H_{25} - H_{24})}{\left(\tilde{H}_{-25}^* D'_{-25} + \tilde{H}_{-24}^* D'_{-24} \right) - \beta^* \left(\frac{P_{24}}{P_{-24}^*} H_{24} D_{24}^* D'_{-24} + \frac{P_{25}}{P_{-25}^*} H_{25} D_{25}^* D'_{-25} \right)} \\
&\approx \frac{\alpha^* (\tilde{H}_{25} - \tilde{H}_{24})}{\left(\tilde{H}_{-25}^* D'_{-25} + \tilde{H}_{-24}^* D'_{-24} \right) - \beta^* \left(\frac{P_{24}}{P_{-24}^*} H_{24} D_{24}^* D'_{-24} + \frac{P_{25}}{P_{-25}^*} H_{25} D_{25}^* D'_{-25} \right)}
\end{aligned} \tag{4.30}$$

The approximation in (4.30) is based on the assumption that the variation of two consecutive channel carriers can be assumed to be small. Equation (4.30) can thus be expressed in the general form

$$\beta \approx \frac{\alpha^* (\tilde{H}_k - \tilde{H}_{k-1})}{\left(\tilde{H}_{-k}^* D'_{-k} + \tilde{H}_{-(k-1)}^* D'_{-(k-1)} \right) - \beta^* \left(\frac{P_{k-1}}{P_{-(k-1)}^*} H_{k-1} D_{k-1}^* D'_{-(k-1)} + \frac{P_k}{P_{-k}^*} H_k D_k^* D'_{-k} \right)} \tag{4.31}$$


To simplify the notation, let

$$\begin{aligned}
m &= \left(\tilde{H}_{-k}^* D'_{-k} + \tilde{H}_{-(k-1)}^* D'_{-(k-1)} \right) \\
n &= \left(\frac{P_{k-1}}{P_{-(k-1)}^*} H_{k-1} D_{k-1}^* D'_{-(k-1)} + \frac{P_k}{P_{-k}^*} H_k D_k^* D'_{-k} \right) \\
p &= \alpha^* (\tilde{H}_k - \tilde{H}_{k-1})
\end{aligned} \tag{4.32}$$

Equation (4.31) is rewritten as

$$\beta = \frac{p}{m - \beta^* n} \Rightarrow |\beta|^2 n - \beta m + p = 0 \tag{4.33}$$

In (4.33), all parameters are complex numbers, and the solution can be found by setting the real part and imaginary part to be equal to zero. Each complex number is denoted separately as $x = (x_R, x_I)$. Therefore, the following equation holds

$$(\beta_R^2 + \beta_I^2)n_R - (\beta_R m_R - \beta_I m_I) + p_R = 0 \quad (4.34)$$

$$(\beta_R^2 + \beta_I^2)n_I - (\beta_R m_I + \beta_I m_R) + p_I = 0 \quad (4.35)$$

From (4.34) and (4.35), β_I can be expressed as

$$\begin{aligned} n_R p_I - n_I p_R &= (\beta_R m_I + \beta_I m_R)n_R - (\beta_R m_R - \beta_I m_I)n_I \\ &= \beta_R (n_R m_I - n_I m_R) + \beta_I (m_I n_I + m_R n_R) \\ &\Rightarrow \beta_I = \frac{(n_R p_I - n_I p_R) - \beta_R (n_R m_I - n_I m_R)}{(m_I n_I + m_R n_R)} \end{aligned} \quad (4.36)$$

In order to simplify the notation, let $u = (n_R p_I - n_I p_R)$, $v = (n_R m_I - n_I m_R)$ and $w = (m_I n_I + m_R n_R)$. Substituting equation (4.36) into equation (4.34) leads into

$$\begin{aligned} &\left(\beta_R^2 + \left(\frac{u - \beta_R v}{w} \right)^2 \right) n_R - \left(\beta_R m_R - \left(\frac{u - \beta_R v}{w} \right) m_I \right) + p_R = 0 \\ &\Rightarrow \left(\beta_R^2 n_R + \frac{u^2 n_R - 2\beta_R u v n_R + \beta_R^2 v^2 n_R}{w^2} \right) - \left(\beta_R m_R - \frac{u m_I - \beta_R v m_I}{w} \right) + p_R = 0 \quad (4.37) \\ &\Rightarrow n_R \left(1 + \frac{v^2}{w^2} \right) \beta_R^2 + \left(-\frac{2u v n_R}{w^2} - \frac{v m_I}{w} - m_R \right) \beta_R + \left(\frac{u^2 n_R}{w^2} - \frac{u m_I}{w} + p_R \right) = 0 \end{aligned}$$

Equation (4.37) is like the quadratic equation, i.e., $ax^2 + bx + c = 0$, and the solutions of the quadratic equation can be obtained by the quadratic formula

$$x = \frac{-b \pm \sqrt{b^2 - 4ac}}{2a} \quad (4.38)$$

The parameter β_R can thus be calculated by the proposed method. After calculating β_R , β_I can then be calculated by the same way. However, we cannot carry out the calculation in the beginning since the IQ-M parameter α is included in (4.32). According to the simulation, we can set the parameter α to be equal to unit at first. After the first calculation, we use the result to calculate IQ-M parameters again, and then accurate IQ-M parameters could be found in enough iterations (five iterations). With the information of estimated CFR and CFO value, we can calculate accuracy IQ-M parameters for data compensation. The received data can then be corrected by using (4.13). Figure 4-5 illustrates the overall estimation and compensation procedure.

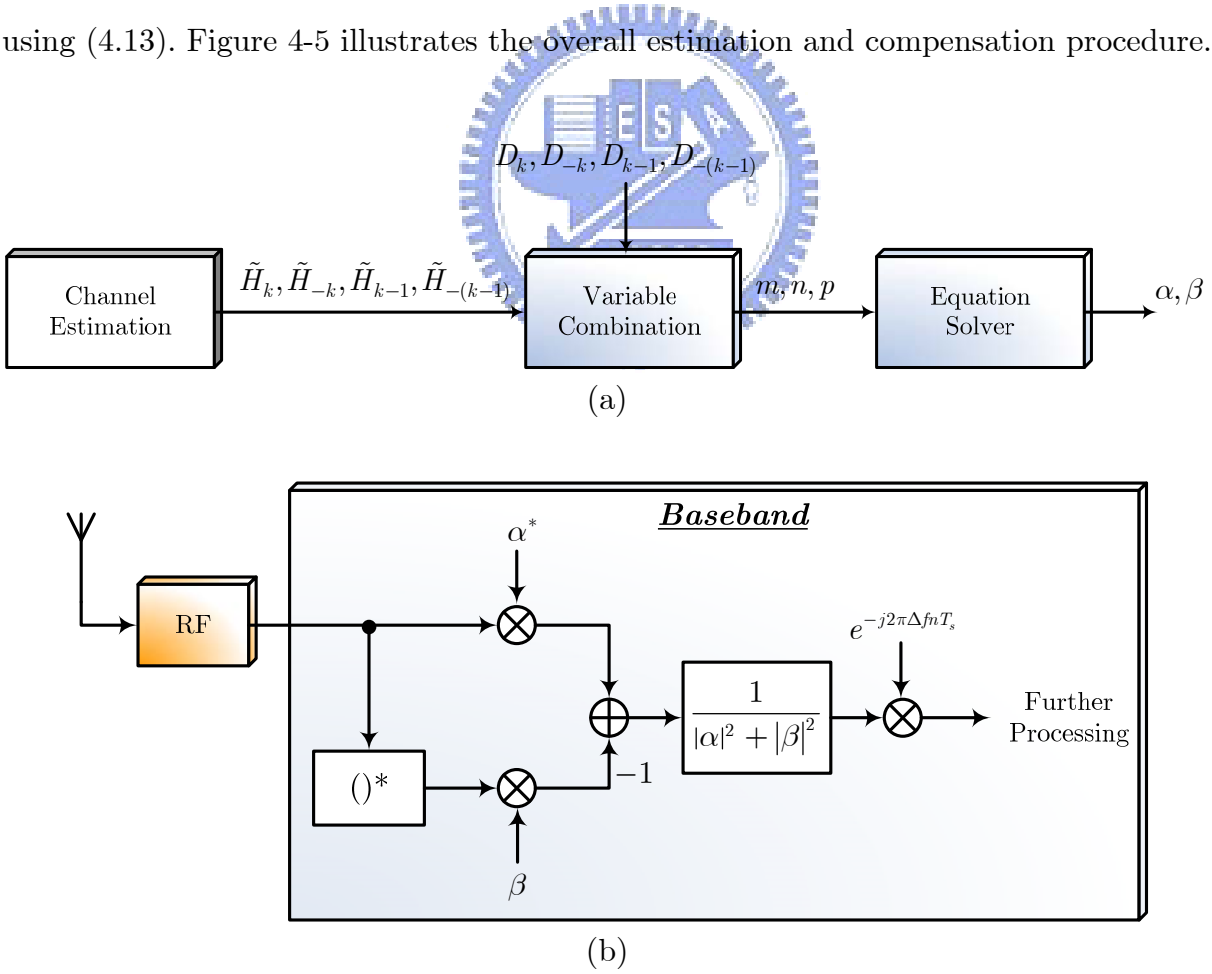


Figure 4-5. (a) The block diagram for the IQ-M estimation. (b) The compensation blocks for IQ-M and CFO.

4.3 Frequency-Dependent IQ-M Estimation

4.3.1 The Proposed Method

The goal here is to estimate the frequency-dependent IQ-M with CFO. The basic strategy for extracting IQ-M parameters is to employ long training symbols. The packet format used in this method is based on IEEE 802.11a/g standards. Let $x(n)$ denote a long training symbol distorted by IQ-M and CFO, as defined in (4.1). The long training symbol after fast Fourier transform (FFT) is given by

$$\begin{aligned}
 Y_k &= \text{FFT}_N \{y(n)\} \\
 &= A_k (R_k D_k + ICI_k) + B_k (R_{-k}^* D_{-k} + ICI_{-k}) + W(k) \\
 &= A_k (H_k X_k D_k + ICI_k) + B_k (H_{-k}^* X_{-k}^* D_{-k} + ICI_{-k}) + W(k)
 \end{aligned} \tag{4.39}$$

where D_k is the distortion, which is accompanied with inter-carrier interference (ICI) due to CFO [28]. X_k is the data sub-carrier and H_k stands for the channel frequency response. X_{-k} and H_{-k} denote the frequency mirror image parts. A_k and B_k are determined as

$$\begin{aligned}
 A_k &= \text{FFT}_N \{\alpha\psi(n) + \beta^*\xi(n)\} \\
 B_k &= \text{FFT}_N \{\beta\psi(n) + \alpha^*\xi(n)\}
 \end{aligned} \tag{4.40}$$

Equation (4.40) clearly indicates that IQ-M results in a mutual interference between symmetric sub-carriers in OFDM systems, as shown in Figure 4-6. Let $x(n)$ and

$x(n + N_l)$ represent two consecutive long training symbols, where N_l is the samples of a long training symbol. In order to simplify the notation, the noise term is ignored in the following derivation.

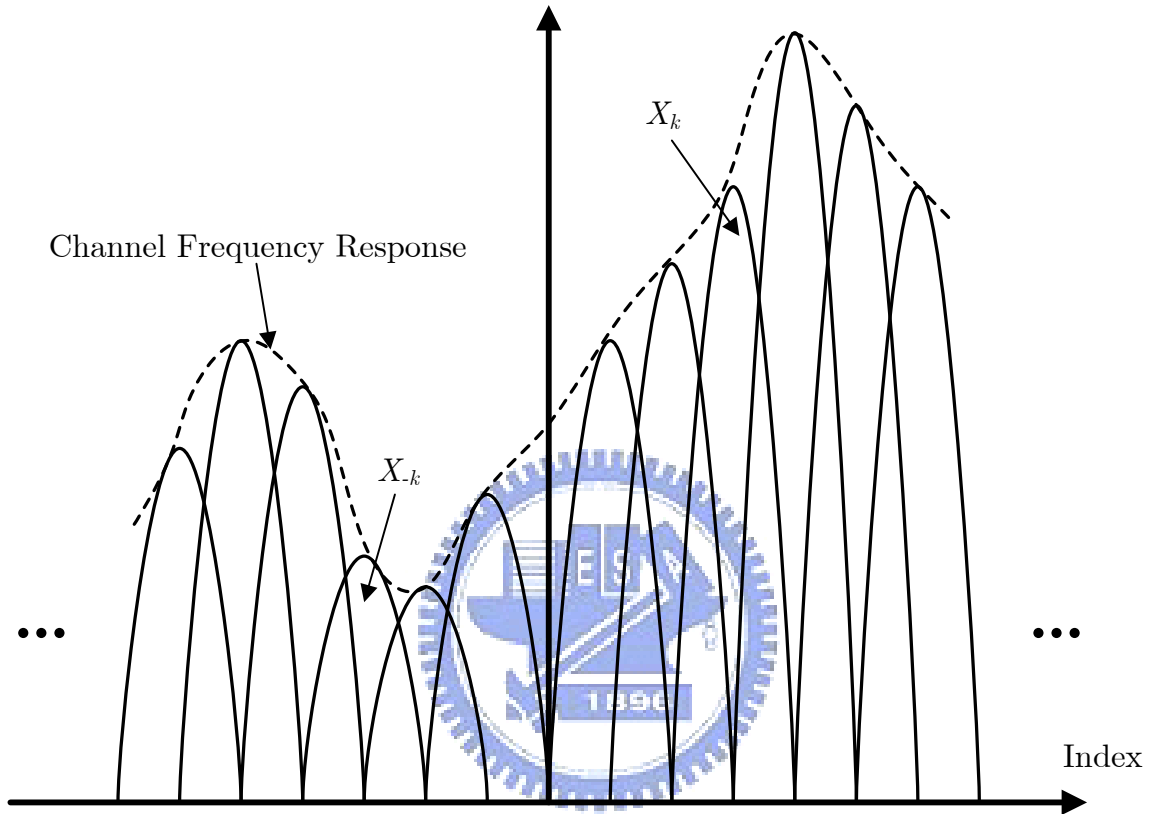


Figure 4-6. Mutual interference due to I/Q mismatch.

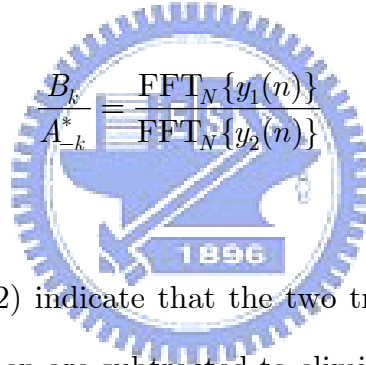
In practice, IQ-M not only introduces unwanted image interference into the desired signal, but also restricts the accuracy of CFO estimation. A basic strategy for computing the CFO is to employ two repeated training symbols [28]. However, the estimation error increases when the gain or phase error is not zero. In [61], a pseudo-CFO (P-CFO) algorithm, which rotates three training symbols by adding extra frequency offset into the received sequence, is developed to improve CFO estimation. Since the P-CFO method can estimate the frequency offset more accurately than the two-repeat preamble-based scheme, it is adopted to estimate the CFO value in this

work. The training symbols are then rotated by the estimated CFO. Because the long training symbols are periodic, the received signals, $r(n)$ and $r(n + N_l)$, can be replaced by $r(n)$. Therefore, the following equations holds:

$$\begin{aligned} y_1(n) &= \frac{x(n)e^{-j(2\pi\Delta f n T_s)} - x(n + N_l)e^{-j(2\pi\Delta f(n+N_l)T_s)}}{e^{-2j(2\pi\Delta f n T_s)} - e^{-2j(2\pi\Delta f(n+N_l)T_s)}} \\ &= (\beta\psi(n) + \alpha^* \xi(n)) \otimes r^*(n) \end{aligned} \quad (4.41)$$

$$\begin{aligned} y_2(n) &= \frac{x(n)^* e^{-j(2\pi\Delta f n T_s)} - x(n + N_l)^* e^{-j(2\pi\Delta f(n+N_l)T_s)}}{e^{-2j(2\pi\Delta f n T_s)} - e^{-2j(2\pi\Delta f(n+N_l)T_s)}} \\ &= ((\alpha\psi(n) + \beta^* \xi(n)) \otimes r(n))^* \end{aligned} \quad (4.42)$$

The IQ-M parameters can be obtained as follows.



$$\frac{B_k}{A_{-k}^*} = \frac{\text{FFT}_N\{y_1(n)\}}{\text{FFT}_N\{y_2(n)\}} \quad (4.43)$$

Equations (4.41) and (4.42) indicate that the two training symbols are multiplied by the estimated CFO and then are subtracted to eliminate the image interference. Once the IQ-M parameters are estimated, the effect of IQ-M could be corrected by the frequency-domain compensation. With the estimated IQ-M parameters, the frequency domain compensation is given by

$$\begin{aligned} Z_k &= \text{FFT}_N \left\{ x(n)e^{-j(2\pi\Delta f n T_s)} \right\} - \frac{B_k}{A_{-k}^*} \text{FFT}_N \left\{ x^*(n)e^{-j(2\pi\Delta f n T_s)} \right\} \\ &= \underbrace{\left(A_k - \frac{B_k B_{-k}^*}{A_{-k}^*} \right)}_{\text{compensation gain}} H_k X_k \end{aligned} \quad (4.44)$$

The compensation gain could be balanced by the channel equalizer. Moreover, the

proposed method could be directly applied to IEEE 802.11a/g standards because it does not require any special packet format.

In the open literature [58], [59], [62], most of them consider the IQ-M only. Therefore, these methods may not be suitable for joint CFO and IQ-M. In other words, these methods can tolerate slight CFO value. By contrast, the proposed method is capable of tolerating large CFO value. In the condition of slight CFO value, the inter-carrier interference is smaller than large CFO value. For instance, if the estimated CFO value is within ± 2 ppm, the existing methods [58], [59], [62] for frequency-dependent IQ-M could be adopted. In the frequency domain, phase tracking is still performed. Since some rotation operations (CFO estimation and compensation) are eliminated, this approach can maintain the system performance with reasonable complexity.

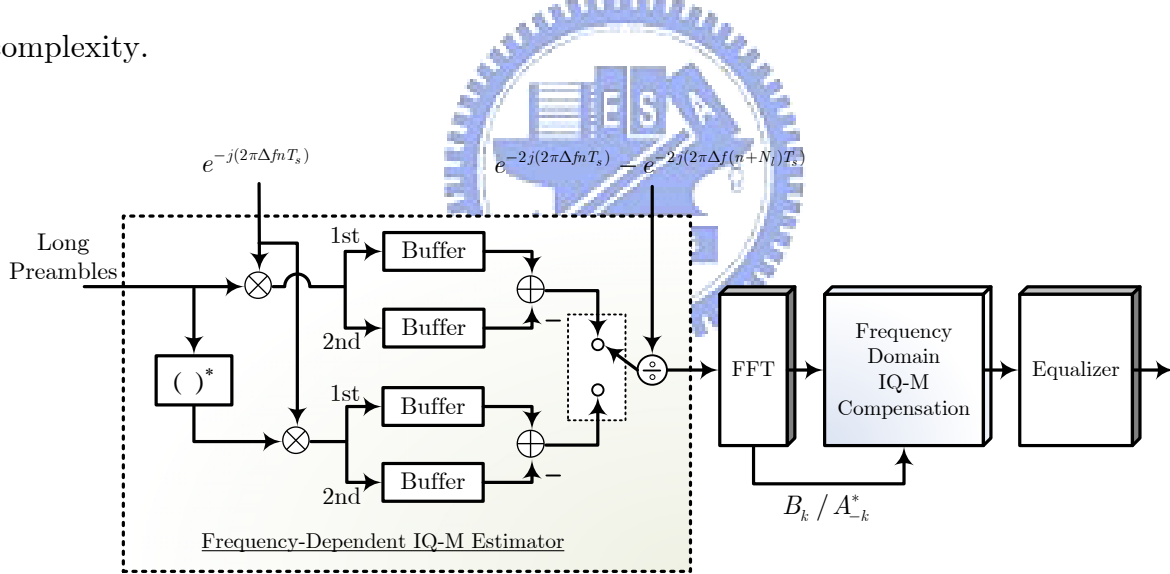


Figure 4-7. The proposed frequency-dependent IQ-M estimation architecture.

Figure 4-7 shows the frequency-dependent IQ-M estimation architecture. The estimator begins to work when long training symbols (preambles) arrive. Firstly, the long preambles are multiplied by the estimated CFO. In order to reduce the image interference due to the IQ-M effect, the 1st training symbol should subtract the 2nd training symbol. At the same time, the conjugate preamble follows the same procedure

described above. After calculating the difference between the first and the second preambles, a complex divider is used to eliminate the phase rotation. Finally, these estimated parameters are applied to compensate for the frequency-dependent IQ-M in the frequency domain.

4.3.2 Simulation and Experiment Results

A typical OFDM system for wireless LAN was adapted as the referred specification to evaluate the performance [4]-[5]. The simulation parameters were OFDM symbol length 64, and cyclic prefix 16. There were ten short training symbols and two long training symbols. The number of taps of frequency-selective fading was of order 8, simulating as an independent and identically distributed (i.i.d.) complex Gaussian random variable. All data are modulated by 16-QAM and 64-QAM. The CFO was set at 50 ppm, and the constant IQ-M parameters were 1 dB gain error and 10 degree phase error. Two-tap FIR filters were adopted to model the frequency-dependent IQ-M [48]. These two LPFs were modeled as

$$\begin{aligned} l_I(n) &= 0.1\delta(n) + \delta(n-1) \\ l_Q(n) &= 0.01\delta(n) + 0.9\delta(n-1) \end{aligned} \tag{4.45}$$

The Z-transform results of these two LPFs are $L_I(z) = 0.1 + z^{-1}$ and $L_Q(z) = 0.01 + 0.9z^{-1}$, respectively. Figures 4-8 and 4-9 show the bit error rate (BER) and packet error rate (PER) performance. In these two figures, the following scenarios are considered. “Multipath only” legend refers to the system with perfect RF front-end and “without comp” means that the estimation scheme is not applied to the system

with frequency-dependent IQ-M. “FD IQ-M” legend means that the estimation scheme is applied to the system with frequency-dependent IQ-M and “constant IQ-M” means that the estimation scheme is applied to the system with constant IQ-M. Figures 4-8 and 4-9 show that the degradation in BER and PER owing to IQ-M was significant, particularly for 64-QAM modulation. After compensation, the performance under the condition of constant IQ-M was close to the case with multipath only. The SNR loss of the proposed scheme for frequency-dependent IQ-M is in the range of 1.6 to 1.8 dB at 10^{-4} BER. This finding implies that the proposed method is robust to the conditions of both frequency-dependent IQ-M and CFO in fading environments.

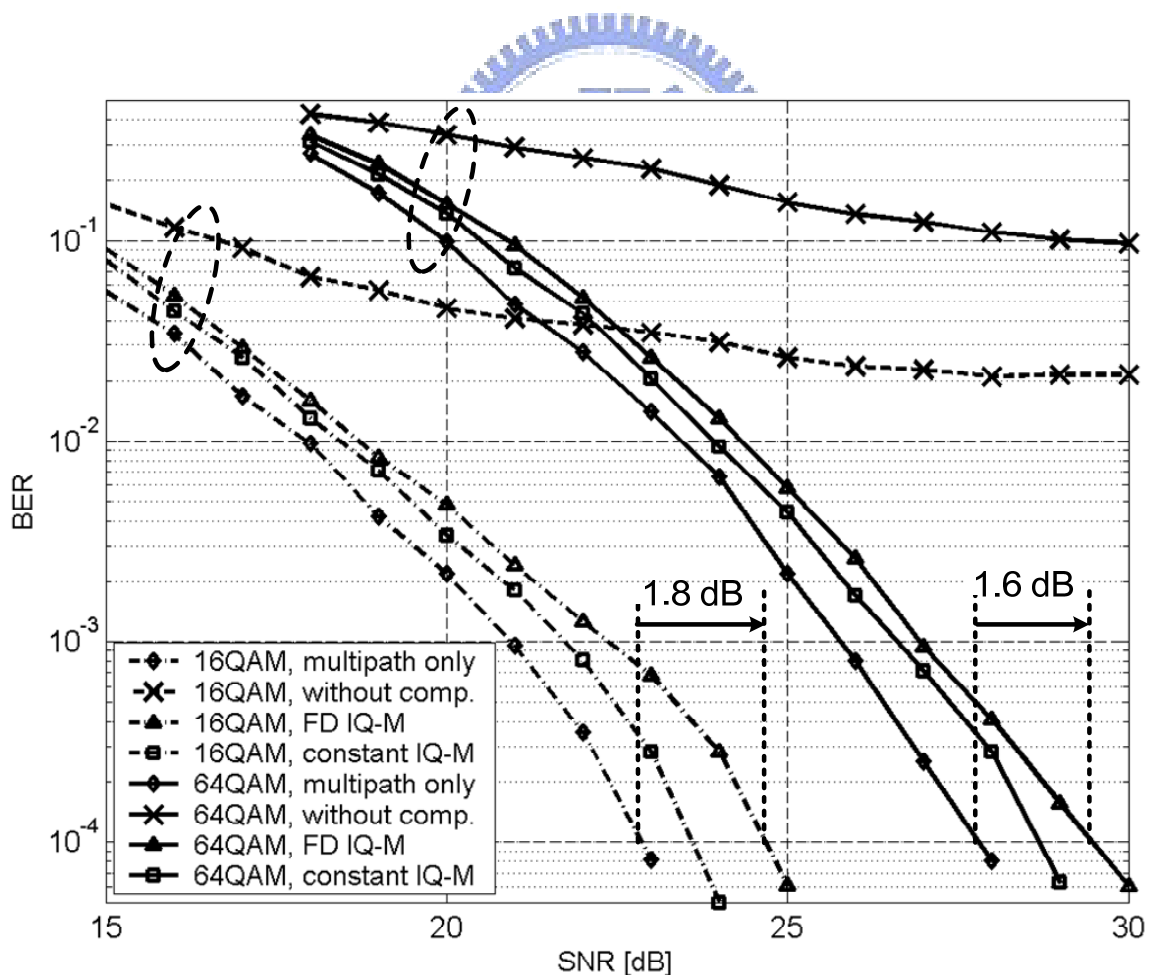


Figure 4-8. BER performance of 16-QAM and 64-QAM modulation.

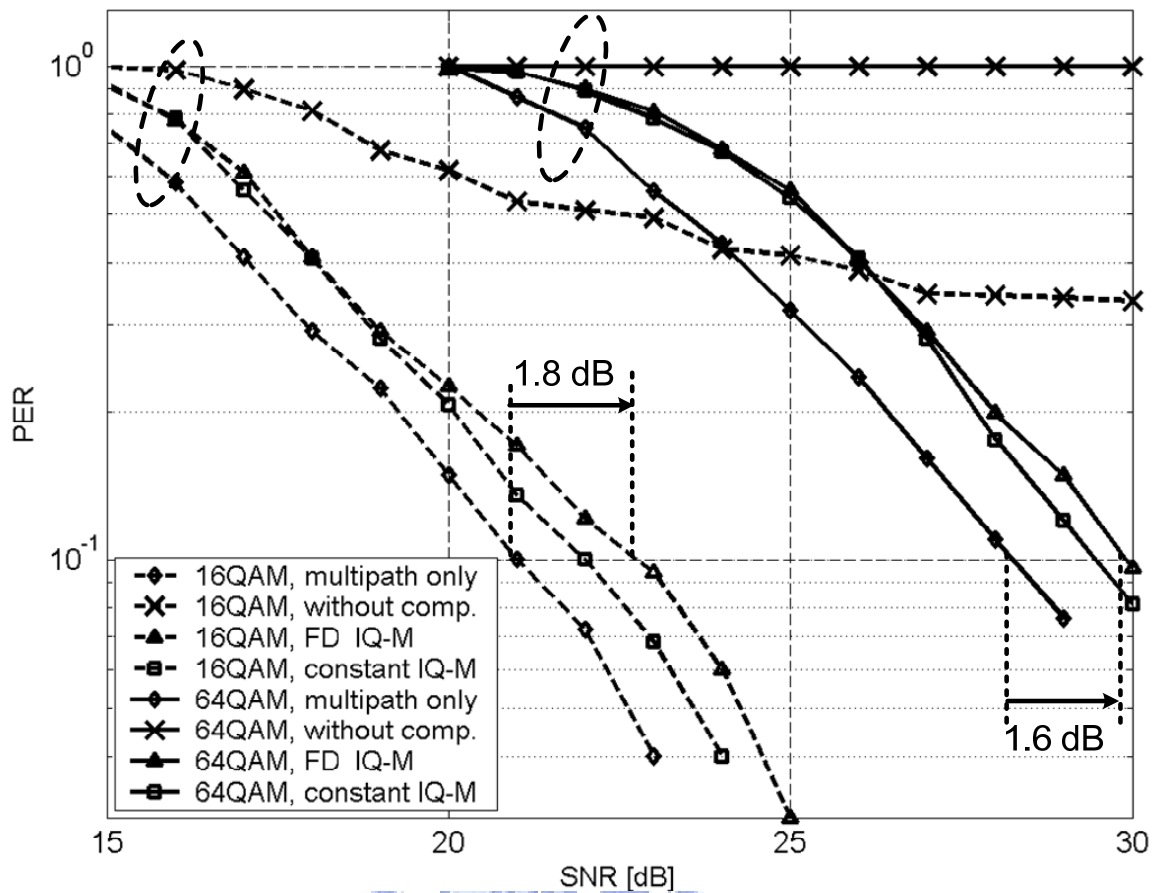


Figure 4-9. PER performance of 16-QAM and 64-QAM modulation.

TABLE 4-1. Experiment Parameters.

<i>Parameter</i>	<i>Value</i>
RF Carrier Frequency	2.4 GHz
RF Power Level	-40 dBm
ADC/DAC Resolution	14 bits
Webcam Resolution	160×120
(I)FFT	64 points
Modulation	16-QAM

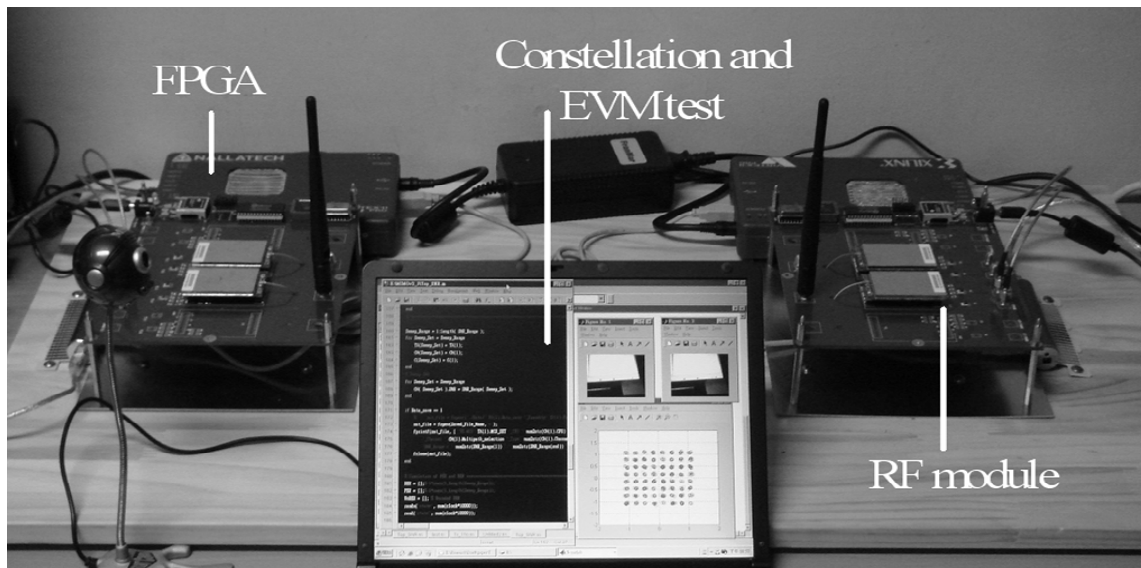


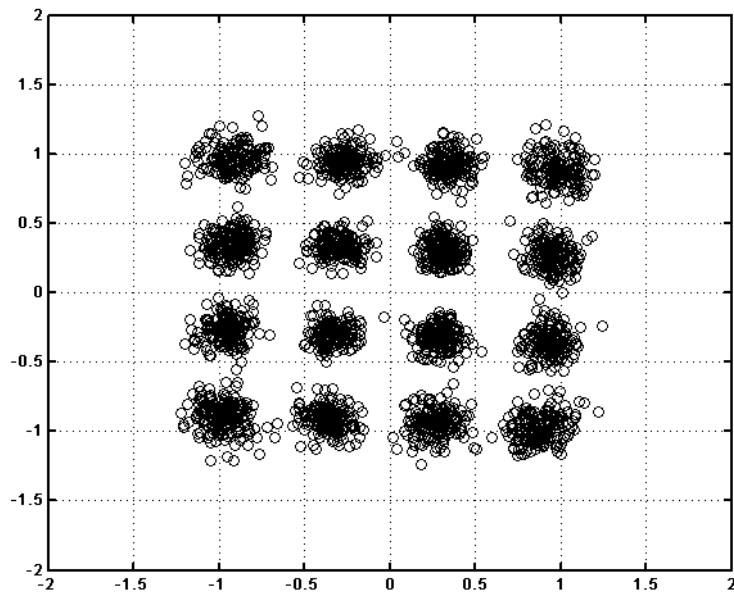
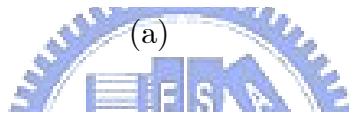
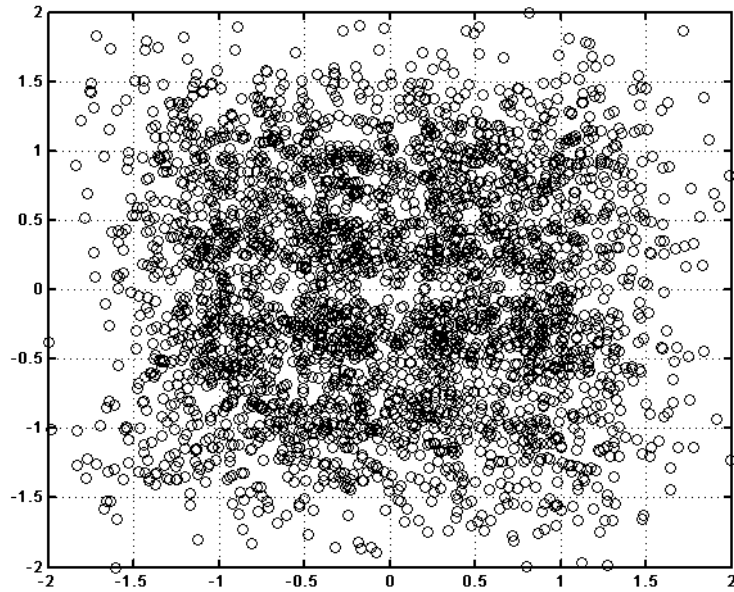
Figure 4-10. Experiment setup for verification.

Figure 4-10 displays the experiment setup for verification. TABLE 4-1 lists the experiment parameters. The in-house RF front-ends are used in the transmitter as well as in the receiver. Therefore, there is also IQ-M at the transmitter part. Some compensation methods for transmitter IQ-M are available in the open literature. Since the goal here is to estimate the receiver IQ-M with CFO, the pre-compensation scheme is applied to reduce the transmitter IQ-M effect. The basic concept is that a training sequence is utilized to estimate the IQ-M. After calculating the IQ-M parameters, the transmitter can compensate for the transmitter IQ-M using the baseband processing. A webcam was attached to the computer, which enables the streaming video transmission. At transmitter part, the streaming video was converted into the binary data through the application programming interface (API) of MATLAB. The proposed design was mapped onto the FPGA chips (Xilinx XtremeDSP, Virtex-II) with on-board 14-bit digital-to-analog converters (DACs) to convert the digital data into analog signals. The signals were then transmitted using an in-house RF front-end. At receiver part, the analog signals were fed to 14-bit analog-to-digital converters (ADCs) after down-conversion. The proposed algorithm processed the down-converted signals.

Figure 4-11 shows the constellation performance before and after compensation. The performance improvement is clearly seen because the constellation becomes more distinguishable after compensation. After IQ-M compensation, the remaining IQ-M parameters are less than 3% (0.13dB) gain error and 2° phase error. In the proposed design, only two long training symbols are acquired to estimate the IQ-M parameters. If there are more training symbols than current standards, the accuracy of the IQ-M parameters could be improved further. The error vector magnitude (EVM) after compensation is 8.6% (-21 dB), meeting the standard (IEEE 802.11a/g) allowed 11.2% (-19 dB). The image rejection ratio (IRR) as a function of the mismatch is given by [32]

$$\text{IRR} = 10 \cdot \log \left[\frac{1 + (1 + \varepsilon)^2 + 2(1 + \varepsilon) \cos(\varphi)}{1 + (1 + \varepsilon)^2 - 2(1 + \varepsilon) \cos(\varphi)} \right] \quad (\text{dB}) \quad (4.46)$$

where ε and φ represent the amplitude and phase mismatch, respectively. After compensation, the remaining gain error and phase error are $\sim 3\%$ and $\sim 2^\circ$. An IRR of ~ 31 dB is achieved. Figure 4-12 shows the estimated CFR. The CFR after compensation becomes more smoother than the distorted CFR. In conjunction with the proposed scheme, accuracy CFR could be calculated. The proposed method is also compatible with current standards. In contrast, recently proposed methods [48], [59] are incompatible with current standards. In addition, the proposed method can estimate the frequency-dependent IQ-M with CFO, whereas reference methods [58]-[59], [60], [62] consider frequency-dependent IQ-M only.



(b)

Figure 4-11. Measurement of constellation diagram: (a) Before compensation. (b) After compensation.

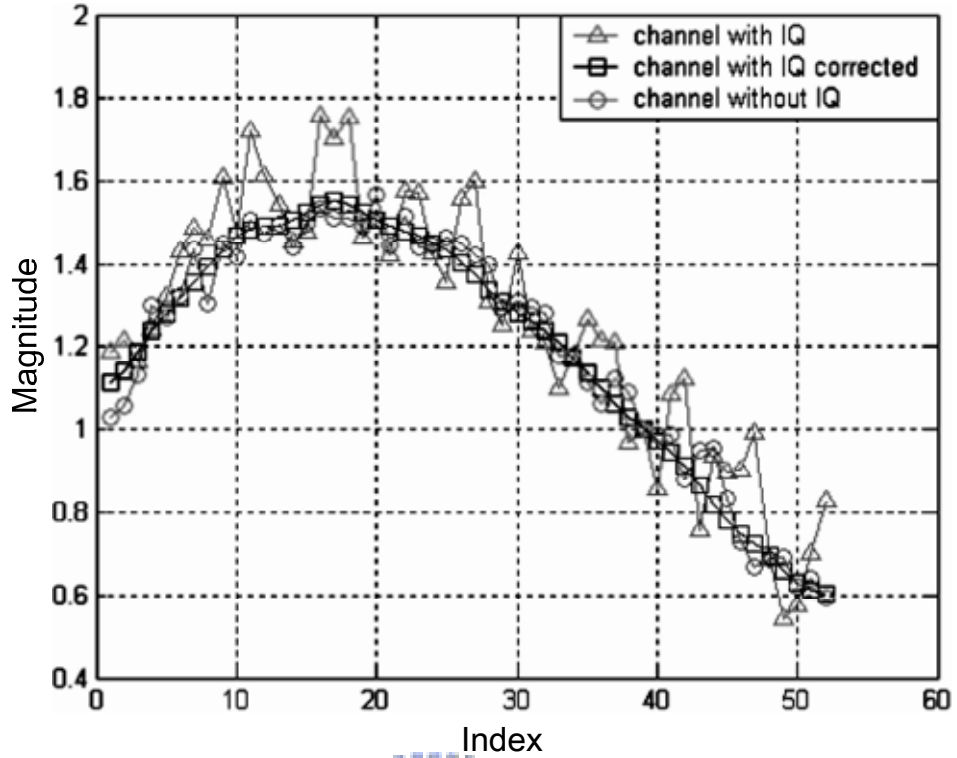


Figure 4-12. Channel frequency response.



4.4 Transmitter IQ-M Estimation

4.4.1 Problem Statement

An OFDM system in the presence of IQ-M and CFO is depicted in Figure 4-13. Let $x(n)$ be the transmitted baseband signal before being distorted by IQ-M. Here we consider the system with constant transmitter (TX) and receiver (RX) IQ-M. The distorted baseband signal is given by

$$\tilde{x}(n) = \xi_{tx}x(n) + \sigma_{tx}x^*(n) \quad (4.47)$$

The TX IQ-M parameters, ξ_{tx} and σ_{tx} , are expressed as

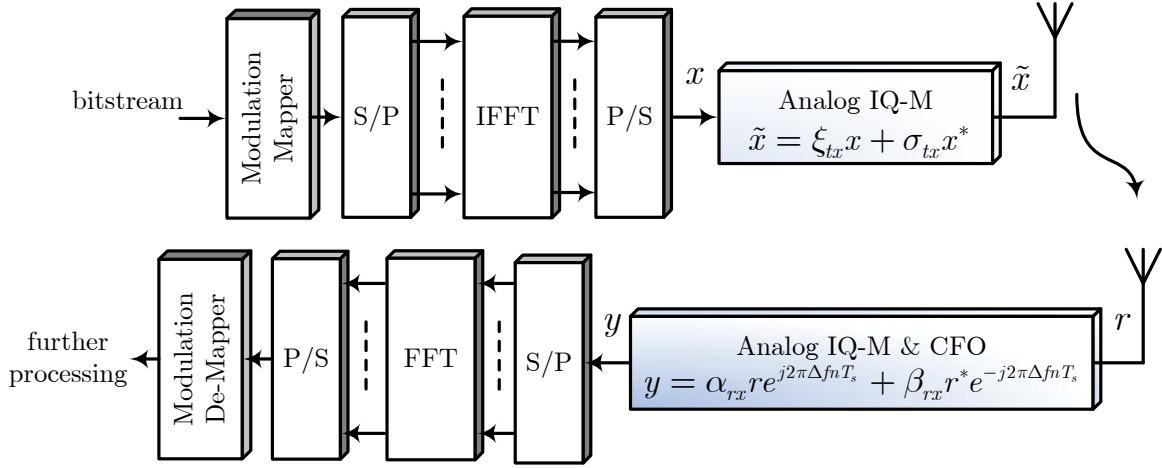


Figure 4-13. An OFDM system with transceiver IQ-M and CFO.

$$\begin{aligned}\xi_{tx} &= 0.5(1 + (1 - \varepsilon_{tx})e^{-j\varphi_{tx}}) \\ \sigma_{tx} &= 0.5(1 - (1 - \varepsilon_{tx})e^{j\varphi_{tx}})\end{aligned}\tag{4.48}$$

where ε_{tx} and φ_{tx} denote the gain error and phase error induced by transmitter RF front-end. The received baseband (digital) signal with sampling period T_s can then be expressed as

$$y(n) = \alpha_{rx}r(n)e^{j(2\pi\Delta f n T_s)} + \beta_{rx}\left(r(n)e^{j(2\pi\Delta f n T_s)}\right)^* + w(n)\tag{4.49}$$

where $r(n)$ and $w(n)$ denote the representations of the received signal and additive white Gaussian noise (AWGN), respectively. Δf denotes the frequency offset. α_{rx} and β_{rx} are defined in (4.2). The received signal can also be expressed as

$$r(n) = h(n) \otimes \tilde{x}(n)\tag{4.50}$$

where $h(n)$ stands for the representation of channel response, and \otimes means convolution operations. The received signal can thus be regarded as a gain, α_{rx} , from

the original signal added to the conjugate multiplied by a sigma value, β_{rx} . If neither gain nor phase error exists, ξ_{tx} or α_{rx} remains at unity, and σ_{tx} or β_{rx} decreases to zero. Note that the phase rotation is inversed in the direction between original signals and their conjugate if the CFO is present. This means that conventional methods, simply multiplied the data by an exponential term, has to be modified in accordance with IQ-M.

4.4.2 The Proposed Method

In order to simplify the notation, noise distribution is ignored. With the estimated CFO value, the RX IQ-M parameters can be calculated by following equation

$$\begin{aligned}
 & \frac{y(n)e^{-j(2\pi\Delta f n T_s)} - y(n + N_l)e^{-j(2\pi\Delta f (n+N_l)T_s)}}{y(n)^* e^{-j(2\pi\Delta f n T_s)} - y(n + N_l)^* e^{-j(2\pi\Delta f (n+N_l)T_s)}} \\
 &= \frac{\beta_{rx} r^*(n) \left(e^{-j(4\pi\Delta f n T_s)} - e^{-j(4\pi\Delta f (n+N_l)T_s)} \right)}{\alpha_{rx}^* r^*(n) \left(e^{-j(4\pi\Delta f n T_s)} - e^{-j(4\pi\Delta f (n+N_l)T_s)} \right)} \quad (4.51) \\
 &= \frac{\beta_{rx}}{\alpha_{rx}^*}
 \end{aligned}$$

where N_l denotes the data samples of a long training symbol. A better estimate of β_{rx}/α_{rx}^* can be obtained by making an average of N_l estimates. It is expressed as

$$\frac{\beta_{rx}}{\alpha_{rx}^*} = \frac{1}{N_l} \sum_{n=0}^{N_l-1} \frac{y(n)e^{-j(2\pi\Delta f n T_s)} - y(n + N_l)e^{-j(2\pi\Delta f (n+N_l)T_s)}}{y(n)^* e^{-j(2\pi\Delta f n T_s)} - y(n + N_l)^* e^{-j(2\pi\Delta f (n+N_l)T_s)}} \quad (4.52)$$

With the ratio between α_{rx}^* and β_{rx} , RX IQ-M can be removed according to

$$\begin{aligned}
y(n) - \left(\frac{\beta_{rx}}{\alpha_{rx}^*} \right) y^*(n) &= \alpha_{rx} r(n) e^{j(2\pi\Delta f n T_s)} - \frac{|\beta_{rx}|^2}{\alpha_{rx}^*} r(n) e^{j(2\pi\Delta f n T_s)} \\
&= \kappa r(n) e^{j(2\pi\Delta f n T_s)}
\end{aligned} \tag{4.53}$$

where κ is defined as

$$\kappa \triangleq \left(\alpha_{rx} - \frac{|\beta_{rx}|^2}{\alpha_{rx}^*} \right) \tag{4.54}$$

From (4.53), it is apparent that the exponential term could be removed by CFO compensation, and the RX IQ-M compensation gain, κ , could be balanced by channel equalization. After CFO compensation, the received signal is demodulated using an FFT as

$$\begin{aligned}
\hat{Y}_k &= \text{FFT}_N \{ \kappa r(n) \} \\
&= \kappa \tilde{X}_k H_k \\
&= \kappa (\xi_{tx} X_k + \sigma_{tx} X_{-k}^*) H_k
\end{aligned} \tag{4.55}$$

where X_k is the sub-carrier in one FFT block, X_{-k} denotes the mirror part, and H_k stands for CFR. It is worth noticing that CFO and RX IQ-M parameters are estimated in time domain (pre-FFT), while TX IQ-M parameter is extracted in frequency domain (post-FFT). With mathematic derivations, one pair of sub-carriers could be arrayed in a matrix form as follows:

$$\begin{aligned}
\begin{bmatrix} \hat{Y}_k \\ \hat{Y}_k^* \end{bmatrix} &= \begin{bmatrix} \kappa & 0 \\ 0 & \kappa^* \end{bmatrix} \begin{bmatrix} H_k & 0 \\ 0 & H_{-k}^* \end{bmatrix} \begin{bmatrix} \xi_{tx} & \sigma_{tx} \\ \sigma_{tx}^* & \xi_{tx}^* \end{bmatrix} \begin{bmatrix} X_k \\ X_{-k}^* \end{bmatrix} = \begin{bmatrix} \phi_{11,k} & \phi_{12,k} \\ \phi_{21,k} & \phi_{22,k} \end{bmatrix} \begin{bmatrix} X_k \\ X_{-k}^* \end{bmatrix} \\
&= \Phi_k \begin{bmatrix} X_k \\ X_{-k}^* \end{bmatrix}
\end{aligned} \tag{4.56}$$

where $\phi_{ij,k}$ denotes the element corresponding to the i th row and the j th column of Φ_k . So the problem is how to estimate the overall distortion matrix, Φ_k . Because the coherence bandwidth of the channel is much larger than the inter-carrier spacing, the variation between two consecutive sub-carriers could be small. It implies that $\Phi_k \approx \Phi_{k+1}$. Therefore, long preambles are used to calculate the distortion matrixes. For instance, if X_k and X_{-k} are all 1, (4.56) can be rewritten as

$$[\hat{Y}_k \quad \hat{Y}_k]^T = \Phi_k [1 \quad 1]^T \tag{4.57}$$

If X_{k+1} and X_{-k-1} are belong to opposite signs ($X_{k+1} = 1$ and $X_{-k-1} = -1$), (4.56) leads to

$$[\hat{Y}_{k+1} \quad \hat{Y}_{-k-1}]^T = \Phi_{k+1} [1 \quad -1]^T \tag{4.58}$$

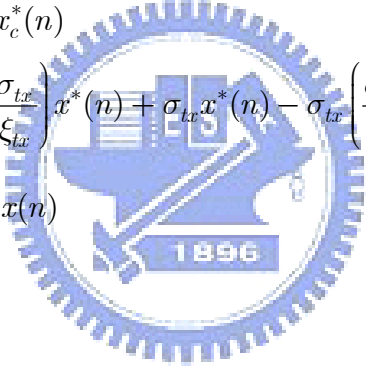
From (4.57) and (4.58), the distortion matrix is estimated by

$$\begin{aligned}
\phi_{11,k} &= 0.5(\hat{Y}_k + \hat{Y}_{k+1}) \\
\phi_{12,k} &= 0.5(\hat{Y}_k - \hat{Y}_{k+1}) \\
\phi_{21,k} &= 0.5(\hat{Y}_{-k}^* + \hat{Y}_{-k-1}^*) \\
\phi_{22,k} &= 0.5(\hat{Y}_{-k}^* - \hat{Y}_{-k-1}^*)
\end{aligned} \tag{4.59}$$

Since distortion matrices are estimated from (4.59), the desired signal can then be recovered. Generally, TX IQ-M could be solved by calibration with carefully designed analog hardware [63]. In order to release the front-end specification, an all-digital estimation method is developed. Recalling from (4.44), a similar approach can be applied at transmitter. The transmitted signal can be pre-compensated according to

$$x_c(n) = x(n) - \left(\frac{\sigma_{tx}}{\xi_{tx}} \right) x^*(n) \quad (4.60)$$

Inserting (4.60) into (4.47) yields

$$\begin{aligned} \tilde{x}(n) &= \xi_{tx} x_c(n) + \sigma_{tx} x_c^*(n) \\ &= \xi_{tx} x(n) - \xi_{tx} \left(\frac{\sigma_{tx}}{\xi_{tx}} \right) x^*(n) + \sigma_{tx} x^*(n) - \sigma_{tx} \left(\frac{\sigma_{tx}^*}{\xi_{tx}^*} \right) x(n) \\ &= \left(\xi_{tx} - \frac{|\sigma_{tx}|^2}{\xi_{tx}^*} \right) x(n) \end{aligned} \quad (4.61)$$


Equation (4.61) indicates that the transmitter can compensate for TX IQ-M by the pre-compensation scheme. The issue now is how to extract TX IQ-M parameters exactly. From (4.56), the matrix, Φ_k , is expressed as

$$\Phi_k = \begin{bmatrix} \phi_{11,k} & \phi_{12,k} \\ \phi_{21,k} & \phi_{22,k} \end{bmatrix} = \begin{bmatrix} \kappa H_k \xi_{tx} & \kappa H_k \sigma_{tx} \\ (\kappa H_{-k} \sigma_{tx})^* & (\kappa H_{-k} \xi_{tx})^* \end{bmatrix} \quad (4.62)$$

It is readily shown that

$$\frac{\sigma_{tx}}{\xi_{tx}} = \frac{\phi_{12,k}}{\phi_{11,k}} = \frac{\phi_{21,k}^*}{\phi_{22,k}^*} \quad (4.63)$$

In order to analyze the sensitivity of noise, a multivariable first order Taylor series³ of (4.63) is expressed as

$$\frac{\phi_{12,k} + n_{12,k}}{\phi_{11,k} + n_{11,k}} = \frac{\sigma_{tx}}{\xi_{tx}} + \frac{1}{\phi_{11,k}} \left(n_{12,k} - \frac{\sigma_{tx}}{\xi_{tx}} n_{11,k} \right) \quad (4.64)$$

where $n_{11,k}$ and $n_{12,k}$ are the small variations of $\phi_{11,k}$ and $\phi_{12,k}$. We define the noise variance as ν_n^2 . The variance of the noise term in (4.64) is

$$\nu^2 = \frac{\nu_n^2}{|\phi_{11,k}|^2} \left(1 + \left(\frac{\sigma_{tx}}{\xi_{tx}} \right)^2 \right) \quad (4.65)$$

which is proportional to $1/|\phi_{11,k}|^2$. By weighting the component inversely proportional to the variance, a better estimate of σ_{tx}/ξ_{tx} could be obtained

$$\frac{\sigma_{tx}}{\xi_{tx}} = \frac{1}{2} \left(\frac{\sum_{k=0}^{N-1} \phi_{12,k} \phi_{11,k}^*}{\sum_{k=0}^{N-1} |\phi_{11,k}|^2} + \frac{\sum_{k=0}^{N-1} \phi_{22,k} \phi_{21,k}^*}{\sum_{k=0}^{N-1} |\phi_{22,k}|^2} \right) \quad (4.66)$$

where N is the data carriers of an OFDM symbol. While TX IQ-M parameters are estimated at receiver, it can be fed back to transmitter (Figure 4-14). This technique may consume link capacity and utilization of packet field. Moreover, the proposed IQ-M compensation method adopts the existing packet format defined in current standards, while the previous literature employs user-defined training symbols [54], [48].

³ For a function that depends on two variables, x and y , the Taylor series to first order about the point (a, b) is written as $f(x, y) = f(a, b) + f_x(a, b)(x - a) + f_y(a, b)(y - b)$, where the subscripts denote the respective partial derivatives.

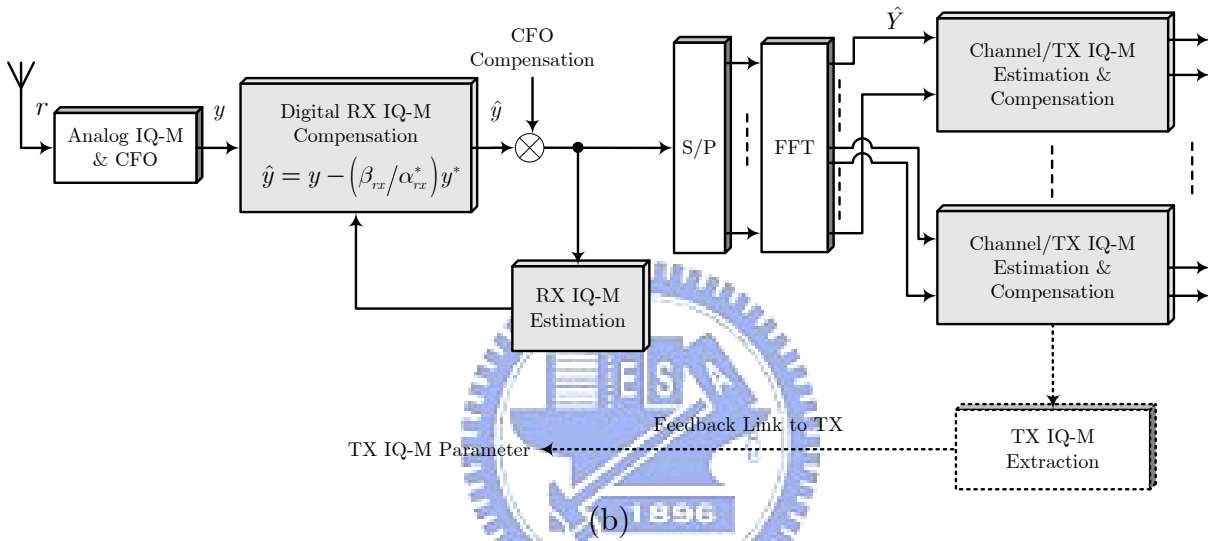
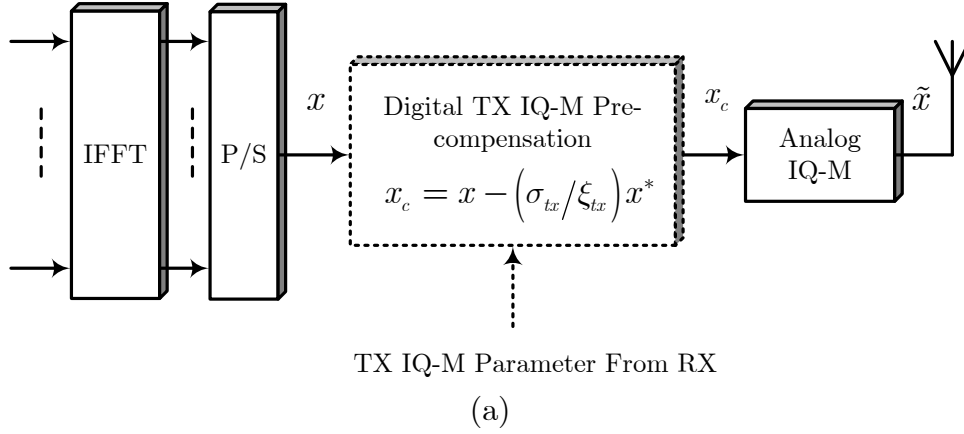


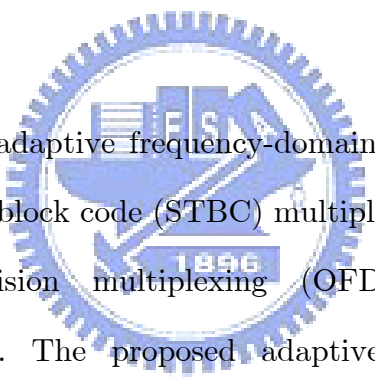
Figure 4-14. Block diagram representation of the proposed method. (a) Transmitter part with pre-compensation scheme. (b) Receiver part with joint compensation scheme.

4.5 Summary

This chapter develops preamble-assisted methods for combating IQ-M with CFO in direct-conversion OFDM receivers. The IQ-M with CFO can be estimated by taking advantage of the relationship between desired sub-carriers and image sub-carriers. Both simulation and experiment results indicate that the proposed method can meet system requirements to prevent from an obvious performance loss under the condition of IQ-M. Furthermore, this method is compatible with current standards because it does not require special packet formats.

Chapter 5

Adaptive Channel Estimation



This chapter presents an adaptive frequency-domain channel estimator (FD-CE) for equalization of space-time block code (STBC) multiple-input multiple-output (MIMO) orthogonal frequency-division multiplexing (OFDM) systems in time-varying frequency-selective fading. The proposed adaptive FD-CE ensures the channel estimation accuracy in each set of four MIMO-OFDM symbols. Performance evaluation shows that the proposed method achieved a 10% packet error rate of 64-QAM modulation at 29.5 dB SNR under 120 km/hr (Doppler shift is 266 Hz) in 4×4 MIMO-OFDM systems. To decrease complexity, the rich feature of Alamouti-like matrix is exploited to derive an efficient VLSI solution. Finally, this adaptive FD-CE using an in-house 0.13- μm CMOS library occupies an area of $3 \times 3.1 \text{ mm}^2$, and the 4×4 MIMO-OFDM modem consumes about 62.8 mW at 1.2V supply voltage.

MIMO-OFDM systems offer reliable communications with bandwidth efficiency and high throughput rate. Space-time block code (STBC) has recently been integrated into MIMO-OFDM systems. The combination of MIMO transmission, OFDM

technology, and the STBC scheme comprises a promising solution for next-generation wireless communications [64]-[65]. The MIMO-OFDM systems, however, require additional complex considerations in signal processing, as compared with single-input single-output (SISO) systems. Recently, the request for wireless communication under mobile conditions is increased. For instance, very high throughput (VHT) study group wants to go beyond the IEEE 802.11n standard. This study group thinks that MIMO-OFDM technology will be a potential solution to increase the data rate. In addition, VHT group also considers to support for moderate mobility or equivalently, improving outdoor operations. VHT study group hopes to not only supply data rate above 1 Gbits/s but also cooperate with metropolitan area network (MAN) network. The ability of fast channel tracking is therefore needed to achieve high performance receivers. Portable applications, such as ultra mobile PCs, personal digital assistants (PDAs) and smart phones, are often used in mobile (time-varying) environments. The accuracy of channel state information (CSI) is critical to ensure the required performance in mobile applications. For successful transmissions, obtaining accurate CSI as soon as possible is extremely important. Advanced military wireless communications and vehicular ad hoc network (VANET) technology (IEEE 802.11p) are other practical applications which will adopt MIMO transmission and STBC. For example, remote controlled vehicles can access the street and battlefield information from the control center or communicate with other moving vehicles. Robust communications in such environments are very important.

Many studies have investigated MIMO detection, and developed and implemented equalization algorithms [66]-[71]. A scalable STBC decoder [66], supporting 2×2 , 8×3 and 8×4 STBCs, was implemented using a low-computational symmetrical approach. A 2×2 MIMO-OFDM detector [67] was developed to offer two modes of space-frequency block code and space division multiplexed OFDM. A vertical-bell

laboratory layered space-time (V-BLAST) detector [68] was based on the square-root algorithm for 4×4 MIMO-OFDM systems. These systems are developed for low mobility. For time-varying environments, Akhtman and Hanzo [69] proposed a decision-directed channel estimation scheme utilizing pilot tones. Song and Lim [70] presented a channel estimation based on particular pilot formats. The channel correlation function [71] was also proposed to exploit the time-varying effects. However, most methods require high complexity and specific pilot for-mats.

To increase throughput, the number of pilots in MIMO-OFDM systems must be significantly smaller than that of data carriers. The objective of this study is to derive an adaptive frequency-domain channel estimator (FD-CE) for frequency-domain equalization without scattered pilots and specific pilot formats in MIMO-OFDM WLAN applications over time-varying fading. Conversely, non-pilot-based channel estimator is built to provide acceptable performance. In the proposed FD-CE, all data carriers are applied to measure channel variations, namely, virtual pilots. Consequently, the system with 64 quadrature amplitude modulation (QAM) can achieve a 10% packet error rate at 29.5 dB signal-to-noise ratio (SNR) at 120 km/hr (Doppler shift is 266 Hz). Furthermore, the adaptive FD-CE utilizes the rich property of an Alamouti-like matrix to derive an efficient architecture for VLSI implementation. By using an in-house 0.13- μm CMOS library, the chip area of the 4×4 MIMO-OFDM modem is $4.6 \times 4.6 \text{ mm}^2$ and power consumption is 62.8 mW at 1.2V supply voltage.

This chapter is organized as follows. Section 5.1 introduces the MIMO-OFDM modem specifications and presents the problem statement. Section 5.2 introduces the STBC scheme. Section 5.3 describes the mathematical derivations for the proposed adaptive FD-CE. Next, Section 5.4 summarizes the simulation results. Section 5.5 then presents the proposed architecture and implementation results. Conclusions are finally drawn in Section 5.6.

5.1 System Description and Problem Statement

5.1.1 Modem Specification

Figure 5-1 presents a block diagram of the 4×4 MIMO-OFDM modem. First, source data is scrambled and then encoded by the convolutional encoder. The encoded bit stream is punctured to the required data rate. According to the number of transmit antennas, the punctured bit stream is parsed into spatial streams. To prevent a burst error, the interleaver changes the bit order for each spatial stream. The interleaved sequence is modulated by the BPSK, QPSK, 16-QAM, or 64-QAM scheme. The STBC encoder is then applied to encode the modulated OFDM (with 64-point IFFT) symbols. Each OFDM symbol has 64 sub-carriers, 52 of which are data carriers and 12 are pilots and null carriers. The time-domain signal is preceded by the guard interval containing the last 16 samples of the OFDM symbol. After all, signal is then transmitted by RF modules.

The receiver synchronizes the received signals to recognize the OFDM symbols. After fast Fourier transform (FFT), the OFDM symbols are decoded by the STBC decoder with the proposed method. Spatial streams are demodulated to bit-level streams, which are then de-interleaved and merged into a single data stream. Finally, the data stream is decoded by the forward error correction (FEC) block, which has a de-puncturer, Viterbi decoder and de-scrambler.

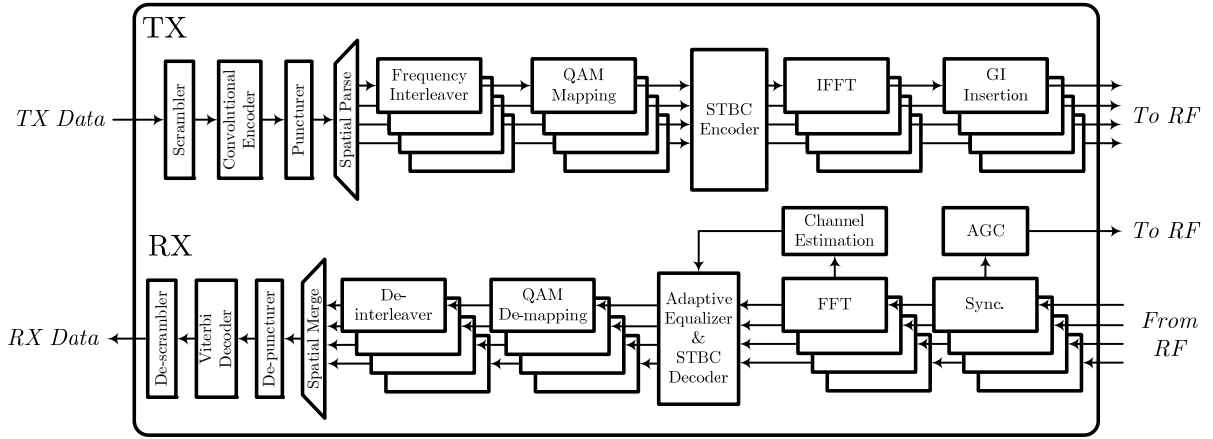


Figure 5-1. Block diagram of the 4×4 STBC MIMO-OFDM modem.

5.1.2 Problem Statement

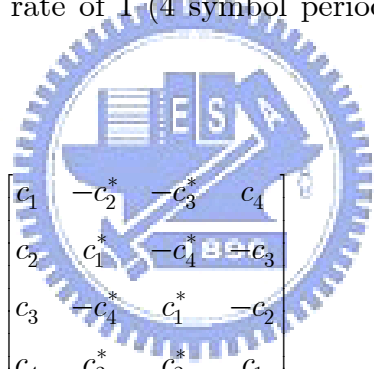
In time-varying fading, the system must measure channel variations to prevent the equalized degradation. It is known that pilot tones can be applied to extract the channel variations. Getting accurate CSI, the system must increase the number of pilot tones, but it also reduces the data rate. The possible solution is to use the scattered pilots to balance the accurate CSI and data rate. The 2-D methods [72]-[73] have been developed for SISO-OFDM applications. However, most WLANs do not include any scattered pilot, and the number of pilots is also much smaller than that of data carriers (e.g., IEEE 802.11 a/g/n and HiperLAN). Due to above limitations, all data carriers should be adopted to ensure accurate estimation of channel variations, namely, virtual pilots.

For VLSI implementation, the hardware complexity of MIMO designs increases greatly; thus, low-complexity architectures are preferred for MIMO-OFDM modems. For example, the coordinate rotation digital computer (CORDIC) algorithm, which is widely used in vector rotation, can be applied for MIMO detection (e.g., QR decomposition [74]-[75]). Although the CORDIC algorithm is advantageous during implementation, the computing latency caused by CORDIC iterations is too long to be

suitable for MIMO-OFDM WLAN applications over time-varying fading. In order to acquire a win-win scenario for latency and throughput, the proposed FD-CE capitalizes on the rich property of an Alamouti-like matrix for an efficient solution.

5.2 STBC Decoder and Equalization

Figure 5-2 shows the STBC scheme applied to a MIMO-OFDM system. In MIMO-OFDM systems, STBC is used independently to each sub-carrier [17]. For the convenience of explanation, four transmit antennas and one receive antenna are considered. To provide the full rate of 1 (4 symbol periods transmit 4 symbols), the following code matrix is chosen



$$C = \begin{bmatrix} c_1 & -c_2^* & -c_3^* & c_4 \\ c_2 & c_1^* & -c_4^* & -c_3 \\ c_3 & -c_4^* & c_1^* & -c_2 \\ c_4 & c_3^* & c_2^* & c_1 \end{bmatrix} \quad (5.1)$$

where c_i , $i = 1, 2, 3, 4$ terms represent the transmitted complex data on the sub-carrier. Let $r_{i,k}$ denote the k th received sub-carrier at the i th symbol duration. The received data over four consecutive symbol periods at receiver one is expressed as

$$\begin{aligned} r_{1,k} &= h_{1,k}x_{1,k} + h_{2,k}x_{2,k} + h_{3,k}x_{3,k} + h_{4,k}x_{4,k} + n_{1,k} \\ r_{2,k} &= -h_{1,k}x_{2,k}^* + h_{2,k}x_{1,k}^* - h_{3,k}x_{4,k}^* + h_{4,k}x_{3,k}^* + n_{2,k} \\ r_{3,k} &= -h_{1,k}x_{3,k}^* - h_{2,k}x_{4,k}^* + h_{3,k}x_{1,k}^* + h_{4,k}x_{2,k}^* + n_{3,k} \\ r_{4,k} &= h_{1,k}x_{4,k} - h_{2,k}x_{3,k} - h_{3,k}x_{2,k} + h_{4,k}x_{1,k} + n_{4,k} \end{aligned} \quad (5.2)$$

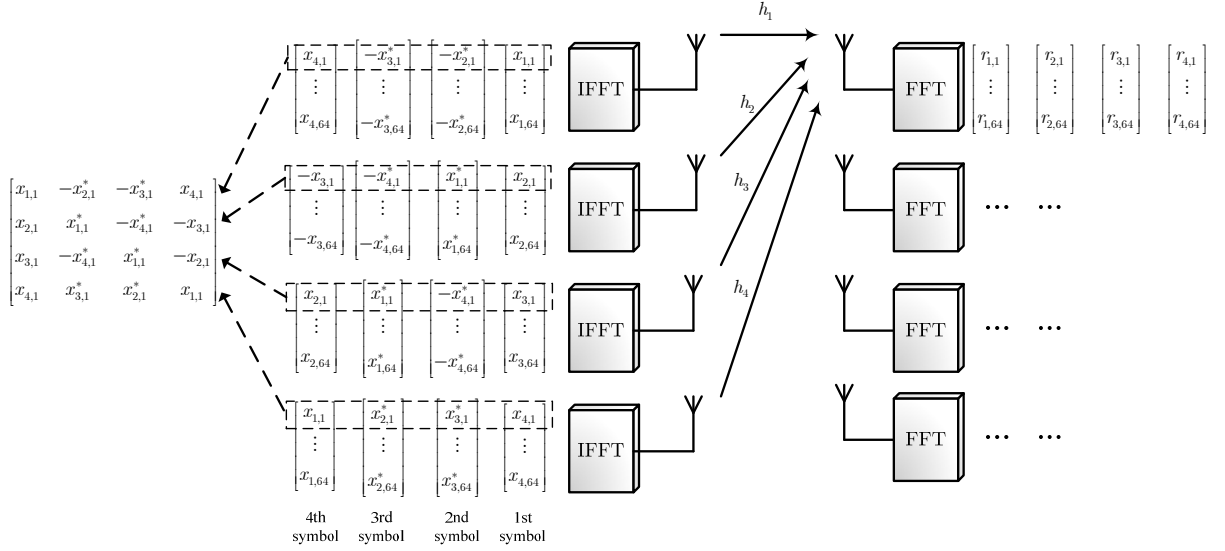


Figure 5-2. Space-time block code in the 4×4 MIMO-OFDM system.

where $h_{i,k}$ is the channel frequency response for the k th sub-carrier from the i th transmit antenna to the receiver and $n_{i,k}$ is the noise term. The received data is then rewritten in matrix form as

$$\begin{bmatrix} r_{1,k} \\ r_{2,k}^* \\ r_{3,k}^* \\ r_{4,k} \end{bmatrix} = \begin{bmatrix} h_{1,k} & h_{2,k} & h_{3,k} & h_{4,k} \\ h_{2,k}^* & -h_{1,k}^* & h_{4,k}^* & -h_{3,k}^* \\ h_{3,k}^* & h_{4,k}^* & -h_{1,k}^* & -h_{2,k}^* \\ h_{4,k} & -h_{3,k} & -h_{2,k} & h_{1,k} \end{bmatrix} \begin{bmatrix} x_{1,k} \\ x_{2,k} \\ x_{3,k} \\ x_{4,k} \end{bmatrix} + \begin{bmatrix} n_{1,k} \\ n_{2,k}^* \\ n_{3,k}^* \\ n_{4,k} \end{bmatrix} \quad (5.3)$$

$$\Rightarrow \mathbf{R}_k = \mathbf{H}_k \mathbf{X}_k + \mathbf{N}_k = \begin{bmatrix} \mathbf{H}_{11,k} & \mathbf{H}_{12,k} \\ \mathbf{H}_{21,k} & \mathbf{H}_{22,k} \end{bmatrix} \mathbf{X}_k + \mathbf{N}_k$$

where \mathbf{R}_k , \mathbf{X}_k , and \mathbf{N}_k are 4×1 vectors and \mathbf{H}_k is a 4×4 matrix. Clearly, all sub-matrices in \mathbf{H}_k are Alamouti-like matrices. The basic 2×2 Alamouti matrix is defined as [16]

$$C_{Alamouti} = \begin{bmatrix} c_1 & -c_2^* \\ c_2 & c_1^* \end{bmatrix} \quad (5.4)$$

where c_i , $i = 1, 2$ terms represent the transmitted complex data on the sub-carrier. The received symbols can be decoded by the STBC decoder with the estimated CSI. The data is equalized by the following equation.

$$\hat{\mathbf{X}}_k = \mathbf{H}_k^{-1} \mathbf{R}_k \quad (5.5)$$

where \mathbf{H}_k can be inverted blockwise using the following inversion formula [76]

$$\mathbf{H}_k^{-1} = \begin{bmatrix} \mathbf{H}_{11,k}^{-1} + \mathbf{H}_{11,k}^{-1} \mathbf{H}_{12,k} \mathbf{D}_k^{-1} \mathbf{H}_{21,k} \mathbf{H}_{11,k}^{-1} & -\mathbf{H}_{11,k}^{-1} \mathbf{H}_{12,k} \mathbf{D}_k^{-1} \\ -\mathbf{D}_k^{-1} \mathbf{H}_{21,k} \mathbf{H}_{11,k}^{-1} & \mathbf{D}_k^{-1} \end{bmatrix} \quad (5.6)$$

where $\mathbf{D}_k = \mathbf{H}_{22,k} - \mathbf{H}_{21,k} \mathbf{H}_{11,k}^{-1} \mathbf{H}_{12,k}$.



5.3 The Proposed Method

5.3.1 Adaptive Frequency-Domain Channel Estimator

Figure 5-3 shows the sub-carrier frequency allocation. Each OFDM symbol employs 64 sub-carriers, 52 are data carriers while the rest are used for pilots and null carries. Four pilots are put in sub-carriers 21, 7, -7 and -21. In general, pilot tones are employed to estimate channel variations in flat-fading channels. In fast-fading channels, it is not suitable to track channel variations of each sub-carrier using only four pilots. By

injecting additional pilots, accuracy channel variations between consecutive OFDM symbols can be estimated; however, this approach can reduce the data rate. Therefore, the proposed method uses four OFDM symbols (total = 208 data carriers + 16 pilots) every time to calculate channel variations without injecting additional pilots. In addition, the proposed method is compatible with the current standard because it does not require special pilot patterns.

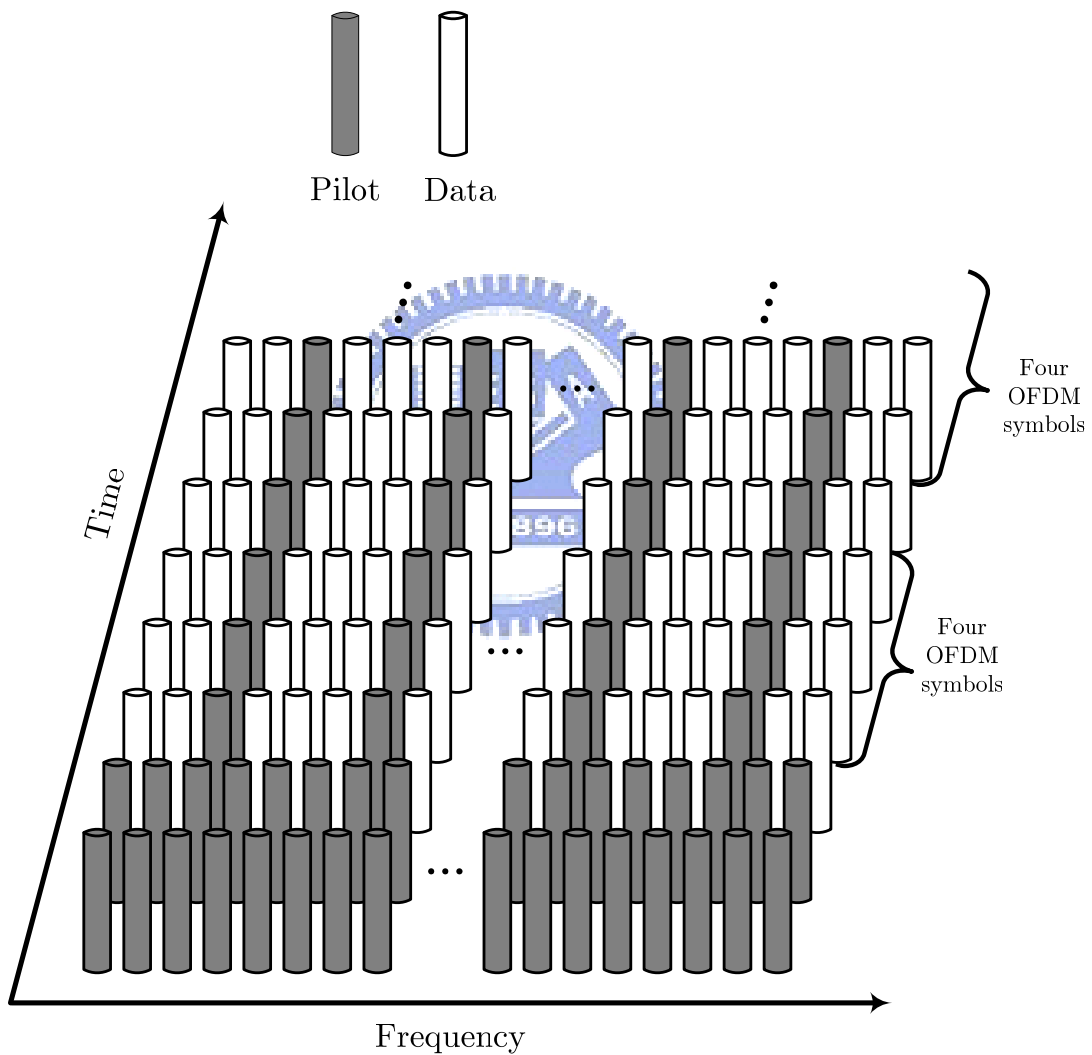


Figure 5-3. Sub-carrier frequency allocation.

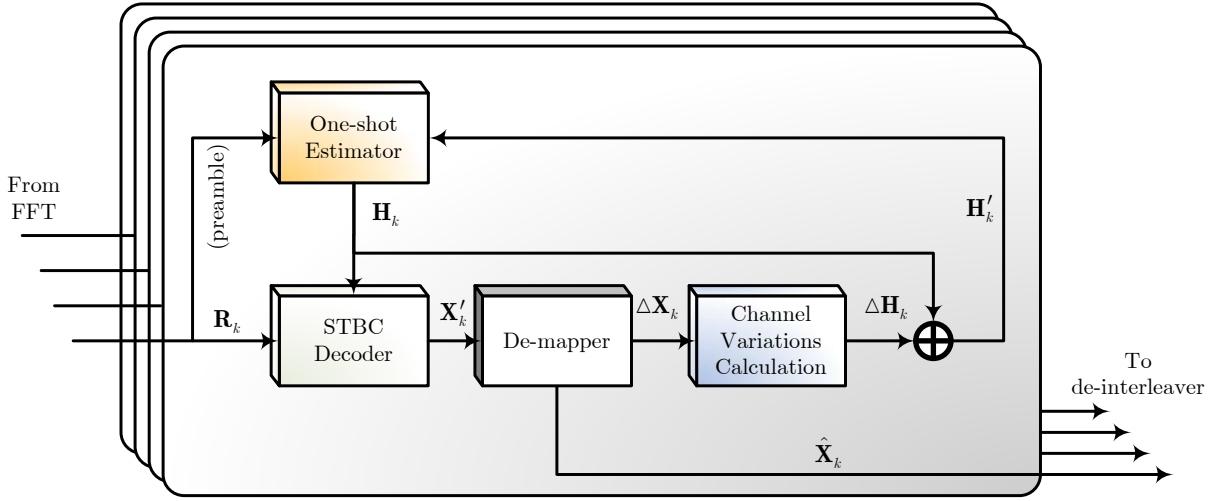


Figure 5-4. Block diagram of the adaptive frequency-domain equalizer.

Figure 5-4 shows a block diagram of the adaptive FD-CE-based frequency-domain equalizer. First, training symbols are employed to estimate channel frequency response (CFR). The decoded symbols are adopted to extract channel variations. Due to time-varying effects, CSI is not consistent within the entire packet. In an adaptive procedure, the estimated CFR is assumed to be \mathbf{H}'_k , which is defined as

$$\mathbf{H}'_k = \mathbf{H}_k + \Delta\mathbf{H}_k \quad (5.7)$$

where

$$\Delta\mathbf{H}_k = \begin{bmatrix} \Delta h_{1,k} & \Delta h_{2,k} & \Delta h_{3,k} & \Delta h_{4,k} \\ \Delta h_{2,k}^* & -\Delta h_{1,k}^* & \Delta h_{4,k}^* & -\Delta h_{3,k}^* \\ \Delta h_{3,k}^* & \Delta h_{4,k}^* & -\Delta h_{1,k}^* & -\Delta h_{2,k}^* \\ \Delta h_{4,k} & -\Delta h_{3,k} & -\Delta h_{2,k} & \Delta h_{1,k} \end{bmatrix} \quad (5.8)$$

Therefore, received data are written as

$$\begin{aligned}
\mathbf{R}_k &= \mathbf{H}'_k \mathbf{X}_k + \mathbf{N}_k \\
&= \mathbf{H}_k \mathbf{X}_k + \Delta \mathbf{H}_k \mathbf{X}_k + \mathbf{N}_k
\end{aligned} \tag{5.9}$$

By multiplying both sides of (5.8) by \mathbf{H}_k^{-1} , the data symbols are estimated by

$$\begin{aligned}
\mathbf{H}_k^{-1} \mathbf{R}_k &= \mathbf{X}_k + \mathbf{H}_k^{-1} \Delta \mathbf{H}_k \mathbf{X}_k + \tilde{\mathbf{N}}_k \\
&= \mathbf{X}_k + \Delta \mathbf{X}_k + \tilde{\mathbf{N}}_k \\
&= \mathbf{X}'_k + \tilde{\mathbf{N}}_k
\end{aligned} \tag{5.10}$$

where \mathbf{X}'_k , $\Delta \mathbf{X}_k$, and $\tilde{\mathbf{N}}_k$ are 4×1 vectors. Due to time-varying fading, the decoded symbol contains a residual term that causes a decision error, as shown in (5.10). The relationship between \mathbf{X}_k and \mathbf{X}'_k can be interpreted geometrically in the complex plane (Figure 5-5). The difference between ideal code sets and received symbols is used to extract channel variations. The residual term is expressed as

$$\begin{aligned}
\Delta \mathbf{X}_k &= \mathbf{H}_k^{-1} \Delta \mathbf{H}_k \mathbf{X}_k \\
&= \mathbf{X}'_k - \mathbf{X}_k \\
&= \begin{bmatrix} \Delta x_{1,k} & \Delta x_{2,k} & \Delta x_{3,k} & \Delta x_{4,k} \end{bmatrix}^T
\end{aligned} \tag{5.11}$$

By defining $\Delta \mathbf{R}_k = \mathbf{H}_k \Delta \mathbf{X}_k$, (5.11) can be rewritten as

$$\begin{aligned}
\Delta \mathbf{R}_k &= \mathbf{H}_k \Delta \mathbf{X}_k \\
&= \Delta \mathbf{H}_k \mathbf{X}_k \\
&= \begin{bmatrix} \Delta r_{1,k} & \Delta r_{2,k} & \Delta r_{3,k} & \Delta r_{4,k} \end{bmatrix}^T
\end{aligned} \tag{5.12}$$

From (5.12), the channel variations can be calculated by the following equation

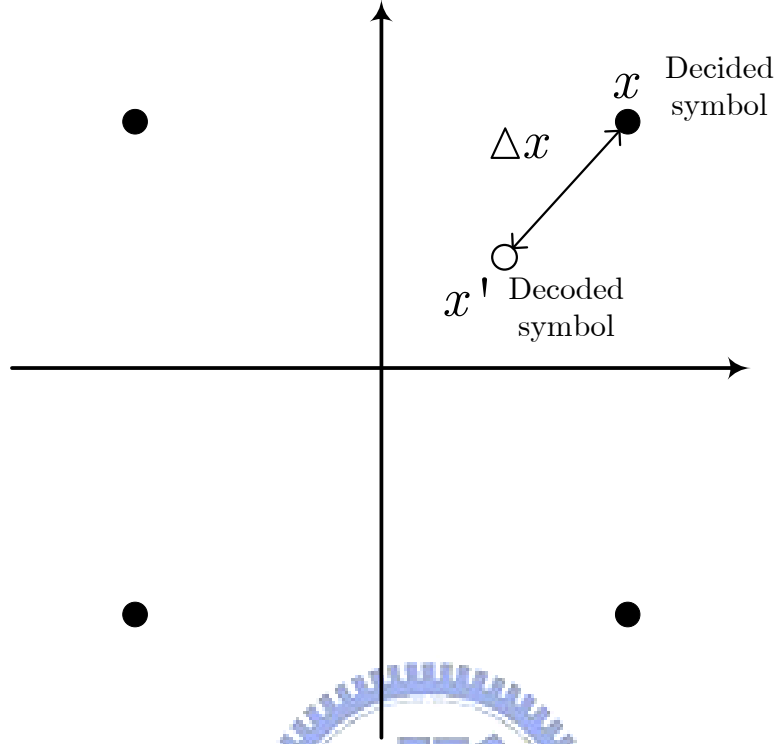


Figure 5-5. Relationship between decided symbol and decoded symbol.

$$\begin{aligned}
 \Delta \mathbf{R}_k &= \Delta \mathbf{H}_k \mathbf{X}_k \\
 \Rightarrow \begin{bmatrix} \Delta r_{1,k} \\ \Delta r_{2,k} \\ \Delta r_{3,k} \\ \Delta r_{4,k} \end{bmatrix} &= \begin{bmatrix} \Delta h_{1,k} & \Delta h_{2,k} & \Delta h_{3,k} & \Delta h_{4,k} \\ \Delta h_{2,k}^* & -\Delta h_{1,k}^* & \Delta h_{4,k}^* & -\Delta h_{3,k}^* \\ \Delta h_{3,k}^* & \Delta h_{4,k}^* & -\Delta h_{1,k}^* & -\Delta h_{2,k}^* \\ \Delta h_{4,k} & -\Delta h_{3,k} & -\Delta h_{2,k} & \Delta h_{1,k} \end{bmatrix} \begin{bmatrix} x_{1,k} \\ x_{2,k} \\ x_{3,k} \\ x_{4,k} \end{bmatrix} \\
 \Rightarrow \begin{bmatrix} \Delta r_{1,k} \\ -\Delta r_{2,k}^* \\ -\Delta r_{3,k}^* \\ \Delta r_{4,k} \end{bmatrix} &= \begin{bmatrix} x_{1,k} & x_{2,k} & x_{3,k} & x_{4,k} \\ x_{2,k}^* & -x_{1,k}^* & x_{4,k}^* & -x_{3,k}^* \\ x_{3,k}^* & x_{4,k}^* & -x_{1,k}^* & -x_{2,k}^* \\ x_{4,k} & -x_{3,k} & -x_{2,k} & x_{1,k} \end{bmatrix} \begin{bmatrix} \Delta h_{1,k} \\ \Delta h_{2,k} \\ \Delta h_{3,k} \\ \Delta h_{4,k} \end{bmatrix} \\
 \Rightarrow \begin{bmatrix} \Delta h_{1,k} \\ \Delta h_{2,k} \\ \Delta h_{3,k} \\ \Delta h_{4,k} \end{bmatrix} &= \begin{bmatrix} x_{1,k} & x_{2,k} & x_{3,k} & x_{4,k} \\ x_{2,k}^* & -x_{1,k}^* & x_{4,k}^* & -x_{3,k}^* \\ x_{3,k}^* & x_{4,k}^* & -x_{1,k}^* & -x_{2,k}^* \\ x_{4,k} & -x_{3,k} & -x_{2,k} & x_{1,k} \end{bmatrix}^{-1} \begin{bmatrix} \Delta r_{1,k} \\ -\Delta r_{2,k}^* \\ -\Delta r_{3,k}^* \\ \Delta r_{4,k} \end{bmatrix}
 \end{aligned} \tag{5.13}$$

TABLE 5-1 summarizes the operations of the adaptive FD-CE. The adaptive FD-CE is applied to every four OFDM symbols for 208 tones. Notably, \mathbf{H}_k^{-1} is multiplied by the received OFDM symbols. The decoded symbols \mathbf{X}'_k are employed to calculate residual term $\Delta\mathbf{X}_k$. To acquire $\Delta\mathbf{R}_k$, channel matrix \mathbf{H}_k is multiplied by the stored distance vector $\Delta\mathbf{X}_k$. After calculating channel variations, \mathbf{H}'_k is updated by (5.7).

TABLE 5-1. Operation of the Adaptive FD-CE.

<i>Step</i>	<i>Operation</i>
1	Estimate the channel state information
2	$\mathbf{X}'_k = \mathbf{H}_k^{-1}\mathbf{R}_k$
3	Calculate the residual term $\Delta\mathbf{X}_k$
4	$\Delta\mathbf{R}_k = \mathbf{H}_k\Delta\mathbf{X}_k$
5	Calculate the channel variation
6	Update the channel matrix \mathbf{H}'_k

The 4×4 code matrix, as defined in (5.1), can be applied to four transmit antennas and any number of receive antennas. In the above derivation, the receiver takes advantage of the orthogonality of code matrix to find a decision statistic. If the receive antenna number is greater than one, we can add all the statistics from all receive antennas. In multiple receive antennas, the additional computational cost includes STBC decoding and scale operations. For instance, the statistics from four receive antennas are given by

$$\sum_{i=1}^4 \hat{\mathbf{X}}_{k,i} = \sum_{i=1}^4 \mathbf{H}_{k,i}^{-1}\mathbf{R}_{k,i}$$

where the subscript i represents the i th receive antenna. It is clear that the estimated symbols will be a scale version. To estimate the symbols that were sent, we can scale the

decision statistics. This result presented above can be directly extended to other STBC codes.

5.3.2 Discussion

We provide the discussion with regard to the $M \times N$ MIMO system for $M > 2$ and $N > 2$. First, we describe the encoding and decoding operations of Alamouti scheme. The Alamouti code is an STBC using $M = 2$ transmit antennas and *any* number of receive antennas ($N > 2$) [Figure 5-6(a)]. The Alamouti code matrix is defined in (5.4). Assuming that the channel coefficients are constant in both consecutive symbol periods, the signal received by antenna one is expressed as

$$\begin{bmatrix} r_{1,k} \\ r_{2,k}^* \end{bmatrix} = \begin{bmatrix} h_{1,k} & h_{2,k} \\ h_{2,k}^* & -h_{1,k}^* \end{bmatrix} \begin{bmatrix} x_{1,k} \\ x_{2,k} \end{bmatrix} + \begin{bmatrix} n_{1,k} \\ n_{2,k}^* \end{bmatrix} \quad (5.14)$$

where the parameters are defined (5.2). Assuming that the receiver has knowledge of the channel coefficients, the decision statistics are given by

$$\begin{bmatrix} \hat{x}_{1,k} \\ \hat{x}_{2,k} \end{bmatrix} = \left(|h_{1,k}|^2 + |h_{2,k}|^2 \right)^{-1} \begin{bmatrix} h_{1,k} & h_{2,k} \\ h_{2,k}^* & -h_{1,k}^* \end{bmatrix}^{-1} \begin{bmatrix} r_{1,k} \\ r_{2,k}^* \end{bmatrix} \quad (5.15)$$

There may be applications where multiple receive antennas are feasible. The Alamouti scheme can be applied for the system with multiple receive antennas. Adding all the decision statistics from all N receive antennas, the estimated symbols will be a scale version. To estimate the symbols, we can scale the decision statistics. This result

presented above can be directly extended to other STBC codes.

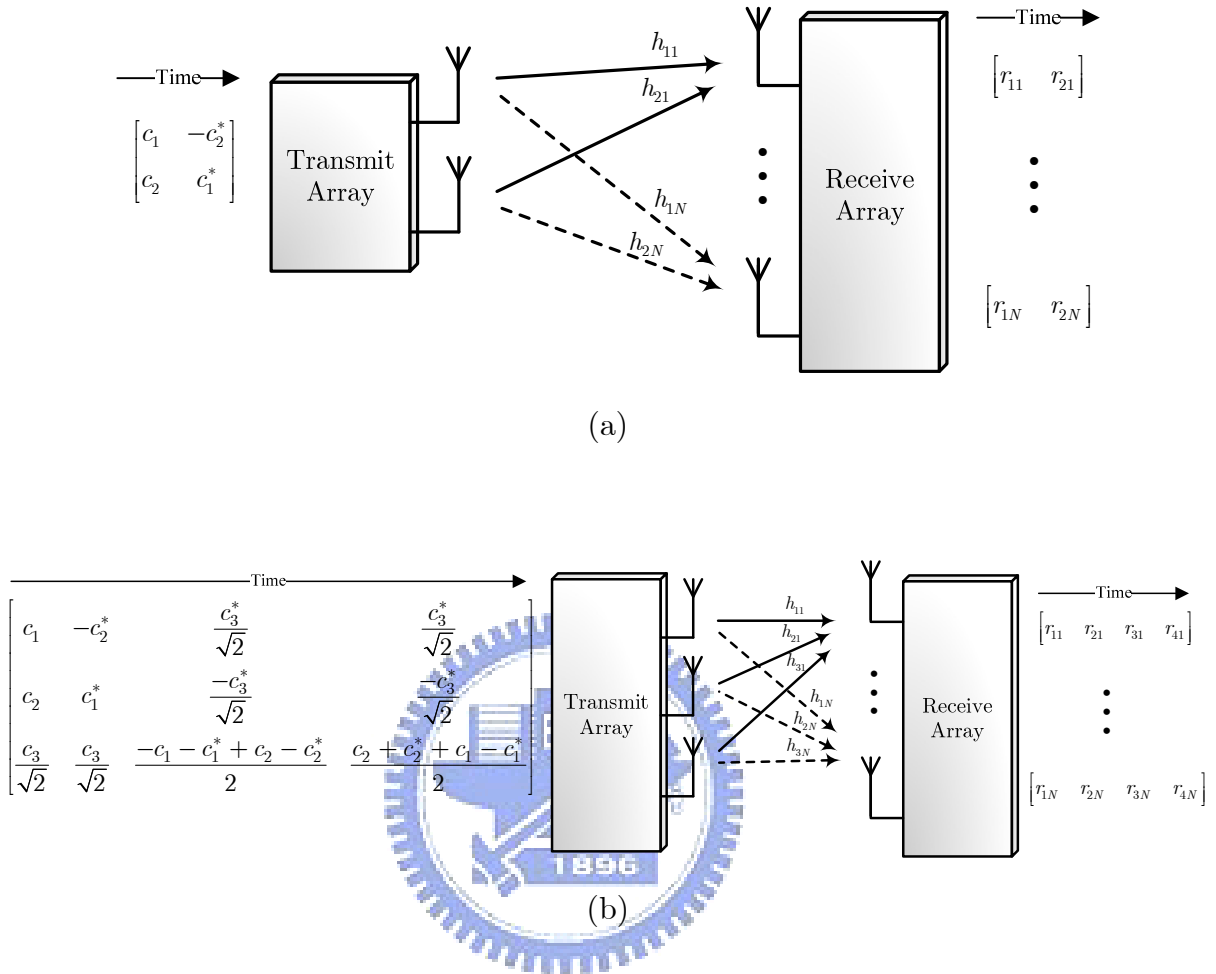


Figure 5-6. (a) The block diagram of the $2 \times N$ MIMO system. (b) The block diagram of the $3 \times N$ MIMO system with STBC matrix C_3 .

We discuss the case with $M > 2$ transmit antennas subsequently. In general, the STBC code can be defined by a $M \times p$ matrix C . The elements of the matrix C are combinations of the symbols c_i , $i = 1, \dots, k$. The columns of the matrix represent time slots and the rows denote transmit antennas. Hence, p time slots are required to transmit k symbols (code rate $R = k/p$, where $R \leq 1$ [15]). For M transmit antennas, we are more interested in the minimum time slots (p) needed to transmit a block. In summary, STBC systems transmit the same information stream via different transmit antennas to obtain transmit diversity. Despite the reduction in the data rate, the STBC

system take the advantage of transmit diversity to obtain a robust communications. For instance, C_3 is the STBC matrix with three transmit antennas [Figure 5-6(b)]. The matrix C_3 (code rate $R = 3/4$) is given below [17]

$$C_3 = \begin{bmatrix} c_1 & -c_2^* & c_3^*/\sqrt{2} & c_3^*/\sqrt{2} \\ c_2 & c_1^* & -c_3^*/\sqrt{2} & -c_3^*/\sqrt{2} \\ c_3/\sqrt{2} & c_3/\sqrt{2} & \frac{-c_1 - c_1^* + c_2 - c_2^*}{2} & \frac{c_2 + c_2^* + c_1 - c_1^*}{2} \end{bmatrix} \quad (5.16)$$

To decode the C_3 , the receiver one constructs the decision statistics as follows:

$$\begin{aligned} \hat{x}_{1,k} &= r_{1,k}h_{1,k}^* + r_{2,k}^*h_{2,k} + \frac{(r_{4,k} - r_{3,k})h_{3,k}^*}{2} - \frac{(r_{4,k} - r_{3,k})^*h_{3,k}}{2} \\ \hat{x}_{2,k} &= r_{1,k}h_{2,k}^* - r_{2,k}^*h_{1,k} + \frac{(r_{4,k} + r_{3,k})h_{3,k}^*}{2} + \frac{(-r_{3,k} + r_{4,k})^*h_{3,k}}{2} \\ \hat{x}_{3,k} &= \frac{(r_{1,k} + r_{2,k})h_{3,k}^*}{\sqrt{2}} + \frac{(h_{1,k} + h_{2,k})r_{3,k}^*}{\sqrt{2}} + \frac{(h_{1,k} - h_{2,k})r_{4,k}^*}{\sqrt{2}} \end{aligned} \quad (5.17)$$

where these parameters are defined in (5.2). Adding all the decision statistics from all receive antennas, the estimated symbols will be a scale version. We can scale the decision statistics to estimate the symbols. After the STBC decoding, the difference between ideal constellation points and the received symbols can be calculated directly, and then channel variations can be extracted. From (5.17), it is clear that the computational complexity is higher than Alamouti-like case adopted in this study. In system designs, we prefer to choose a feasible STBC matrix which can be decoded by simple liner processing. Alamouti-like matrix is one potential candidate for simple processing among various STBC codewords.

In addition, the complexity of channel estimation scheme also depends on the

MIMO detection method. To achieve higher throughput, spatial-division multiplexing (SDM) technique can be used. With SDM, multiple transmit antennas transmit independent data streams, which can be individually recovered at receiver. An applicable method is required to separate each transmitted stream from other transmitted streams (interference cancellation). Many approaches are known for the detection of SDM signals. For instance, zero-forcing (ZF), minimum mean square error (MMSE), and maximum likelihood (ML) detectors estimate the transmitted signals with the estimated channel state information. In general, ML detector provides improved performance over ZF, MMSE detectors. However, the computation complexity of performing a full search for ML detection is too high to be suitable for practical applications. To reduce the complexity, sphere decoding technique or K-best algorithm can be applied to the ML detector. In ZF detector, the detector finds the inversion of the channel matrix to eliminate interference (i.e., $\mathbf{H}^{-1}\mathbf{H} = \mathbf{I}$). If the number of transmit antennas is the same as the number of receive antennas, channel matrix (\mathbf{H}) is a square matrix and the ZF detector has a unique solution (\mathbf{H}^{-1}). If the channel matrix is not invertible, the ZF detector has a pseudo inverse solution (i.e., $(\mathbf{H}^H\mathbf{H})^{-1}\mathbf{H}^H$, where \mathbf{H}^H denotes the Hermitian conjugate). For MMSE detector, the detector finds a matrix \mathbf{C} to minimize the mean square error (MSE)¹. From the above discussion, it is clear that matrix inversion and matrix multiply are required to complete the MIMO detection. Different data detection methods have different criteria, and therefore it is preferred to adopt a reduced-complexity data detection scheme in MIMO systems.

¹ $\text{MSE} = \text{E}[\|\mathbf{C}\mathbf{R} - \mathbf{X}\|^2]$, where \mathbf{R} is the received data vector and \mathbf{X} is the transmitted data vector.

5.4 Performance Evolution

Similar to IEEE 802.11n [2], the parameters of the 4×4 MIMO-OFDM system employed are as follows: FFT size is 64; the cyclic prefix (CP) is 16 long; system bandwidth is 20 MHz; and, carrier frequency is 2.4 GHz. To ensure the effectiveness of the proposed method, each packet length is set to 1024 bytes. The Jakes method is used to generate time-varying effects during simulations. The Doppler shifts are set to 133 Hz (speed, 60 km/hr) and 266 Hz (speed, 120 km/hr)². Frequency synchronization is performed to compensate for the frequency shift. The amplitude and phase of channel change significantly at high Doppler shift. Figure 5-7 displays the bit error rate (BER) and packet error rate (PER) of the 4×4 MIMO-OFDM system with and without the proposed adaptive FD-CE. In Figure 5-7, “one-shot” legend refers to the case when the proposed adaptive channel estimator is not applied. Obviously, the degradation in BER and PER is significant without proper channel tracking in time-varying fading. Simulations also indicate the effectiveness of the proposed adaptive FD-CE, which performs well at 28-30 dB SNR for 64-QAM modulation without any irreducible error floor. Thus, this study can be widely applied to time-varying fading.

² The Doppler shift can be expressed as $f_d = v \cdot f_c / c$, where f_c is the carrier frequency, c is the velocity of light, and v is the receiver speed.

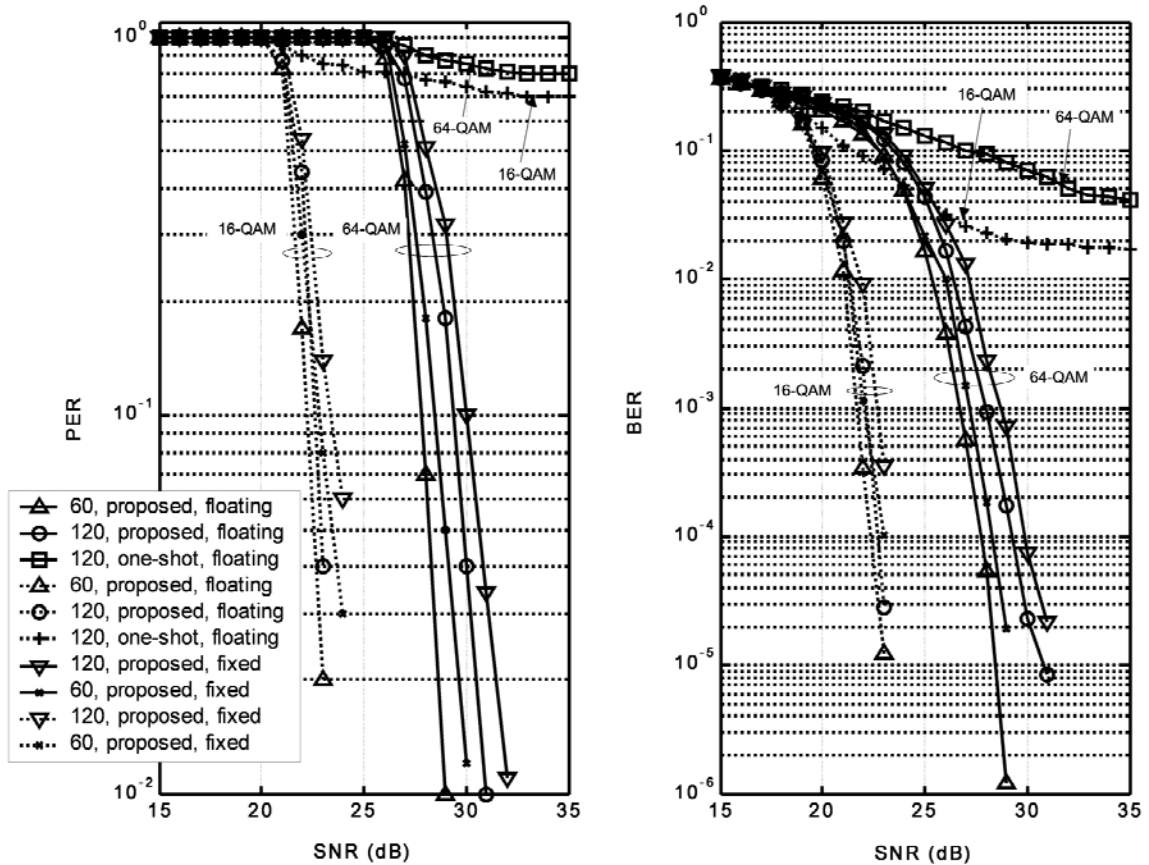


Figure 5-7. BER and PER performance.



5.5 Architecture and Implementation

5.5.1 Proposed Architecture

Figure 5-8 shows the architecture of the proposed adaptive FD-CE, which has four major modules: 1) a one-shot estimator; 2) matrix multiplier (MM); 3) matrix inverter (MI); 4) de-mapper. The adaptive FD-CE is pipelined to 8 levels since the latency of MI is long. The one-shot estimator is adopted to measure an initial CSI obtained from training symbols (long preambles) [21], and then updated by means of feedback

mechanism. The de-mapper outputs the point of QAM constellation that has the minimum distance to its input. The key issue of implementations is to build efficient architectures for matrix operations, where the functions of MM and MI are discussed as follows.

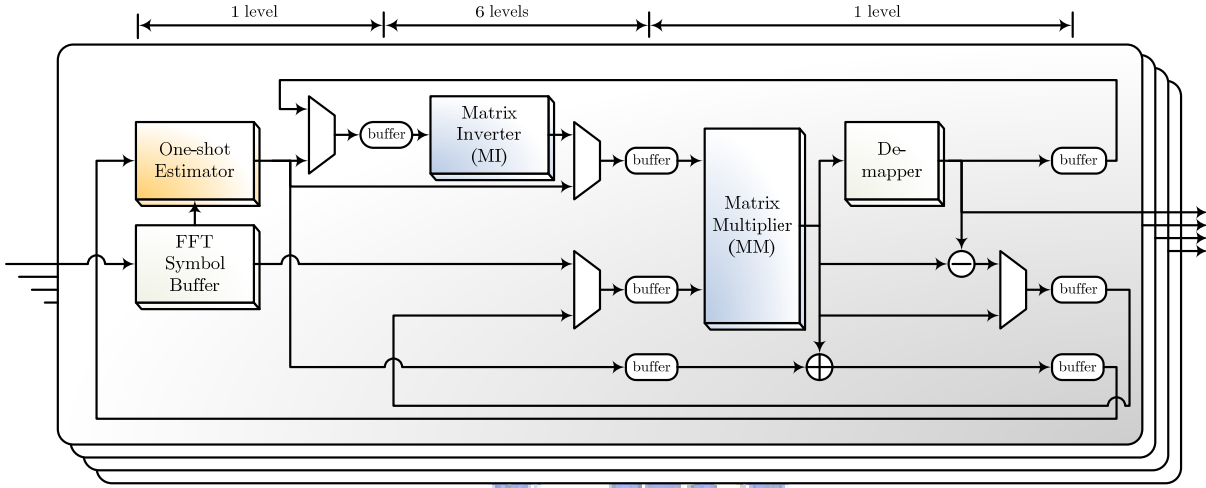


Figure 5-8. Architecture of the adaptive FD-CE.

From (5.6), \mathbf{H}_k^{-1} is a square matrix with 2×2 Alamouti sub-blocks. Three 2×2 matrix multipliers and two 2×2 matrix inverters are needed by the MI. Figure 5-9 illustrates the flowchart of matrix inverse computation. For convenience, four letters, u , v , p , and q , are used to denote the elements in the matrices. In Figure 5-9, the outputs of these three 2×2 matrix multipliers are simply expressed as

$$\begin{aligned} & \mathbf{H}_{21,k} \mathbf{H}_{11,k}^{-1} \\ \Rightarrow & \begin{bmatrix} u & v \\ v^* & -u^* \end{bmatrix} \cdot \begin{bmatrix} p & q \\ q^* & -p^* \end{bmatrix} = \begin{bmatrix} up + vq^* & uq - vp^* \\ v^*p - u^*q^* & v^*q + u^*p^* \end{bmatrix} \end{aligned} \quad (5.18)$$

$$\begin{aligned} & \mathbf{H}_{21,k} \mathbf{H}_{11,k}^{-1} \mathbf{H}_{12,k} \\ \Rightarrow & \begin{bmatrix} u & v \\ -v^* & u^* \end{bmatrix} \cdot \begin{bmatrix} p & q \\ q^* & -p^* \end{bmatrix} = \begin{bmatrix} up + vq^* & uq - vp^* \\ -v^*p + u^*q^* & -v^*q - u^*p^* \end{bmatrix} \end{aligned} \quad (5.19)$$

$$\mathbf{D}_k^{-1} \mathbf{H}_{21,k} \mathbf{H}_{11,k}^{-1} \Rightarrow \begin{bmatrix} u & v \\ v^* & -u^* \end{bmatrix} \cdot \begin{bmatrix} p & q \\ -q^* & p^* \end{bmatrix} = \begin{bmatrix} up - vq^* & uq + vp^* \\ v^*p + u^*q^* & v^*q - u^*p^* \end{bmatrix} \quad (5.20)$$

$$\mathbf{H}_k^{-1} = \begin{bmatrix} -c^* & -d^* & a^* & b^* \\ -d & c & b & -a \\ a & b & c & d \\ b^* & -a^* & d^* & -c^* \end{bmatrix}$$

Only these four elements need to be computed.

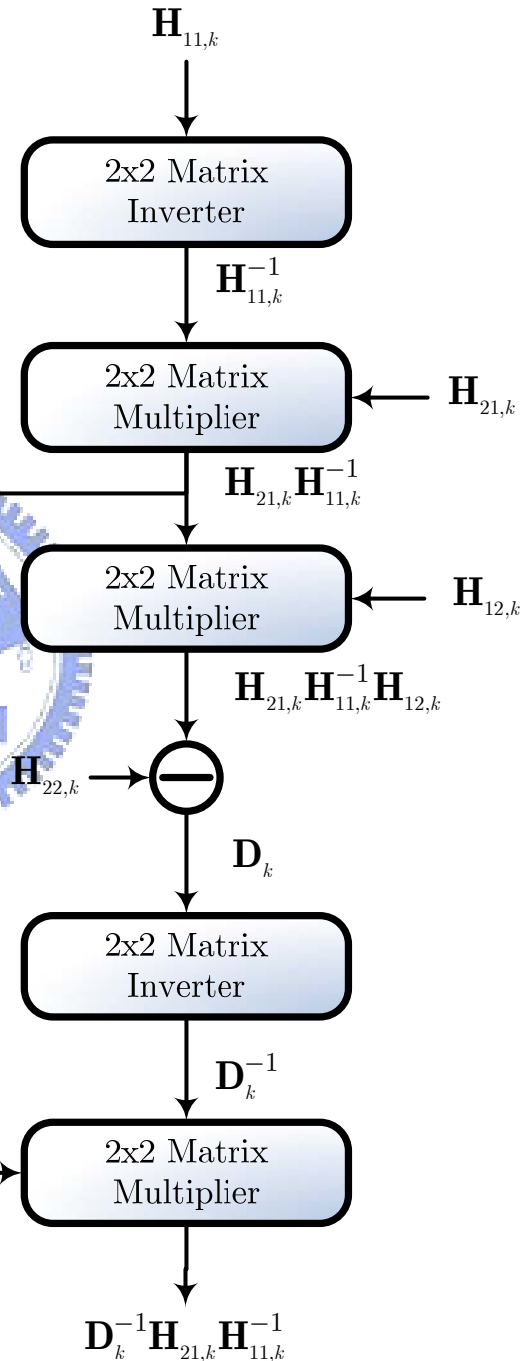
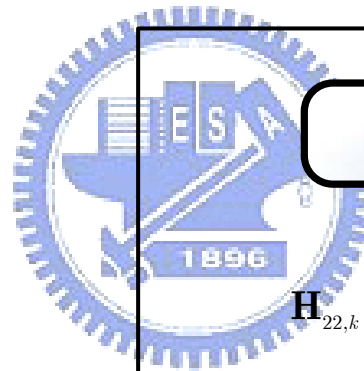


Figure 5-9. Flowchart of matrix inverse computation.

They are all Alamouti-like matrices. Figure 5-10 shows the architectures, where 4 complex multipliers and 2 complex adders are needed in a 2×2 matrix multiplier. Figure 5-11 shows the architecture of the 2×2 matrix inverter consisting of four square units, three adders and four dividers. The inverse of a 2×2 Alamouti matrix is still an Alamouti matrix [16]. Notably, only half of the Alamouti-like matrix must be computed — the other half can be derived from the first half via simple sign-flipping operations. This characteristic is extremely useful as it can be exploited to derive an efficient architecture for implementation. The MM is utilized for symbol detection, as shown in (5.10). For convenience, four letters, a , b , c and d , are used to denote the elements in the matrices. Then, (5.10) can be rewritten as

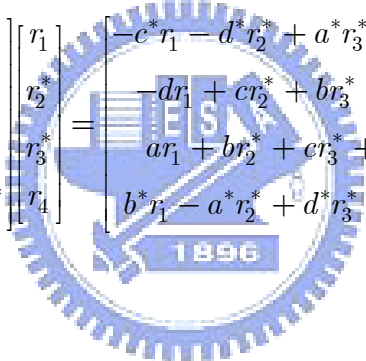
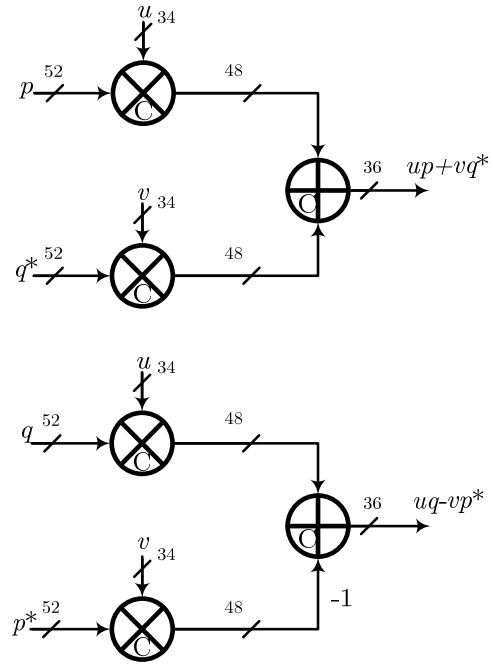
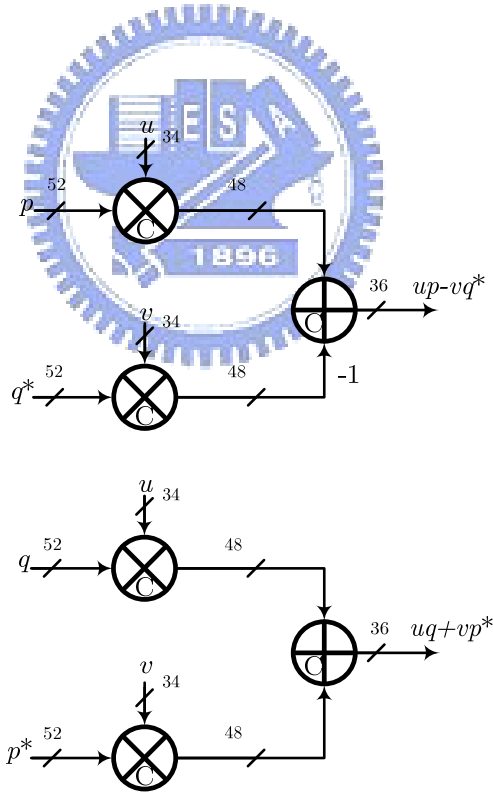
$$\begin{bmatrix} -c^* & -d^* & a^* & b^* \\ -d & c & b & -a \\ a & b & c & d \\ b^* & -a^* & d^* & -c^* \end{bmatrix} \begin{bmatrix} r_1 \\ r_2^* \\ r_3^* \\ r_4 \end{bmatrix} = \begin{bmatrix} -c^*r_1 - d^*r_2^* + a^*r_3^* + b^*r_4 \\ -dr_1 + cr_2^* + br_3^* - ar_4 \\ ar_1 + br_2^* + cr_3^* + dr_4 \\ b^*r_1 - a^*r_2^* + d^*r_3^* - c^*r_4 \end{bmatrix} \quad (5.21)$$


Figure 5-12 shows the architecture of MM. To obtain outputs simultaneously, 16 complex multipliers and 12 complex adders are required. Through share and reuse, the implemented cost can be saved.



(a)



(b)

Figure 5-10. Architecture of MI. The bit width includes real and image parts. (a) Matrix multiplier for $\mathbf{H}_{21,k}\mathbf{H}_{11,k}^{-1}$ and $\mathbf{H}_{21,k}\mathbf{H}_{11,k}^{-1}\mathbf{H}_{12,k}$. (b) Matrix multiplier for $\mathbf{D}_k^{-1}\mathbf{H}_{21,k}\mathbf{H}_{11,k}^{-1}$.

$$\begin{bmatrix} u & v \\ v^* & -u^* \end{bmatrix}^{-1} = \frac{1}{|u|^2 + |v|^2} \begin{bmatrix} u^* & v \\ v^* & -u \end{bmatrix}$$

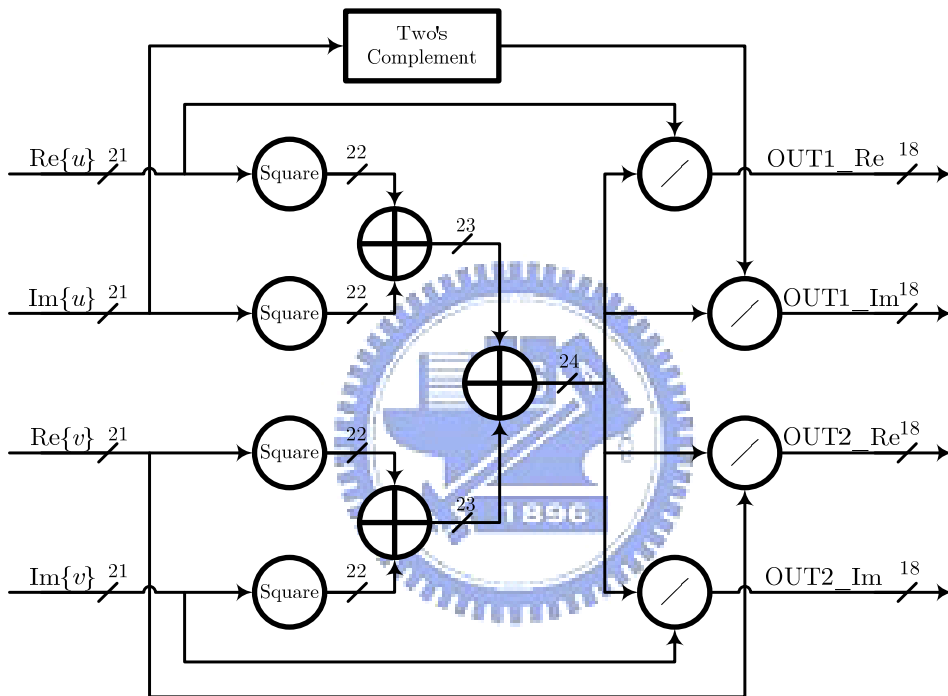


Figure 5-11. Architecture of matrix inverter (Alamouti matrix).

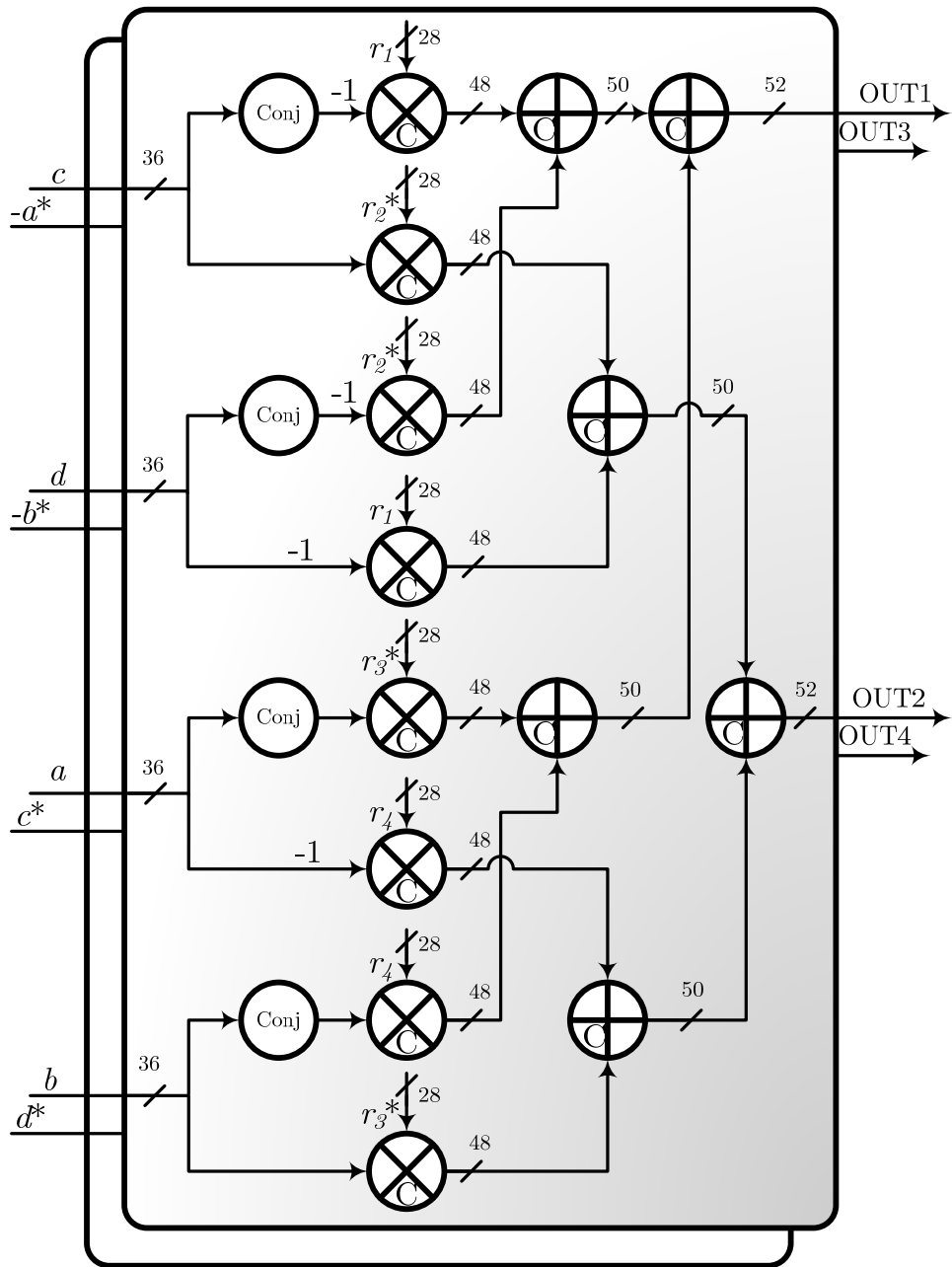


Figure 5-12. Architecture of MM. The bit width includes real and image parts.

5.5.2 Implementation Results

In the MATLAB platform, an overall system (transmitter, inner and outer receiver) is constructed to evaluate the performance. In this chip, the Viterbi decoder is not implemented (limited by chip area). For rapid verification, a 2×2 software-defined radio (SDR), as displayed in Figure 5-13, is constructed. TABLE 5-2 lists the experimental parameters in the software-defined radio. The carrier frequency of each transmit antenna is 2.4 GHz. At the transmitter part, the transmitted data are produced by the MATLAB module and then these data are stored in memory. The proposed method is mapped onto the field programmable gate array (FPGA) chips (Xilinx Virtex-II) with on-board 14-bit digital-to-analog converters (DACs). The signals are then transmitted using an in-house RF front-end. Because it is essential to make MIMO transmissions coherent at all DACs and antennas, there is an additional DAC module as a hardware trigger of TX, namely “Sync” in Figure 5-13, to control four DACs coherently. After down-converting the RF signals to baseband at the receiver, analog signals are fed into 14-bit analog-to-digital converters (ADCs). The proposed algorithm then processes the down-converted signals. The hardware-description language (HDL) can be generated as soon as the architecture with a fixed-point evaluation has been created. After performance assessment and HDL validation, the 4×4 MIMO-OFDM modem (Figure 5-1) is implemented by Taiwan Semiconductor Manufacturing Company (TSMC) 0.13- μm one-poly eight-metal layer (1P8M) CMOS library. TABLE 5-3 presents the synthesized results. Based on synthesis, automatic place and route (APR) can be carried out by SOC encounter (Cadence). Layout versus schematic (LVS) and design rule checking (DRC) must be performed to assess the APR result. Finally, post-layout simulations are performed to verify the clocking, timing, and power of the proposed design. The proposed design passes the SS model (supply voltage:

1.08V) and temperature 125 °C corner simulation. The received data from SDR platform is applied to the chip testing, which is performed to verify the full functionality of the chip using Agilent 93000 SOC Test System. The modem area is $4.1 \times 4.1 \text{ mm}^2$, and the area of the proposed FD-CE is $3 \times 3.1 \text{ mm}^2$ (Figure 5-14). The memory requirement for the proposed FD-CE is 50 K bits. Since one adaptive procedure requires 24.6 μs to measure 4 OFDM symbols (208 carriers), the efficient throughput is 50 Mbps with a 64-QAM modulation at 20 MHz. If we use all carriers ($64 \times 4 = 256$) of four OFDM symbols to compute the data rate, the data rate is 62.4 Mbps. The chip area with I/O pads and a power ring is $4.6 \times 4.6 \text{ mm}^2$. At 1.2V supply voltage, the power consumption is about 62.8 mW. TABLE 5-4 lists chip summary of the 4×4 MIMO-OFDM modem.

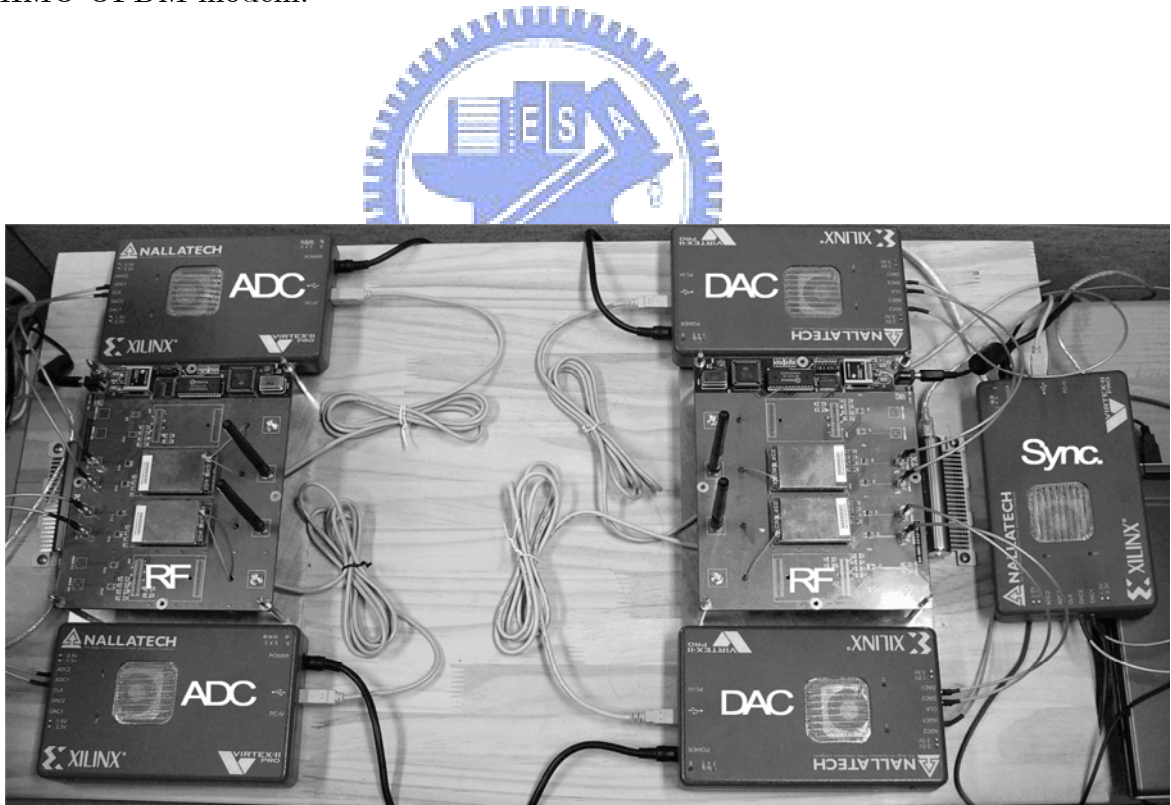


Figure 5-13. Software-defined radio platform.

TABLE 5-2. Experimental Parameters.

<i>Parameters</i>	<i>Value</i>
RF carrier frequency	2.4 GHz
RF power level	−40 dBm
ADC/DAC resolution	14 bits
(I)FFT	64 points

TABLE 5-3. Synthesized Results (Gate Count).

<i># of RX</i>	<i>Module</i>	<i>Gates</i>
1 RX	Channel estimation	10,976
	Matrix inverter (MI)	142,412
	Matrix multiplier (MM)	105,224
	De-mapper	1,206
	Others (control unit & buffers)	214,482
	Total	474,300
4 RX	Total	1,901,644

TABLE 5-4. Chip Summary of The 4×4 MIMO-OFDM Modem.

System	4×4 MIMO OFDM with STBC
Modulation	BPSK, QPSK, 16QAM, 64QAM
Technology	0.13- μ m 1P8M CMOS
Package	160 CQFP
Area	4.6×4.6 mm ² (Modem) 3×3.1 mm ² (FD-CE)
Gate Count	2580 K (Modem) 1901 K (FD-CE)
I/O Voltage	3.3V
System Clock	20 MHz
Core Power	82.8 mW @ 1.32V Core 62.8 mW @ 1.2V Core 43.6 mW @ 1.08V Core

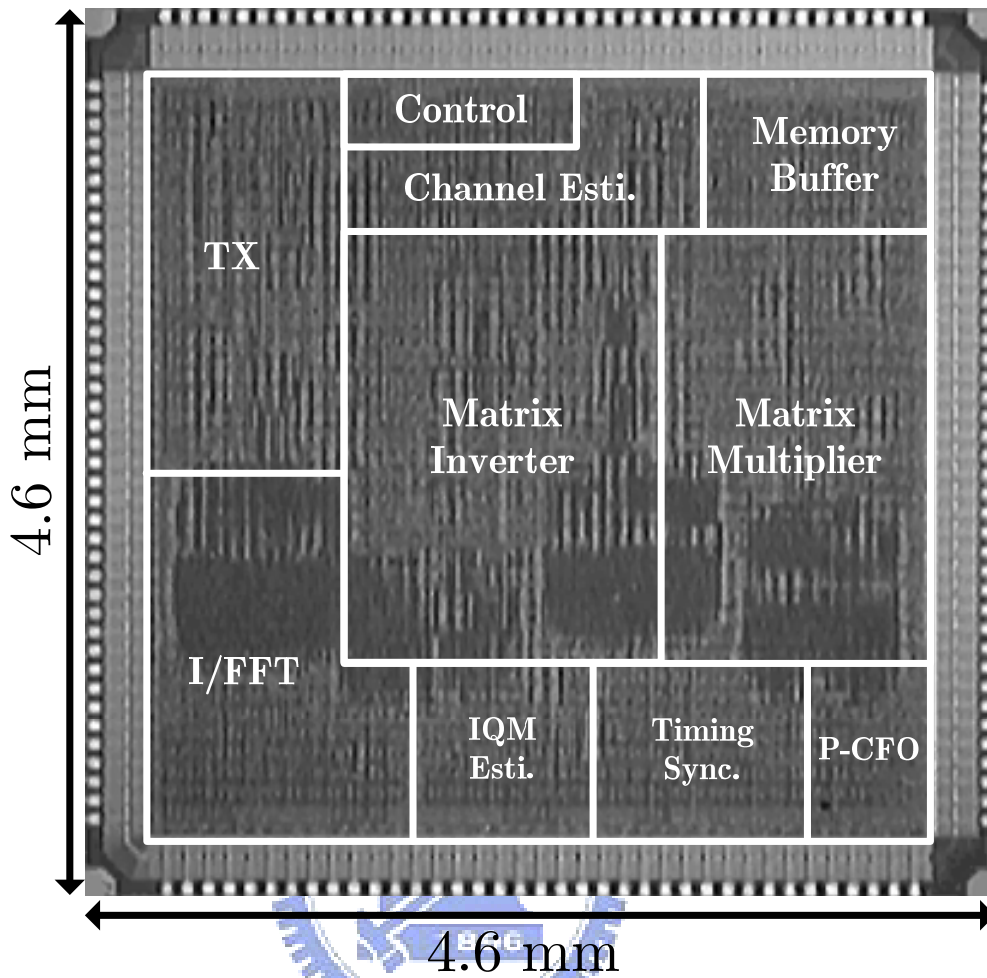


Figure 5-14. Chip microphotograph of the 4×4 MIMO-OFDM modem.

5.6 Summary


This chapter presents an adaptive FD-CE that measures channel variations and prevents performance loss in time-varying frequency-selective fading. Without both specific formats and scattered pilots, all data carriers can be utilized to ensure accurate estimation of channel variations, namely, virtual pilots. Moreover, the proposed FD-CE utilizes the property of the Alamouti-like matrix to decrease the implementation costs of complex operators. Performance evaluations indicate that the proposed FD-CE can

be widely applied in time-varying environments. Consequently, the 4×4 MIMO-OFDM modem implemented using an in-house $0.13\text{-}\mu\text{m}$ 1P8M CMOS library occupies an area of $4.6 \times 4.6 \text{ mm}^2$ and consumes about 62.8 mW at 1.2V supply voltage.



Chapter 6

Digital Beamforming



This chapter presents the digital beamforming for wireless communication systems. In communications, beamforming is used to point an antenna at the signal source to reduce interference and improve signal quality. Digital beamforming is a marriage between antenna and digital technology. In digital beamforming, the operations of phase shifting and amplitude scaling for each antenna element, and summation for receiving, are performed digitally to form the desired output. The process of digital beamforming is carried out by a digital signal processor. It is the digital signal processing capability which makes the system smart.

The rest of this chapter is organized as follows. Section 6.1 introduces the basics of digital beamforming. Section 6.2 then describes the angle-of-arrival estimation. Next, adaptive beamforming technology is presented in Section 6.3. Section 6.4 describes the digital beamforming in multiple-input multiple-output (MIMO) transmissions. Conclusions are finally drawn in Section 6.5.

6.1 The Basics of Digital Beamforming

A generic digital beamforming system is shown in Figure 6-1. This beamforming system consists of three major components: the antenna array, the beamforming unit, and the signal processing unit [77]-[78]. At the receiver part, the system consists of down-conversion chains and analog-to-digital conversion. Based on the received signal, the signal processing unit calculates the complex weights which the received signal from each antenna is multiplied with. These complex weights are adjusted until the array output matches the desired signal. These weights can also determine the array factor.

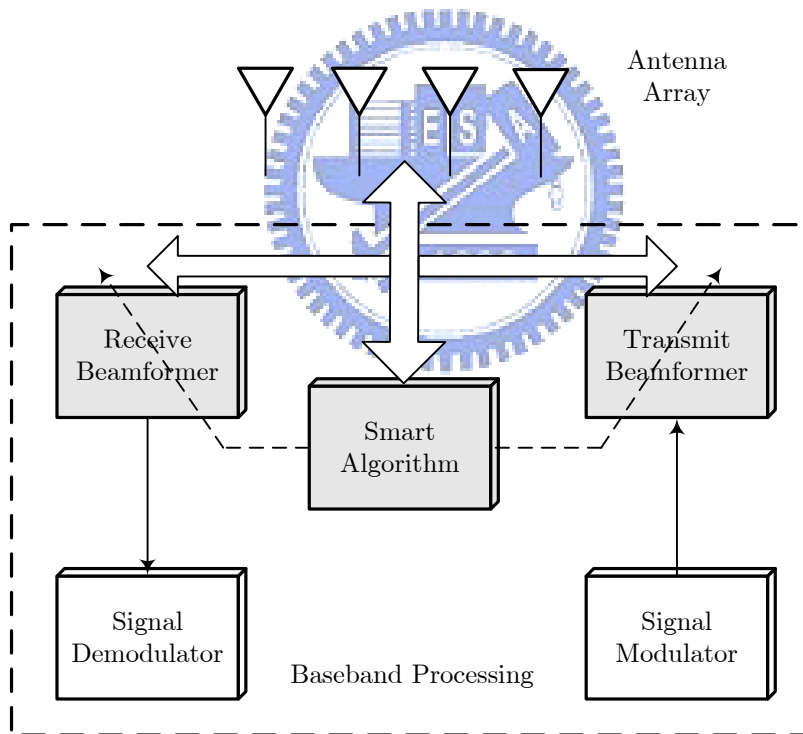


Figure 6-1. A generic digital beamforming system.

In antenna field, the principle of pattern multiplication states that the radiation pattern of an array is the product of the element pattern and the array factor. In this work, we focus on the determination of the array factor. Digital beamforming is driven by digital

processing to produce different types of beams. The procedure used for modifying the beam pattern to enhance the reception of a desired signal is illustrated by the following example. Figure 6-2 shows a two-element array for interference suppression. The most fundamental and simplest array to analyze is the two-element array. In this example, we consider a uniform linear array consisting of two identical omnidirectional antenna with $\lambda/2$ spacing, where λ denotes the wavelength corresponding to the carrier frequency.

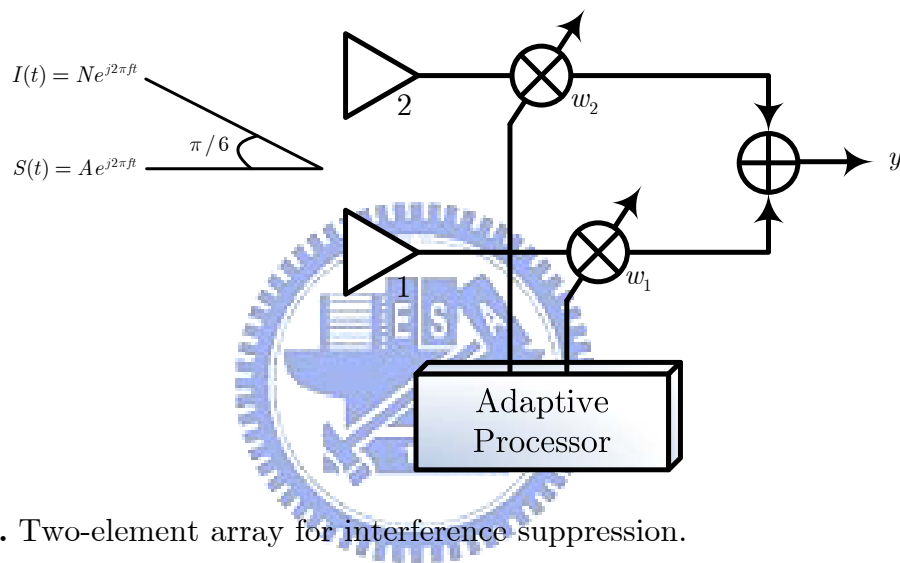


Figure 6-2. Two-element array for interference suppression.

The desired signal, $S(t)$, arrives from the boresight direction, and the interference signal, $I(t)$, arrives from the angle $\pi/6$ radians. The signal from each antenna is multiplied by a complex weight, and the weighted signals are summed to form the array output. The criterion which is applied to enhancing the desired signal and minimizing the interference signal is based on maximizing the signal-to-interference ratio (SIR) [78]-[79]. The array output due to the desired signal is

$$y_S(t) = Ae^{j2\pi ft}(w_1 + w_2) \quad (6.1)$$

For $y_s(t)$ to be equal to $S(t)$, it is necessary that

$$\begin{cases} \text{Re}[w_1] + \text{Re}[w_2] = 1 \\ \text{Im}[w_1] + \text{Im}[w_2] = 0 \end{cases} \quad (6.2)$$

The interference signal arrives at antenna 2 with a phase lead with respect to antenna 1 of value $\pi/2$. The array output due to the interference signal is

$$\begin{aligned} y_I(t) &= Ne^{j2\pi ft}w_1 + Ne^{j(2\pi ft + \pi/2)}w_2 \\ &= Ne^{j2\pi ft}w_1 + j \cdot Ne^{j2\pi ft}w_2 \end{aligned} \quad (6.3)$$

For the interference to be zero, it is necessary that

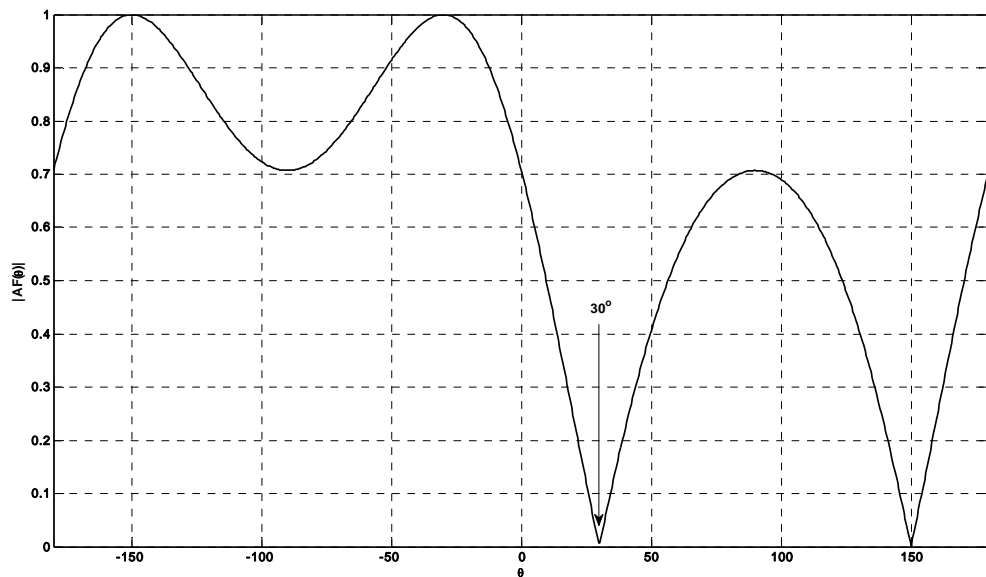
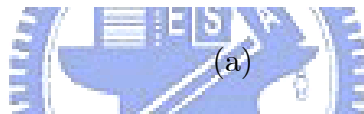
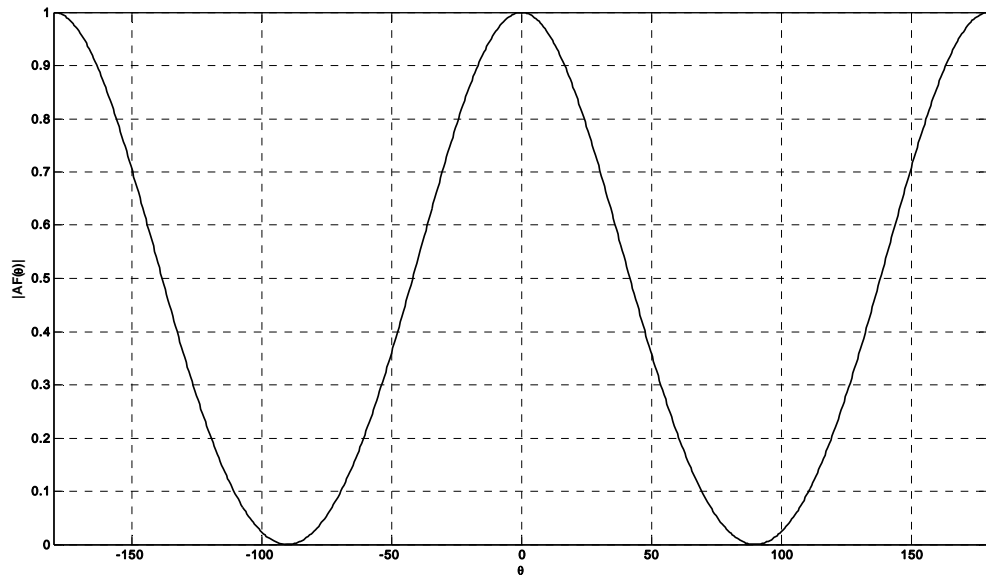
$$\begin{cases} \text{Re}[w_1] + \text{Re}[jw_2] = 0 \\ \text{Im}[w_1] + \text{Im}[jw_2] = 0 \end{cases} \quad (6.4)$$

From (6.2) and (6.4), the necessary weights can be calculated to be

$$\begin{cases} w_1 = 0.5 - 0.5j \\ w_2 = 0.5 + 0.5j \end{cases} \quad (6.5)$$

Figure 6-3(a) shows the array factor for a two-element antenna array without any weighting in the pattern forming network. Figure 6-3(b) shows the array factor for a two-element antenna array when the weights of (6.5) are applied in the pattern forming network. It is clear that now a null is placed exactly at an azimuth of 30° , the direction of the interference signal. In fact, one can change the weighting vector to point the

beam in any wanted direction. Therefore, the flexibility of digital beamforming allows the implementation of adaptive beamforming.



(b)

Figure 6-3. (a) Array factor for a non-weighted two-element array. (b) Array factor for a weighted two-element array.

6.2 Angle-of-Arrival Estimation

If several transmitters are operating simultaneously, each transmitter can create many multipath components at the receiver. Therefore, it is important for a receive array to be able to estimate the angles of arrival in order to resolve which emitters are present and what are their possible angular locations. This information can be used to eliminate or combine signals. Angle-of-arrival (AOA) estimation is also known as spectral estimation, direction-of-arrival (DOA) estimation. The goal of AOA estimation techniques is to define a function that gives an indication of the angles of arrival. This function is traditionally called the pseudospectrum. There are several approaches to defining the pseudospectrum via beamforming, the array correlation matrix, eigenanalysis, linear prediction, minimum variance, maximum likelihood, minimum-norm, and MUSIC [80]-[84]. In this section, we will discuss Capon and MUSIC pseudospectrum solutions.

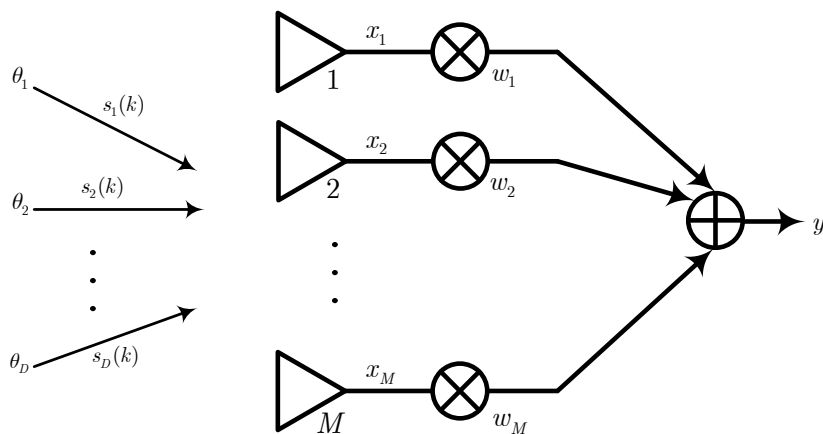
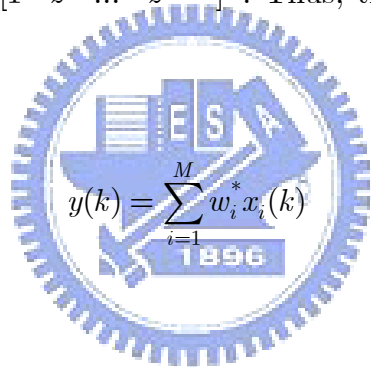


Figure 6-4. M -element array with arriving signals.

Many of the AOA algorithms rely on the array correlation matrix [78]. Figure 6-4 shows D signals arriving from D directions. These signals are received by an M -element array with M complex weights. Time is represented by the k th time sample. Each received signal includes AWGN. Let $\mathbf{a}(\theta)$ denote the array vector for an M -element linear array

$$\mathbf{a}(\theta) = \begin{bmatrix} 1 & e^{j\frac{2\pi}{\lambda}d \sin \theta} & \dots & e^{j\frac{2\pi}{\lambda}(M-1)d \sin \theta} \end{bmatrix}^T \quad (6.6)$$

where d denotes the element spacing. The vector $\mathbf{a}(\theta)$ is a Vandermonde vector because it is in the form $[1 \ z \ \dots \ z^{M-1}]^T$. Thus, the array output y is given in the following form



$$y(k) = \sum_{i=1}^M w_i^* x_i(k) \quad (6.7)$$

In vector form, (6.7) can be written as

$$y(k) = \mathbf{w}^H \mathbf{x}(k) \quad (6.8)$$

where the superscript H denotes Hermitian matrix operation and

$$\begin{aligned}
\mathbf{w} &= [w_1 \quad w_2 \quad \dots \quad w_M]^T \\
\mathbf{x}(k) &= \begin{bmatrix} \mathbf{a}(\theta_1) & \mathbf{a}(\theta_2) & \dots & \mathbf{a}(\theta_D) \end{bmatrix} \begin{bmatrix} s_1(k) \\ s_2(k) \\ \vdots \\ s_D(k) \end{bmatrix} + \mathbf{n}(k) \\
&= \mathbf{A}\mathbf{s}(k) + \mathbf{n}(k)
\end{aligned} \tag{6.9}$$

Thus, the array correlation matrix \mathbf{R}_{xx} is

$$\begin{aligned}
\mathbf{R}_{xx} &= \mathbf{E}[\mathbf{x} \cdot \mathbf{x}^H] \\
&= \mathbf{E}[(\mathbf{A}\mathbf{s} + \mathbf{n}) \cdot (\mathbf{s}^H \mathbf{A}^H + \mathbf{n}^H)] \\
&= \mathbf{A}\mathbf{E}[\mathbf{s} \cdot \mathbf{s}^H] \mathbf{A}^H + \mathbf{E}[\mathbf{n} \cdot \mathbf{n}^H] \\
&= \mathbf{A}\mathbf{R}_{ss} \mathbf{A}^H + \mathbf{R}_{nn}
\end{aligned} \tag{6.10}$$

The array correlation matrix \mathbf{R}_{xx} and the source correlation matrix \mathbf{R}_{ss} are calculated by the expected value of the respective absolute values squared.

6.2.1 Capon AOA Estimate

The Capon AOA estimate is also known as the minimum variance distortionless response. The Capon AOA estimate is a maximum likelihood estimate of the power arriving from one direction while all other sources are considered as interference. In this method, the array output power is minimized with the constraint that the gain in the desired direction $\mathbf{a}(\theta)$ remains unity. This constrained quadratic problem can be expressed as

$$\min_{\mathbf{w}} \mathbf{w}^H \mathbf{R}_{xx} \mathbf{w} \quad \text{subject to } \mathbf{w}^H \mathbf{a}(\theta) = 1 \quad (6.11)$$

Solving this constraint optimization problem, the array weights are given by [81]

$$\mathbf{w} = \frac{\mathbf{R}_{xx}^{-1} \mathbf{a}(\theta)}{\mathbf{a}^H(\theta) \mathbf{R}_{xx}^{-1} \mathbf{a}(\theta)} \quad (6.12)$$

Substituting the weights of (6.12) into the array of Figure 6-4, the pseudospectrum is then given by

$$P_{\text{Capon}}(\theta) = \frac{1}{\mathbf{a}^H(\theta) \mathbf{R}_{xx}^{-1} \mathbf{a}(\theta)} \quad (6.13)$$

The estimate of the desired direction of arrival is the angle θ that corresponds to the peak value in the pseudospectrum.

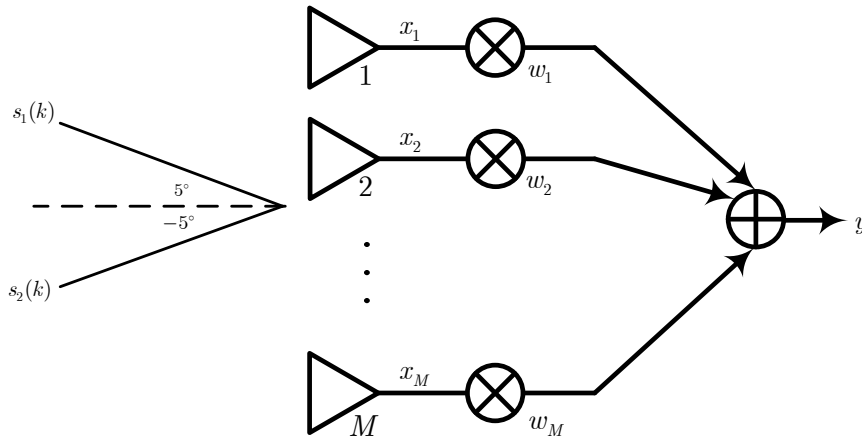


Figure 6-5. M -element array with two arriving signals.

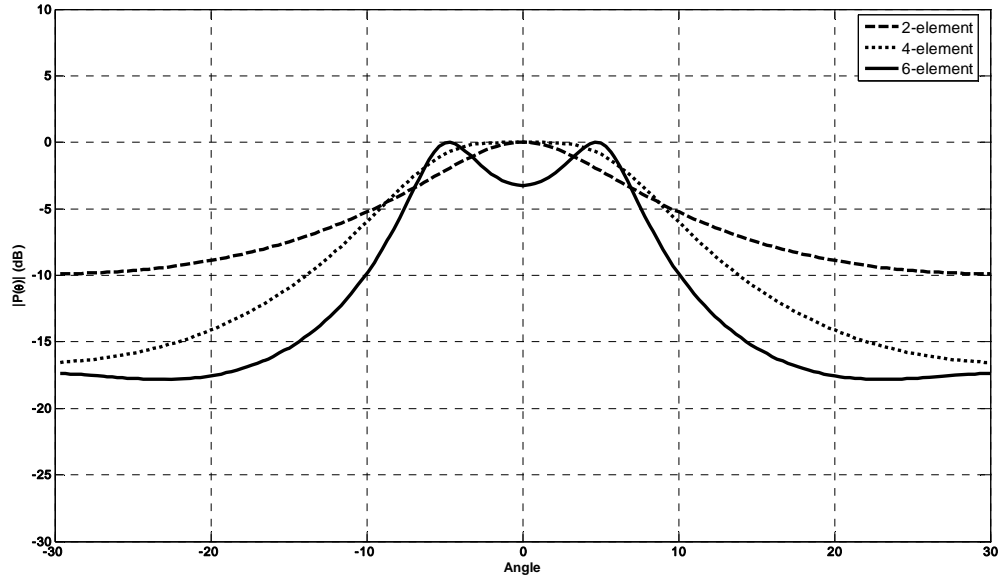


Figure 6-6. Capon pseudospectrum.

Figure 6-5 shows an M -element array with $\lambda/2$ element spacing. The signals are assumed to be uncorrelated and equal amplitude. The arrival angles are $\pm 5^\circ$ and the AWGN variance is 0.1. From the information, the following parameters are obtained [78]

$$\begin{aligned}
 \mathbf{s} &= \begin{bmatrix} 1 \\ 1 \end{bmatrix} \\
 \mathbf{a}(\theta) &= \begin{bmatrix} 1 & e^{j\pi \sin \theta} \end{bmatrix}^T \\
 \mathbf{A} &= \begin{bmatrix} \mathbf{a}(\theta_{5^\circ}) & \mathbf{a}(\theta_{-5^\circ}) \end{bmatrix} \\
 \mathbf{R}_{ss} &= \begin{bmatrix} 1 & 0 \\ 0 & 1 \end{bmatrix}
 \end{aligned} \tag{6.14}$$

Applying (6.10) we can find \mathbf{R}_{xx} for both sets of angles. Substituting \mathbf{R}_{ss} into (6.13), we can plot the pseudospectrum as shown in Figure 6-6. It is clear that the two sources are not resolvable if a two-element antenna array is used. However, the Capon AOA

estimate can resolve these two sources if a six-element antenna array is used. The reason is that the ability to resolve angles is limited by the array half-power beamwidth. In order to increase the resolution, a larger array is thus required.

6.2.2 MUSIC AOA Estimate

MUSIC is an acronym which stands for *multiple signal classification*. The MUSIC algorithm was developed by Schmidt [85] by noting that the desired signal array response is orthogonal to the noise subspace. The signal and noise subspaces are first identified using decomposition of the array correlation matrix. The eigenvalues and eigenvectors of \mathbf{R}_{xx} can be calculated. We then produce D signal eigenvectors and $(M - D)$ noise eigenvectors. The eigenvalues and eigenvectors are sorted from the least to the greatest. The $M \times (M - D)$ dimensional subspace spanned by the noise eigenvectors is then given by

$$\mathbf{E}_N = [\mathbf{e}_1 \quad \mathbf{e}_2 \quad \dots \quad \mathbf{e}_{M-D}] \quad (6.15)$$

Once the subspaces are determined, the MUSIC pseudospectrum is given by [85]

$$P_{MUSIC}(\theta) = \frac{\mathbf{a}^H(\theta)\mathbf{a}(\theta)}{\mathbf{a}^H(\theta)\mathbf{E}_N\mathbf{E}_N^H\mathbf{a}(\theta)} \quad (6.16)$$

Because the desired array response vectors \mathbf{A} are orthogonal to the noise subspace, the peaks in the MUSIC spatial spectrum represent the AOA estimates for the desired signals. One can show that the Euclidean distance $\mathbf{a}^H(\theta)\mathbf{E}_N\mathbf{E}_N^H\mathbf{a}(\theta) = 0$ for each arrival

angle. Placing this distance expression in the denominator creates sharp peaks at the angles of arrival.

Assume that there is a 6-element antenna array with $\lambda/2$ element spacing. The signals are assumed to be uncorrelated and equal amplitude. The arrival angles are $\pm 5^\circ$ and the AWGN variance is 0.1. From the information, the following parameters are obtained [78]

$$\begin{aligned}\lambda_1 &= \lambda_2 = \lambda_3 = \lambda_4 = 0.1 \\ \lambda_5 &= 2.95 \\ \lambda_6 &= 9.25\end{aligned}\tag{6.17}$$

The subspace created by four noise eigenvectors is given by

$$\mathbf{E}_N = \begin{bmatrix} 0.017 & -0.66 & -0.076 & 0.092 \\ -0.33 & 0.47 & -0.29 & -0.53 \\ 0.032 & 0.24 & 0.82 & 0.19 \\ 0.14 & 0.23 & -0.48 & 0.69 \\ 0.68 & -0.2 & -0.055 & -0.45 \\ -0.64 & -0.42 & 0.03 & -0.041 \end{bmatrix}\tag{6.18}$$

Applying this information to (6.16), we can plot the pseudospectrum as shown in Figure 6-7. From Figure 6-7, it is clear that MUSIC AOA estimate has better resolution than Capon AOA estimate. The price of increased resolution comes at the cost of greater computational complexity.

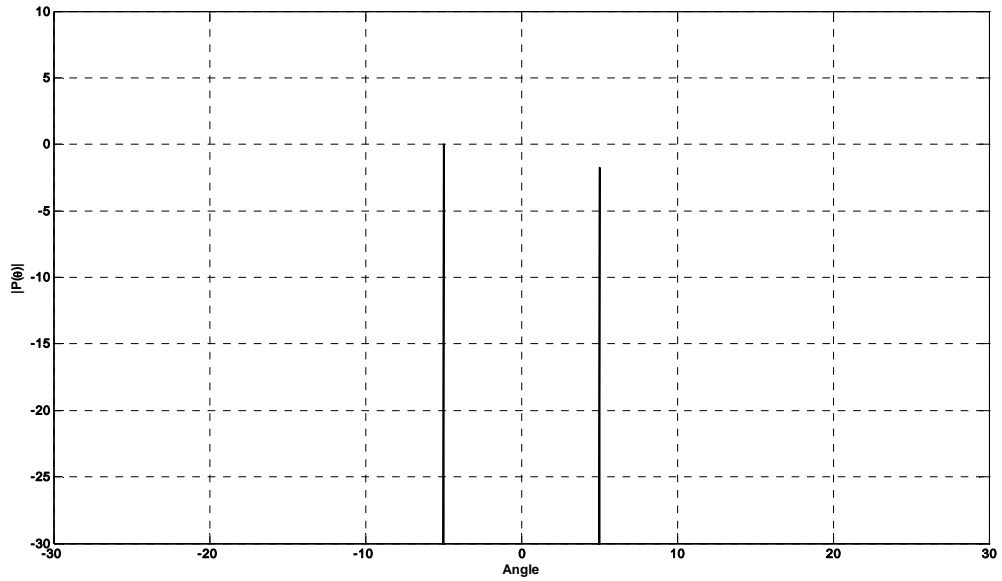
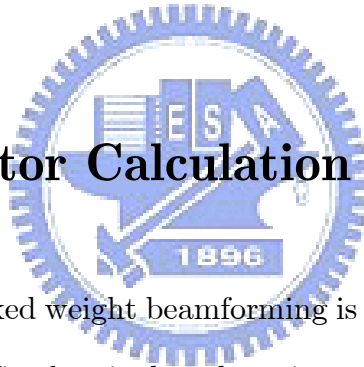


Figure 6-7. MUSIC pseudospectrum.

6.3 Array Factor Calculation



In previous sections, the fixed weight beamforming is presented. The fixed beamforming approaches are applied to fixed arrival angle emitters. If the arrival angles don't change with time, the optimum array weights won't need to be adjusted. However, in mobile wireless communications, the desired arrival angles can change with time. The receiver must allow for the continuous adaptation to an ever-changing environment.

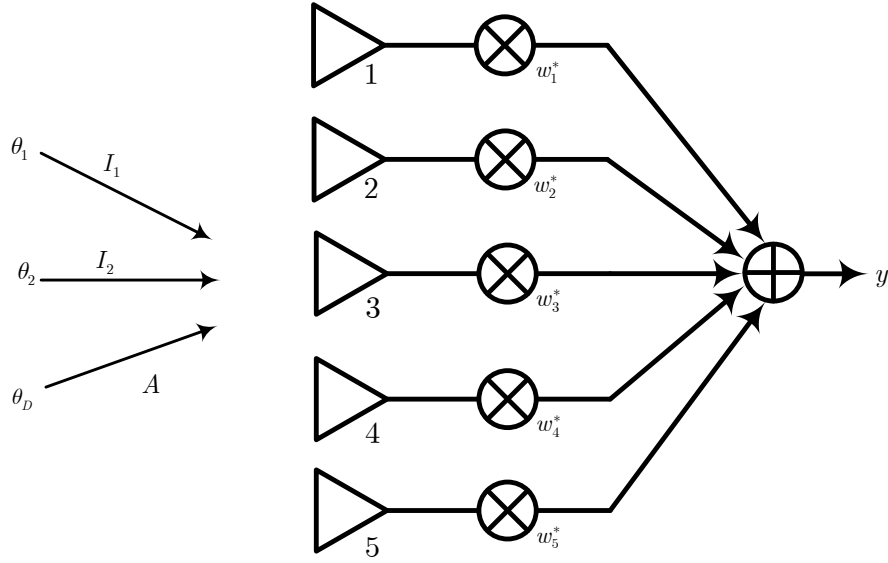


Figure 6-8. Five-element antenna array.

Let assume a five-element antenna array with one desired signal and two unwanted interferences, as shown in Figure 6-8. The element spacing is $\lambda/2$. The array vector is given by

$$\mathbf{a}(\theta) = \begin{bmatrix} e^{-j2\pi \sin \theta} & e^{-j\pi \sin \theta} & 1 & e^{j\pi \sin \theta} & e^{j2\pi \sin \theta} \end{bmatrix}^T \quad (6.19)$$

Therefore, the total array output is given as

$$\begin{aligned} y = & w_1^* \cdot A e^{-j2\pi \sin \theta_D} + w_2^* \cdot A e^{-j\pi \sin \theta_D} + w_3^* \cdot A + w_4^* \cdot A e^{j\pi \sin \theta_D} + w_5^* \cdot A e^{j2\pi \sin \theta_D} \\ & + w_1^* \cdot I_1 e^{-j2\pi \sin \theta_1} + w_2^* \cdot I_1 e^{-j\pi \sin \theta_1} + w_3^* \cdot I_1 + w_4^* \cdot I_1 e^{j\pi \sin \theta_1} + w_5^* \cdot I_1 e^{j2\pi \sin \theta_1} \\ & + w_1^* \cdot I_2 e^{-j2\pi \sin \theta_2} + w_2^* \cdot I_2 e^{-j\pi \sin \theta_2} + w_3^* \cdot I_2 + w_4^* \cdot I_2 e^{j\pi \sin \theta_2} + w_5^* \cdot I_2 e^{j2\pi \sin \theta_2} \end{aligned} \quad (6.20)$$

In matrix form, (6.20) can be written as

$$\begin{aligned}
y &= \begin{bmatrix} w_1^* & w_2^* & w_3^* & w_4^* & w_5^* \end{bmatrix} \begin{bmatrix} e^{-j2\pi \sin \theta_D} & e^{-j2\pi \sin \theta_1} & e^{-j2\pi \sin \theta_2} \\ e^{-j\pi \sin \theta_D} & e^{-j\pi \sin \theta_1} & e^{-j\pi \sin \theta_2} \\ 1 & 1 & 1 \\ e^{j\pi \sin \theta_D} & e^{j\pi \sin \theta_1} & e^{j\pi \sin \theta_2} \\ e^{j2\pi \sin \theta_D} & e^{j2\pi \sin \theta_1} & e^{j2\pi \sin \theta_2} \end{bmatrix} \begin{bmatrix} A \\ I_1 \\ I_2 \end{bmatrix} \\
&= \mathbf{w}^H \mathbf{A} \mathbf{s}
\end{aligned} \tag{6.21}$$

For the interference to be zero, it is necessary that

$$\begin{aligned}
\mathbf{w}^H \mathbf{A} &= [1 \ 0 \ 0] \\
&= \mathbf{u}_1
\end{aligned} \tag{6.22}$$

Therefore the required complex weight is [86]-[87]

$$\mathbf{w}^H = \mathbf{u}_1 \cdot \mathbf{A}^H (\mathbf{A} \mathbf{A}^H + \eta \mathbf{I})^{-1} \tag{6.23}$$

where \mathbf{I} denotes the identity matrix and η is a particular number. If the matrix inversion is singular, the particular number can be used to calculate a approximate solution. As an example, the desired signal is arriving from $\theta_D = 0^\circ$ while $\theta_1 = -15^\circ$ and $\theta_2 = 25^\circ$. If the particular number is 0.001, the necessary weights are calculated to be

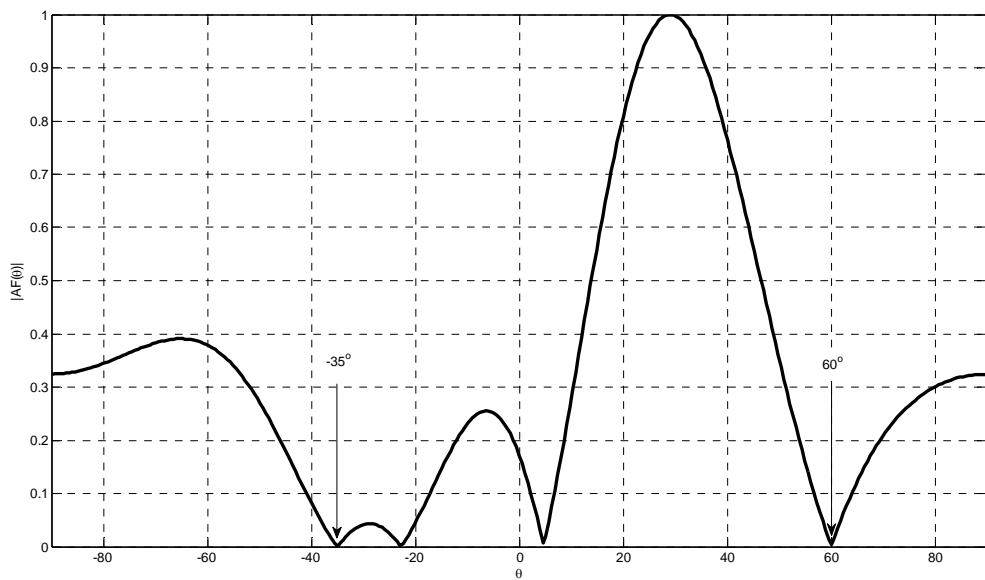
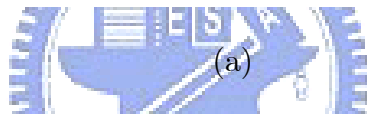
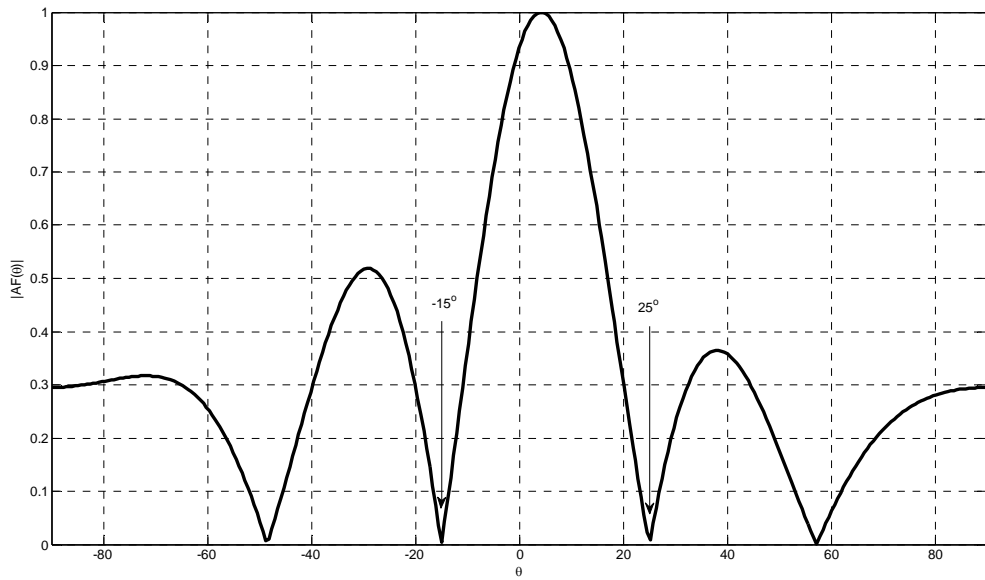
$$\mathbf{w}^H = \begin{bmatrix} 0.26 - 0.11j \\ 0.17 - 0.08j \\ 0.13 \\ 0.17 + 0.08j \\ 0.26 + 0.11j \end{bmatrix}^T \tag{6.24}$$

If the desired signal is arriving from $\theta_D = 30^\circ$ while $\theta_1 = -35^\circ$ and $\theta_2 = 60^\circ$, the necessary weights are calculated to be

$$\mathbf{w}^H = \begin{bmatrix} -0.19 \\ 0.04 - 0.24j \\ 0.14 \\ 0.04 + 0.24j \\ -0.19 \end{bmatrix}^T \quad (6.25)$$

The corresponding array factor is plotted in Figure 6-9. In order to make it better, a possible scheme is to make the choices of the weighting vectors adaptive. In adaptive processing, there are many existing adaptive algorithms, such as least mean-square algorithm, recursive least-square algorithm, etc. Different adaptive algorithms result in different convergence speed and computational complexity [88].

In previous discussion, we have showed that how to calculate the complex weight, w_i . However, the computational complexity could be very high if the number of antennas is increased. In fact, there are some simple weight functions. A two-element uniform linear array and a four-element uniform linear array with $\lambda/2$ element spacing are considered as examples. The weight vectors for the two-element uniform linear array and the four-element uniform linear array are shown in TABLE 6-1 and TABLE 6-2, respectively. The corresponding array factors are shown in Figure 6-10 and Figure 6-11, respectively. Note that the plots have been normalized so that the peak of the radiation pattern is equal to one.



(b)

Figure 6-9. (a) Array factor for $\theta_D = 0^\circ$. (b) Array factor for $\theta_D = 30^\circ$.

TABLE 6-1. Weight Vectors for the Two-Element Array.

	<i>Antenna No.</i>		<i>Mainlobe Angle</i>
	<i>1</i>	<i>2</i>	
Case 1	+1	+1	0°
Case 2	+1	-1	90°

TABLE 6-2. Weight Vectors for the Four-Element Array.

	<i>Antenna No.</i>				<i>Mainlobe Angle</i>
	<i>1</i>	<i>2</i>	<i>3</i>	<i>4</i>	
Case 1	+1	+1	+1	+1	0°
Case 2	+1	-1	+1	-1	90°
Case 3	+1	-j	-1	+j	-30°
Case 4	+1	+j	-1	-j	30°

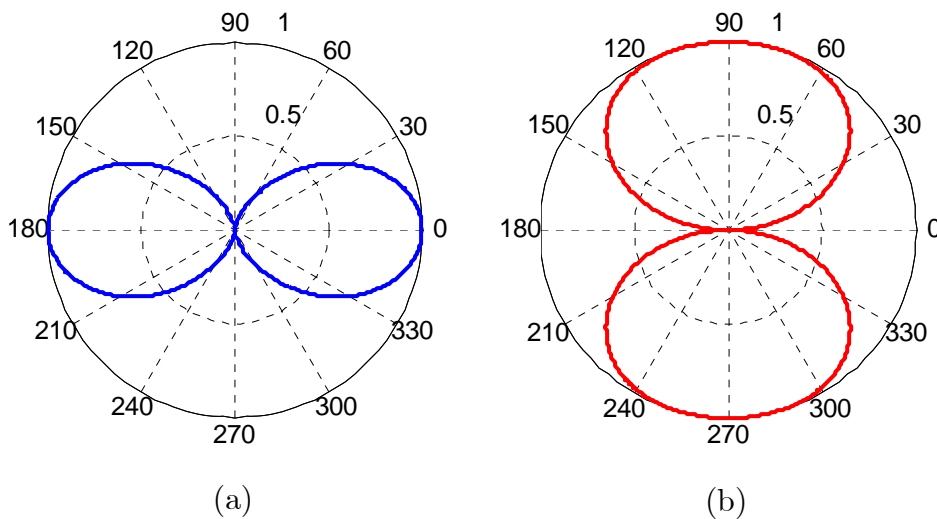


Figure 6-10. Corresponding array factors. (a) Weight vector = $[+1 +1]$. (b) Weight vector = $[+1 -1]$.

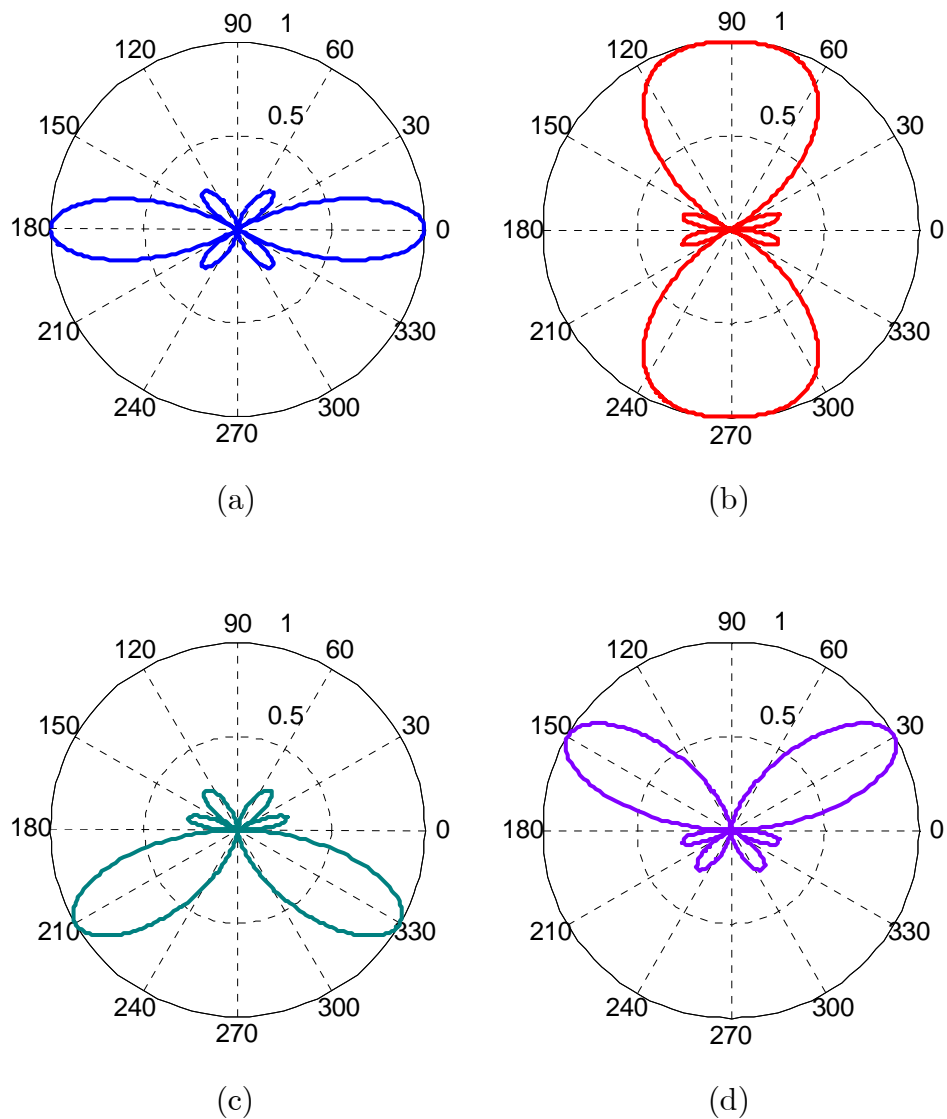


Figure 6-11. Corresponding array factors. (a) Weight vector = $[+1 +1 +1 +1]$. (b) Weight vector = $[+1 -1 +1 -1]$. (c) Weight vector = $[+1 -j -1 +j]$. (d) Weight vector = $[+1 +j -1 -j]$.

From TABLE 6-1, the case 1 gives uniform weighting to the array. The resulting pattern is shown in Figure 6-10(a). Other cases for the two-element uniform linear array and the four-element uniform linear array are shown in Figure 6-10 and Figure 6-11, respectively. In order to reduce the computational complexity, the simple weight functions could be applied in some conditions. Sidelobes could be controlled to some

extent by employing weight functions. These weight functions are observed in terms of mainlobe beamwidth, mainlobe angle, and sidelobe level.

6.4 Digital Beamforming in MIMO Transmission

In previous section, we have assumed that there is only one signal of interest. It has been shown that the signals from each antenna element are multiplied by a complex weight and summed to form the array output. In fact, there are more than one signals of interest in MIMO WLAN. In addition, the channel status in MIMO WLAM is complex. Under this condition, it is difficult to find a unique weight vector to form the desired output.

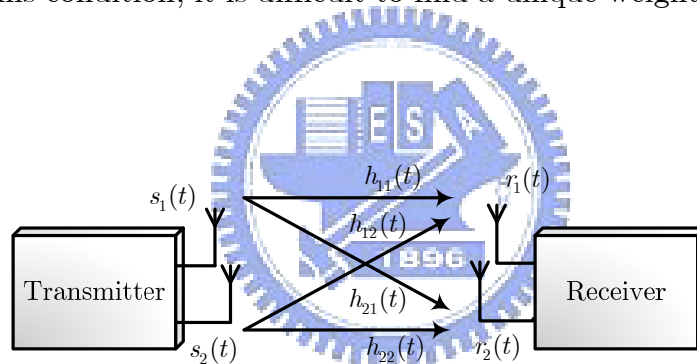


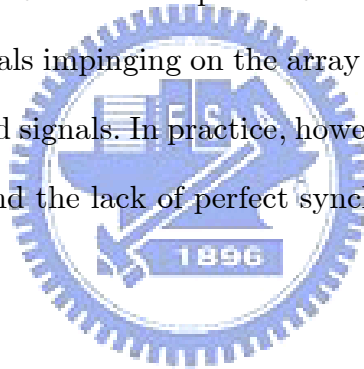
Figure 6-12. 2×2 MIMO WLAN system.

A 2×2 MIMO WLAN system is depicted in Figure 6-12. Each antenna at the transmitter transmits a different data stream. At the receiver part, the received signal is expressed as

$$\begin{aligned} r_1(t) &= h_{11}(t) \otimes s_1(t) + h_{12}(t) \otimes s_2(t) \\ r_2(t) &= h_{21}(t) \otimes s_1(t) + h_{22}(t) \otimes s_2(t) \end{aligned} \quad (6.26)$$

where “ \otimes ” denotes the convolution operator. From (6.26), it is difficult to find an

optimum weighting function to attain the desired output $s_1(t)$ and $s_2(t)$ simultaneously. In practical applications, the channel status can also change with time. Figure 6-13 shows the channel with angle-time pattern. From Figure 6-13, the channel pattern could be time-varying and the arrival time of desired signals may also be different. In order to overcome this situation, a potential solution is to augment the simple linear combiner with space-time architecture shown in Figure 6-14. In Figure 6-14, each receiver antenna's output is applied to a finite impulse filter. The filter outputs are summed to produce the desired signal. If there is no temporal filter, the space-time beamforming architecture is reduced to the linear combiner architecture. The filter bank-based beamforming can accept the outputs of N antenna elements and coherently combine them to a desired output. In addition, the weighting functions could null out the undesired signals impinging on the array and it could equalize the effects of propagation on the received signals. In practice, however, such joint reduction is limited by the presence of noise and the lack of perfect synchronization.



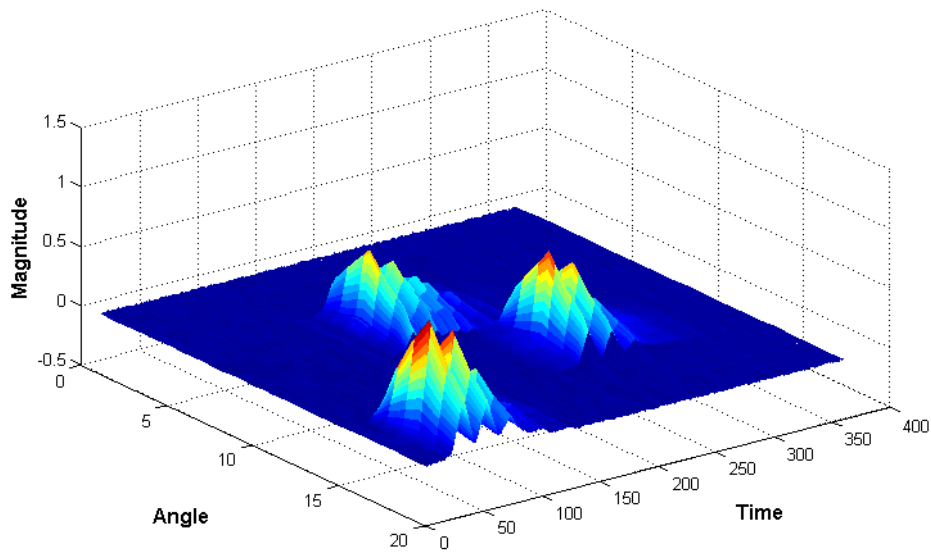


Figure 6-13. Channel with angle-time pattern.

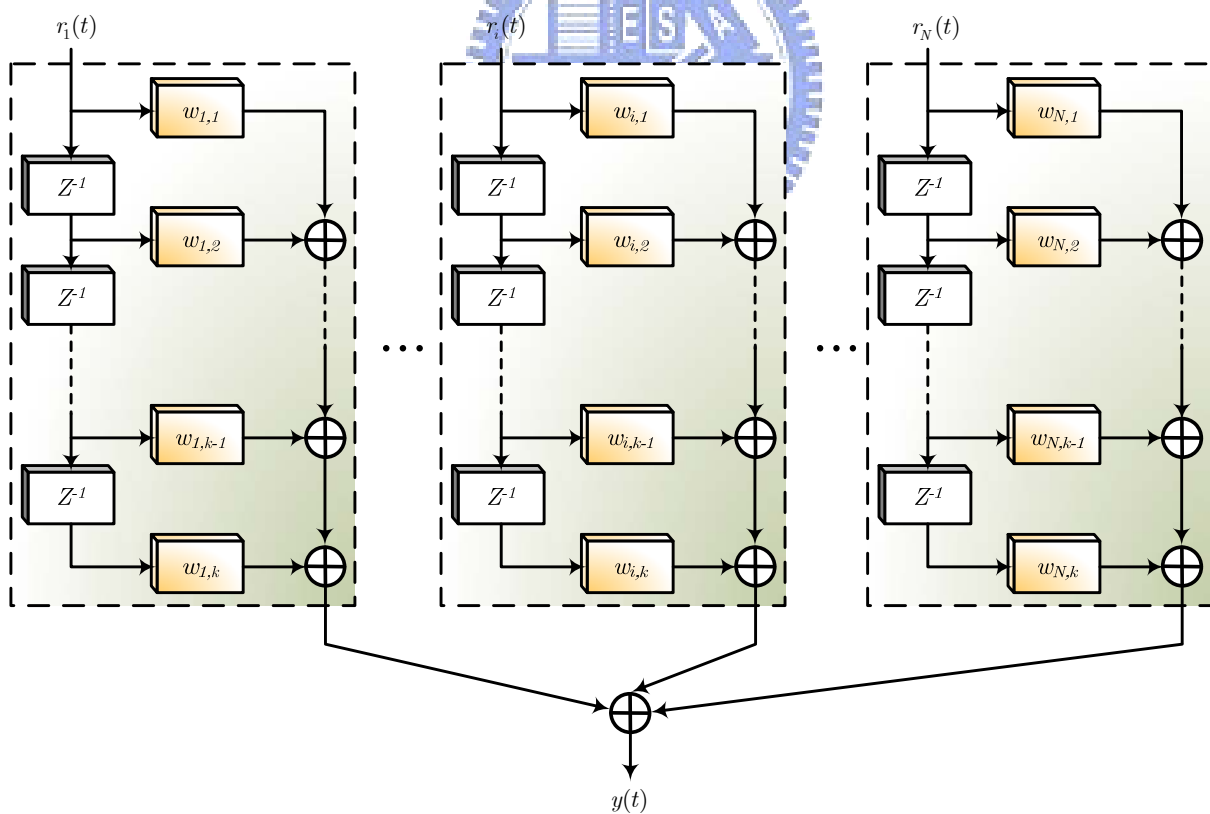


Figure 6-14. Space-time beamforming architecture.

6.5 Summary

This chapter presents the digital beamforming technology in wireless communication systems. Digital beamforming technology has numerous benefits in wireless communications. In wireless communications, digital beamforming can improve the signal-to-noise ratio and provide higher system capacity. Digital beamforming can be interpreted as linear filtering in the spatial domain. In mobile communications, digital beamforming technology has the potential for tracking the location of a particular mobile user. In addition, digital beamforming technology can also null multipath signals. This can dramatically reduce fading in the received signal.





Chapter 7

Conclusion

The research on multi-input multi-output (MIMO) orthogonal frequency-division multiplexing (OFDM) systems is presented in this dissertation. We investigate the carrier frequency offset (CFO) estimation, I/Q mismatch (IQ-M) estimation, adaptive channel estimation, and digital beamforming.

7.1 Summary

In this work, a 4×4 MIMO-OFDM communication system is implemented. For the frequency synchronization in the MIMO-OFDM system, a pseudo CFO (P-CFO) algorithm is developed to estimate the CFO value under the condition of IQ-M in direct-conversion OFDM receivers. The proposed synchronization algorithm is suitable for application-specific integrated circuit (ASIC) implementation. The proposed algorithm adopts three short training symbols to estimate the frequency offset from

−50 ppm to +50 ppm under a 2.4 GHz carrier frequency with 2 dB gain error and 20 degree phase error in frequency-selective channels. Simulation results indicate that the average estimation error of the proposed P-CFO algorithm can fulfill many system requirements, preventing obvious performance loss under different IQ-M conditions. The proposed design is implemented in a chip with $3.3 \times 0.4 \text{ mm}^2$ core area and 10 mW power dissipation at 54 Mbits/s data rate. Hence, the proposed algorithm can enhance the performance of wireless OFDM systems, enabling low-cost systems to be achieved.

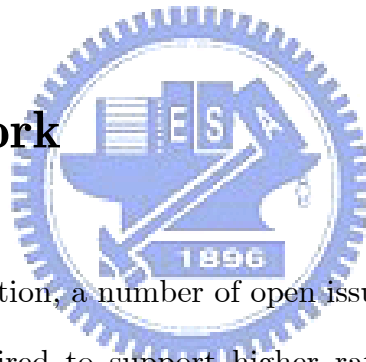
Direct-conversion architecture is one potential candidate for simple integration among different architectures. However, direct-conversion receivers suffer from mismatch between the I and Q channels, e.g., IQ-M. In order to combat IQ-M with CFO in direct-conversion receivers, preamble-assisted methods are developed. IQ-M with CFO can be estimated by taking advantage of the relationship between desired sub-carriers and image sub-carriers. Moreover, the proposed IQ-M estimator can estimate not only constant IQ-M but also frequency-dependent IQ-M. Both simulation and experiment results indicate that the proposed method can meet system requirements to prevent from an obvious performance loss under the condition of IQ-M. Furthermore, the proposed method is compatible with current wireless standards because it does not require special packet formats.

In order to realize the gain obtained from MIMO channels, an adaptive frequency-domain channel estimator (FD-CE) is developed. The proposed adaptive FD-CE ensures the channel estimation accuracy in each set of four MIMO-OFDM symbols. Without both specific formats and scattered pilots, all data carriers can be utilized to ensure accurate estimation of channel variations, namely, virtual pilots. Moreover, the proposed channel estimator utilizes the property of the Alamouti-like matrix to decrease the implementation costs of complex operators. Performance

evaluations indicate that the proposed FD-CE can be widely applied in time-varying environments. Consequently, the 4×4 MIMO-OFDM modem implemented using an in-house 0.13- μm 1P8M CMOS library occupies an area of $4.6 \times 4.6 \text{ mm}^2$ and consumes about 62.8 mW at 1.2V supply voltage.

Digital beamforming technology uses sophisticated signal processing techniques to manipulate signals at the transmitter or receiver and dynamically control transmission and reception. Using digital beamforming technology, radio transmission and reception is optimized by selectively amplifying signals to and from users of interest and rejecting unwanted signals. This mainly increases the signal quality and suppresses and mitigates interference, resulting in increased coverage and system capacity.

7.2 Future Work



At the end of this dissertation, a number of open issues are discussed. Next-generation wireless systems are required to support higher rates, better reliability, and higher mobility while targeting lower cost, lower power consumption, and higher levels of integration [89]. In order to support higher data rate, the trend is to operate at higher carrier frequencies and use higher-order signal constellations which are more sensitive to analog front-end impairments. In this study, we have studied joint effects of IQ-M and CFO. However, there are other issues, such as dynamic acquisition errors of analog-to-digital convertors and amplifier nonlinearity, which could be handled in the digital domain. It is worthy of developing smart signal processing for analog front-end impairments.

Due to the development of new wireless technologies and the improvement of existing ones, the number of users, the demand for spectrum efficiency, and the demand

for higher data rate are increasing. However, the spread of the technology brings different interference sources or jamming [90], [91]. Interference or jamming can interfere with others' radio and degrade the communication quality. In order to minimize the jamming level and recover the transmitted signal, an appropriate anti-jamming scheme must be applied.

In practice, a communication system can be modeled by a layered approach, such as physical layer and medium access control (MAC), where each layer has a specific role. The role of the physical layer is to deliver information bits across a wireless channel in an efficient and reliable manner given a limited bandwidth or transmit power. On the one hand, the MAC layer is responsible for the resource management among multiple users. In traditional designs, there is no cross-optimization across layers. However, optimizing the individual layer is not always the best approach from a system performance perspective. In order to achieve cross-layer optimization, an adaptive cross-layer approach is thus required [92].

With the rapid evolution of wireless standards and increasing demand for multi-standard products, the need for flexible baseband solutions is growing. Efficiently programmable baseband processors are important for multi-standard radio platforms and software defined radio systems. In order to save development cost and silicon area for multi-standard systems, novel baseband processing and efficient VLSI architecture are worthy of developing.

In addition, mobile communications have evolved rapidly in recent years. The existing 3G standard, universal mobile telecommunication system (UMTS), is currently being upgraded with high speed packet access. The 3rd Generation Partnership Project (3GPP) has investigated the long term evolution (LTE) of UMTS to meet future demands. In LTE, it will introduce new access schemes on the air interface, e.g., orthogonal frequency-division multiple access (OFDMA) in downlink and single

carrier – frequency division multiple access (SC-FDMA) in uplink. LTE will also use MIMO to support peak data rates of 100 Mbps in downlink and 50 Mbps in uplink within a 20 MHz spectrum with two receive antennas and one transmit antenna at the user equipment. Hence, LTE is going to be a promising research issue.





References

- [1] 3GPP TR 25.814, 3rd Generation Partnership Project; Technical Specification Group Radio Access Network; Physical Layer Aspects for Evolved Universal Terrestrial Radio Access (UTRA), 2006.
- [2] IEEE P802.11n/D3.00, Wireless LAN Medium Access Control (MAC) and Physical Layer (PHY) Specifications: Amendment 4: Enhancements for Higher Throughput, 2007.
- [3] IEEE Standard 802.16e-2005. Part16: Air Interface for Fixed and Mobile Broadband Wireless Access Systems-Amendment for Physical and Medium Access Control Layers for Combined Fixed and Mobile Operation in Licensed Band, December 2005.
- [4] Wireless LAN Medium Access Control (MAC) and Physical Layer (PHY) Specifications, IEEE Std 802.11a, 1999.
- [5] Wireless LAN Medium Access Control (MAC) and Physical Layer (PHY) Specifications, IEEE Std 802.11g, 2003.
- [6] Eur. Telecommunication Standard, *Radio Broadcasting Systems: Digital Audio Broadcasting to Mobile, Portable and Fixed Receivers*, February 1995.
- [7] Eur. Telecommunication Standard, *Digital Video Broadcasting: Framing Structure, Channel Coding, and Modulation for Digital Terrestrial Television*, August 1997.
- [8] J. Mietzner, R. Schober, L. Lampe, W. H. Gerstacker, and P. A. Hoeher, “Multiple-antenna techniques for wireless communications – a comprehensive literature survey,” *IEEE Communications Surveys & Tutorials*, vol. 11, no. 2, pp. 87-105, Second Quarter 2009.
- [9] A. Goldsmith, *Wireless Communications*, Cambridge University Press, 2005.
- [10] A. J. Paulraj and B. C. Ng, “Space-time modems for wireless personal communications,” *IEEE Personal Communications Magazine*, vol. 5, pp. 36–48, February 1998.
- [11] G. J. Foschini and M. J. Gans, “On limits of wireless communications in a fading environment when using multiple antennas,” *Wireless Personal Communications*, vol. 6, pp. 311–335, 1998.

- [12] D. Gesbert, M. Shafi, D. S. Shiu, P. J. Smith and A. Naguib, "From theory to practice: an overview of MIMO space-time coded wireless systems," *IEEE Journal on Selected Areas in Communications*, vol. 21, no. 3, pp. 281–302, April 2003.
- [13] D. S. Shiu, G. J. Foschini, M. J. Gans, and J. M. Kahn, "Fading correlation and its effect on the capacity of multielement antenna system", *IEEE Transactions on Communications*, vol. 48, no. 3, pp. 502–513, March 2000.
- [14] V. Tarokh, H. Jafarkhani, and A. R. Calderbank, "Space-time block coding for wireless communications: performance results," *IEEE Journal on Selected Areas in Communications*, vol. 17, no. 3, pp. 451–460, March 1999.
- [15] V. Tarkoh, H. Jafarkhani, and A.R. Calderbank, "Space-time block codes from orthogonal designs," *IEEE Transactions on Information Theory*, vol. 45, no. 5, pp. 1456–1467, July 1999.
- [16] S. Alamouti, "A simple transmit diversity technique for wireless communications," *IEEE Journal on Selected Areas in Communications*, vol. 16, no. 8, pp. 1451–1458, October 1998.
- [17] B. Vucetic and J. Yuan, *Space-Time Coding*, Wiley, 2003.
- [18] G. Foschini, "Layered space-time architecture for wireless communication in a fading environment when using multi-element antennas," *Bell Labs Technical Journal*, pp. 41–59, Autumn 1996.
- [19] A. Burg, M. Borgmann, M. Wenk, M. Zellweger, W. Fichtner, and H. Bolcskei, "VLSI implementation of MIMO detection using the sphere decoding algorithm," *IEEE Journal of Solid-State Circuits*, vol. 40, no. 7, pp. 1566–1577, July 2005.
- [20] Z. Guo and P. Nilsson, "Algorithm and implementation of the K-best sphere decoding for MIMO detection," *IEEE Journal on Selected Areas in Communications*, vol. 24, no. 3, pp. 491–503, March 2006.
- [21] J. Heiskala and J. Terry, *OFDM Wireless LANs: A Theoretical and Practical Guide*, Sams, Indianapolis, Indiana, 2001.
- [22] S. B. Weinstein and P. M. Ebert, "Data transmission by frequency division multiplexing using the discrete Fourier transform," *IEEE Transactions on Communications*, vol. 19, no. 5, pp. 628–634, October 1971.

- [23] R. W. Chang, "Orthogonal frequency division multiplexing," *U.S. Patent* 3,488,445, filed November 1966 issued January 1970.
- [24] A. A. Abidi, "Direct-conversion radio transceivers for digital communications," *IEEE Journal of Solid-State Circuits*, vol. 30, no. 12, pp. 1399–1410, December 1995.
- [25] B. Razavi, "Design consideration for direct-conversion receivers," *IEEE Transactions on Circuits and Systems II, Analog and Digital Signal Processing*, vol. 44, no. 6, pp. 428–435, June 1997.
- [26] B. Razavi, *RF Microelectronics*. Upper Saddle River, NJ: Prentice-Hall, 1998.
- [27] F. Horlin and A. Bourdoux, *Digital Compensation for Analog Front-Ends : A New Approach to Wireless Transceiver Design*, Wiley, 2008.
- [28] P. H. Moose, "A technique for orthogonal frequency division multiplexing frequency offset correction," *IEEE Transactions on Communications*, vol. 42, no. 10, pp. 2908–2914, October 1994.
- [29] S. R. Saunders and A. A. Zavala, *Antennas and Propagation for Wireless Communication Systems*, Wiley, 2007.
- [30] J. Tubbax, A. Fort, L. Van der Perre, S. Donnay, M. Engels, and H. De Man, "Joint compensation of IQ imbalance and frequency offset in OFDM systems," in *Proceedings of IEEE GLOBECOM*, December 2003, pp. 2365–2369.
- [31] S. Fouladifard and H. Shafiee, "Frequency offset estimation in OFDM systems in the presence of IQ imbalance," in *Proceedings of IEEE International Conference on Communications*, May 2003, pp. 2071–2075.
- [32] J. C. Rudell, J. J. Ou, T. B. Cho, G. Chien, F. Brianti, J. A. Weldon, and P. R. Gray, "A 1.9 GHz wide-band IF double conversion CMOS receiver for cordless telephone applications," *IEEE Journal of Solid-State Circuits*, vol. 32, no. 12, pp. 2071–2088, December 1997.
- [33] A. Saleh, "Frequency-independent and frequency-dependent nonlinear models of TWT amplifiers," *IEEE Transactions on Communications*, vol. 29, no. 11, pp. 1715–1720, November 1981.
- [34] T. D. Chiueh and P. Y. Tsai, *OFDM Baseband Receiver Design for Wireless Communications*, Wiley, 2007.

- [35] *TGn Channel Models*, IEEE Std. 802.11-03/940r4, May 2004.
- [36] A. Saleh and R. Valenzuela, “A statistical model for indoor multipath propagation,” *IEEE Journal on Selected Areas in Communications*, vol. 5, no. 2, pp. 138–146, February 1987.
- [37] T. S. Rappaport, *Wireless Communications: Principles and Practice*, NJ: Prentice-Hall, 2002.
- [38] T. Paul and T. Ogunfunmi, “Wireless LAN comes of age: understanding the IEEE 802.11n amendment,” *IEEE Circuits and Systems Magazine*, vol. 8, no. 1, pp. 28-54, First Quarter 2008.
- [39] R. V. Nee and R. Parsed, *OFDM for Wireless Multimedia Communication*, MA: Artech House, 2000.
- [40] F. Classen and Myer, “Frequency synchronization algorithms for OFDM systems suitable for communication over frequency selective fading channels,” in *Proceedings of IEEE Vehicular Technology Conference*, June 1994, pp. 1655–1659.
- [41] F. Daffara and A. Chouly, “Maximum likelihood frequency detectors for orthogonal multicarrier systems,” in *Proceedings of IEEE International Conference on Communications*, May 1993, pp. 766–771.
- [42] M. Luise and R. Reggiannini, “Carrier frequency acquisition and tracking for OFDM systems,” *IEEE Transactions on Communications*, vol. 44, pp. 1590–1598, November 1996.
- [43] F. Daffara and O. Adami, “A new frequency detector for orthogonal multicarrier transmission techniques,” in *Proceedings of IEEE Vehicular Technology Conference*, July 1995, pp. 804-809.
- [44] M. Okada, S. Hara, S. Komaki, and N. Morinaga, “Optimum synchronization of orthogonal multi-carrier modulated signals,” in *Proceedings of IEEE PIMRC*, October 1996, pp. 863–867.
- [45] B. Chen and H. Wang, “Blind estimation of OFDM carrier frequency offset via oversampling,” *IEEE Transactions on Signal Processing*, vol. 52, no. 7, pp. 2047–2057, July 2004.

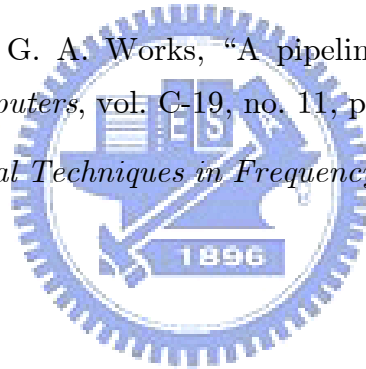
- [46] M. Luisem M. Marselli, and R. Reggiannini, “Low-complexity blind carrier frequency recovery for OFDM signals over frequency-selective radio channels,” *IEEE Transactions on Communications*, vol. 50, no. 7, pp.1182–1188, July 2002.
- [47] G. T. Gil, I. H. Sohn, J. K. Park, and Y. H. Lee, “Joint ML estimation of carrier frequency, channel, I/Q mismatch, and DC offset in communication receivers,” *IEEE Transactions on Vehicular Technology*, vol. 54, no. 1, pp. 338–349, January 2005.
- [48] G. Xing, M. Shen, and H. Liu, “Frequency offset and I/Q imbalance compensation for direct-conversion receivers,” *IEEE Transactions on Wireless Communications*, vol. 4, no. 2, pp. 673–680, March 2005.
- [49] P. Zhang, T. Nguyen, C. Lam, D. Gambetta, T. Soorapanth, B. Cheng, S. Hart, I. Sever, T. Bourdi, A. Tham, and B. Razavi, “A 5-GHz direct conversion CMOS transceiver,” *IEEE Journal of Solid-State Circuits*, vol. 38, no. 12, pp. 2232–2238, December 2003.
- [50] J. Y. Yu, M. F. Sun, T. Y. Hsu, and C. Y. Lee, "A novel technique for I/Q imbalance and CFO compensation in OFDM systems," in *Proceedings of IEEE ISCAS*, May 2005, pp. 6030–6033.
- [51] T. Pollet, M. van Bladel, M. Moeneclaey, “BER sensitivity of OFDM systems to carrier frequency offset and wiener phase noise,” *IEEE Transactions on Communications*, vol. 43, pp.191–193, April 1995.
- [52] P. Kenington, *RF and Baseband Techniques for Software Defined Radio*, Norwood, MA: Artech House, 2005.
- [53] T. Yuba and Y. Sanada, “Decision directed scheme for IQ imbalance compensation on OFCDM direct conversion receiver,” *IEICE Transactions on Communications*, vol. E89-B, no. 1, pp. 184–190, January 2006.
- [54] A. Tarighat, R. Bagheri, and A. H. Sayed, “Compensation schemes and performance analysis of IQ imbalance in OFDM receivers,” *IEEE Transactions on Signal Processing*, vol. 53, no. 8, pp. 3257–3268, August 2005.
- [55] J. Tubbax, B. Come, L. Van der Perre, S. Donnay, M. Engels, H. De Man, and M. Moonen, “Compensation of IQ imbalance and phase noise in OFDM systems,” *IEEE Transactions on Wireless Communications*, vol. 4, no. 3, pp. 872–877, May 2005.

- [56] G. T. Gil, Y. D. Kim, and Y. H. Lee, "Non-data-aided approach to I/Q mismatch compensation in low-IF receivers," *IEEE Transactions on Signal Processing*, vol. 55, no. 7, pp. 3360–3365, July 2007.
- [57] F. Horlin, S. De Rore, E. Lopez-Estraviz, F. Naessens, and L. Van der Perre, "Impact of frequency offsets and IQ imbalance on MC-CDMA reception based on channel tracking," *IEEE Journal on Selected Areas in Communications*, vol. 24, no. 6, pp. 1179–1188, June 2006.
- [58] L. Anttila, M. Valkama, and M. Renfors, "Frequency-selective I/Q mismatch calibration of wideband direct-conversion transmitters," *IEEE Transactions on Circuits and Systems II, Express Briefs*, vol. 55, no. 4, pp. 359–363, April 2008.
- [59] E. Lopez-Estraviz, S. De Rore, F. Horlin, and L. Van der Perre, "Optimal training sequences for joint channel and frequency-dependent IQ imbalance estimation in OFDM-based receivers," in *Proceedings of IEEE International Conference on Communications*, June 2006, pp. 4595–4600.
- [60] E. Cetin, I. Kale, and R.C.S. Morling, "Adaptive self-calibrating image rejection receiver," in *Proceedings of IEEE International Conference on Communications*, June 2004, pp. 2731–2735.
- [61] M. F. Sun, J. Y. Yu, and T. Y. Hsu, "Estimation of carrier frequency offset with I/Q mismatch using pseudo-offset injection in OFDM systems," *IEEE Transactions on Circuits and Systems I, Regular Papers*, vol. 55, no. 3, pp. 943–952, April 2008.
- [62] M. Valkama, M. Renfors, and V. Koivunen, "Compensation of frequency-selective I/Q imbalances in wideband receivers: models and algorithms," in *Proceedings of IEEE Workshop on Signal Processing Advances in Wireless Communications*, March 2001, pp. 42–45.
- [63] J. Tuthill and A. Cantoni, "Efficient compensation for frequency-dependent errors in analog reconstruction filters used in IQ modulators," *IEEE Transactions on Communications*, vol. 53, no. 3, pp. 489–496, March 2005.
- [64] J. G. Andrews, A. Ghosh, and R. Muhamed, *Fundamentals of WiMAX: Understanding Broadband Wireless Networking*, Prentice Hall, 2007.

- [65] H. H. Chen, Y. C. Yeh, Q. Bi, and A. Jamalipour, "On a MIMO-based open wireless architecture: space-time complementary coding," *IEEE Communications Magazine*, vol. 45, no. 2, pp. 104–112, February 2007.
- [66] E. Cavus and B. Daneshrad, "A very low-complexity space-time block decoder (STBD) ASIC for wireless systems," *IEEE Transactions on Circuits and Systems I. Regular Papers*, vol. 53, no. 1, pp. 60–69, January 2006.
- [67] S. Noh, Y. Jung, S. Lee, and J. Kim, "Low-complexity symbol detector for MIMO-OFDM-based wireless LANs," *IEEE Transactions on Circuits and Systems II, Express Briefs*, vol. 53, no. 12, pp. 1403–1407, December 2006.
- [68] Z. Guo and P. Nilsson, "A VLSI implementation of MIMO detection for future wireless communications," in *Proceedings of IEEE PIMRC*, September 2003, pp. 2852–2856.
- [69] J. Akhtman and L. Hanzo, "Advanced channel estimation for MIMO-OFDM in realistic channel conditions," in *Proceedings of IEEE International Conference on Communications*, June 2007, pp. 2528–2533.
- [70] W. G. Song and J. T. Lim, "Channel estimation and signal detection for MIMO-OFDM with time varying channels," *IEEE Communications Letters*, vol. 10, no. 7, pp. 540–542, July 2006.
- [71] Y. Li, N. Seshadri, and S. Ariyavisitakul, "Channel estimation for OFDM systems with transmitter diversity in mobile wireless channels," *IEEE Journal on Selected Areas in Communications*, vol. 17, no. 3, pp. 461–471, March 1999.
- [72] R. Nilsson, O. Edfors, M. Sandell, and P. O. Borjesson, "An analysis of two-dimensional pilot symbol assisted modulation for OFDM," in *Proceedings of IEEE International Conference on Personal Wireless Communications*, December 1997, pp. 71–74.
- [73] S. Coleri, M. Ergen, A. Puri, and A. Bahai, "Channel estimation techniques based on pilot arrangement in OFDM systems," *IEEE Transactions on Broadcasting*, vol. 48, no. 3, pp. 223–229, September 2002.
- [74] A. Maltsev, V. Pestretsov, R. Maslennikov, and A. Khoryaev, "Triangular systolic array with reduced latency for QR-decomposition of complex matrices," in *Proceedings of IEEE ISCAS*, May 2006, pp. 385–388.

- [75] L. Boher, R. Rabineau, and M. Helard, “An efficient MMSE equalizer implementation for 4×4 MIMO-OFDM systems in frequency selective fast varying channels,” in *Proceedings of IEEE PIMRC*, September 2007, pp. 1–5.
- [76] G. H. Golub and C. F. Van Loan, *Matrix Computations*, The Johns Hopkins University Press, 1996.
- [77] J. Litva and T. K.-Y. Lo, *Digital Beamforming in Wireless Communications*, Artech House, 1996.
- [78] F. B. Gross, *Smart Antennas for Wireless Communications*, Mcgraw-Hill, 2005.
- [79] C. Balanis and P. I. Ioannides, *Introduction to Smart Antennas*, Morgan and Claypool Publishers, 2007.
- [80] M. Bartlett, *An Introduction to Stochastic Processes with Special References to Methods and Applications*, Cambridge University Press, 1961.
- [81] J. Capon, “High resolution frequency-wavenumber spectrum analysis,” *Proceedings of the IEEE*, vol. 57, no. 8, pp. 1408–1418, August 1969.
- [82] H. Van Trees, *Optimum Array Processing: Part IV of Detection, Estimation, and Modulation Theory*, Wiley, 2002.
- [83] A. Barabell, “Improving the resolution performance of eigenstructure-based direction-finding algorithms,” in *Proceedings of IEEE ICASSP*, April 1983, pp. 336–339.
- [84] V. T. Ermolaev and A. B. Gershman, “Fast algorithm for minimum-norm direction-of-arrival estimation,” *IEEE Transactions on Signal Processing*, vol. 42, no. 9, pp. 2389–2394, September 1994.
- [85] R. Schmidt, “Multiple emitter location and signal parameter estimation,” *IEEE Transactions on Antennas and Propagation*, vol. AP-34, no. 2, pp. 276–280, March 1986.
- [86] L. C. Godara, “Applications of antenna arrays to mobile communications, part I: performance improvement, feasibility, and system considerations,” *Proceedings of the IEEE*, vol. 85, no. 7, pp. 1031–1060, July 1997.
- [87] L. C. Godara, “Application of antenna arrays to mobile communications, part II: beam-forming and direction-of-arrival considerations,” *Proceedings of the IEEE*, vol. 85, no. 8, pp. 1195–1245, August 1997.

- [88] A. H. Sayed, *Fundamentals of Adaptive Filtering*, Wiley , 2003.
- [89] G. Hueber, Y. Zou, K. Dufrene, R. Stuhlberger, and M. Valkama, “Smart front-end signal processing for advanced wireless receivers,” *IEEE Journal of Selected Topics in Signal Processing*, vol. 3, no. 3, pp. 472–487, June 2009.
- [90] N. Prasad and X. Wang, “Interference suppression receivers for the cellular downlink channel,” *IEEE Journal on Selected Areas in Communications*, vol. 26, no. 3, pp. 517–529, April 2008.
- [91] L. Giacomini, L. Agarossi, G. Paltenghi, S. Okamura, M. Okada, and S. Komaki, “Co-channel interference cancellation based on MIMO OFDM systems,” *IEEE Wireless Communications*, vol. 9, no. 6, pp. 8–17, December 2002.
- [92] Vincent K. N. Lau and Yu-Kwong Ricky Kwok, *Channel Adaptive Technologies and Cross Layer Designs for Wireless Systems with Multiple Antennas: Theory and Applications*, Wiley, 2006.
- [93] H. L. Groginsky and G. A. Works, “A pipeline fast Fourier transform,” *IEEE Transactions on Computers*, vol. C-19, no. 11, pp. 1015–1019, November, 1970.
- [94] B. G. Goldberg, *Digital Techniques in Frequency Synthesis*, Mcgraw-Hill, 1995.





Appendix A

Derivation of (2.15)

The received frequency domain data Y_k in (2.15) is shown in (A.1). The first term of the right hand side is the decayed original signal transmitted in the k th sub-carrier, and the second term denotes the inter-carrier interference (ICI) from others.

$$Y_k = X_k H_k \left\{ \frac{(\sin \pi \varepsilon)}{N (\sin \pi \varepsilon / N)} \right\} e^{j\pi \varepsilon (N-1) / N} + \sum_{k=-K, l \neq k}^K X_l H_l \left\{ \frac{(\sin \pi \varepsilon)}{N (\sin \pi (l-k + \varepsilon) / N)} \right\} e^{j\pi \varepsilon (N-1) / N} e^{-j\pi (l-k) / N} + W_k \quad (\text{A.1})$$

The carrier frequency offset Δf is normalized to the sub-channel bandwidth ($\text{BW}_{\text{sub-carrier}} = 1 / NT_s$), and the relative frequency offset is shown as ε , i.e., $\varepsilon = \Delta f / (1 / NT_s) = NT_s \Delta f$. The detailed derivation of (A.1) is given below. The OFDM transmission symbol is given by the N point complex modulation sequence

$$x_n = \frac{1}{N} \sum_{k=-K}^K X_k e^{j2\pi nk / N} ; n = 0, \dots, N-1 \quad (\text{A.2})$$

It consists of $2K + 1$ complex sinusoids which have been modulated with $2K + 1$ complex modulation values X_k . After passing through the band-pass channel, the received sequence can be expressed as

$$y_n = \frac{1}{N} \left[\sum_{k=-K}^K X_k H_k e^{j2\pi n(k+\varepsilon)/N} \right] + w_n ; n = 0, \dots, N-1 \quad (\text{A.3})$$

After the fast Fourier transform (FFT) in the receiver, the frequency domain data is given by

$$\begin{aligned} Y_l &= \sum_{n=0}^{N-1} y_n e^{-j2\pi ln/N} \\ &= \sum_{n=0}^{N-1} \frac{1}{N} \left[\sum_{k=-K}^K X_k H_k e^{j2\pi n(k+\varepsilon)/N} \right] e^{-j2\pi ln/N} + \sum_{n=0}^{N-1} w_n e^{-j2\pi ln/N} \\ &= \frac{1}{N} \sum_{n=0}^{N-1} \sum_{k=-K}^K X_k H_k e^{j2\pi n(k+\varepsilon)/N} e^{-j2\pi ln/N} + W_k \\ &= \frac{1}{N} \sum_{n=0}^{N-1} \sum_{k=-K}^K X_k H_k e^{j2\pi n(k-l+\varepsilon)/N} + W_k \\ &= \frac{1}{N} \sum_{k=-K}^K X_k H_k \left(1 + e^{j2\pi \cdot 1 \cdot (k-l+\varepsilon)/N} + \dots + e^{j2\pi \cdot (N-1) \cdot (k-l+\varepsilon)/N} \right) + W_k \end{aligned} \quad (\text{A.4})$$

To simplify the notation, the noise term is ignored in the following derivation. Firstly, we consider the l_{th} term ($k = l$) only, and the result is given by

$$\begin{aligned} \frac{1}{N} X_l H_l \left(1 + e^{j2\pi \cdot 1 \cdot \varepsilon/N} + \dots + e^{j2\pi \cdot (N-1) \cdot \varepsilon/N} \right) &= \frac{1}{N} X_l H_l \frac{1 - \left(e^{j2\pi \varepsilon/N} \right)^N}{1 - e^{j2\pi \varepsilon/N}} \\ &= \frac{1}{N} X_l H_l \frac{1 - e^{j2\pi \varepsilon}}{1 - e^{j2\pi \varepsilon/N}} \end{aligned} \quad (\text{A.5})$$

Furthermore, $1 - e^{j2\pi \varepsilon}$ and $1 - e^{j2\pi \varepsilon/N}$ can be expressed as

$$\begin{aligned}
1 - e^{j2\pi\varepsilon} &= 1 - (\cos(\pi\varepsilon) + j \sin(\pi\varepsilon))^2 \\
&= [\cos^2(\pi\varepsilon) + \sin^2(\pi\varepsilon)] - [\cos^2(\pi\varepsilon) - \sin^2(\pi\varepsilon) + 2j \cos(\pi\varepsilon) \sin(\pi\varepsilon)] \\
&= 2 \sin^2(\pi\varepsilon) - 2j \cos(\pi\varepsilon) \sin(\pi\varepsilon) \\
&= -2j \sin(\pi\varepsilon) [\cos(\pi\varepsilon) + j \sin(\pi\varepsilon)] \\
&= -2j \sin(\pi\varepsilon) e^{j\pi\varepsilon}
\end{aligned} \tag{A.6}$$

$$\begin{aligned}
1 - e^{j2\pi\varepsilon/N} &= 1 - (\cos(\pi\varepsilon/N) + j \sin(\pi\varepsilon/N))^2 \\
&= -2j \sin(\pi\varepsilon/N) e^{j\pi\varepsilon/N}
\end{aligned} \tag{A.7}$$

From (A.6) and (A.7), (A.5) can be rewritten as

$$\begin{aligned}
\frac{1}{N} X_l H_l \frac{-2j \sin(\pi\varepsilon) e^{j\pi\varepsilon}}{-2j \sin(\pi\varepsilon/N) e^{j\pi\varepsilon/N}} \\
= \frac{1}{N} X_l H_l \frac{\sin(\pi\varepsilon)}{\sin(\pi\varepsilon/N)} e^{j\pi\varepsilon(1-1/N)}
\end{aligned} \tag{A.8}$$

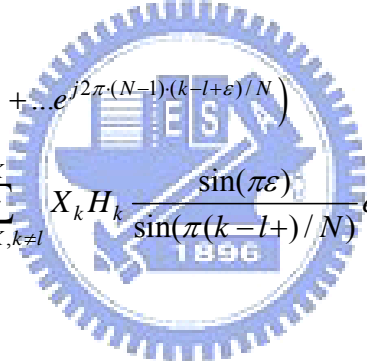
It is clear to see that (A.8) is the first term of the right hand side in (A.1). For the case $k \neq l$, i.e., ICI, the result is given by

$$\begin{aligned}
\frac{1}{N} \sum_{k=-K, k \neq l}^K X_k H_k \left(1 + e^{j2\pi \cdot 1 \cdot (k-l+\varepsilon)/N} + \dots + e^{j2\pi \cdot (N-1) \cdot (k-l+\varepsilon)/N} \right) \\
= \frac{1}{N} \sum_{k=-K, k \neq l}^K X_k H_k \frac{1 - e^{j2\pi(k-l+\varepsilon)}}{1 - e^{j2\pi(k-l+\varepsilon)/N}}
\end{aligned} \tag{A.9}$$

By the same technique described above, the following equation holds

$$\begin{aligned}
& \frac{1 - e^{j2\pi(k-l+\varepsilon)}}{1 - e^{j2\pi(k-l+\varepsilon)/N}} \\
&= \frac{-2j \sin(\pi(k-l+\varepsilon)) e^{j\pi(k-l+\varepsilon)}}{-2j \sin(\pi(k-l+\varepsilon)/N) e^{j\pi(k-l+\varepsilon)/N}} \\
&= \frac{\sin(\pi(k-l+\varepsilon))}{\sin(\pi(k-l+\varepsilon)/N)} e^{j\pi(k-l+\varepsilon)(1-1/N)} \\
&= \frac{\sin(\pi(k-l+\varepsilon))}{\sin(\pi(k-l+\varepsilon)/N)} e^{j\varepsilon(1-1/N)} e^{j\pi(k-l)} e^{-j\pi(k-l)/N} \\
&= \begin{cases} \frac{-\sin(\pi\varepsilon)}{\sin(\pi(k-l+\varepsilon)/N)} e^{j\varepsilon(1-1/N)} \cdot (-1) \cdot e^{-j\pi(k-l)/N}, & k-l = \pm 1, \pm 3, \dots \\ \frac{\sin(\pi\varepsilon)}{\sin(\pi(k-l+\varepsilon)/N)} e^{j\varepsilon(1-1/N)} \cdot (1) \cdot e^{-j\pi(k-l)/N}, & k-l = \pm 2, \pm 4, \dots \end{cases} \tag{A.10}
\end{aligned}$$

Therefore, (A.9) is rewritten as

$$\begin{aligned}
& \frac{1}{N} \sum_{k=-K, k \neq l}^K X_k H_k \left(1 + e^{j2\pi \cdot 1 \cdot (k-l+\varepsilon)/N} + \dots + e^{j2\pi \cdot (N-1) \cdot (k-l+\varepsilon)/N} \right) \\
&= \frac{1}{N} \sum_{k=-K, k \neq l}^K X_k H_k \frac{\sin(\pi\varepsilon)}{\sin(\pi(k-l+\varepsilon)/N)} e^{j\pi\varepsilon(N-1)/N} e^{-j\pi(k-l)/N} \tag{A.11}
\end{aligned}$$


It is clear that (A.11) denotes the second term of the right hand side in (A.1).

Appendix B

Derivation of (3.13)

To simplify the notation, let $2\pi\Delta fnT_s - \varphi = \alpha$, $2\pi\Delta fN_sT_s = \beta$, $2\pi\Delta fnT_s = \gamma$, $2\pi\Delta\theta nT_s = \mu$, and $2\pi\Delta\theta N_sT_s = \nu$.

Using (3.10) ~ (3.12), we have

$$\begin{aligned}
 & \text{Im}\{y_2\}\text{Re}\{y_1\} \\
 &= [(1-\varepsilon)\sin(\alpha+\beta)\cos(\mu+\nu) + \cos(\beta+\gamma)\sin(\mu+\nu)] \\
 &\quad \cdot \left\{ \text{Re}\{r\}^2 [\cos\gamma\cos\mu - (1-\varepsilon)\sin\alpha\sin\mu] \right. \\
 &\quad \left. - \text{Re}\{r\}\text{Im}\{r\} [\sin\gamma\cos\mu + (1-\varepsilon)\cos\alpha\sin\mu] \right\} \\
 &+ [(1-\varepsilon)\cos(\alpha+\beta)\cos(\mu+\nu) - \sin(\beta+\gamma)\sin(\mu+\nu)] \\
 &\quad \cdot \left\{ -\text{Im}\{r\}^2 [\sin\gamma\cos\mu + (1-\varepsilon)\cos\alpha\sin\mu] \right. \\
 &\quad \left. + \text{Re}\{r\}\text{Im}\{r\} [\cos\gamma\cos\mu - (1-\varepsilon)\sin\alpha\sin\mu] \right\}
 \end{aligned} \tag{B.1}$$

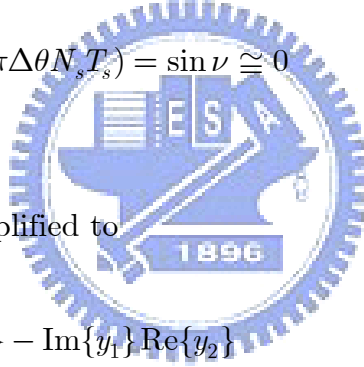
$$\begin{aligned}
 & \text{Im}\{y_1\}\text{Re}\{y_2\} \\
 &= [(1-\varepsilon)\sin\alpha\cos\mu + \cos\gamma\sin\mu] \\
 &\quad \cdot \left\{ \text{Re}\{r\}^2 [\cos(\beta+\gamma)\cos(\mu+\nu) - (1-\varepsilon)\sin(\alpha+\beta)\sin(\mu+\nu)] \right. \\
 &\quad \left. - \text{Re}\{r\}\text{Im}\{r\} [\sin(\beta+\gamma)\cos(\mu+\nu) + (1-\varepsilon)\cos(\alpha+\beta)\sin(\mu+\nu)] \right\} \\
 &+ [(1-\varepsilon)\cos\alpha\cos\mu - \sin\gamma\sin\mu] \\
 &\quad \cdot \left\{ -\text{Im}\{r\}^2 [\sin(\beta+\gamma)\cos(\mu+\nu) + (1-\varepsilon)\cos(\alpha+\beta)\sin(\mu+\nu)] \right. \\
 &\quad \left. + \text{Re}\{r\}\text{Im}\{r\} [\cos(\beta+\gamma)\cos(\mu+\nu) - (1-\varepsilon)\sin(\alpha+\beta)\sin(\mu+\nu)] \right\}
 \end{aligned} \tag{B.2}$$

Furthermore, $\text{Im}\{y_2\}\text{Re}\{y_1\} - \text{Im}\{y_1\}\text{Re}\{y_2\}$ can be expressed as

$$\begin{aligned}
& \text{Im}\{y_2\} \text{Re}\{y_1\} - \text{Im}\{y_1\} \text{Re}\{y_2\} \\
&= \text{Re}\{r\} \text{Im}\{r\} \left\{ \left[-\sin \nu \cos(\mu - \nu) \right] (1 - \varepsilon)^2 \right. \\
&\quad \cdot \left[-2 \sin \alpha \cos \alpha \cos \beta + \sin \alpha \sin \alpha \sin \beta - \cos \alpha \cos \alpha \sin \beta \right] \\
&\quad + \left[\sin \nu \cos(\mu - \nu) \right] \\
&\quad \cdot \left[-\sin \beta \cos \gamma \cos \gamma - 2 \cos \beta \sin \gamma \cos \gamma + \sin \gamma \sin \beta \sin \gamma \right] \left. \right\} \\
&\quad + \text{Re}\{r\}^2 (1 - \varepsilon) \sin \beta \cos \varphi \cos \nu \\
&\quad + \text{Im}\{r\}^2 (1 - \varepsilon) \sin \beta \cos \varphi \cos \nu
\end{aligned} \tag{B.3}$$

Since the sampling period T_s is 50ns and the P-CFO $\Delta\theta$ is set to 30 ppm, $\sin(2\pi\Delta\theta N_s T_s)$ can be approximated as (the value of $2\pi\Delta\theta N_s T_s$ is $2\pi \cdot 30 \cdot 10^{-6} \cdot 16 \cdot 50 \cdot 10^{-9}$)

$$\sin(2\pi\Delta\theta N_s T_s) = \sin \nu \cong 0 \tag{B.4}$$



Consequently, (B.3) can be simplified to

$$\begin{aligned}
& \text{Im}\{y_2\} \text{Re}\{y_1\} - \text{Im}\{y_1\} \text{Re}\{y_2\} \\
&\cong (1 - \varepsilon) \left(\text{Re}\{r\}^2 + \text{Im}\{r\}^2 \right) \sin \beta \cos \nu \cos \varphi
\end{aligned} \tag{B.5}$$

It is clear to know that (B.5) is the same as (3.13). Thus (3.14) can also be derived by the same technique described above.

Appendix C

Derivation of (4.12)

In the previous analysis, H_{24} is assumed to be equal to H_{25} since the coherence bandwidth of the channel is much larger than the inter-carrier spacing. After calculation of channel frequency response (CFR) from the 1st long training symbol, the CFR can be utilized to estimate the final IQ-M parameters. When the 2nd long training symbol is received, $\tilde{H}_{2,24}$ and $\tilde{H}_{2,25}$ can be expressed as

$$\tilde{H}_{2,24} = \alpha \cdot H_{2,24} + \beta \cdot \frac{P_{-24}^*}{P_{24}} \cdot H_{2,-24}^* \quad (\text{C.1})$$

$$\tilde{H}_{2,25} = \alpha \cdot H_{2,25} + \beta \cdot \frac{P_{-25}^*}{P_{25}} \cdot H_{2,-25}^* \quad (\text{C.2})$$

From (C.2), IQ-M parameters can be obtained by

$$\alpha = \frac{1}{H_{2,25}} \left(\tilde{H}_{2,25} - \beta \cdot \frac{P_{-25}^*}{P_{25}} \cdot H_{2,-25}^* \right) \quad (\text{C.3})$$

Replace the parameter α in (C.1) with (C.3), (C.1) can be rewritten as

$$\begin{aligned} \tilde{H}_{2,24} &= \frac{1}{H_{2,25}} \left(\tilde{H}_{2,25} - \beta \cdot \frac{P_{-25}^*}{P_{25}} \cdot H_{2,-25}^* \right) \cdot H_{2,24} + \beta \cdot \frac{P_{-24}^*}{P_{24}} \cdot H_{2,-24}^* \\ &= \frac{H_{2,24}}{H_{2,25}} \tilde{H}_{2,25} + \beta \left(\frac{P_{-24}^*}{P_{24}} \cdot H_{2,-24}^* - \frac{H_{2,24}}{H_{2,25}} \cdot \frac{P_{-25}^*}{P_{25}} \cdot H_{2,-25}^* \right) \end{aligned} \quad (\text{C.4})$$

From (C.4), IQ-M parameters can be solved by

$$\beta = \left(\tilde{H}_{2,24} - \frac{H_{2,24}}{H_{2,25}} \tilde{H}_{2,25} \right) \left/ \left(\frac{P_{-24}^*}{P_{24}} \cdot H_{2,-24}^* - \frac{H_{2,24}}{H_{2,25}} \cdot \frac{P_{-25}^*}{P_{25}} \cdot H_{2,-25}^* \right) \right. \quad (\text{C.5})$$

From (C.5), the original CFR $H_{2,k}$ is still unavailable now; however, we can apply the compensated CFR from the 1st long preamble to replace $H_{2,k}$. The final IQ-M parameters are

$$\beta = \left(\tilde{H}_{2,24} - \frac{\tilde{H}_{1,24}}{\tilde{H}_{1,25}} \tilde{H}_{2,25} \right) \left/ \left(\frac{P_{-24}^*}{P_{24}} \cdot H_{2,-24}^* - \frac{\tilde{H}_{1,24}}{\tilde{H}_{1,25}} \cdot \frac{P_{-25}^*}{P_{25}} \cdot H_{2,-25}^* \right) \right. \quad (\text{C.6})$$

$$\alpha = 1 - \beta^*$$



Appendix D

Supplementary of OFDM-Based System Specification

This appendix describes the characteristic of the OFDM-based communication systems used in this dissertation. The system parameters are summarized below.

D.1 SISO-OFDM Systems

D.1.1 Air Interface



The transmitter block diagram is shown in Figure D-1.

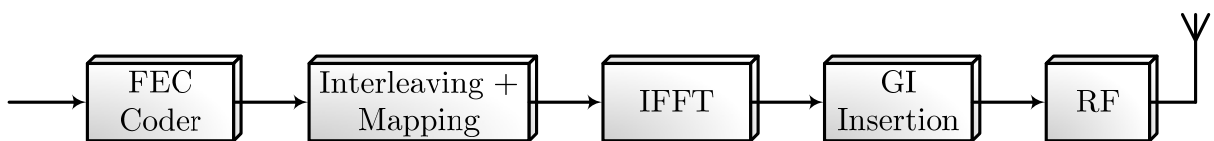


Figure D-1. Transmitter block diagram for IEEE 802.11g (ERP-OFDM only).

The generation of transmit signal is carried out by the following procedure:

- 1) Scrambler: the source data is scrambled to lower the probability of long sequences of ones or zeros.
- 2) Forward error correction (FEC) : the data is encoded to aid error correction.
- 3) Interleaving: it interleaves the bits to avoid the burst error.

- 4) QAM mapping: the sequence of bits are mapped to constellation points in the complex plane. It provides BPSK, QPSK, 16-QAM and 64-QAM modulation schemes.
- 5) Inverse fast Fourier transform (IFFT): it converts a block of frequency-domain constellation points to a time-domain block.
- 6) Guard interval (GI) insertion: the time-domain signal is preceded by the guard interval containing the last 16 samples of the OFDM symbol to enable the frequency-domain equalization.
- 7) Finally, the signal is transmitted by the RF module.

D.1.2 Major Parameters



IEEE 802.11g provides five modulation schemes: ERP-DSSS, ERP-CCK, ERP-OFDM, DSSS-OFDM and ERP-PBCC. In the following part, we only describe the ERP-OFDM mode, which is similar to IEEE 802.11a standard. The OFDM modulation parameters of IEEE 802.11g physical layer (PHY) are listed in TABLE D-1. It provides data rate from 6 to 54 Mbits/s with respect to the modulation BPSK, QPSK, 16-QAM, 64-QAM and the coding rate of convolutional encoder from 1/2 to 3/4. Each OFDM symbol consists of 48 data carriers and 4 pilots. TABLE D-2 lists the timing parameters. The duration of guard interval is 0.8 μ s. It implies that the tolerance of the maximum length of the channel impulse response is 0.8 μ s. The FFT symbol duration can be expressed as

$$T_{\text{FFT}} = \frac{1}{BW} \times N \quad (\text{D.1})$$

where BW and N are the signal bandwidth (20 MHz) and FFT size (64-point),

respectively. Thus, the OFDM symbol duration is

$$T_{\text{SYM}} = T_{\text{FFT}} + T_{\text{GI}} = 3.2 + 0.8 \mu\text{s} \quad (\text{D.2})$$

From TABLE D-1 and TABLE D-2, the data rate can be derived as

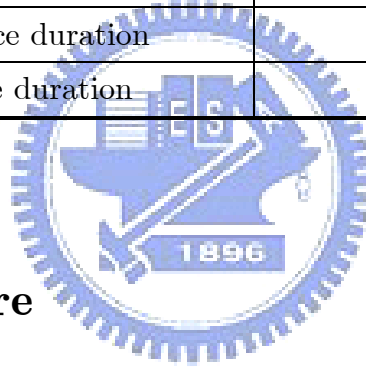
$$\text{Data rate} = \frac{N_{\text{SD}} \cdot N_{\text{BPSC}} \cdot R}{T_{\text{SYM}}} \quad (\text{D.3})$$

TABLE D-1. Modulation Parameters.

Data rate (Mbits/s)	Modulation	Coding rate (R)	Coded bits per sub-carrier (N_{BPSC})	Coded bits per OFDM symbol (N_{CBPS})	Data bits per OFDM symbol (N_{DBPS})
6	BPSK	1/2	1	48	24
9		3/4			36
12	QPSK	1/2	2	96	48
18		3/4			72
24	16-QAM	1/2	4	192	96
36		3/4			144
48	64-QAM	2/3	6	288	192
54		3/4			216

TABLE D-2. Timing Related Parameters.

Parameter	Value
N_{SD} : Number of data carriers	48
N_{SP} : Number of pilots	4
N_{ST} : Number of sub-carriers, total	$52(N_{SD}+N_{SP})$
Δ_F : sub-carrier frequency spacing	0.3125 MHz
T_{FFT} : IFFT/FFT period	3.2 μ s
$T_{PREAMBLE}$: PLCP preamble duration	16 μ s
T_{SIGNAL} : Duration of the Signal Field	4 μ s
T_{GI} : GI duration	0.8 μ s
T_{GI2} : Long training symbol GI duration	1.6 μ s
T_{SYM} : Symbol duration	4 μ s
T_{SHORT} : Short training sequence duration	8 μ s
T_{LONG} : Long training sequence duration	8 μ s



D.1.3 Frame Structure

As shown in Figure D-2, a complete PPDU defined in the IEEE 802.11g standard consists of the OFDM PLCP preamble, OFDM PLCP header, PHY service data unit (PSDU), tail bits and pad bits. In the standard, the OFDM PLCP preamble includes two kinds of OFDM training signals with different symbol periods, which are used for synchronization in the receiver. The PLCP header of the PPDU frame is composed of several fields, and the information conveyed in these fields is processed in the receiver to aid the demodulation and delivery of PSDU from the Data Field.

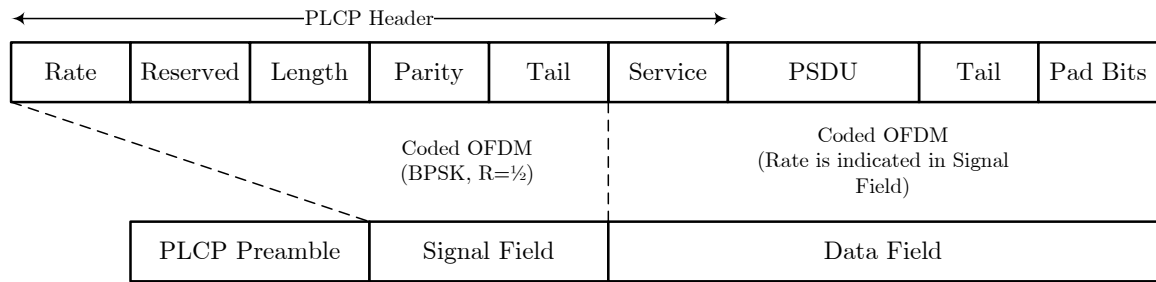


Figure D-2. PSDU frame format.

The main function of the PLCP Preamble field is for receiver synchronization, and the structure of the preamble defined in the IEEE 802.11g standard is shown in Figure D-3. The preamble includes two parts. The first part is composed of 10 repetitions of a short OFDM training signal with a symbol period of $0.8 \mu\text{s}$, which is a quarter of the fast Fourier transform (FFT) interval of a normal OFDM symbol, $3.2 \mu\text{s}$. The second part of the preamble consists of one cyclic prefix with $1.6 \mu\text{s}$ and two successive long preambles. The period of a long preamble is $3.2 \mu\text{s}$. Note that the length of the cyclic prefix in the second part of the preamble is two times longer than that of a normal data OFDM symbol, and the cyclic prefix is a copy of the latter half of the long OFDM training signal. In the following, the characteristics and functions of the training signals are described.

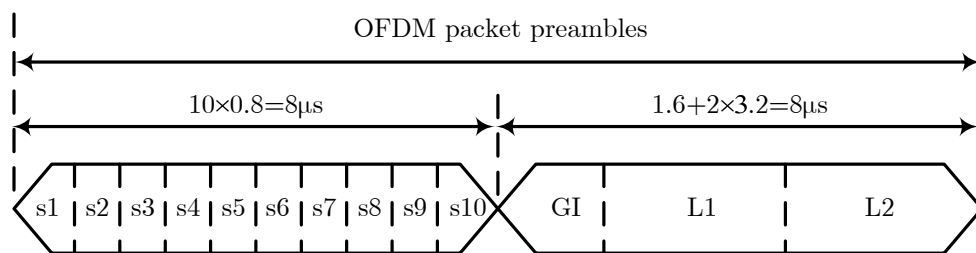


Figure D-3. OFDM training structure.

The short preamble is a periodic training sequence, i.e., t_1 to t_{10} are all the same short training symbols. The structure of short period could be utilized to estimate the timing and frequency quickly. The short preambles are constructed by the power normalized BPSK signals in the frequency domain. The long training symbol is two long training symbols, e.g., T_1 and T_2 . The long preamble is consisted of 52 BPSK signals in frequency domain, and these long preambles can facilitate the estimation of fading channel. These preambles in front of the packet is capable of synchronizing the received frame and estimating the channel state information. The PLCP training symbols are followed by Signal Field. Signal Field contains the information of the type of modulation and coding rate. It is always the BPSK modulation with coding rate 1/2. The symbols following the Signal Field is the Data Filed which is used to transmit the general information.



D.2 MIMO-OFDM Systems

D.2.1 Air Interface

The transmitter block diagram is shown in Figure D-4. The generation of transmit signal is carried out by the following procedure:

- 1) Scrambler: the source data is scrambled to lower the probability of long sequences of ones or zeros.
- 2) Forward error correction (FEC) : the data is encoded to aid error correction.
- 3) Spatial parser: the coded data is divided into blocks that are sent to different interleaving and QAM mapping devices.
- 4) Interleaving: it interleaves the bits to avoid the burst error.

- 5) QAM mapping: the sequence of bits are mapped to constellation points in the complex plane. It provides BPSK, QPSK, 16-QAM and 64-QAM modulation schemes.
- 6) STBC encoder: the constellation points from the spatial streams are separated into space-time streams using the STBC codeword.
- 7) Inverse fast Fourier transform (IFFT): it converts a block of frequency-domain constellation points to a time-domain block.
- 8) Guard interval (GI) insertion: the time-domain signal is preceded by the guard interval containing the last 16 samples of the OFDM symbol to enable the frequency-domain equalization.
- 9) Finally, the signal is transmitted by the RF modules.

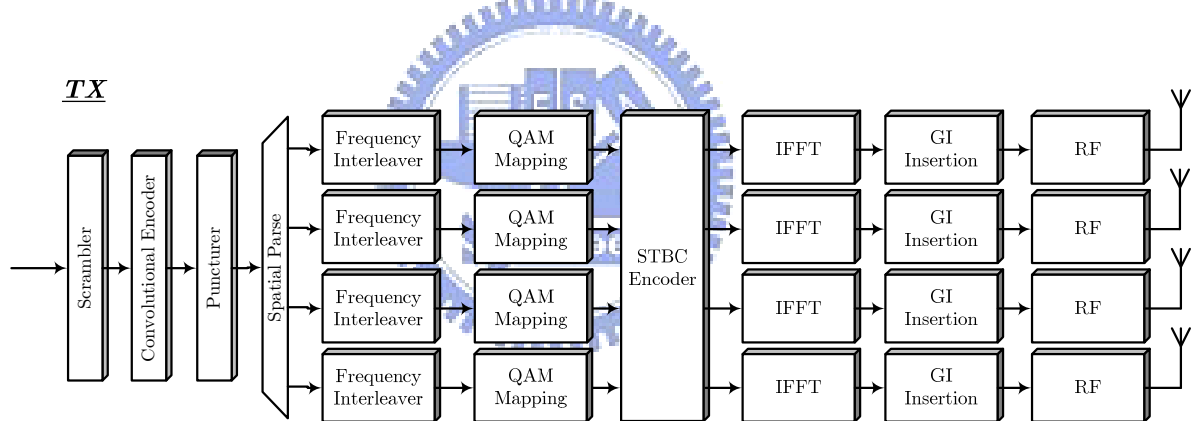


Figure D-4. Transmitter block diagram for MIMO-OFDM systems.

D.2.2 Major Parameters

The modulation and timing parameters of IEEE 802.11n PHY are listed in TABLE D-3 and TABLE D-4, respectively. Firstly, we consider the case without STBC encoding. Each OFDM symbol consists of 52 data carriers and 4 pilots. If there are N_{TX} transmit antennas, the data rate can be derived as

$$\text{Data rate} = \frac{N_{SD} \cdot N_{BPSK} \cdot R}{T_{SYM}} \cdot N_{TX} \quad (\text{D.4})$$

It provides data rate from $6.5 \times N_{TX}$ to $58.5 \times N_{TX}$ Mbits/s with respect to the modulation BPSK, QPSK, 16-QAM, 64-QAM and the coding rate of convolutional encoder from 1/2 to 3/4. If STBC encoding is applied in the MIMO transmission, the overall data rate can be reduced. For the sake of simplicity, we describe a 2×2 MIMO system with Alamouti scheme. The code matrix is defined as

$$C_{Alamouti} = \begin{bmatrix} c_1 & c_2 \\ c_2^* & -c_1^* \end{bmatrix} \quad (\text{D.5})$$

The elements of code matrix are the symbols to be transmitted. The columns of the matrix represent time slots and rows denote antennas. Hence, two time slots are required to transmit two symbols (code rate = 1). In the SISO system, the symbols c_1 and c_2 are transmitted in the first and the second time slot, respectively (Figure D-5). Hence, the data rate (efficient throughput) of the 2×2 MIMO system with Alamouti scheme equals the SISO case. However, the advantage of STBC systems is that the MIMO channel is exploited to provide reliable communications.

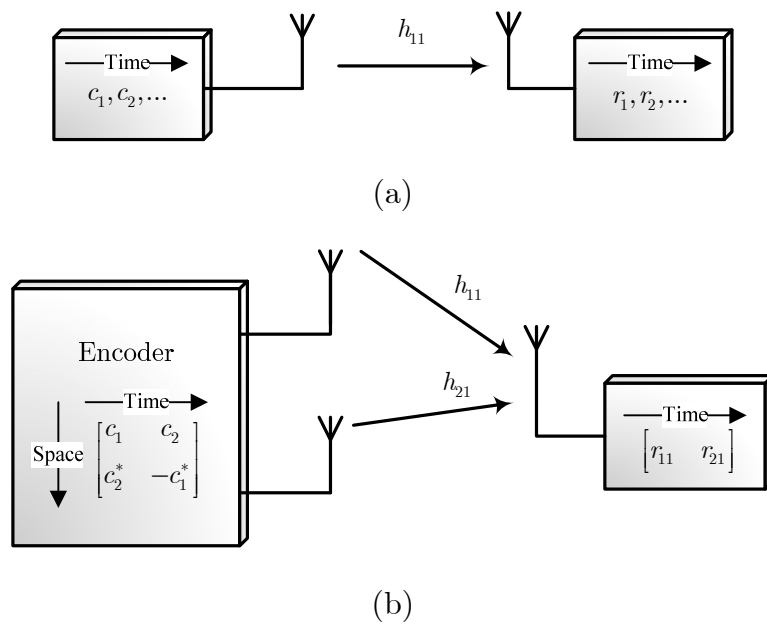


Figure D-5. (a) The block diagram of the SISO system. (b) The block diagram of the MIMO system with Alamouti scheme.

TABLE D-3. Modulation Parameters.

Data rate (Mbits/s)	Modulation	Coding rate (R)	Coded bits per sub-carrier (N_{BPSC})	Coded bits per OFDM symbol (N_{CBPS})	Data bits per OFDM symbol (N_{DBPS})
6.5	BPSK	1/2	1	52	26
9.75		3/4			39
13	QPSK	1/2	2	104	52
19.5		3/4			78
26	16-QAM	1/2	4	208	104
39		3/4			156
52	64-QAM	2/3	6	312	208
58.5		3/4			234

TABLE D-4. Timing Related Parameters.

Parameter	Value
N_{SD} : Number of data carriers	52
N_{SP} : Number of pilots	4
N_{ST} : Number of sub-carriers, total	$56(N_{SD}+N_{SP})$
Δ_F : sub-carrier frequency spacing	0.3125 MHz
T_{FFT} : IFFT/FFT period	3.2 μ s
$T_{PREAMBLE}$: PLCP preamble duration	16 μ s
T_{GI} : GI duration	0.8 μ s
T_{SYM} : Symbol duration	4 μ s

D.2.3 Frame Structure

As shown in Figure D-6, a complete PPDU defined in the IEEE 802.11n standard consists of the OFDM PLCP preamble, OFDM PLCP header, PHY service data unit (PSDU), tail bits and pad bits. In the standard, there are two kinds of preambles, i.e., legacy preamble and high throughput preamble. The PLCP header of the PPDU frame is composed of several fields, and the information conveyed in these fields is processed in the receiver to aid the demodulation and delivery of PSDU from the Data Field. The main function of the PLCP Preamble field is for receiver synchronization. The legacy preamble includes two parts. The first part is composed of 10 repetitions of a short OFDM training signal with a symbol period of 0.8 μ s, which is a quarter of the fast Fourier transform (FFT) interval of a normal OFDM symbol, 3.2 μ s. The second part of the preamble consists of one cyclic prefix with 1.6 μ s and two successive long preambles. The period of a long preamble is 3.2 μ s. Note that the length of the cyclic prefix in the second part of the preamble is two times longer than that of a normal data OFDM

symbol, and the cyclic prefix is a copy of the latter half of the long OFDM training signal. The characteristics and functions of legacy training signals are similar to the SISO system. Basically, high throughput short preamble is applied for timing and frequency acquisition and high throughput long preamble provides as a way for the receiver to estimate the channel state information.

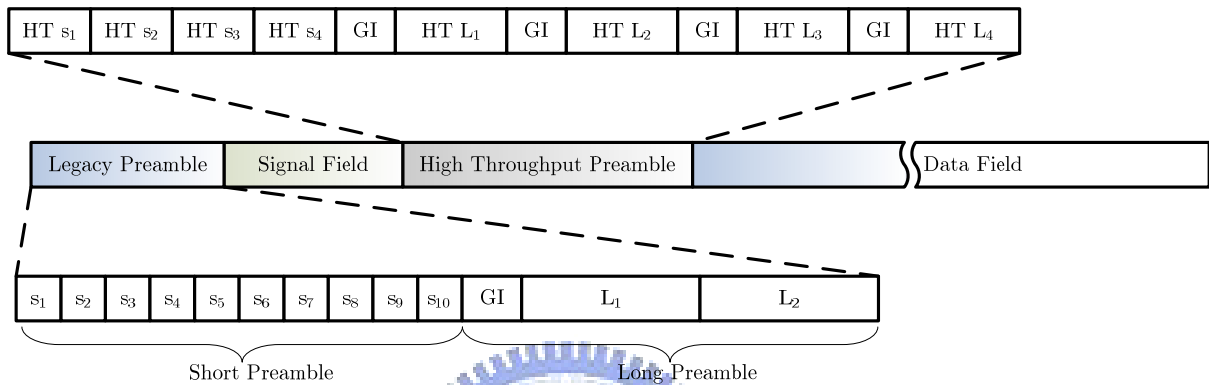
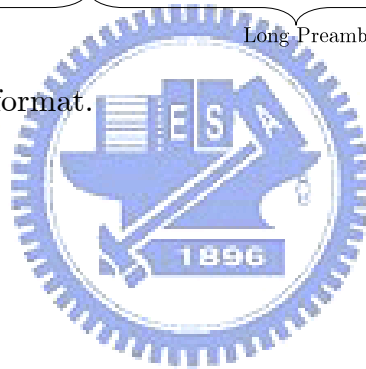


Figure D-6. PSDU frame format.



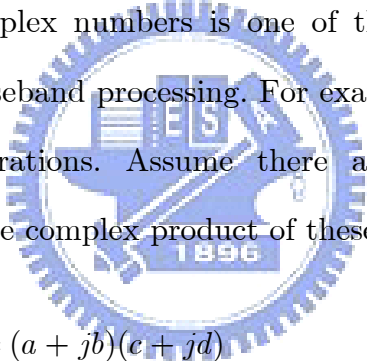
Appendix E

Some Circuit Implementation Issues

In this appendix, we describe some circuit techniques applied in this work.

E.1 Complex Multiplier

The multiplication of two complex numbers is one of the most common functions performed in MIMO-OFDM baseband processing. For example, it's mandatory in fast Fourier transform (FFT) operations. Assume there are two complex numbers, $A = a + jb$ and $B = c + jd$, the complex product of these two complex numbers is


$$\begin{aligned} A \cdot B &= (a + jb)(c + jd) \\ &= (ac - bd) + j(bc + ad) \end{aligned} \tag{E.1}$$

Form (E.1), it requires four multiplications and two additions. Instead of using direct implementation, the modified implementation is

$$\begin{aligned} \text{Real} &: ac - bd \\ \text{Imag} &: (a + b)(c + d) - ac - bd \end{aligned} \tag{E.2}$$

Form (E.2), it requires three multipliers and five adders. Therefore, one of the multiplications required in (E.1) is traded for three addition operations needed by (E.2).

The modified implementation requires three multipliers and five adders to lower the hardware cost (if the wordlength is sufficiently long). If the hardware uses fewer clock cycles to perform three additions than a single multiplication, the processing speed could be gained.

E.2 Fast Fourier Transform

To implement MIMO-OFDM modulation, four 64-point FFT module are used in this work. In MIMO-OFDM baseband processing, FFT and inverse FFT (IFFT) modules transform signals between the time domain and the frequency domain. In order to reduce the hardware complexity, a pipelined FFT structure in the MIMO-OFDM system is used. In this work, the FFT hardware architecture is radix-2 single-path delay feedback (R2SDF) pipeline structure [34], [93]. Figure E-1 shows the R2SDF pipeline architecture. This pipeline structure is suitable for real-time applications where input data arrive in sequential order. In the R2SDF, a modified radix-2 butterfly is used (Figure E-2). This architecture (multipliers and butterfly units) has 50% utilization rate since they are bypassed half of the time.

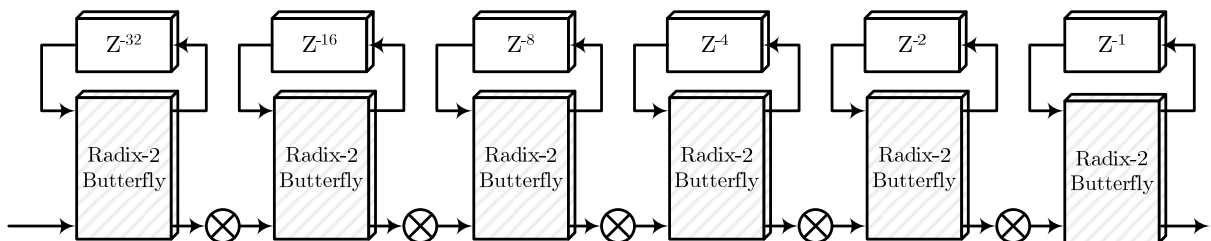


Figure E-1. The radix-2 single-path delay feedback architecture.

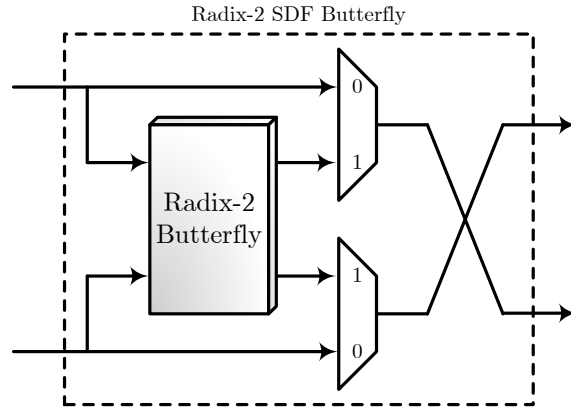


Figure E-2. Radix-2 SDF butterfly unit.

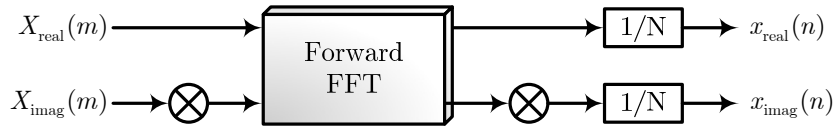


Figure E-3. The processing for IFFT operations.

For IFFT operations, it can be implemented by the forward FFT structure with some slick ways. Figure E-3 shows the IFFT calculation scheme. The expressions for N -point FFT and IFFT are

$$\text{FFT} : X(m) = \sum_{n=0}^{N-1} x(n)e^{-j2\pi nm/N} \quad (\text{E.3})$$

$$\text{IFFT} : x(n) = \frac{1}{N} \sum_{m=0}^{N-1} X(m)e^{j2\pi mn/N} \quad (\text{E.4})$$

From (E.4), the following equation holds

$$\begin{aligned} x^*(n) &= \frac{1}{N} \left[\sum_{m=0}^{N-1} X(m)e^{j2\pi mn/N} \right]^* \\ &= \frac{1}{N} \sum_{m=0}^{N-1} X^*(m)e^{-j2\pi mn/N} \end{aligned} \quad (\text{E.5})$$

Taking the complex conjugate of both sides of (E.5), a more straightforward expression for $x(n)$ can be obtained:

$$x(n) = \frac{1}{N} \left[\sum_{m=0}^{N-1} X^*(m) e^{-j2\pi mn/N} \right]^* \quad (\text{E.6})$$

It is clear to see that (E.6) is similar to the original forward FFT expression (E.3).

E.3 Numerically Controlled Oscillator

The numerically controlled oscillator (NCO) is used for frequency offset correction in MIMO-OFDM baseband processing. NCO generates sine and cosine waves that are mixed with the incoming baseband signal to correct the frequency error (Figure E-4). In the implantation of NCO, a direct digital frequency synthesizer (DDFS) is applied [94]. DDFS uses a digital technique to synthesize sine or cosine waves. The basic concept of DDFS is shown in Figure E-5. The frequency of the sine wave is proportional to the frequency control word. The phase accumulator outputs an address to the sine look-up table. The look-up table then outputs a samples value of the sine wave.

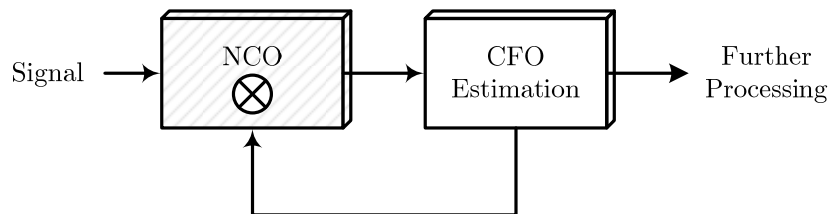


Figure E-4. Frequency offset correction with NCO.

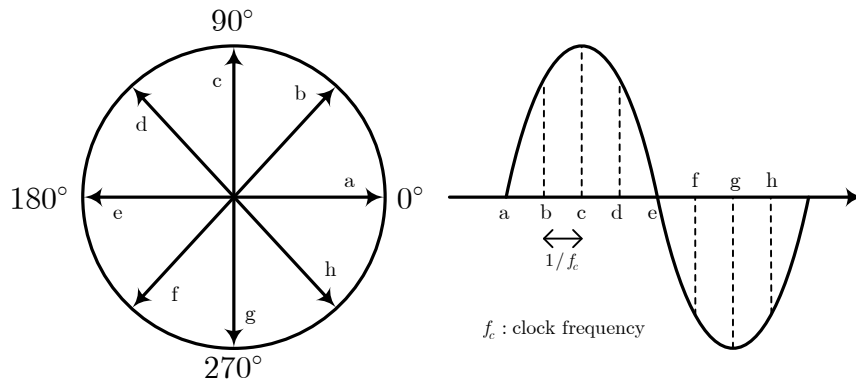


Figure E-5. The basic concept of DDFS.

In addition, the sine look-up table can be compressed using the symmetry property of the sine wave (Figure E-6). Therefore, look-up tables storing the sine and cosine values within $[0, \pi/4]$ are sufficient.

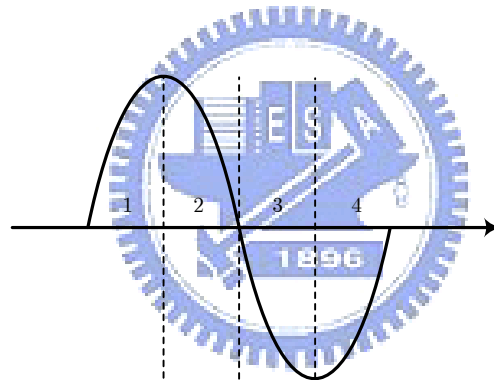


Figure E-6. The sine wave which is separated into four regions.

Appendix F

Fourier Transforms and Operations

Commonly used Fourier transforms and operations in this dissertation are listed in TABLE F-1 and TABLE F-2, respectively.

TABLE F-1. Fourier Transforms.

$x(t)$	$X(f)$
$\delta(t)$	1
1	$\delta(f)$
$\cos 2\pi f_0 t$	$\frac{1}{2}[\delta(f - f_0) + \delta(f + f_0)]$
$\sin 2\pi f_0 t$	$\frac{1}{2j}[\delta(f - f_0) - \delta(f + f_0)]$
$\delta(t - t_0)$	$\exp(-j2\pi f t_0)$
$\exp(j2\pi f_0 t)$	$\delta(f - f_0)$
$\exp(-a t), a > 0$	$\frac{2a}{a^2 + (2\pi f)^2}$
$u(t) = \begin{cases} 1 & t > 0 \\ 0 & t < 0 \end{cases}$	$\frac{1}{2}\delta(f) + \frac{1}{j2\pi f}$

TABLE F-2. Fourier Operations.

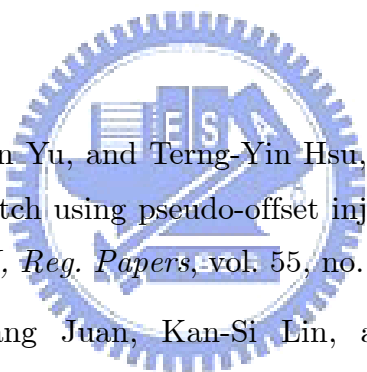
<i>Operations</i>	$x(t)$	$X(f)$
Scaling	$x(at)$	$\frac{1}{ a } X\left(\frac{f}{a}\right)$
Time Shifting	$x(t - t_0)$	$X(f) \exp(-j2\pi f t_0)$
Frequency Shifting	$x(t) \exp(j2\pi f_0 t)$	$X(f - f_0)$
Time Convolution	$x_1(t) * x_2(t)$	$X_1(f) X_2(f)$
Frequency Convolution	$x_1(t) x_2(t)$	$X_1(f) * X_2(f)$

About the Author

Ming-Fu Sun received the B.S. and M.S. degrees in Computer Science and Information Engineering from National Chiao Tung University, Hsinchu, Taiwan, R.O.C., in 2003 and 2005, respectively. In 2005, he joined the Institute of Computer Science of National Chiao Tung University, where he is currently working toward the Ph.D. degree. During 2006, he was a Lecturer in the Department of Electronics Engineering, Ming Hsin University of Science and Technology. In 2008, he received the outstanding research award from the Institute of Computer Science. His major research interests include signal processing for wireless communications, MIMO-OFDM systems, and associated digital VLSI circuits and systems.

Publication Lists

Journal papers:

- 
- [1] **Ming-Fu Sun**, Jui-Yuan Yu, and Terng-Yin Hsu, “Estimation of carrier frequency offset with I/Q mismatch using pseudo-offset injection in OFDM systems,” *IEEE Trans. Circuits Syst. I, Reg. Papers*, vol. 55, no. 3, pp. 943–952, April 2008.
 - [2] **Ming-Fu Sun**, Ta-Yang Juan, Kan-Si Lin, and Terng-Yin Hsu, “Adaptive frequency-domain channel estimator in 4×4 MIMO-OFDM modems,” *IEEE Trans. Very Large Scale Integr. (VLSI) Syst.*, Accepted, 2008.
 - [3] **Ming-Fu Sun** and Terng-Yin Hsu, “Preamble-assisted estimation for frequency-dependent I/Q mismatch in direct-conversion OFDM receivers,” *IEICE Trans. Commun.*, Accepted, 2009.

Conference papers:

- [1] Jui-Yuan Yu, **Ming-Fu Sun**, Terng-Yin Hsu, Chen-Yi Lee, “A novel technique for I/Q imbalance and CFO compensation in OFDM systems,” in *Proc. IEEE International Symposium on Circuits and Systems*, May 2005, pp. 6030-6033.
- [2] **Ming-Fu Sun**, You-Hsien Lin, Wei-Chi Lai, Ta-Yang Juan, Cheng-Yuan Lee, Yen-Her Chen, Chang-Ying Chuang, and Terng-Yin Hsu, “A 62.8 mW 4×4 MIMO-OFDM modem with one-symbol-locked timing recovery,”

frequency-dependent I/Q mismatch estimation and adaptive equalization,” submitted to *Proc. IEEE Asian Solid-State Circuits Conf.*, 2009.

Patents:

- [1] 劉炳傳, 李宗杰, 阮大洋, 孫明福, “運用點對點代理服務之點對點通訊裝置與方法,” 中華民國專利/申請中.
- [2] 劉炳傳, 李宗杰, 阮大洋, 孫明福, “Apparatus and method for providing peer-to-peer proxy services in peer-to-peer communications,” 美國專利/申請中.

